

Applications of the  
Similarity Renormalization Group  
to the Nuclear Interaction

DISSERTATION

Presented in Partial Fulfillment of the Requirements for  
the Degree Doctor of Philosophy in the  
Graduate School of The Ohio State University

By

Eric Jurgenson, B.A., M.S.  
Graduate Program in Physics  
The Ohio State University

2019

Dissertation Committee:

Prof. R. J. Furnstahl, Advisor

Prof. R. Perry

Prof. E. Sugarbaker

Prof. T. Ho

© Copyright by

Eric Jurgenson

2019

## ABSTRACT

The Similarity Renormalization Group (SRG) is investigated as a powerful yet practical method to modify nuclear potentials so as to reduce computational requirements for calculations of observables. The SRG proves to be versatile and robust in its treatment of these interactions and opens the door to a deeper understanding of the renormalization process.

Chiral Effective Field Theory ( $\chi$ EFT) provides a consistent and rigorous parametrization of the inter-nucleon interaction. While already softer than other available potentials, transformation via the Similarity Renormalization Group (SRG) brings numerous computational benefits. The hierarchy of many-body forces inherent in  $\chi$ EFT's are also treated consistently by the SRG's simple formalism. The SRG is a natural partner to this modern program of formulating the nuclear interaction.

The key feature of SRG transformations that leads to computational benefits is the decoupling of low-energy nuclear physics from high-energy details of the inter-nucleon interaction. We examine decoupling quantitatively for two-body observables and few-body binding energies. The universal nature of this decoupling is illustrated and errors from suppressing high-momentum modes above the decoupling scale are shown to be perturbatively small.

As implemented here, the SRG provides freedom to choose the form of its transformations and can be tailored to a given application. We explore the impacts of

various choices and their decoupling properties, specifically a block-type transformation inspired by previous renormalization group techniques. Sharp and smooth block-diagonal forms of phase-shift equivalent nucleon-nucleon potentials in momentum space are generated as examples and compared to analogous low-momentum interactions (“ $V_{\text{low } k}$ ”).

To explore the SRG evolution of many-body forces, we use as a laboratory a one-dimensional system of bosons with short-range repulsion and mid-range attraction, which emulates realistic nuclear forces. The free-space SRG is implemented for few-body systems in a symmetrized harmonic oscillator basis using a recursive construction analogous to no-core shell model implementations. This approach is fully unitary up to induced  $A$ -body forces when applied with an  $A$ -particle basis (e.g.,  $A$ -body bound-state energies are exactly preserved). The oscillator matrix elements for a given  $A$  can then be used in larger systems. Errors from omitted induced many-body forces show a hierarchy of decreasing contribution to binding energies. An analysis of individual contributions to the growth of many-body forces demonstrates such a hierarchy and provides an understanding of its origins. Several other important sample calculations are explored in this model for future use in realistic systems.

Building on one-dimensional results we performed the first practical evolution of three-dimensional many-body forces within the No-Core Shell Model basis. Results for the  ${}^3\text{H}$  binding energy are consistent with previous calculations involving momentum-space evolution of only two-body forces, and validate expectations from calculations in the one-dimensional oscillator basis. When applied to  ${}^4\text{He}$  calculations, the two- and three-body oscillator matrix elements yield rapid convergence of

the ground-state energy with a small net contribution of the induced four-body force. The radius of light nuclei is also explored in the three-dimensional basis.

For Adrienne and Ethan

## ACKNOWLEDGMENTS

I am deeply indebted to my adviser, Dr. Richard Furnstahl, for his tireless efforts in my education. I am honored and privileged to have worked with him. I can only hope I have absorbed some measure of his educational, scientific, and collaborative ethics.

I am equally grateful to all the other members, past and present, of the Nuclear Theory Group who have contributed to a vibrant atmosphere of curiosity and helpfulness in research efforts. Especially Robert Perry, my almost-co-adviser, Eric Anderson my office mate, and the several postdocs, Scott Bogner, Lucas Platter, and Joaquín Drut.

Of course, without my collaborators much of this work would not have happened. Among those not already named, I want to thank especially Petr Navrátil and Achim Schwenk for their helpful discussions and guidance.

I also want to thank my committee members for their time and effort in evaluating and guiding me along this program.

This work would not be possible without the love and support of my wife Adrienne and son Ethan. Their constant presence has given me the emotional fuel for the day-to-day work.

I want to thank my parents and siblings, though far away, for their quiet understanding and encouragement of my challenges and successes.

Many friends have helped to make life fun here in Columbus - Jake and Nichole Knepper, our graduate school peers and pinochle partners, and their boys Joel and Zach, the Gethsemane Choir for all their love and support especially our good friends, Dick and Judy Reunning, Barb and Byron Ford, Bill Alsnauer for keeping me on my toes, and John Jacobs for being the friend that he always is.

I also must mention the numerous teachers who have instilled in me the perseverance to take this career path: Julie Britton, Joe Hunt, Barb Harken, Tom Stevens, Pat Mason, Uriel Nauenberg, and many others.



## VITA

April 3, 1981 .....	Born - New Brunswick, NJ, U.S.A.
May 2003 .....	B.A. Physics, University of Colorado, Boulder, Colorado
December 2008 .....	M.S. Physics, The Ohio State Univer- sity, Columbus, Ohio
September 2003 - present .....	Department of Physics, The Ohio State University, Columbus, Ohio

## PUBLICATIONS

### Research Publications

“Decoupling in the Similarity Renormalization Group for Nucleon-Nucleon Forces”, E.D. Jurgenson, S.K. Bogner, R.J. Furnstahl, R.J. Perry, Phys. Rev. **C** 78, 014003 (2008). arXiv:0711.4252 [nucl-th]

“Block Diagonalization using SRG Flow Equations”, E. Anderson, S.K. Bogner, R.J. Furnstahl, E.D. Jurgenson, R.J. Perry, A. Schwenk, Phys. Rev. **C** 77, 037001 (2008). arXiv:0801.1098 [nucl-th]

“Similarity Renormalization Group Evolution of Many-Body Forces in a One-Dimensional Model”, E.D. Jurgenson, R.J. Furnstahl, Nucl. Phys. **A** 818, 152 (2009). arXiv:0809.4199 [nucl-th]

“Evolution of Nuclear Many-Body Forces with the Similarity Renormalization Group”, E.D. Jurgenson, P. Navrátil, R.J. Furnstahl, Phys. Rev. Lett. **103**, 082501 (2009). arXiv:0905.1873 [nucl-th]

## **FIELDS OF STUDY**

Major Field: Physics

Studies in The Similarity Renormalization Group Approach to the Nuclear Interaction: Prof. Richard J. Furnstahl

# TABLE OF CONTENTS

	Page
Abstract . . . . .	ii
Dedication . . . . .	v
Acknowledgments . . . . .	vi
Vita . . . . .	viii
List of Tables . . . . .	xv
List of Figures . . . . .	xvii
Chapters:	
1. Introduction . . . . .	1
1.1 History . . . . .	1
1.2 Modern Many-Body Nuclear Physics . . . . .	4
1.3 Resolution and Renormalization . . . . .	7
1.4 Chiral Effective Field Theories . . . . .	10
1.5 Similarity Renormalization Group . . . . .	15

1.6	Thesis Organization . . . . .	18
2.	Similarity Renormalization Group . . . . .	21
2.1	Derivation . . . . .	21
2.2	Second Quantization . . . . .	31
3.	Decoupling in the momentum representation . . . . .	38
3.1	Benefits of Decoupling . . . . .	38
3.2	Mechanics of Decoupling . . . . .	42
3.3	Phase Shift Errors . . . . .	46
3.4	Decoupling and Deuteron Observables . . . . .	53
3.5	Decoupling and Few-Body Energies with the NCSM . . . . .	54
3.6	Block Diagonalization . . . . .	58
4.	One-Dimensional Model in the Harmonic Oscillator Basis . . . . .	71
4.1	Symmetrized Jacobi Harmonic Oscillator Basis . . . . .	73
4.2	One Dimension Potential . . . . .	78
4.3	Evolution of Many-Body Forces in Bound States . . . . .	82
4.3.1	Two-body Results . . . . .	82
4.3.2	Three-body Results . . . . .	84
4.3.3	Results for $A = 4$ and $A = 5$ . . . . .	85
4.4	Diagrammatic Analysis of Many-Body Force Evolution . . . . .	89

4.5	Fitting Three-Body Forces . . . . .	98
4.6	Evolving Individual Operators: A Study of Cutoff Behavior . . . . .	101
4.7	Convergence in the Oscillator Basis . . . . .	106
5.	Evolution of Many-Body Forces in the No-Core Shell Model (NCSM) . . . . .	112
5.1	Induced Many-Body Forces . . . . .	115
5.2	Convergence in $N_{\max} : G = T_{\text{rel}}$ . . . . .	119
5.3	Convergence in $N_{\max} : G = H_{\text{ho}}$ . . . . .	125
5.4	Radius Calculations . . . . .	127
6.	Concluding Remarks . . . . .	132
6.1	Recapitulation . . . . .	132
6.2	Plans for Future Investigations . . . . .	136
	Bibliography . . . . .	140
Appendices:		
A.	Chiral Effective Field Theories . . . . .	146
A.1	Basics of power counting . . . . .	147
A.2	Many-body forces . . . . .	150
A.3	The role of the $\Delta$ resonance . . . . .	155

B.	General Features of the Harmonic Oscillator Basis . . . . .	158
B.1	One-Dimensional Harmonic Oscillator Wavefunctions . . . . .	158
B.2	Truncation . . . . .	160
B.3	Cutoff Derivation . . . . .	163
B.4	Three-Dimensional Harmonic Oscillators . . . . .	165
B.5	Variational Properties . . . . .	167
C.	Symmetric Jacobi Oscillator Basis in One and Three Dimensions . . . . .	169
C.1	Jacobi Coordinates . . . . .	169
C.2	Transformation Brackets . . . . .	170
C.3	Symmetrization . . . . .	173
C.4	Hamiltonian Matrix Elements . . . . .	179
C.5	Three-Dimensional NCSM . . . . .	183
D.	Scaling properties . . . . .	187
D.1	Momentum Space NN calculations . . . . .	187
D.2	One Dimensional Jacobi Model . . . . .	188
D.3	Three Dimensional Jacobi NCSM . . . . .	190
D.4	Lab Frame in One and Three Dimensions . . . . .	193
E.	Spurious States from $G_s = H_{ho}$ . . . . .	195

F.	Single Particle Coordinate Oscillator Basis . . . . .	203
F.1	Embedding . . . . .	203
F.2	Symmetrization . . . . .	205
F.3	Center of Mass Separation . . . . .	210
F.4	Evolution Results . . . . .	213

## LIST OF TABLES

Table	Page
2.1 Various choices for $G_s$ considered to date. . . . .	23
4.1 Parameter sets for the two-body potential of Eq. (4.3). . . . .	79
4.2 Ground-state energies for two-body potentials from Table 4.1 with various strengths of the initial three-body potential Eqs. (4.4)–(4.5) with $\Lambda = 2$ and $n = 4$ for $A = 2, 3$ , and 4. . . . .	81
4.3 Optimal $\hbar\omega$ s for the potentials in Table 4.2 with $A = 2, 3$ , and 4. . .	82
5.1 Definitions of the various calculations used to study SRG evolution. .	113
E.1 A sampling of evolving $A = 3$ spectra under the choice $G_s = H_{\text{ho}}$ . The table uses values at $N_{\text{max}} = 20$ , which is large enough to display the effect, but small enough to display the entire spectrum. . . . .	197
E.2 A sampling of evolving spectra for $A = 4$ under the choice $G_s = H_{\text{ho}}$ . Again the table uses values at $N_{\text{max}} = 20$ . The upper block displays the two-body-only calculation while the lower block includes the two- and induced three-body forces. . . . .	200
E.3 A sampling of evolving ${}^3\text{H}$ spectra under the choice $G_s = H_{\text{ho}}$ in the realistic three-dimensional NCSM. The table uses values at $N_{\text{max}} = 20$ which is large enough to display the effect, but small enough to display the entire spectrum. . . . .	201



F.1 A sample of the spectrum resulting from the lab-frame basis at a small  $N_{\max}$  before and after separation by a  $H_{\text{cm}}$  term. The columns right of each list of energies show the center of mass and intrinsic energy level numbers,  $n$  and  $l$ . The last column shows the effective  $N_{\max}$  for the right-most spectra. The value of  $\beta\hbar\omega$  here is 5000. Note the “separated” values should be scaled by  $10^4$ . . . . . 212

## LIST OF FIGURES

Figure	Page
1.1 The Argonne V18 nuclear potential in coordinate (left) and momentum (right) representations. Notice the hard repulsive core at short-distance/high-momentum and small mid-range attractive well. The typical spacing within nuclei is indicated by the arrow. . . . .	2
1.2 Scientific interconnections within the UNEDF collaboration. . . . .	5
1.3 Two pictures illustrating common degrees of freedom (dof), interactions, and calculational techniques used in theoretical nuclear physics.	7
1.4 Two pictures of our 16th president. . . . .	9
1.5 A table showing the organization of EFT terms in Weinberg power counting. The figure is from [21]. . . . .	13
1.6 A simple illustration of $V_{low k}$ 's block diagonalizing and SRG's band diagonalizing forms. . . . .	16
2.1 Film strips of evolution for representative partial waves in the N <sup>3</sup> LO (500 MeV) interaction of Ref. [49] in the momentum representation. Partial waves shown are $^1S_0$ , $^3S_1$ , $^1P_1$ , and $^3F_3$ . . . . .	26
2.2 Film strips of evolution for representative partial waves in the N <sup>3</sup> LO (600 MeV) interaction of Ref. [49] in the momentum representation. Partial waves shown are $^1S_0$ , $^3S_1$ , $^1P_1$ , and $^3F_3$ . . . . .	27
2.3 Film strips of evolution for representative partial waves in the N <sup>3</sup> LO (550/600 MeV) interaction of Ref. [50] in the momentum representation. Partial waves shown are $^1S_0$ , $^3S_1$ , $^1P_1$ , and $^3F_3$ . . . . .	28

2.4	Film strips of evolution for representative partial waves in the AV18 interaction of Ref. [9] in the momentum representation. Partial waves shown are $^1S_0$ , $^3S_1$ , $^1P_1$ , and $^3F_3$ . . . . .	29
2.5	A diagrammatic decomposition of the SRG induced forces [47]. A circle at a vertex denotes a commutator with $T_{\text{rel}}$ . . . . .	34
3.1	Phase shifts and relative errors in the $^1S_0$ channel for SRG potentials evolved from the Argonne $v_{18}$ potential of Ref. [9]. The upper row shows cut and uncut potentials and phase shifts for the unevolved initial potential. The lower row shows the same for the initial potential evolved to $\lambda = 2.0 \text{ fm}^{-1}$ . . . . .	39
3.2	A snapshot of the contributions to the flow of the potential when using the $G_s = T_{\text{rel}}$ choice of SRG. From left to right, the pictures are $V_{\lambda=2.5}$ , 1st and 2nd rhs terms from Eq. (3.5), and $V_{\lambda=1.5}$ . The color scale for the middle pictures is scaled up for visibility. . . . .	43
3.3	Absolute value of the matrix element $\langle k V_s k' \rangle$ for a representative sampling of off-diagonal $(k, k')$ pairs as a function of $s$ , compared with the simple solutions from Eq. (3.7), which are straight lines (they agree at $s = 0$ ). The partial waves $^3S_1$ and $^3P_1$ are shown. . . . .	44
3.4	Phase shifts and relative errors in the $^1S_0$ channel for SRG potentials evolved from the N <sup>3</sup> LO (500 MeV) potential of Ref. [49]. The upper-left graph shows the phase shifts vs. energy for the uncut $\lambda = 2 \text{ fm}^{-1}$ potential and several cut versions with $n = 8$ . The other panels show the relative error as a function of the momentum cut parameter $\Lambda$ at various energies $E$ , $\lambda$ 's, and $n$ 's, respectively. . . . .	47
3.5	The phase shift errors computed in select partial waves. Other channels exhibit the same power-law dependence of the error for $\Lambda > \lambda$ . . . . .	50
3.6	The phase shift errors computed in the $^1S_0$ channel of the Argonne $V_{18}$ potential. Here the onset of the power-law slope is much less saturated at higher $\lambda$ 's, because this potential has higher-momentum components to be renormalized. . . . .	51
3.7	Sample phase shift error plots using other choices of $G_s$ . On the left is $G_s = T_{\text{rel}}^2$ and on the right is $G_s = H_D$ for partial waves $^1S_0$ (top) and $^3S_1$ (bottom). . . . .	52

3.8	The relative error vs. cut parameter $\Lambda$ of the deuteron energy (left), rms radius (center), and quadrupole moment (left) of the deuteron with several values of the regulator parameter $n$ indicated in the legends. In each case, the relative error is confirmed by the first-order perturbation theory shown in Eq. (3.13). . . . .	54
3.9	Calculations of the ${}^4\text{He}$ ground-state energy using the NCSM. On the left is the energy obtained from the NCSM for potentials evolved to several different $\lambda$ values as a function of the cut (regulator) momentum $\Lambda$ with $n = 8$ . On the right is the relative error of the energy for the $\lambda = 2 \text{ fm}^{-1}$ case as a function of the cut momentum (with $n = 8$ ) for several different harmonic oscillator basis sizes. Also shown is the slope of the error in the decoupling region predicted from perturbation theory (dotted line). . . . .	56
3.10	Calculations of the ${}^6\text{Li}$ ground-state energy using the NCSM. On the left is the energy obtained from the NCSM for potentials evolved to several different $\lambda$ values as a function of the cut (regulator) momentum $\Lambda$ with $n = 8$ . On the right is the relative error of the energy for the same $\lambda$ 's as a function of the cut momentum for the same $\lambda$ values but with two values of $n$ . . . . .	57
3.11	Comparison of momentum-space $V_{\text{low } k}$ (a) and SRG (b) block-diagonal potentials with $\Lambda_{\text{BD}} = 2 \text{ fm}^{-1}$ evolved from an $\text{N}^3\text{LO } {}^3\text{S}_1$ potential [49].	59
3.12	Comparison of momentum-space $V_{\text{low } k}$ (a) and SRG (b) block-diagonal potentials with $\Lambda_{\text{BD}} = 2 \text{ fm}^{-1}$ evolved from an $\text{N}^3\text{LO } {}^3\text{S}_1$ potential [49].	60
3.13	Evolution of the ${}^3\text{S}_1$ partial wave with a sharp block-diagonal flow equation with $\Lambda_{\text{BD}} = 2 \text{ fm}^{-1}$ at $\lambda = 4, 3, 2,$ and $1 \text{ fm}^{-1}$ . The initial $\text{N}^3\text{LO}$ potential is from Ref. [49]. The axes are in units of $k^2$ from 0–11 $\text{fm}^{-2}$ . The color scale ranges from $-0.5$ to $+0.5 \text{ fm}$ as in Fig. 3.11. . .	62
3.14	Same as Fig. 3.13 but for the ${}^1\text{P}_1$ partial wave. . . . .	62
3.15	Phase shifts for the ${}^3\text{S}_1$ partial wave from initial potentials $\text{N}^3\text{LO}$ and AV18 and the evolved sharp SRG block-diagonal potential with $\Lambda_{\text{BD}} = 2 \text{ fm}^{-1}$ at various $\lambda$ , in each case with the potential set identically to zero above $\Lambda_{\text{BD}}$ . . . . .	63

3.16	Errors in the phase shift (two partial waves) at $E_{\text{lab}} = 100$ MeV and three deuteron observables for the evolved sharp SRG block-diagonal potential with $\Lambda_{\text{BD}} = 2 \text{ fm}^{-1}$ for a range of $\lambda$ 's and a regulator with $n = 8$ . Two partial waves are shown. . . . .	64
3.17	Decoupling error plots using the sharp block-diagonal generator on two partial waves ( ${}^3S_1$ and ${}^1P_1$ ) in two different initial potentials (AV18 and N <sup>3</sup> LO (500 MeV)). . . . .	66
3.18	Evolution of the ${}^3S_1$ partial wave with a smooth ( $n = 4$ ) block-diagonal flow equation with $\Lambda_{\text{BD}} = 2.0 \text{ fm}^{-1}$ , starting with the N <sup>3</sup> LO potential from Ref. [49]. The flow parameter $\lambda$ is 3, 2, 1.5, and $1 \text{ fm}^{-1}$ . The axes are in units of $k^2$ from 0–11 $\text{fm}^{-2}$ . The color scale ranges from $-0.5$ to $+0.5 \text{ fm}$ as in Fig. 3.11. . . . .	67
3.19	Phase shift errors from potentials evolved with the smooth block-diagonal SRG. The block parameter is $\Lambda_{\text{BD}} = 2$ . Here the regulator of Eq. (3.23) uses $n = 4$ . . . . .	67
3.20	Evolution of the ${}^3S_1$ partial wave with a second-order exact block-diagonal flow of equation 3.25 with $\Lambda_{\text{BD}} = 2 \text{ fm}^{-1}$ at $\lambda = 4, 3, 2,$ and $1 \text{ fm}^{-1}$ . The initial N <sup>3</sup> LO potential is from Ref. [49]. The axes are in units of $k^2$ from 0–11 $\text{fm}^{-2}$ . The color scale ranges from $-0.5$ to $+0.5 \text{ fm}$ as in Fig. 3.11. . . . .	68
3.21	Evolved SRG potentials starting from Argonne $v_{18}$ in the ${}^1S_0$ (left) and ${}^1P_1$ (right) partial waves to $\lambda = 1 \text{ fm}^{-1}$ using a bizarre choice for $G_s$ (see text). . . . .	69
4.1	A snapshot of the embedding process involving the initial (unevolved) two-body potential. The far left is a two-body, one-dimensional, potential in momentum space [62] with axes labelled by $k^2$ , the middle shows that potential converted to the two-body symmetric oscillator space, and the far right shows it embedded in the symmetric three-body basis. Each box is a matrix element in the oscillator basis, and the matrix elements are organized in order of increasing energy. The oscillator basis axes are unmarked due to the complicated organization of those bases (see text). For visibility, a small basis with $N_{\text{max}} = 12$ is shown. . . . .	75

4.2	Same as in 4.1 but each matrix is now evolved to $\lambda = 2$ in each basis shown. Again, $N_{\max} = 12$ . . . . .	77
4.3	Potentials (dotted line, with axis on right) and probability distributions (other lines, with axis on left) for the lowest two-body bound state as a function of $x =  x_1 - x_2 $ at different stages in the SRG evolution ( $\lambda = 1/s^{1/4}$ ). The left plot is $V_\alpha$ and the right plot is $V_\beta$ (see Table 4.1).	80
4.4	Even part of the SRG potential $[V_s^{(2)}(p, p') + V_s^{(2)}(p, -p')]$ in dimensionless units as a function of $p$ and $p'$ for $\lambda = \infty, 5, 3,$ and $2$ (where $\lambda = 1/s^{1/4}$ ). The initial potential is $V_\alpha$ from Table 4.1. . . . .	83
4.5	The lowest bound-state energy $E_3$ for a three-particle system as a function of $\lambda$ with the initial two-body-only potential $V_\alpha$ . The (red) curves with squares include the full evolution of the Hamiltonian while the (black) curves with circles use the two-body potential evolved in the two-particle system. The right frame shows two additional results from varying $\sigma_1$ and $V_2$ from the values in Table 4.1. . . . .	84
4.6	Same as Fig. 4.5 but with initial potential $V_\beta$ . The right frame shows two additional results from varying $\sigma_2$ and $V_2$ from the values in Table 4.1.	86
4.7	The lowest bound-state energy $E_4$ for a four-particle system as a function of $\lambda$ with the initial two-body potential $V_\alpha$ and different initial three-body force strengths ( $c_E = \pm 0.05$ ). . . . .	87
4.8	The lowest bound-state energy $E_5$ for a 5-particle system as a function of $\lambda$ with an initial two-body-only $V_\alpha$ potential for several values of $N_{\max}$ . . . . .	89
4.9	Differences of two-body-only and two-plus-three-body $A = 3$ ground-state energies as a function of $\lambda$ . Each of the parameters of the potential $V_\alpha$ are varied in each plot as the other parameters are held constant. The upper panels vary the ranges while the lower vary the strengths; the left vary the attractive part and the right vary the repulsive part.	90
4.10	Same as Fig. 4.9 but for $V_\beta$ . . . . .	91
4.11	A diagrammatic decomposition of the SRG Eq. (4.6). A circle at a vertex denotes a commutator with $T_{\text{rel}}$ . . . . .	92

4.12	Contributions from individual terms to the $A = 3$ ground-state expectation value $d\langle V_\lambda^{(3)} \rangle / d\lambda$ for several different two- and three-body potentials, as indicated in the plots. We emphasize that $\lambda \leq 2$ is very small, comparable to $\lambda \leq 1.5 \text{ fm}^{-1}$ for NN forces in analogous calculations with the NCSM [35]. . . . .	95
4.13	Contributions from individual terms to the $A = 4$ ground-state expectation value $d\langle V_\lambda^{(4)} \rangle / d\lambda$ for several different initial three-body potentials, as indicated in the plots. We emphasize that $\lambda \leq 2$ is very small, comparable to $\lambda \leq 1.5 \text{ fm}^{-1}$ for NN forces in analogous calculations with the NCSM [35]. . . . .	97
4.14	Ground-state energy of the $A = 4$ system with $NN$ interaction evolved and then a three-body interaction term (with an exponential regulator) fit to the $A = 3$ ground-state energy. The calculation is repeated with a variation of the range parameter, $\Lambda$ . . . . .	99
4.15	Same as Fig. 4.14 but at one value of $\Lambda$ and a range over the regulator's sharpness parameter, $n_{\text{exp}}$ . . . . .	99
4.16	Same as Fig. 4.14 but now the $A = 3$ ground-state energy and a second piece of data, the first excited state for $A = 3$ , are fit to two three-body interaction terms. The first term is the same as in Fig. 4.14 and the second includes a gradient correction. . . . .	100
4.17	A sequence of plots showing the evolving components of the 3-body wavefunction for increasing $N_{\text{max}}$ . Each of these plots uses $\hbar\omega = 5$ . . . . .	103
4.18	A sequence of plots showing the evolving components of the 3-body wavefunction for fixed $N_{\text{max}}$ and varied $\hbar\omega$ . . . . .	104
4.19	A sequence of plots showing the evolving components of the 3-body wavefunction for fixed $\hbar\omega$ and varied $N_{\text{max}}$ . . . . .	105
4.20	A sequence of plots at high $N_{\text{max}}$ showing the evolving components of the many-body wavefunction for $A = 2, 3$ , and 4. . . . .	106

4.21	Decoupling in the three-particle system using the choice $G_s = T_{\text{rel}}$ . The initial $V_\alpha$ potential is evolved to each $\lambda$ shown in a basis with $N_{\text{max}} = 40$ . On the left only the two-body potential is evolved and embedded while the right involves the full unitarily transformed potential. Matrix elements of the potential are set to zero if one or both states have $N > N_{\text{cut}}$ and the resulting Hamiltonian is diagonalized to obtain the ground-state energies plotted. . . . .	107
4.22	Decoupling in the four-particle system using $G_s = T_{\text{rel}}$ . The initial $V_\alpha$ potential is evolved to each $\lambda$ shown in a basis with $N_{\text{max}} = 40$ . On the left only the two-body potential is evolved and embedded while the right involves the full unitarily transformed potential. Matrix elements of the potential are set to zero if one or both states have $N > N_{\text{cut}}$ and the resulting Hamiltonian is diagonalized to obtain the ground-state energies plotted. . . . .	108
4.23	Decoupling in the three-particle system with $G_s = H_{\text{ho}}$ . The initial $V_\alpha$ potential is evolved to each $\lambda$ shown in a basis with $N_{\text{max}} = 40$ . On the left only the two-body potential is evolved and embedded while the right involves the full unitarily transformed potential. Matrix elements of the potential are set to zero if one or both states have $N > N_{\text{cut}}$ and the resulting Hamiltonian is diagonalized to obtain the ground-state energies plotted. . . . .	110
4.24	Same as for Fig. 4.23 but for the $A = 4$ binding energy. On the left only the two+three-body potential is evolved and embedded while the right involves the full unitarily transformed potential. . . . .	111
5.1	Ground-state energy of ${}^3\text{H}$ as a function of the SRG evolution parameter, $\lambda$ . See Table 5 for the nomenclature of the curves. . . . .	115
5.2	Ground-state energy of ${}^4\text{He}$ as a function of $\lambda$ . Two $\hbar\omega$ s (left and right) and two $N_{\text{max}}$ 's (overlaid) are shown for comparison. . . . .	116
5.3	Binding energy of the alpha particle vs. the binding energy of the triton. The Tjon line from phenomenological NN potentials (dotted) is compared with the trajectory of SRG energies when only the NN interaction is kept (circles). When the initial and induced NNN interactions are included, the trajectory lies close to experiment for $\lambda > 1.7 \text{ fm}^{-1}$ (see inset). . . . .	118



5.4	Ground-state energy of ${}^3\text{H}$ as a function of the basis size $N_{\text{max}}$ for an $\text{N}^3\text{LO}$ NN interaction [49] evolved with the SRG using $G_s = T_{\text{rel}}$ to selected $\lambda$ 's. The same calculation is shown at two values of $\hbar\omega$ . . . . .	119
5.5	Ground-state energy of ${}^3\text{H}$ as a function of the basis size $N_{\text{max}}$ for an $\text{N}^3\text{LO}$ NN interaction [49] plus an initial NNN interaction [70, 74] evolved with the SRG using $G_s = T_{\text{rel}}$ to selected $\lambda$ s. . . . .	121
5.6	Ground-state energy of ${}^3\text{H}$ as a function of the basis size $N_{\text{max}}$ for an $\text{N}^3\text{LO}$ NN interaction [49] with and without an initial NNN interaction [70, 74]. Unevolved (“bare”) and Lee-Suzuki (L-S) results with $\hbar\Omega = 28 \text{ MeV}$ are compared with SRG at $\hbar\omega = 20 \text{ MeV}$ evolved to $\lambda = 2.0 \text{ fm}^{-1}$ . . . . .	122
5.7	Ground-state energy of ${}^4\text{He}$ as a function of the basis size $N_{\text{max}}$ for an $\text{N}^3\text{LO}$ NN interaction [49] with an initial NNN interaction [70, 74]. Unevolved (bare) results are compared with Lee-Suzuki (L-S) and SRG evolved to $\lambda = 2.0 \text{ fm}^{-1}$ at $\hbar\omega = 28$ and $36 \text{ MeV}$ . . . . .	124
5.8	Ground-state energy of ${}^3\text{H}$ as a function of the basis size $N_{\text{max}}$ for an evolving $\text{N}^3\text{LO}$ NN interaction [49] without an initial NNN interaction. Three values of oscillator parameter, $\hbar\omega = 28, 20,$ and $12 \text{ MeV}$ are shown for comparison. . . . .	125
5.9	Same as in Figure 5.8 but now including the initial NNN force [70, 74]. Note the qualitative form of convergence is not affected. . . . .	126
5.10	The ${}^3\text{H}$ radius as a function of basis size $N_{\text{max}}$ for two choices of $\hbar\omega$ , 20, and 28 MeV, corresponding to the optimal values for the bare and some evolved Hamiltonians. The straight dashed line indicates the best converged value at the optimal $\hbar\omega$ (28 MeV) for the LS effective potential at $N_{\text{max}} = 36$ . . . . .	129
5.11	The ${}^4\text{He}$ radius as a function of basis size $N_{\text{max}}$ for three choices of $\hbar\omega$ , 20, 28, and 36 MeV (corresponding to the optimal values for the bare and some evolved Hamiltonians). The solid lines are calculations that include induced NNN forces. The dashed lines are NN-only calculations. The straight dashed line indicates the best converged value at the optimal $\hbar\omega$ (36 MeV) for the LS effective potential at $N_{\text{max}} = 20$ . . . . .	130

A.1	3 and 4 nucleon amplitudes that occur at $\nu = 2$ . These terms will cancel each other out in an energy-independent formulation. Figure courtesy of Ref. [80]. . . . .	151
A.2	The leading order 3NFs at $\nu = 3$ . Figure courtesy of Ref. [80] . . . .	152
A.3	Sample 3NF corrections and leading 4NFs at $\nu = 4$ . A more complete list of 4NFs is in Fig. A.4. Figure courtesy of Ref. [80] . . . . .	153
A.4	Leading 4NFs at $\nu = 4$ . Permutations of vertex ordering and nucleon lines are implicit. Figure courtesy of Ref. [87] . . . . .	154
A.5	Leading NN two pion exchange graphs with explicit $\Delta$ (double solid line) arising at $\nu = 2$ . Figure courtesy of Ref. [80] . . . . .	156
A.6	Leading order 3NFs with explicit $\Delta$ arising at $\nu = 3$ , an enhancement over the deltaless theory. Figure courtesy of Ref. [80] . . . . .	156
B.1	On the left are shown the harmonic oscillator functions. On the right is the truncated momentum delta function $\delta(p - p')\Theta(p_{\max} - p)$ . In this MATLAB color scheme the red is positive and blue is negative. .	160
B.2	A two-body potential in the momentum representation. The axes are initial and final momenta, $k$ and $k'$ , from $-k_{\max}$ to $k_{\max}$ . On the upper-left is the original momentum basis two-body potential. The other three plots are the same potential after being converted to an oscillator basis and back. Notice the truncation of matrix elements above each $p_{\max}$ of the oscillator basis. . . . .	161
B.3	Harmonic oscillator functions up to $N_{\max}=28$ for $\hbar\omega = 2, 4, 8,$ and $16$ .	162
B.4	Variation of $p_{\max}$ with $\hbar\omega$ on the left and with $n$ on the right. . . . .	163
B.5	Plots showing the variational nature of the harmonic oscillator basis and the effect of SRG transformations within it. . . . .	167
C.1	The full symmetrizer for the $ N_2i_2; n_2\rangle$ space, with both physical and spurious states. A small, $N_{\max} = 10$ , basis is shown for clarity. Note also that Matlab has chopped off the last column when making the figure; this is a symptom of my very simple plotting routine. . . . .	176

C.2	The physical eigenvectors of the symmetrizer. Note vector components corresponding to $N_{\max}$ blocks in Fig. C.1. The same size basis as in Fig. C.1, $N_{\max} = 10$ , is shown. Again, Matlab has chopped off the last column. . . . .	177
D.1	SRG timings vs the parameter $s$ show no stiffening for large $s$ (small $\lambda$ ). The left shows timing results for N <sup>3</sup> LO (500 MeV) potentials in several partial waves and the right shows the same for Argonne $v_{18}$ but in a log-log plot. . . . .	188
D.2	Plots showing the scaling of One-D NCSM basis size and time to build those bases as a function of $N_{\max}$ for $A = 2, 3, 4, 5$ , and 6 bosons. . .	189
D.3	SRG timings vs the parameter $s$ show no stiffening for large $s$ (small $\lambda$ ). The log-log plot on the right gives a better view of the low $N_{\max}$ samples. . . . .	190
D.4	The left plot shows scaling of NCSM basis size with $N_{\max}$ for the two-, three-, and four-body systems. The right plot shows evolution timings vs. $s$ in realistic NCSM calculations for selected $A = 3$ partial waves. The legend indicates the dimension of the matrices being evolved. . .	191
D.5	Size of $m$ -scheme basis as a function of $N_{\max}$ for several light nuclei. Note the logarithmic scale in basis size. . . . .	192
D.6	A plot showing the scaling of One-D NCSM lab-frame basis or “ $m$ -scheme” size as a function of $N_{\max}$ for $A = 2, 3, 4$ bosons. Compare to Jacobi plots of Jacobi basis size in Fig. D.2. . . . .	194
E.1	A series of plots of the oscillator basis Hamiltonian in a reduced $N_{\max}$ basis as it is evolved using $G_s = T_{\text{rel}}$ (top) and $G_s = H_{\text{ho}}$ (bottom) to $\lambda = 7, 5, 4, 3, 2$ . The size of the basis shown is only $N_{\max} = 12$ for visibility. Larger bases look qualitatively similar. . . . .	196
E.2	An example of the discontinuous curves of two-body-only calculations characteristic of the $G_s = H_{\text{ho}}$ SRG. The two-body-only curves computed by evolving the $A = 2$ potential using $G_s = H_{\text{ho}}$ and embedding the result in the $A = 3$ basis to obtain the three-boson binding energy. The straight line labeled “2+3-body” is a check on the unitary evolution in the $A = 3$ space. . . . .	196

E.3	A series of plots of the $A = 3$ oscillator basis Hamiltonian in a reduced $N_{\max}$ basis as it is evolved using $G_s = H_{\text{ho}}$ . . . . .	198
E.4	A series of plots of the $A = 2$ oscillator basis Hamiltonian in a reduced $N_{\max}$ basis as it is evolved using $G_s = H_{\text{ho}}$ . . . . .	198
E.5	A series of plots of the $A = 2$ oscillator basis Hamiltonian in a reduced $N_{\max}$ basis as it is evolved using $G_s = H_{\text{d,osc}}$ . . . . .	200
F.1	A sample of the symmetrizer for the 2-body lab-frame problem on the top, and the corresponding non-zero eigenstates of the symmetrizer on the bottom. Here $N_{\max} = 12$ as a more realistic $N_{\max}$ would not be visible on the page. . . . .	207
F.2	The same as for Fig. F.1 but for $A = 3$ . Here $N_{\max} = 6$ as a more realistic $N_{\max}$ would not be visible on the page. . . . .	209

# CHAPTER 1

## INTRODUCTION

### 1.1 History

A complete understanding of the interaction between nucleons has been sought by physicists for more than seventy years, beginning with the pion exchange theory of Hideki Yukawa [1] in the 1930's, which set the paradigm of heavy boson exchange. Shortly after the discovery of the pion and confirmation of Yukawa's conjecture, nucleon-nucleon (NN) scattering experiments were interpreted as meaning that the NN interaction had a strong repulsive core, an intermediate ranged attraction, and strong tensor and spin-orbit forces [2]. Efforts to build an accurate NN potential that incorporated these features and was based on Yukawa's meson exchange idea were eventually quite successful by the late 1990's [3]. However, attempts to apply these meson-exchange interactions to many-body problems proved difficult.

Figure 1.1 shows an example of such an NN potential in both coordinate and momentum representations. The hard repulsive core in the left panel and the corresponding strong high-momentum matrix elements in the right panel represent short-distance physics, the details of which are irrelevant to low-energy physics. The specific coupling of the low- and high-energy states in the high-energy matrix elements shown

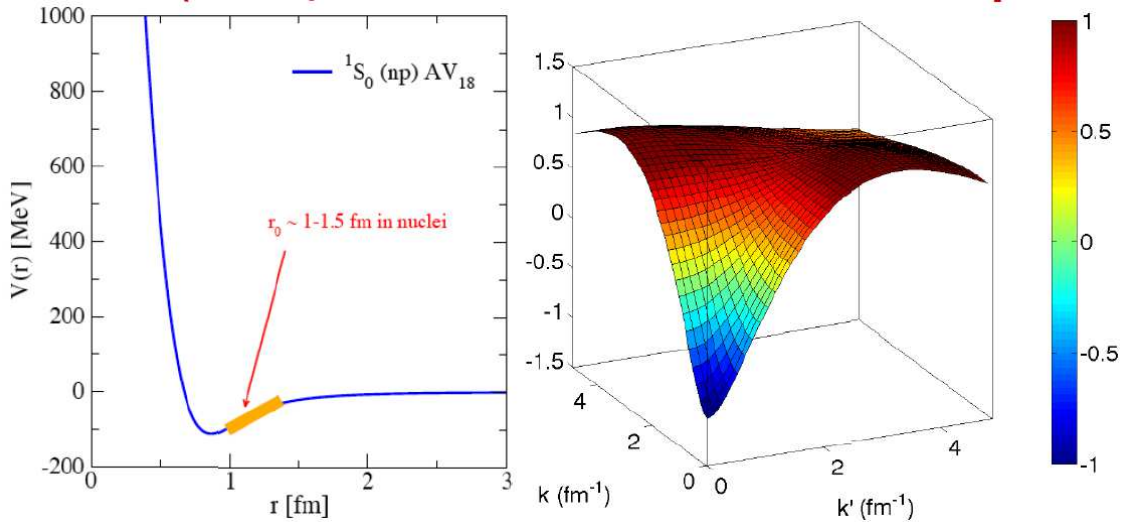


Figure 1.1: The Argonne V18 nuclear potential in coordinate (left) and momentum (right) representations. Notice the hard repulsive core at short-distance/high-momentum and small mid-range attractive well. The typical spacing within nuclei is indicated by the arrow.

here inflates the required basis size and hinders attempts to compute larger nuclei ( $A \geq 4$ ) using *ab initio* methods. A softened potential, which has the low- and high-energy degrees of freedom decoupled, would enable a truncation of the two-body basis and ease the computational requirements of *ab initio* many-body problems. Such soft potentials were tried long ago but deemed insufficient, because they could not reproduce empirical nuclear matter saturation properties [4]. The problem was that many-body forces were not correctly considered. Subsequently, the need for many-body forces to accurately describe nuclear systems became apparent. For instance, the highly successful NN interactions could not account for the total binding energy of the triton [5]. However, it proved to be difficult to systematically account for even three-body forces.

Then in the early 1990's Steve Weinberg proposed generalizing chiral perturbation theory [6] to develop an expansion consistent with the symmetries of the known underlying theory of the strong interaction, Quantum Chromodynamics (QCD).<sup>1</sup> Such a program would provide a systematic expansion of contributions, with controlled errors at every order, known as Chiral Effective Field Theories ( $\chi$ EFT's). The idea sparked an industry in developing and properly parametrizing such a theory of the nuclear interaction. Chiral EFTs provide a systematic and controlled expansion of not only the NN interactions, but also many-body forces with controlled errors, and in a natural framework for including consistent external currents (electromagnetic) and relativistic effects.

Chiral EFTs have provided softer interactions because there is a lower cutoff of high-energy physics than in conventional potentials, but *ab initio* methods are still computationally very difficult. Simply using a lower cutoff to further soften  $\chi$ EFT potentials has resulted in pathologies in the potentials and significantly diminished their accuracy [7]. Recent work that softens these interactions using a unitary block-diagonal transformation referred to as  $V_{\text{low } k}$  have had many successes, but many-body forces have only been included approximately. The Similarity Renormalization Group (SRG), which generates unitary transformations that can be used to soften potentials, can also consistently treat many-body forces and is particularly suited to the needs of the  $\chi$ EFT program.

Now, in an era of rapidly expanding computational capacity, nuclear structure physics is experiencing a renaissance and helping to renew collaborations across the

<sup>1</sup>Due to asymptotic freedom, QCD is weakly coupled at high energies and thus easier to analyze. Unfortunately, it is strongly coupled at low energies and not suitable for perturbative calculations in the regime relevant to nuclear structure.

larger physics community. Of paramount importance to this program is the development of new techniques to make nuclear many-body problems more tractable in a given computational environment. The Similarity Renormalization Group promises to be a cornerstone of these techniques for many years to come. This thesis represents some of the earliest development of applications of the SRG to problems in nuclear physics.

## 1.2 Modern Many-Body Nuclear Physics

The UNEDF (Universal Nuclear Energy Density Functional) collaboration is a broad effort within the nuclear structure community to develop a wide-reaching and self-consistent model of the structure and behavior of large nuclei based on Density Functional Theory (DFT), which describes the bulk properties of many-body systems in terms of functionals of the nucleon densities. Because of its scaling properties, it is suited for large many-body systems. The DFT strategy has been employed successfully for atoms and molecules in quantum chemistry and also in nuclear theory using empirical EDF's that are fit to nuclear properties. The UNEDF collaboration is attempting to improve the nuclear DFT approach with microscopic input such as from Chiral EFT.

Figure 1.2 shows a chart indicating the relationships between the various scientific efforts involved in the UNEDF project. The work in this thesis is directly connected to the top two bubbles in the chart, and enables work on *ab initio* DFT's represented in the center bubble [8]. The upper left corner represents work on the basic nuclear forces in few-body systems and efforts to find optimal and practical parametrizations of the nuclear interaction. Some examples listed are Argonne  $v_{18}$  (also denoted as



## Universal Nuclear Energy Density Functional

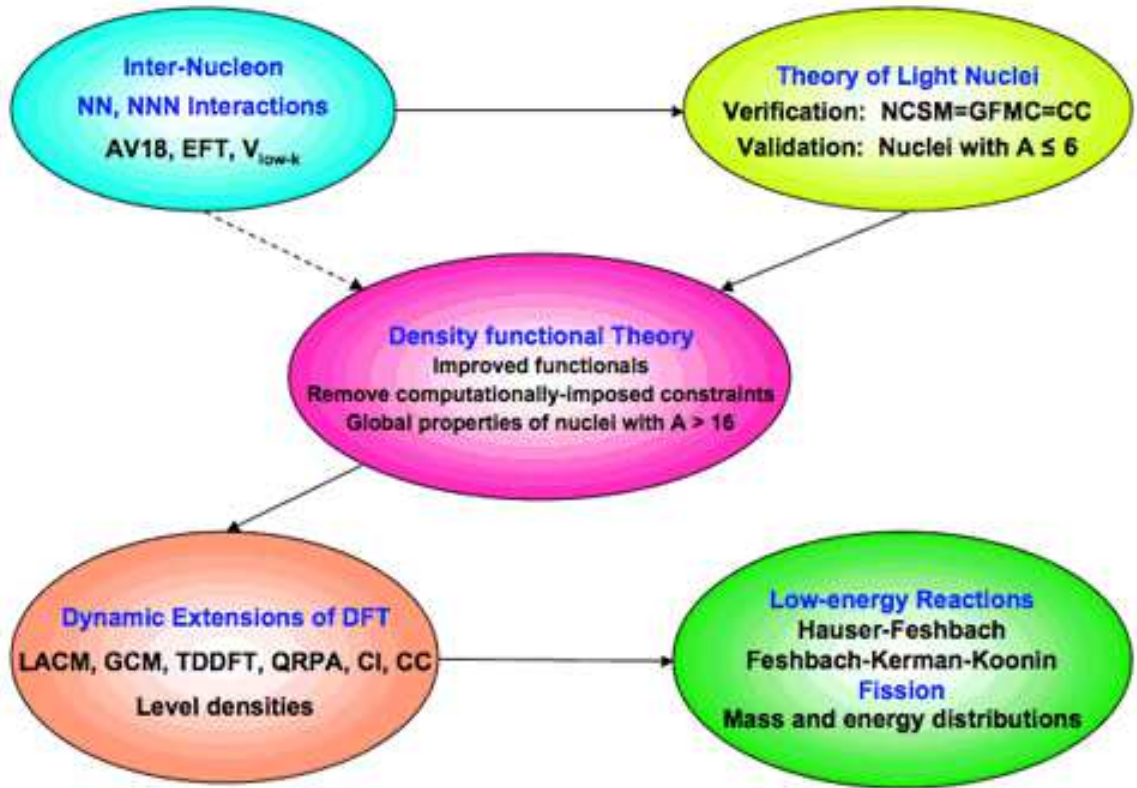


Figure 1.2: Scientific interconnections within the UNEDF collaboration.

AV18) [9], a phenomenological potential developed in the mid-nineties and widely used today, EFT, which refers to the Chiral Effective Field Theories described further in section 1.4 and appendix A, and  $V_{low k}$ , which is a renormalization technique related to the SRG. The SRG is applied in this thesis to treat the “initial” interactions (such as AV18 and  $\chi$ EFT’s) to ease computational requirements for calculations elsewhere in the UNEDF program. Like  $V_{low k}$ , it works to soften potentials and is generally

applicable to any interaction. However, unlike  $V_{\text{low } k}$ , the SRG handles many-body forces in a straightforward way.

The upper right corner depicts the first step in practical calculations with a given initial interaction. In this area of research, *ab initio* calculations of the lightest nuclei are performed to validate the properties of the initial interactions. This is a computationally intensive program requiring large clusters of processors numbering into the tens of thousands to accurately compute the nuclei above  ${}^6\text{Li}$  ( $A = 6$ ). The examples listed here are the No-Core Shell Model<sup>2</sup> (NCSM), which utilizes a finite basis of harmonic oscillator wavefunctions, Green’s Function Monte Carlo (GFMC), which stochastically computes coordinate-representation integrals numerically, and the Coupled-Cluster (CC) method, which is a many-body technique based on a wavefunction ansatz organized in subclusters of the total system. The GFMC is currently limited to nuclei with  $A \leq 12$  due to its scaling properties and is limited to using local potentials like the phenomenological potential, AV18. However, work is proceeding to address these challenges [14, 15]. Coupled-Cluster calculations [16, 17] have the farthest reach up the chart of nuclides of all *ab initio* techniques and are an important source of validation of DFT efforts, but they are limited to a small subset of nuclei near closed shells.

The few-body calculations done in this thesis make use of the NCSM and its antisymmetrized basis of harmonic oscillator (HO) wavefunctions. The NCSM basis provides for a variational calculation in both the size of the basis,  $N_{\text{max}}$ , and the size of the oscillator parameter,  $\hbar\omega$ . As  $N_{\text{max}}$  is increased the results converge, and at a given  $N_{\text{max}}$  the oscillator parameter  $\hbar\omega$  must be optimized, balancing infrared

<sup>2</sup>The moniker “No-Core” simply means that all nucleons are active instead of the more traditional shell model which considers valence nucleons around an inert closed shell [10, 11, 12, 13].

and ultraviolet cutoffs. These features are explored in more detail in appendix B. In the literature, the name NCSM usually implies use of the Lee-Suzuki (LS) procedure to obtain an effective interaction that is not variational in the HO basis parameters. Here, we will forgo this method in favor of the SRG, which will provide a softened effective interaction and retain the variational features of the basis.

### 1.3 Resolution and Renormalization

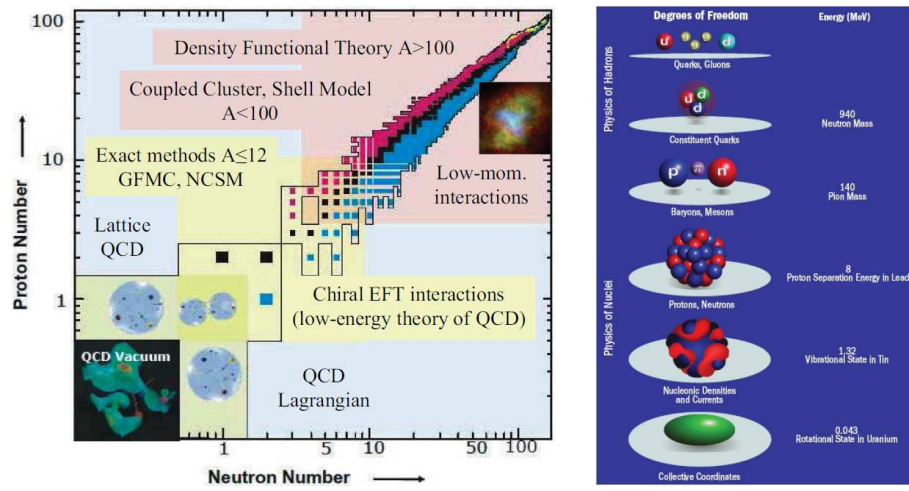


Figure 1.3: Two pictures illustrating common degrees of freedom (dof), interactions, and calculational techniques used in theoretical nuclear physics.

Figure 1.3 displays an overview of important aspects of theoretical nuclear structure physics. The picture on the left is the chart of nuclides on a log-log plot [18]. Above the diagonal of the chart are indicated various calculational techniques positioned near their relevant regimes, and below are listed interactions that can be used in various parts of the chart. The right side of Fig. 1.3 is a picture from the UN-EDF collaboration showing some explicit degrees of freedom used in studying nuclear

phenomena [19]. Any calculation can be performed using any degree of freedom, but many choices may be intractable. We should pick the degrees of freedom most useful to the problem at hand. For instance, while Quantum Chromodynamics (QCD) is the underlying theory to all nuclear interactions, trying to calculate even the smallest nuclei with quark and gluon degrees of freedom is computationally impossible with current techniques (though calculating up to  $A = 4$  is a long-term goal for the next generation of computers [20]). Independent checks on calculations from different methods is very important to the UNEDF program, and a technique like the SRG is crucial to extending the overlap of techniques like DFT, Coupled-Cluster, and NCSM.

In addition to the choice of gross degrees of freedom, the capacity to adjust the parameters of an interaction within a given formulation is desirable. The *ab initio* calculations in this thesis deal with explicit nucleon degrees of freedom with interactions formulated in terms of relative nucleon momenta. The computational difficulty of the few- and many-body problem can be eased with an appropriate treatment of this initial interaction. As the number of nucleons increases, the size of the basis required for convergence increases very rapidly. Thus, reducing the size of the basis required to encode NN physics will reduce the required size of the  $A$ -body basis in which the NN physics must be embedded. The SRG will provide a convenient way to accomplish this adjustment in a manner that preserves initially chosen physics. In addition it will also consistently treat many-body forces and other observables.

Figure 1.4 presents a simple analogy of what the SRG can do for us. The picture on the left is a photomosaic image where the image of President Lincoln has been made up from hundreds of smaller photos that have been fit to their particular location in the whole image. The picture on the right is just the original photograph

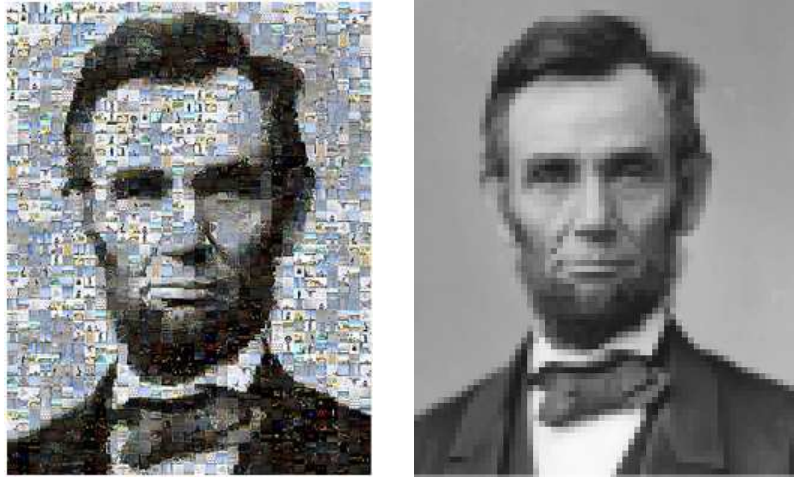


Figure 1.4: Two pictures of our 16th president.

that has been pixelated by standard photo software. Both of these images get the basic long-distance information correct – both show Lincoln’s face about equally well. However, the mosaic image of Lincoln contains a lot of extra information that the viewer’s brain must work to filter and process, using lots of memory and power. Not only is the image on the left harder to use but the extra information it contains is even incorrect. All the details in the individual photographs are not actually part of Lincoln’s face and the viewer has to filter them out. The image on the right has much less information but still contains what is needed to recognize the face. Ideally, a calculation requiring only the long distance information of the right picture would benefit from a technique which transforms the mosaic into a version of the pixelated right-hand side. This is analogous to the renormalization group technique implemented here, in which irrelevant details of the short distance information are removed in favor of the dof’s consistent with the relevant physical information, simplifying the interaction for subsequent calculations. The AV18 potential is like the

photomosaic on the left because it contains a lot of short distance details irrelevant to low-energy nuclear structure physics. The SRG is going to help filter out those details and retain the long-distance, low-momentum, information like the picture on the right.<sup>3</sup>

## 1.4 Chiral Effective Field Theories

As mentioned above, Chiral Effective Field Theories ( $\chi$ EFT's) have evolved to play an important role in the development of a quantitative understanding of the nuclear interaction. Here we give a brief overview of their features, with various additional details involved in constructing  $\chi$ EFT's discussed in appendix A.

All these theories are called “effective” because they encode the details of short-distance (high-energy) physics in their coupling constants, which are called Low Energy Constants (LECs). These are the parameters that we must fit to make the  $\chi$ EFT's consistent with the data and predictive of low-energy physics. Ultimately, short-distance behavior of the strong interaction is governed by Quantum Chromodynamics (QCD). The degrees of freedom in a nuclear  $\chi$ EFT are not the same as those in QCD because the quarks and gluons are confined at the low energies we are considering. However,  $\chi$ EFT's do not need to incorporate explicitly the details of high-energy physics in their Lagrangians because the high-energy behavior is parametrized in a general way. Thus,  $\chi$ EFT's exploit the fact that any of an infinite number of possible parameterizations is sufficient to predict the correct low-energy observables of nuclei.

<sup>3</sup>This analogy breaks down in the sense that a simple low-pass filter works well on the photomosaic but not on the potential. The first is a classical problem, and the second is quantum mechanical; the photo-mosaic *is* the observable, while the potential is not. This will be described in more detail in chapter 3.

Few-body forces are inevitable in any effective theory as a result of elimination of degrees of freedom. In any process involving three incoming nucleons there are a large number of possible intermediate states, some of which will have high energy and occur at very small distance and time scales. Because the details of this high-energy physics are irrelevant to low-energy observables, we can use a cutoff to eliminate explicit high-energy degrees of freedom. However to account for their effects, we must introduce local interactions, including many-body forces. The new LECs that come with such terms must be fit to some experimental observables. A major advantage of  $\chi$ EFT's is that they provide a consistent and systematic framework with which to formulate such low-energy few-body interaction terms in addition to the basic two-body (NN) interaction between nucleons. We will consider in appendix A the explicit form of three- and four-body forces (3NF and 4NF). These terms become important for reproducing the properties of larger nuclei (i.e.  $A \geq 3$ ).

Building any good EFT depends on following three basic rules [22]. First, we must identify the degrees of freedom we want the theory to encompass and write down the most general Lagrangian that obeys the symmetries of the underlying theory (QCD). In pionless EFT (EFT( $\overline{\pi}$ )), we use only nucleons ( $m_N \sim 1$  GeV) as the degrees of freedom; any pion contributions will be parametrized in the LEC's. With the pion mass ( $m_\pi \sim 140$  MeV) as the cutoff scale this theory will only be valid for nucleon momenta well below the pion mass. In  $\chi$ EFT, we will take the cutoff scale to be much larger, such as the nucleon or  $\rho$  meson mass. Then we must include pions explicitly and the spontaneous breaking of chiral symmetry found in low energy QCD. Hence the name "Chiral" in  $\chi$ EFT. The  $\Delta$ -isobar ( $m_\Delta = 1232$  MeV) might also be included in the theory due to its mass being so close to the nucleon. Second, we must declare a

regularization and renormalization procedure. Several different types have been used with  $\chi$ EFT's including dimensional, cutoff, and spectral regularization procedures combined with minimal and power divergence (only used with dimensional regularization) subtraction schemes. Due to its symmetry preserving properties, dimensional regularization is often preferred but has not been successfully applied within the non-perturbative resummations involved in calculating nuclear bound states in  $\chi$ EFT. Instead, cutoff regularization is used. Finally, we must choose a method of organizing the contributions to the potential. The various methods of organization are collectively referred to as *power counting* schemes. In any effective theory we integrate out higher momentum contributions, and introduce an expansion of correction terms to account for the removed degrees of freedom. Thus, we need a formal scheme to keep track of the importance of these various contributions and decide which terms are important at a desired level of accuracy. The power counting one uses will lead to a particular expansion, or hierarchy, of contributions to the total inter-nucleon interaction.

A picture showing a particular power counting scheme for  $\chi$ EFT terms is given in Fig. 1.5. The vertical axis in the table is the relative importance of terms entering into the amplitude of a process. The order of the graph is expressed in powers of momenta ( $Q/\Lambda$ ) where  $Q$  is a momentum characteristic of the transfer between interacting nucleons and  $\Lambda$  is some large momentum scale associated with the underlying physics and hence the scale at which the EFT's predictive power fails.<sup>4</sup> Each row is seen as a correction to the previous row. Those higher-order terms require higher

<sup>4</sup>Examples of  $\Lambda$  are: for EFT( $\not{t}$ )  $\Lambda \approx m_\pi = 140$  MeV, for  $\chi$ EFT any one QCD scale such as  $m_\rho, m_N \simeq 1$  GeV, and for the Fermi theory of weak interactions  $\Lambda = M_W, M_Z \approx 80 - 90$  GeV respectively.



	2N forces	3N forces	4N forces
LO ( $\frac{Q^0}{\Lambda^0}$ )			
NLO ( $\frac{Q^2}{\Lambda^2}$ )			
N <sup>2</sup> LO ( $\frac{Q^3}{\Lambda^3}$ )			
N <sup>3</sup> LO ( $\frac{Q^4}{\Lambda^4}$ )			
	+	+	+

Figure 1.5: A table showing the organization of EFT terms in Weinberg power counting. The figure is from [21].

momenta in order to become significant effects and therefore are suppressed at the low scale of  $Q$ . The columns are separating basic types of terms for multi-body processes. For instance, three body forces (3NF) first contribute at the third-to-leading order although in a two-body problem they would never be relevant.<sup>5</sup> Note that this represents a particular power counting choice originally proposed by Weinberg [6]. The graphs displayed in the figure are considered as a perturbative expansion of the relevant contributions to the nuclear interaction, but at a desired order in  $Q/\Lambda$  all contributions must be summed non-perturbatively to calculate bound states (in other schemes only the leading order terms are summed).

The various LECs in a  $\chi$ EFT are currently obtained by fitting to experimental data. The fit theory can then be used to make predictions about other observables. When more LECs enter the expansion, they must be fit to additional experimental observables. At the outset, this situation seems to limit the predictive power of  $\chi$ EFT's in general, but it is currently the most practical way to proceed with the  $\chi$ EFT program of many-body physics within large nuclei. The relevant question is whether we can reach a desired accuracy with a number of terms that we can handle. For example, hopefully nuclear matter will only need a small set of  $A$ -body forces (hopefully no more than 4NFs) for an accurate description and therefore a relatively small number of LECs must be fit from experiment. Ultimately one would like to have an *ab initio* calculation of nuclear LECs from the underlying theory, QCD. Work is currently underway to develop techniques to calculate  $\chi$ EFTLECs in this way, and recent progress makes this a plausible future [23, 20, 24, 25]. In light of

<sup>5</sup>3N “tadpole” graphs don't contribute to NN amplitudes because  $\bar{N}$ 's are not in the EFT. The pair production that produces them requires a high energy and has been integrated out. Thus, these effects are encoded in the NN contact LECs.

these two approaches the  $\chi$ EFT program requires the development of techniques both for controlling errors induced by fitting procedures, and for self-consistent  $A$ -body renormalization capable of dealing with each term in the EFT expansion, preserving the input physics. The SRG is a prime example of a technique that satisfies both of these needs.

## 1.5 Similarity Renormalization Group

While  $\chi$ EFT's are already significantly softer than many phenomenological potentials, further softening of these potentials provides increased convergence in calculations of larger nuclei. A potential like Argonne  $v_{18}$  usually uses a momentum mesh out to  $\approx 30 \text{ fm}^{-1}$  while  $\chi$ EFT's need around  $\approx 7 \text{ fm}^{-1}$ . Even with the softer  $\chi$ EFT potentials the task of calculating properties of  ${}^4\text{He}$  is computationally difficult, requiring large spaces in the NCSM basis to achieve convergence (e.g., for  $A = 4$  at  $N_{\text{max}} = 18$ , the basis dimension is 4750 states and the  ${}^4\text{He}$  binding energy is just beginning to converge). However, typical momenta inside a nucleus are of order  $1 \text{ fm}^{-1}$  so we should be able to soften these potentials much further and increase their convergence properties.

A common established technique, called  $V_{\text{low } k}$  [26, 27], softens potentials and improves convergence by transforming potentials to a block-diagonal form.<sup>6</sup> In contrast the SRG, as typically implemented here, evolves the potential into a band-diagonal form [28]. A schematic is shown in Fig. 1.6 of the difference in form between a

<sup>6</sup> $V_{\text{low } k}$  is a momentum space implementation of the block-diagonal transformation idea of Lee and Suzuki [29], though in the literature the term Lee-Suzuki usually refers to a different implementation in the NCSM basis.

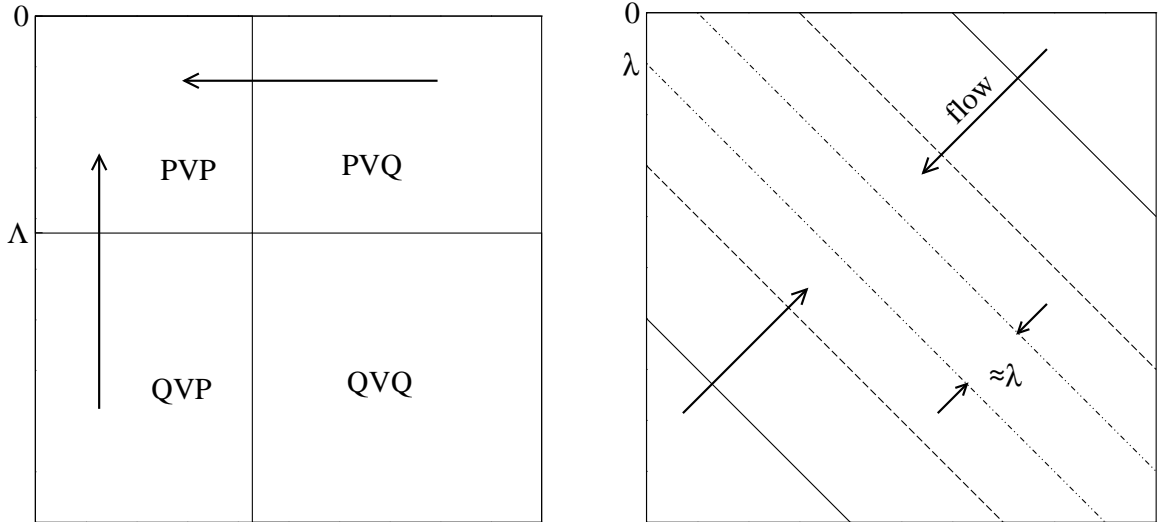


Figure 1.6: A simple illustration of  $V_{\text{low } k}$ 's block diagonalizing and SRG's band diagonalizing forms.

potential renormalized by  $V_{\text{low } k}$  (left) and by the SRG (right). Both of these renormalization strategies use a unitary transformation to soften the initial potential and thus decouple high- and low-energy degrees of freedom. On the left,  $V_{\text{low } k}$  transforms the potential so that all interaction strength is contained in the two diagonal blocks,  $PVP$  and  $QVQ$  (or simply  $P$  and  $Q$  blocks), defined by the cutoff scale  $\Lambda$ <sup>7</sup>. In contrast the SRG smoothly evolves the matrix element strength towards a chosen form, here usually band diagonal in momentum with a width  $\sim \lambda$  which indicates the amount of coupling left between neighboring states. However, the general form of SRG evolution is a matter of choice and we will see that a particular choice reproduces  $V_{\text{low } k}$  evolution. Note that the  $V_{\text{low } k}$  renormalization can be achieved through both differential and integral procedures, while the SRG currently only exists as a differential procedure (as fully explained in chapter 2). In addition, a  $V_{\text{low } k}$  treatment of

<sup>7</sup>Usually the  $V_{\text{low } k}$   $Q$  block is set to zero in practice, but this is not required.

many-body forces is not straightforward and limits its practical implementation with regard to many-body forces. A quantitative investigation of the decoupling properties of the SRG (and the behavior of residual coupling) is presented in chapter 3.

In the NCSM's oscillator basis, a block-diagonal transformation similar to that suggested by Lee and Suzuki [29] has successfully improved convergence properties for calculations of many-body observables, it has significant drawbacks which the SRG is able to address. This transformation is model-space dependent and not variational and extrapolating its behavior in the basis size,  $N_{\max}$ , is difficult. The SRG's improved convergence properties are smoothly variational and therefore lend themselves to extrapolation in basis size. This thesis shows SRG calculations to have improved convergence over traditional Lee-Suzuki types of treatments. As mentioned above, many-body forces are a natural consequence of any renormalization program. Their hierarchy is articulated naturally in the  $\chi$ EFT framework as opposed to the more *ad hoc* parametrizations using phenomenological potentials such as IL-IX [30], which was designed for use with AV18. The SRG provides for the consistent treatment of many-body forces and is seen to work with this natural hierarchy as input and complements  $\chi$ EFT's as a general renormalization technique.

In addition, the formal basis of the SRG allows a term-by-term application to analyze its transformation of the initial  $\chi$ EFT hierarchy. This program was begun in this thesis by exploring how the SRG preserves the hierarchy of input interaction terms in a one-dimensional model and can be easily extended to the three-dimensional case within the NCSM framework. A topic of future investigations involves an analytic implementation of the SRG to study its preservation of the initial hierarchy and how it adjusts LEC's in a realistic  $\chi$ EFT setting. Ultimately, this should provide a deeper

understanding of renormalization in the broader EFT hierarchy and may lead to predictions about the quantitative importance and relation of particular mechanisms and processes within nuclear systems.

While this work focuses on the few-body *ab initio* program of nuclear structure physics, the SRG is a general  $A$ -body technique that is also being applied to infinite matter and density functional calculations. These methods are currently under heavy development and will also depend on the ability to soften the initial Hamiltonian input. The SRG is a prime mover in bringing the few-body and many-body regimes into quantitative contact with each other. Specifically, the SRG will expand the useful range of wavefunction based methods like the NCSM used in this thesis. This will be an important check on the validity of the DFT calculations that develop.

## 1.6 Thesis Organization

The following topics in this thesis are original contributions to the field:

1. A quantitative study of decoupling afforded by the SRG in momentum representation NN forces and the calculational benefits it provides.
2. The first studies using alternative forms of the SRG to test different types of renormalization for nuclear interactions.
3. Development of a one-dimensional Jacobi coordinate harmonic oscillator shell model as a laboratory to explore the behavior of the SRG as it applies to the evolution of many-body forces. Within this model we studied:
  - Vacuum expectation value decomposition and analysis of the many-body force evolution.

- Basis dependence issues and other SRG generators in the oscillator representation.
  - Additional procedures such as fitting three-body forces to evolved two-body interactions and evolving individual operators in few-body systems.
4. First evolution of 3NFs for  ${}^3\text{H}$  and  ${}^4\text{He}$  using an established No-Core Shell Model code, based on insight and experience gained from the one-dimensional model.

Decoupling between high- and low-energy states is the feature of SRG evolution that leads to increased convergence with basis size in calculations of nuclear observables. While first demonstrated for the NN interaction in Ref. [31], in this work we achieved a quantitative understanding of its roots and its behavior in the NN partial-wave momentum representation. Residual coupling in the interaction above momenta of interest is perturbatively small and extends universally to many-body calculations like NCSM binding energies. The form of the SRG's transformations can be tailored by prudent choice of the operators entering the equations. We show that such choices have little effect on the qualitative behavior of decoupling in NN interactions.

The formal equations of the SRG indicate that decoupling should occur for many-body forces in a similar manner as in the NN case. While the SRG can be applied in any basis, momentum-basis calculations of three-body potentials are less straightforward because of spectator nucleons (those not participating in an interaction). Instead, we choose to work in a discrete basis of harmonic oscillator wavefunctions inspired by the no-core shell model. We first built a model in one dimension (1D) for the purpose of rapid development and intuition in SRG calculations involving

many-body forces. Many different types of calculations have been performed in one dimension to gain intuition for their behavior in three-dimensional calculations and provide a sanity check when working with the more complex three-dimensional codes. It has also provided a simpler environment in which to explore issues of basis dependence in calculations in general and SRG calculations in particular.

Finally, we apply the insights gained in 1D to the full realistic three-dimensional calculation of the NCSM. Here the 1D model has proved to be highly predictive of the behavior of decoupling in realistic calculations. The SRG improves convergence in calculations of  ${}^3\text{H}$  and  ${}^4\text{He}$ , and the input hierarchy of many-body forces is maintained as expected from the one-dimensional studies. These evolved many-body interactions, which have much improved convergence properties and well controlled errors, will be highly sought inputs to various *ab initio* many-body calculations from across the UNEDF collaboration.

The general layout of this thesis is as follows: Chapter 2 gives a brief introduction to the formalism employed in making SRG calculations. In chapter 3, a quantitative study is made of the decoupling between high- and low-energy states and its universal nature. With an eye towards realistic many-body calculations, chapter 4 develops a one-dimensional analog to the No-Core Shell Model (NCSM) to explore the behavior of SRG evolution in an  $A$ -body space. Many different types of calculations are tried here to gain intuition for the real three-dimensional case. Chapter 5 applies the insight gained from the one-dimensional model to realistic few-body calculations using the Jacobi coordinate NCSM. Finally, we conclude in chapter 6 and discuss possible future investigations. Several appendices explore technical details of the basis and potentials involved in this work.



## CHAPTER 2

### SIMILARITY RENORMALIZATION GROUP

The Similarity Renormalization Group (SRG) [32, 33, 34] provides a compelling method for evolving internucleon forces to softer forms [28, 31]. While observables are unchanged by the SRG's unitary transformations, the contributions from high-momentum intermediate states to low-energy observables is modified by the running transformation. These transformations soften initial interactions and can dramatically reduce the computational requirements of low-energy many-body calculations [28, 31, 35]. At the same time, the SRG induces many-body forces in response to its transformation of the high-energy states in the Hamiltonian. In this chapter I present the formalism used for analyzing SRG evolution and the subsequently induced many-body forces.

#### 2.1 Derivation

We apply the similarity renormalization group (SRG) transformations to internucleon interactions based on the flow equation formalism of Wegner [33]. The evolution or flow of the Hamiltonian with a parameter  $s$  is a series of unitary transformations

$$H_s = U_s H U_s^\dagger \equiv T_{\text{rel}} + V_s , \quad (2.1)$$

where  $T_{\text{rel}}$  is the relative kinetic energy,  $H = T_{\text{rel}} + V$  is the initial Hamiltonian in the center-of-mass system, and  $U_s$  is the unitary transformation. Equation (2.1) defines the evolved potential  $V_s$ , with  $T_{\text{rel}}$  here defined to be independent of  $s$  in all spaces<sup>8</sup>.

Then  $\frac{dH_s}{ds} = \frac{dV_s}{ds}$  evolves according to

$$\begin{aligned} \frac{dV_s}{ds} &= \frac{dU_s}{ds} H U_s^\dagger + U_s H \frac{dU_s^\dagger}{ds} \\ &= \frac{dU_s}{ds} U_s^\dagger U_s H U_s^\dagger + U_s H U_s^\dagger U_s \frac{dU_s^\dagger}{ds} \\ &= \frac{dU_s}{ds} U_s^\dagger H_s + H_s U_s \frac{dU_s^\dagger}{ds}, \end{aligned} \quad (2.2)$$

which motivates us to focus on  $\eta_s \equiv \frac{dU_s}{ds} U_s^\dagger \Rightarrow \eta_s^\dagger \equiv U_s \frac{dU_s^\dagger}{ds}$ . Therefore,

$$\frac{dV_s}{ds} = \eta_s H_s + H_s \eta_s^\dagger. \quad (2.3)$$

Using  $U_s U_s^\dagger = 1$ , we can establish the following

$$\frac{d}{ds}(U_s U_s^\dagger) = 0 \Rightarrow \left(\frac{d}{ds} U_s\right) U_s^\dagger + U_s \left(\frac{d}{ds} U_s^\dagger\right) = 0 \quad (2.4)$$

$$\Rightarrow \eta_s + \eta_s^\dagger = 0. \quad (2.5)$$

Therefore Eq. (2.3) can be written as

$$\frac{dV_s}{ds} = \eta_s H_s - H_s \eta_s = [\eta_s, H_s]. \quad (2.6)$$

The choice of  $\eta_s$ , as long as it is antihermitian, is mathematically free and specifies the transformation. A natural choice would involve parts of the Hamiltonian itself which, along with a commutator structure, would satisfy the antihermiticity requirement. Choosing one commutator argument to be the evolving Hamiltonian,  $H_s$ , and leaving the other choice open, we can write

$$\eta_s = [G_s, H_s]. \quad (2.7)$$

<sup>8</sup>The center of mass kinetic energy,  $T_{\text{cm}}$ , will not contribute because we are working in a translationally invariant system and it will commute with the other operators in Eq. (2.1)

Table 2.1: Various choices for  $G_s$  considered to date.

Name	Description
$T_{\text{rel}}$	Relative kinetic energy between nucleons [28]
$H_{\text{D}}$	Running diagonal part of the Hamiltonian advocated by Wegner: $T_{\text{rel}} + V_{s,\text{diag}}$ [33]
$H_{\text{D,fixed}}$	Fixed, initial diagonal of the Hamiltonian: $T_{\text{rel}} + V_{s=0,\text{diag}}$
$H_{\text{BD,sharp}}$	The running block diagonal part of the Hamiltonian. $P$ and $Q$ spaces defined by a sharp cutoff at $\Lambda$ [36]
$H_{\text{BD,smooth}}$	Block diagonal as above but with a smooth regulator of sharpness $n$
$H_{\text{weird}}$	A strange choice with three different block diagonal regions defined by two different cutoff $\Lambda$ s [36]
$H_{\text{ho}}$	The harmonic oscillator Hamiltonian in an $A$ -body space, which is diagonal in the HO basis
$T_{\text{rel}} + \alpha r^2$	A hybrid $H_{\text{ho}}$ type choice for use in the oscillator basis [42]
$T_{\text{rel}} + V^{(2)}$	The two-body Hamiltonian, suggested as a way to renormalize only three-body forces

The flow Eq. (2.6) now becomes

$$\frac{dV_s}{ds} = [[G_s, H_s], H_s] , \quad (2.8)$$

where  $G_s$  will be referred to as the generator, following conventional usage, though technically the generator of the group is  $\eta_s$ . Various possibilities for  $G_s$  have been proposed [34, 28, 36], though the most common in this thesis is  $G_s = T_{\text{rel}}$ , for which the flow equation simplifies to

$$\frac{dV_s}{ds} = [[T_{\text{rel}}, V_s], H_s] . \quad (2.9)$$

Other choices that have been investigated to varying degrees are listed in Table 2.1.

Equations (2.8) or (2.9) are operator equations, independent of any basis. They can be applied numerically by projecting onto any convenient basis. For two-body

systems, a partial-wave momentum basis with states labeled by the initial and final relative momenta,  $k$  and  $k'$ , is convenient, accurate, and straightforward. In higher-body systems we will resort to a discrete basis<sup>9</sup> in which all the states can be enumerated up to some basis limiting parameter. The bulk of this thesis will employ a basis of harmonic oscillator functions known as the No-Core Shell Model (NCSM) [39, 40, 41]. The NCSM usually uses a renormalization procedure inspired by a Lee-Suzuki type transformation [11, 12, 13]. Calculations in this thesis will not include any such transformations; the SRG is applied to the “bare” or initial potentials as given by the various models/ $\chi$ EFT’s available. The SRG provides renormalization in addition to that intrinsic to the formulation of input potentials (especially those from  $\chi$ EFT).

Note that the dimension of  $s$  is  $1/\text{energy}^2$ . We can define a momentum variable  $\lambda = 1/s^{1/4}$ , with units of  $\text{fm}^{-1}$ , that measures the spread of the off-diagonal strength in units relevant to the basis. Using  $\lambda$  as the flow parameter Eq. (2.9) becomes

$$\frac{dV_\lambda}{d\lambda} = \frac{-4}{\lambda^5} [[T_{\text{rel}}, V_\lambda], H_\lambda] , \quad (2.10)$$

so that the flow goes from  $\lambda = \infty$  toward zero instead of starting at  $s = 0$  and going toward infinity. Most of our formalism is presented using  $s$  for simplicity (since the flow is linear in  $s$ ) but most calculations are done using  $\lambda$ . Chapter 3 will demonstrate how  $\lambda$  is a physically relevant measure of the extent of evolution specifically as it applies to the decoupling of high- and low-energy degrees of freedom. Matrix elements connecting states with (kinetic) energies differing by more than  $\lambda^2$  are largely suppressed and therefore decoupled.

<sup>9</sup>Work is underway to develop a three-body momentum representation code which incorporates SRG calculations [37].

The earliest applications to nuclear physics have been in a partial-wave momentum basis using  $G_s = T_{\text{rel}}$  [28]. It is a straightforward matter to project Eq. (2.9) into this basis. After some algebra we can show that, for each partial-wave, Eq. (2.9) can be specified in the momentum basis as

$$\frac{dV_s(k', k)}{ds} = -(k^2 - k'^2)^2 V_s(k', k) + \frac{2}{\pi} \int_0^\infty q^2 dq (k^2 + k'^2 - 2q^2) V_s(k', q) V_s(q, k). \quad (2.11)$$

In fact, it is simpler to implement the commutator form of the flow equations on platforms like MATLAB or Fortran which can easily handle matrix operations and coupled differential equations. Once the Hamiltonian has been projected onto a chosen mesh (usually Gaussian quadrature), the matrix multiplications follow directly.

Figures 2.1–2.4 document the evolution of various partial waves from several different NN interactions in the momentum representation. Note the blue areas, which indicate attraction and contribute to binding phenomena seen at low energies, and the red areas which indicate repulsion and the hard core probed by large momenta. However, the off-diagonal red matrix elements which are coupling low- and high-momentum states are also contributing to low-energy observables. The major feature to notice looking across the film strips from, left to right, is that the potential is driven to a band diagonal form with a width proportional to the square of the momentum parameter  $\lambda$ . This behavior is a major subject of chapter 3. In all of the cases, the SRG is successful at transforming the potential to this band-diagonal form, regardless of the specific input physics. Rather the form of the SRG-evolved potentials is determined by the choice of  $G_s$ , as shown formally in section 3.2. The evolved potential approaches a universal soft form in a given partial wave, regardless of the initial Hamiltonian. This suggests a natural underlying hierarchy of renormalization

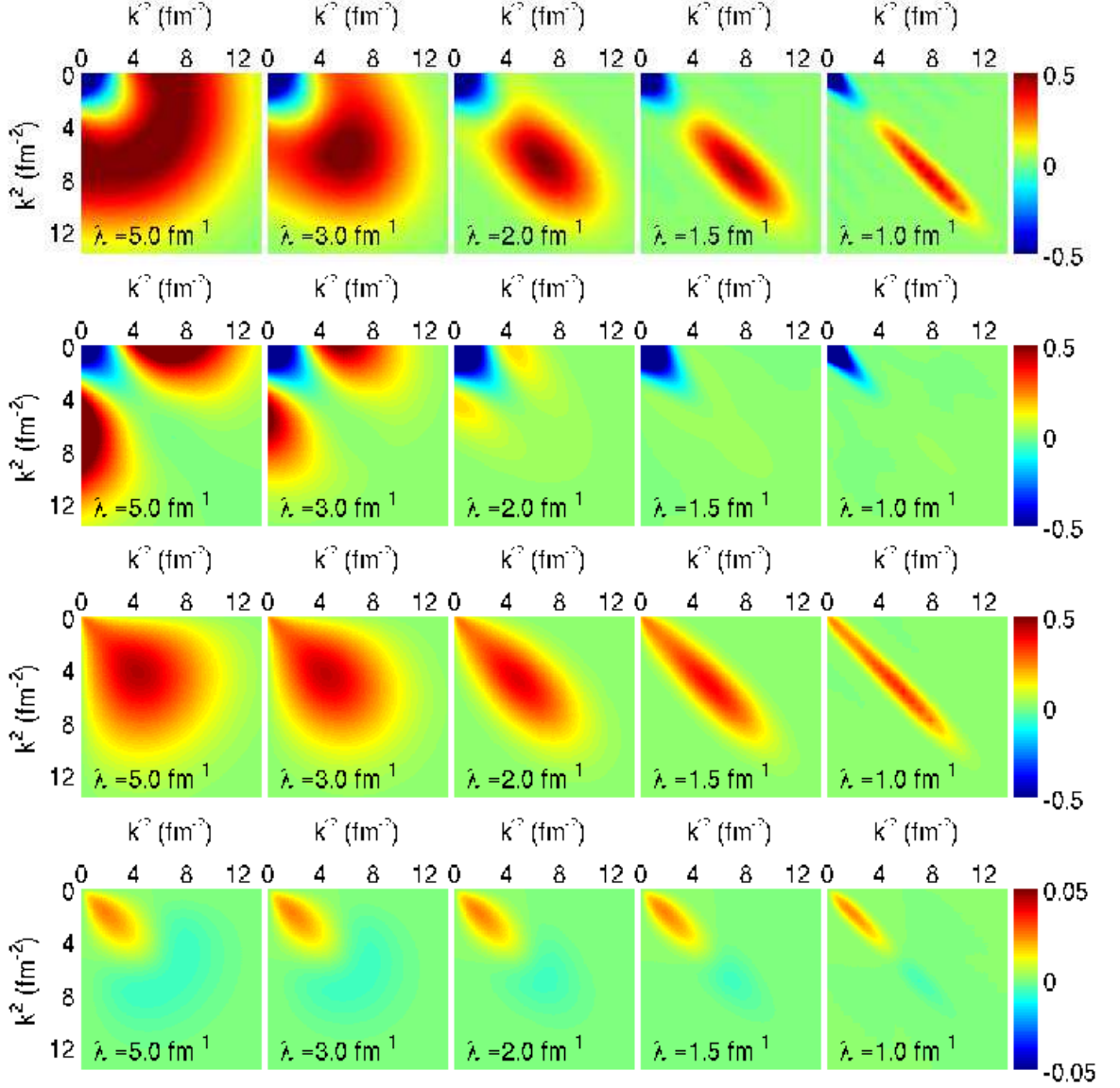


Figure 2.1: Film strips of evolution for representative partial waves in the  $N^3\text{LO}$  (500 MeV) interaction of Ref. [49] in the momentum representation. Partial waves shown are  $^1S_0$ ,  $^3S_1$ ,  $^1P_1$ , and  $^3F_3$ .

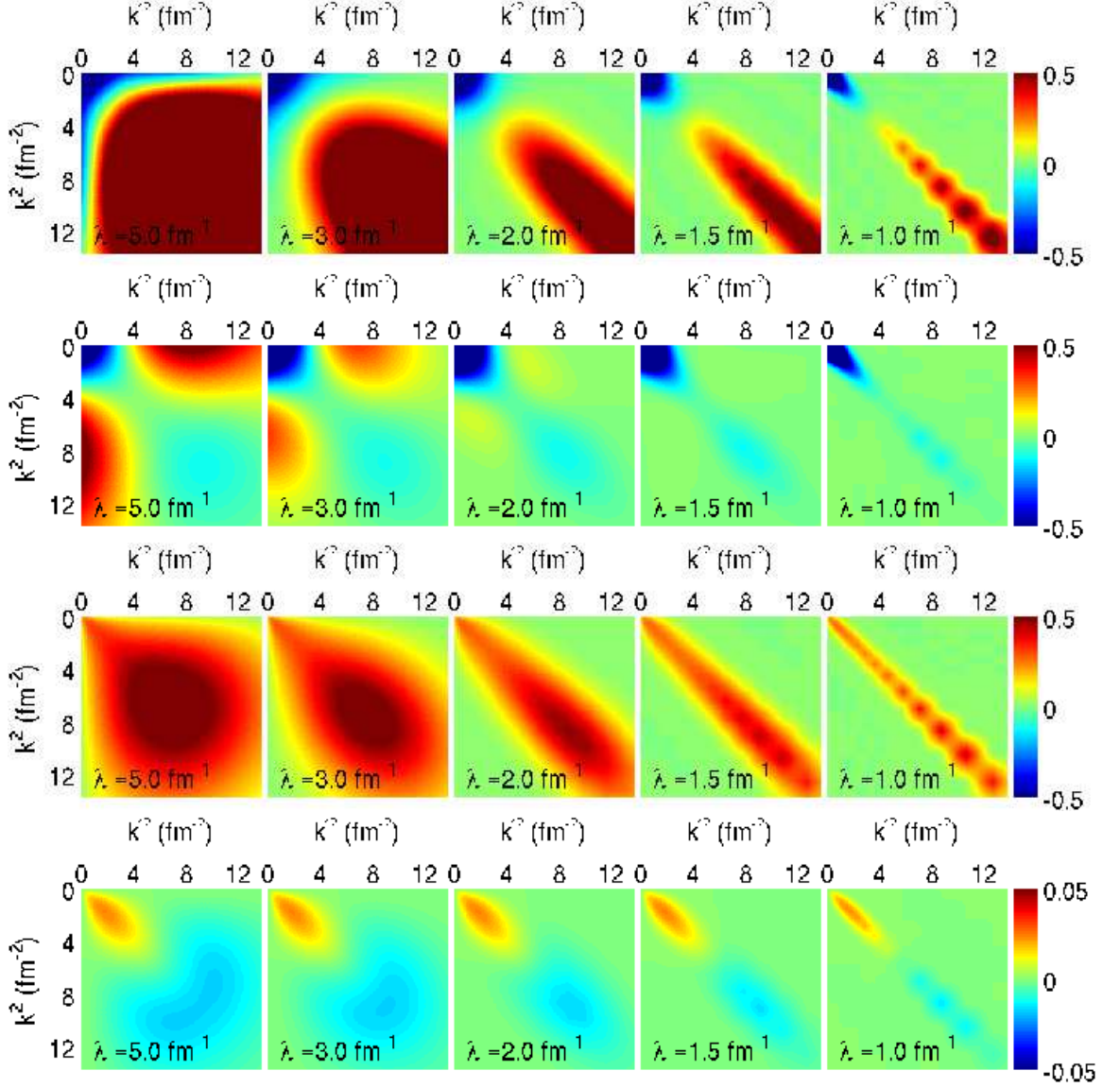


Figure 2.2: Film strips of evolution for representative partial waves in the N<sup>3</sup>LO (600 MeV) interaction of Ref. [49] in the momentum representation. Partial waves shown are  $^1S_0$ ,  $^3S_1$ ,  $^1P_1$ , and  $^3F_3$ .

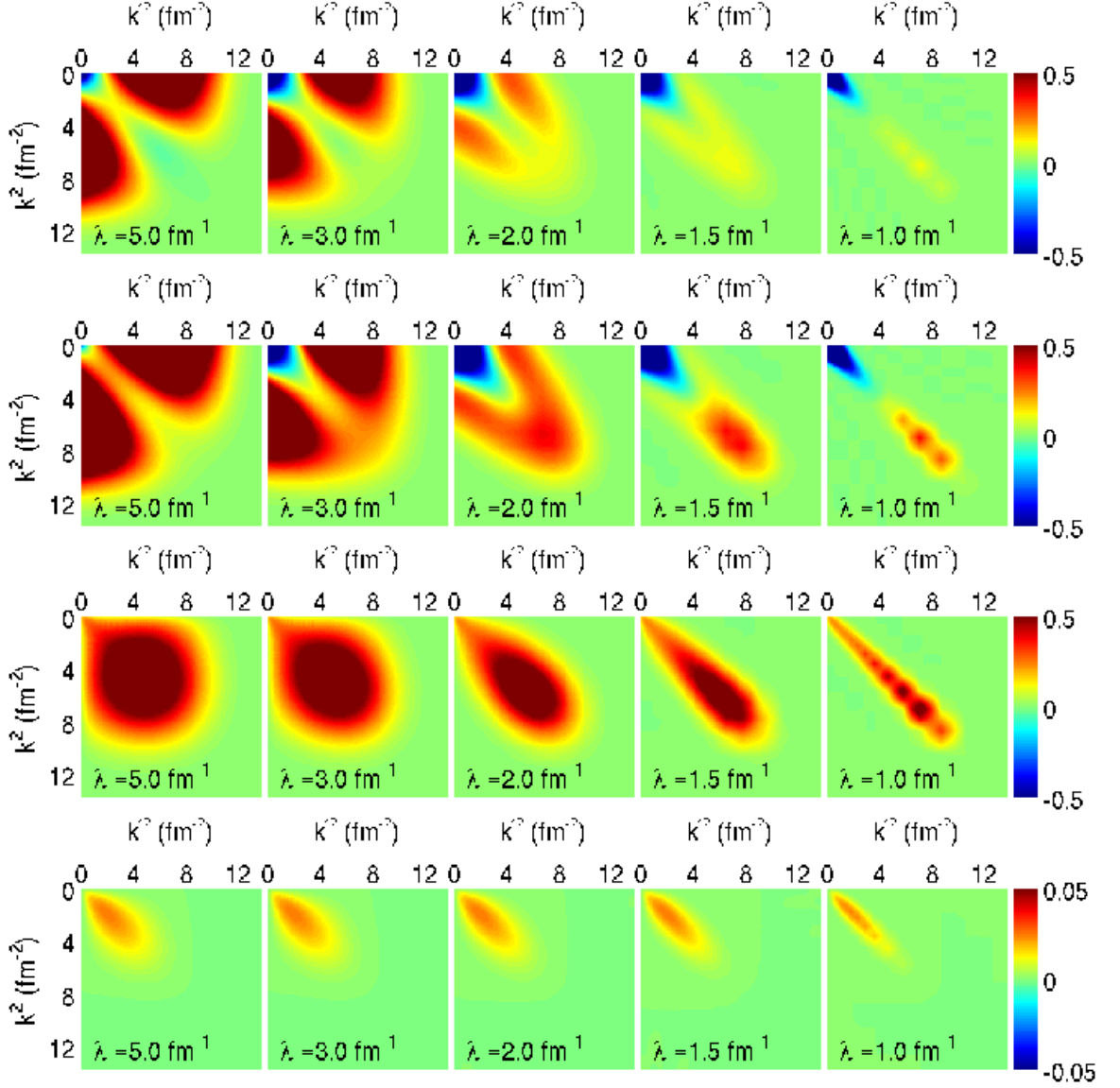


Figure 2.3: Film strips of evolution for representative partial waves in the  $N^3\text{LO}$  (550/600 MeV) interaction of Ref. [50] in the momentum representation. Partial waves shown are  $^1S_0$ ,  $^3S_1$ ,  $^1P_1$ , and  $^3F_3$ .



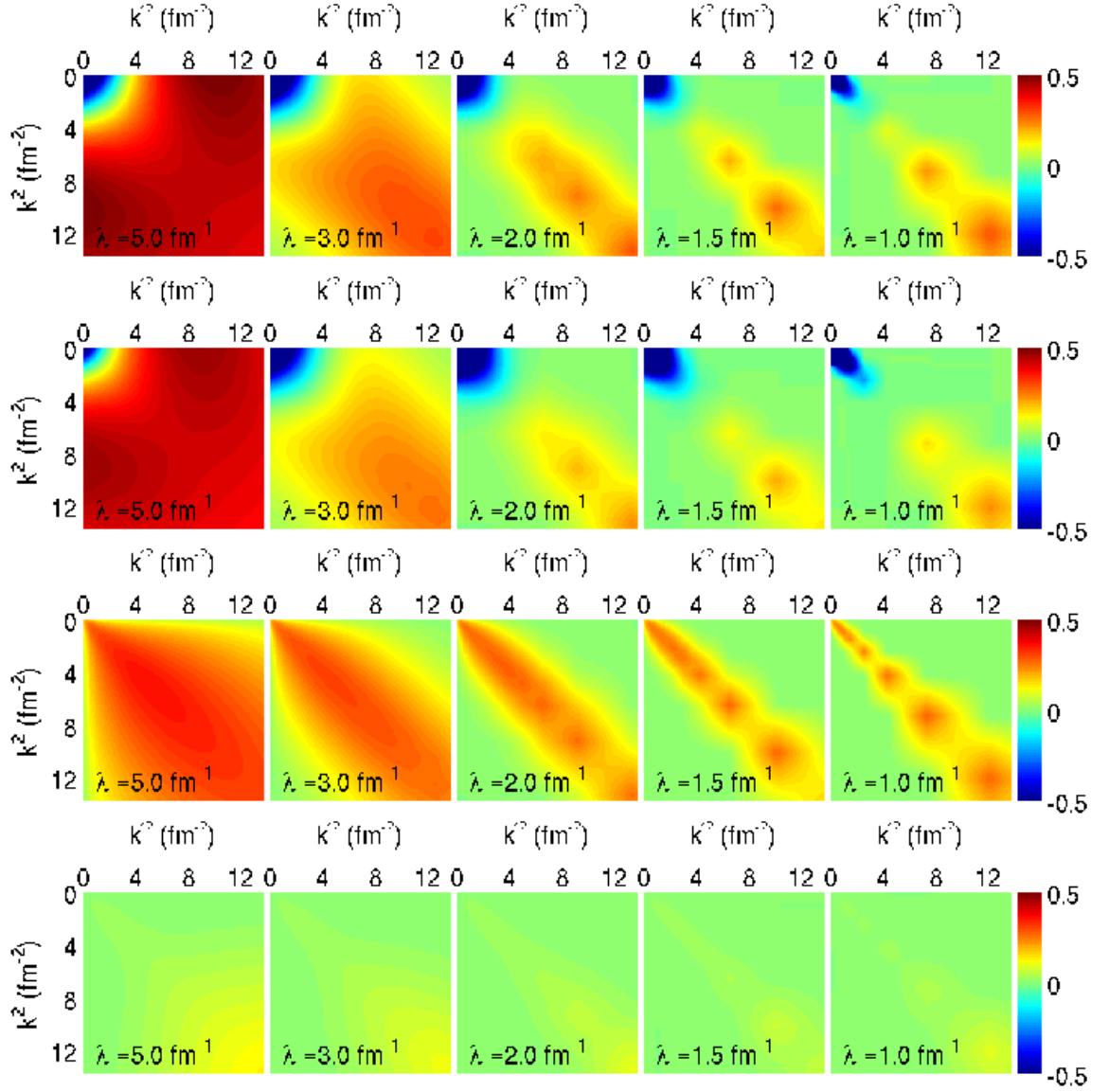


Figure 2.4: Film strips of evolution for representative partial waves in the AV18 interaction of Ref. [9] in the momentum representation. Partial waves shown are  $^1S_0$ ,  $^3S_1$ ,  $^1P_1$ , and  $^3F_3$ .

particularly suitable to the  $\chi$ EFT program, though it is equally successful at softening relatively hard potentials such as AV18 (see Fig. 2.4)<sup>10</sup>.

Once we have obtained wavefunctions of the evolved Hamiltonian through the flow equations of Eq. (2.8), we can directly construct the unitary transformation,  $U_s$ , at each  $s$  explicitly [31]. Given a complete set of eigenstates of  $H_s$ ,  $\{|\psi_\alpha(s)\rangle\}$ ,  $U_s$  can be written as,

$$U_s = \sum_{\alpha} |\psi_\alpha(s)\rangle \langle \psi_\alpha(0)| . \quad (2.12)$$

Because of the discretization, the summation over  $\alpha$  is finite and can be achieved through simple matrix multiplications using platforms such as Fortran and MATLAB.

With  $U_s$ , the wavefunctions can be evolved independently,

$$\begin{aligned} U_s |\psi_\beta(0)\rangle &= \sum_{\alpha} |\psi_\alpha(s)\rangle \langle \psi_\alpha(0)| \psi_\beta(0)\rangle \\ &= \sum_{\alpha} |\psi_\alpha(s)\rangle \delta_{\alpha,\beta} \\ &= |\psi_\beta(s)\rangle . \end{aligned} \quad (2.13)$$

This form is particularly convenient for evolving individual operators in parallel with the chosen initial interaction. In particular, any operator can be evolved directly as

$$O_s = U_s O U_s^\dagger , \quad (2.14)$$

as opposed to solving another flow equation,

$$\frac{dO_s}{ds} = [[G_s, H_s], O_s] , \quad (2.15)$$

just as for the Hamiltonian. These are identical strategies, but for some operators evolving the potential and using  $U_s$  as in Eq. (2.14) is more numerically robust [43].

<sup>10</sup>Note however that SRG evolution does in general introduce nonlocality to the initially local AV18, spoiling its use in the GFMC program.

Ultimately, having the explicit unitary transformation matrix facilitates rapid calculation of many different operators with minimal coding.

To carry out the SRG evolution, we use a built-in MATLAB differential equation solver, such as the MATLAB function `ode23` [44], which is an implementation of a Runge-Kutta differential equation algorithm [45]. We studied the running time to evolve the various SRG schemes (i.e., the choice of  $G_s$ ) by plotting the time to run versus the evolution parameter,  $s$ . We find a linear relationship to  $s$ , indicating no stiffness, in every combination of potential and SRG scheme used to date. Details regarding these timing studies and other computational scaling issues are reviewed in Appendix D.

## 2.2 Second Quantization

To see how the two-, three-, and higher-body potentials are identified, it is useful to decompose  $H_s$  in second-quantized form [46] which was first used for this purpose in Ref. [47]. We can write an  $A$ -body Hamiltonian in general as:

$$H = \sum_{ij} T_{ij} a_i^\dagger a_j + \frac{1}{2!} \sum_{ijkl} V_{ijkl}^{(2)} a_i^\dagger a_j^\dagger a_l a_k + \frac{1}{3!} \sum_{ijklmn} V_{ijklmn}^{(3)} a_i^\dagger a_j^\dagger a_k^\dagger a_n a_m a_l + \dots, \quad (2.16)$$

where  $a_i^\dagger$  and  $a_i$  represent creation and destruction operators with respect to the vacuum in some single-particle basis. The quantities  $T_{ij}$ ,  $V_{ijkl}^{(2)}$ , and  $V_{ijklmn}^{(3)}$  represent matrix elements of their respective operators.

As a straightforward way to see how the SRG induces many-body forces in an  $A$  body space, one can evaluate the flow equations using the Hamiltonian in the form of Eq. (2.16):

$$\frac{dH_s}{ds} = \left[ \left[ \sum_{ij} T_{ij} a_i^\dagger a_j, \sum_{ijkl} V_{ijkl,s}^{(2)} a_i^\dagger a_j^\dagger a_l a_k + \dots \right], \sum_{ij} T_{ij} a_i^\dagger a_j + \sum_{ijkl} V_{ijkl,s}^{(2)} a_i^\dagger a_j^\dagger a_l a_k + \dots \right] \quad (2.17)$$

For example consider the evolution of the potential,  $V_s$ , with the Hamiltonian truncated to just the two-body interactions:

$$\begin{aligned}
\frac{dV_s}{ds} &= \left[ \left[ \sum_{ij} T_{ij} a_i^\dagger a_j, \sum_{ijkl} V_{klmn,s}^{(2)} a_k^\dagger a_l^\dagger a_n a_m \right], \sum_{ijkl} V_{opqr,s}^{(2)} a_o^\dagger a_p^\dagger a_r a_q \right] \\
&= T_{ij} V_{klmn} V_{opqr} \times \left[ (a_i^\dagger a_j a_k^\dagger a_l^\dagger a_n a_m - a_k^\dagger a_l^\dagger a_n a_m a_i^\dagger a_j), a_o^\dagger a_p^\dagger a_r a_q \right] \\
&= T_{ij} V_{klmn} V_{opqr} \times \left( a_i^\dagger a_j a_k^\dagger a_l^\dagger a_n a_m a_o^\dagger a_p^\dagger a_r a_q - a_k^\dagger a_l^\dagger a_n a_m a_i^\dagger a_j a_o^\dagger a_p^\dagger a_r a_q \right. \\
&\quad \left. - a_o^\dagger a_p^\dagger a_r a_q a_i^\dagger a_j a_k^\dagger a_l^\dagger a_n a_m + a_o^\dagger a_p^\dagger a_r a_q a_k^\dagger a_l^\dagger a_n a_m a_i^\dagger a_j \right), \tag{2.18}
\end{aligned}$$

resulting in the large strings of  $a$ 's and  $a^\dagger$ 's.

These terms can be brought into normal order with respect to the vacuum to simplify them. For this we will employ Wick's theorem [48], which states (using  $A_i$  to represent  $a_i$  or  $a_i^\dagger$ )

$$\begin{aligned}
A_i A_j A_k \cdots A_m &= N(A_i A_j A_k A_l \cdots A_m) \\
&\quad + N \left( \overbrace{(A_i A_j A_k A_l \cdots A_m)} + \text{all single contractions} \right) \\
&\quad + N \left( \overbrace{(A_i A_j A_k A_l \cdots A_m)} + \text{all double contractions} \right) \\
&\quad \vdots \\
&\quad + N (\text{all full contractions}) , \tag{2.19}
\end{aligned}$$

and its corollary

$$\begin{aligned}
N(A_i A_j) N(A_k A_l) &= N(A_i A_j A_k A_l) + N(\overbrace{A_i A_j A_k A_l}) + N(\overbrace{A_i A_j A_k A_l}) \\
&\quad + N(A_i \overbrace{A_j A_k A_l}) + N(A_i \overbrace{A_j A_k A_l}) + N(\overbrace{A_i A_j A_k A_l}) \\
&\quad + N(\overbrace{A_i A_j A_k A_l}) , \tag{2.20}
\end{aligned}$$

which helps to simplify products of multiple, individually normal-ordered operator strings. There is one non-vanishing type of contraction in the vacuum

$$\overline{a_i a_j^\dagger} = \delta_{ij} , \quad (2.21)$$

and the other three,  $\overline{a_i^\dagger a_j}$ ,  $\overline{a_i a_j}$ , and  $\overline{a_i^\dagger a_j^\dagger}$ , give zero.

Returning to the result of Eq. (2.18), we can now see what many-body contributions it contains. The normal order of all operators in each term is the same for all terms and thus cancel, so no-five body operator survives at this order. All terms resulting from a single contraction also cancel each other because of the double commutator structure. For example  $N(a_i^\dagger \overline{a_j^\dagger a_k^\dagger} a_l^\dagger a_n a_m a_o^\dagger a_p^\dagger a_r a_q)$  and  $N(-a_o^\dagger a_p^\dagger a_r a_q a_i^\dagger \overline{a_j^\dagger a_k^\dagger} a_l^\dagger a_n a_m)$  are equal and opposite. At the level of double contractions the commutator cannot cancel all the terms and three-body terms survive. For example the first term gives:

$$\begin{aligned} a_i^\dagger a_j a_k^\dagger a_l^\dagger a_n a_m a_o^\dagger a_p^\dagger a_r a_q &= T_{ij} V_{klmn} V_{opqr} \times (a_i^\dagger a_l^\dagger a_p^\dagger a_n a_r a_q \delta_{jk} \delta_{mo} + a_i^\dagger a_l^\dagger a_p^\dagger a_m a_r a_q \delta_{jk} \delta_{no} \\ &\quad + a_i^\dagger a_l^\dagger a_o^\dagger a_n a_r a_q \delta_{jk} \delta_{mp} + a_i^\dagger a_l^\dagger a_o^\dagger a_m a_r a_q \delta_{jk} \delta_{np} \\ &\quad + a_i^\dagger a_k^\dagger a_p^\dagger a_n a_r a_q \delta_{jl} \delta_{mo} + a_i^\dagger a_k^\dagger a_p^\dagger a_m a_r a_q \delta_{jl} \delta_{no} \\ &\quad + a_i^\dagger a_k^\dagger a_o^\dagger a_n a_r a_q \delta_{jl} \delta_{mp} + a_i^\dagger a_k^\dagger a_o^\dagger a_m a_r a_q \delta_{jl} \delta_{np}) , \end{aligned} \quad (2.22)$$

which can be simplified due to the symmetry of the potential matrix elements. In fact all of these terms are permutations of a single contribution in a diagrammatic representation shown in Fig. 2.5. Equation (2.22) lists the explicit legs of the second diagram on the bottom, which is the lone two-body only contribution to the induced three-body force. Carrying out the same calculation for all triple contractions will result in enumerating the legs associated with the two diagrams in the top right of Fig. 2.5 which contribute to two-body evolution. In an  $A$ -body system this means all disconnected combinations of these two-body contributions.

$$\begin{aligned}
\frac{dV_2}{ds} &= \text{Diagram 1} + \text{Diagram 2} - \text{Diagram 3} \\
\frac{dV_3}{ds} &= \text{Diagram 4} + \text{Diagram 5} + \text{Diagram 6} + \text{Diagram 7} + \dots
\end{aligned}$$

Figure 2.5: A diagrammatic decomposition of the SRG induced forces [47]. A circle at a vertex denotes a commutator with  $T_{\text{rel}}$ .

As follows from these normal-ordering calculations,  $A$ -body forces cannot be affected by the value of any initial higher-body terms; e.g., two-body evolution cannot be influenced by three-body forces. This can be seen in second quantized form by writing out commutators involving an  $A$ -body force. One can quickly see that it is impossible to contract such terms to have less than  $A$  pairs of  $a^\dagger$ 's and  $a$ 's. So for instance, an initial four-body force cannot contribute to the evolution of two- or three-body forces. This feature is true for calculations done in the vacuum. However, when the SRG is implemented in the background of a nuclear medium, the rules for contractions change. This has profound consequences for the use of the SRG in nuclear matter calculations. Those calculations are outside the scope of this thesis, so the “in-medium SRG” will not be considered further here.

The correspondence between equations like Eq. (2.22) and Fig. 2.5 can be written more concisely by expanding the commutators of the SRG flow equation, Eq. (2.8). For instance the top row of Fig. 2.5 corresponds to the expansion of Eq. (2.8) in

2-body space:

$$\begin{aligned}
\frac{dV_s^{(2)}}{ds} &= [[T_{\text{rel}}, V_s], H_s] \\
&= [(T_{\text{rel}}V_s - V_sT_{\text{rel}}), (T_{\text{rel}} + V_s)] \\
&= [\overline{V}_s^{(2)}, (T_{\text{rel}} + V_s)] \\
&= [\overline{V}_s^{(2)}, T_{\text{rel}}] + \overline{V}_s^{(2)}V_s^{(2)} - V_s^{(2)}\overline{V}_s^{(2)} \\
&= \overline{\overline{V}}_s^{(2)} + \overline{V}_s^{(2)}V_s^{(2)} - V_s^{(2)}\overline{V}_s^{(2)}, \tag{2.23}
\end{aligned}$$

where  $\overline{V}_s^{(2)}$  represents a single commutator with  $T_{\text{rel}}$  and  $\overline{\overline{V}}_s^{(2)}$  represents a double commutator with  $T_{\text{rel}}$ ,  $[[T_{\text{rel}}, V_s^{(2)}], T_{\text{rel}}]$ . These correspond to the vertices with one and two circles in the top row of Fig. 2.5, so the last line of Eq. (2.23) is represented by those diagrams. Similarly the bottom row represents the expansion in the 3-body space,

$$\frac{dV_s^{(3)}}{ds} = \overline{\overline{\overline{V}}}_s^{(3)} + [\overline{V}_s^{(2)}, V_s^{(2)}] + [\overline{V}_s^{(2)}, V_s^{(3)}] + [\overline{V}_s^{(3)}, V_s^{(2)}] + [\overline{V}_s^{(3)}, V_s^{(3)}]. \tag{2.24}$$

We stress that these diagrams are not Feynman diagrams, but merely a mnemonic to summarize the contributions to the SRG transformation. However, each vertex does represent a particular type of interaction and the diagrammatic treatment can be used to explore the interplay within the flow equations. An example of this kind of investigation will be presented in chapter 4.

Disconnected diagrams for each  $A$ -sector are canceled out by the evolutions defined in lower sectors. Consider the flow equation for the general three-body Hamiltonian [28] (in a modified notation),

$$\frac{dV_s}{ds} = \frac{dV_{12}}{ds} + \frac{dV_{13}}{ds} + \frac{dV_{23}}{ds} + \frac{dV_{123}}{ds} = [[T_{\text{rel}}, V_s], H_s], \tag{2.25}$$

where  $V_{ij}$  is the two-body potential between the  $i$ th and  $j$ th particles and  $V_{123}$  is the three-body potential. The relative kinetic energy  $T_{\text{rel}}$  is the combination of the relative kinetic energy between the  $i$ th and  $j$ th particles,  $T_{ij} = (k_i - k_j)^2/2m$ , and the relative kinetic between that pair's center of mass and the third particle,  $T_k = \frac{3}{2}((k_i + k_j)/2 - k_k)^2/m$ . Because  $T_i$  and  $V_{jk}$  commute the commutator of  $T_{\text{rel}}$  and  $V_{ij}$  is

$$[T_{\text{rel}}, V_{ij}] = [T_{ij}, V_{ij}] , \quad (2.26)$$

so the flow equation for the two-body system is

$$\frac{dV_{ij}}{ds} = [[T_{ij}, V_{ij}], (T_{ij} + V_{ij})] . \quad (2.27)$$

We can expand the three-body flow equation, shown in Eq. (2.25), and using Eqs. 2.26 and 2.27 see that the two-body evolution cancels out precisely, leaving

$$\begin{aligned} \frac{dV_{123}}{ds} &= [[T_{12}, V_{12}], (T_3 + V_{13} + V_{23} + V_{123})] \\ &\quad + [[T_{13}, V_{13}], (T_2 + V_{12} + V_{23} + V_{123})] \\ &\quad + [[T_{23}, V_{23}], (T_1 + V_{12} + V_{13} + V_{123})] \\ &\quad + [[T_{\text{rel}}, V_{123}], H_s] . \end{aligned} \quad (2.28)$$

So the three-body evolution contains no spectator graphs, but only connected commutators of the form  $[\overline{V}_{ij}, V_{jk}]$ ,  $[\overline{V}_{ij}, V_{ijk}]$ , or  $[\overline{V}_{ijk}, V_{ijk}]$ . The two-body evolution equations have completely cancelled out of the three-body sector and are completely determined by the two-body evolution. In other words, free-space  $A$ -body forces are *defined* by evolution in the  $A$ -body space and are not altered or evolved differently in higher sectors.

We can also see these cancellations in second-quantized form by considering the one-loop two-body graphs on the top of Fig. 2.5 coupled with a single line representing



a spectator particle in a three-particle system. Such graphs cannot be generated from Eq. (2.18), there not being enough contraction opportunities to generate the necessary creation/annihilation operators and momentum delta functions.

So, the SRG induces  $A$ -body forces using connected terms involving lower-body forces; three-body forces can be initially zero but will grow due to two-body-only contributions. Eventually  $A$ -body forces are induced as one can see by taking successive infinitesimal steps in the evolution. In the first step, three-body forces appear which allow induction of four-body forces in the next step. These in turn allow higher-body forces ad infinitum. Including induced  $A$ -body forces is a unitary calculation in an  $A$ -body space. In a two body-space, three-body forces cannot be represented so evolution in the two-body space is only approximately unitary when the evolved Hamiltonian is used in the three-particle system. Because the induced three-body forces are not included, we speak of “missing induced  $A$ -body forces”. These induced forces appear in a hierarchy of decreasing strength, which will be explored quantitatively in chapter 4.

## CHAPTER 3

### DECOUPLING IN THE MOMENTUM REPRESENTATION

#### 3.1 Benefits of Decoupling

While observables are unchanged by the SRG's unitary transformations, the contributions from high-momentum intermediate eigenstate components to low-energy observables is modified by the running transformation. In particular, the SRG as implemented in Refs. [28, 31] has the effect of partially diagonalizing the momentum-space potential to a width of order the evolution parameter. Because of this partial diagonalization, one anticipates a direct decoupling of low-energy observables from high-energy degrees of freedom.

In Ref. [31], evidence for decoupling at low momentum was shown for the Argonne  $v_{18}$  [9] potential in calculations of phase shifts and the deuteron. In this chapter, we extend the demonstration of decoupling to nucleon-nucleon (NN) potentials from chiral effective field theory (EFT) [49, 50] and to few-body nuclei up to  $A = 6$  to verify its universal nature and to show quantitatively that the residual coupling is perturbative above the energy corresponding to the SRG evolution parameter.

The practical test for decoupling is whether changing high-momentum matrix elements of the potential changes low-energy observables. The strategy here is to first evolve the initial potential  $V_{NN}$  with the SRG equations to obtain the SRG potential  $V_s$ , where  $s$  denotes the flow parameter of the transformation. Then we apply a parametrized regulator to cut off the high-momentum part of the evolved potential in a controlled way. This cutoff potential is used to calculate few-body observables and their relative errors. By varying the parameters of the regulator and correlating them with errors in the calculated observables, we have a diagnostic tool to quantitatively analyze the decoupling.

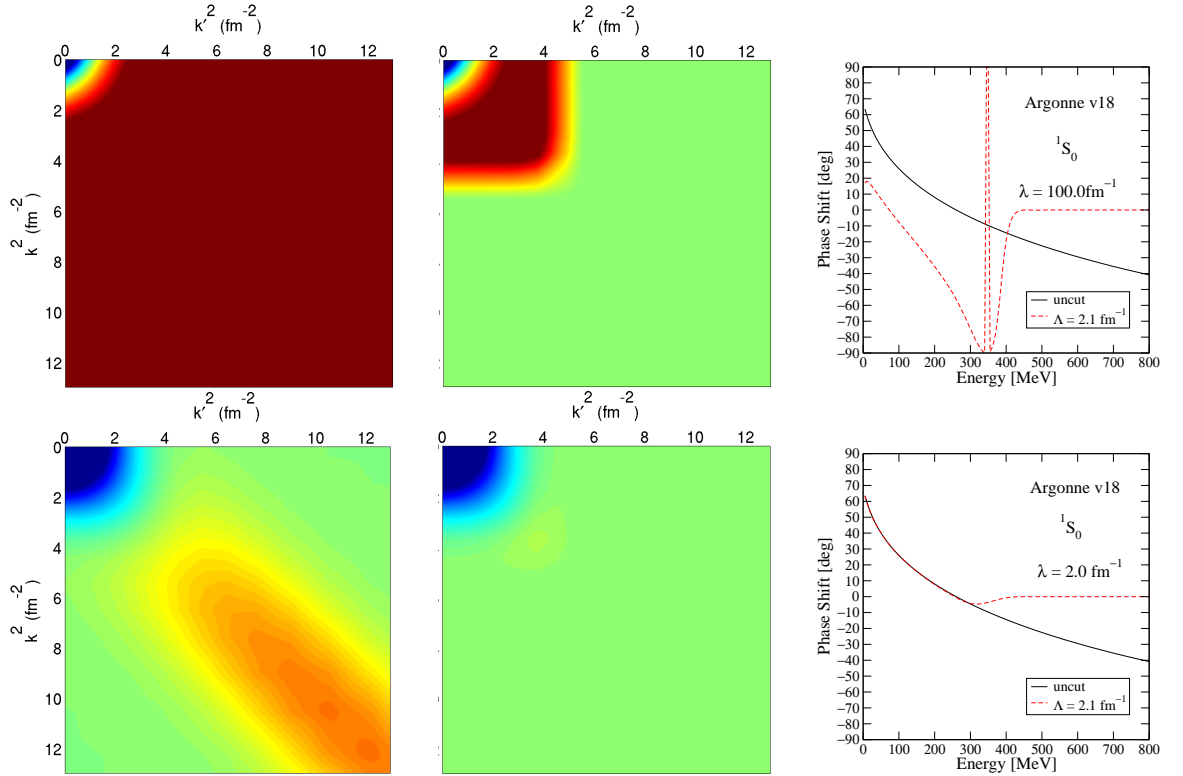


Figure 3.1: Phase shifts and relative errors in the  $^1S_0$  channel for SRG potentials evolved from the Argonne  $v_{18}$  potential of Ref. [9]. The upper row shows cut and uncut potentials and phase shifts for the unevolved initial potential. The lower row shows the same for the initial potential evolved to  $\lambda = 2.0 \text{ fm}^{-1}$ .

Shown in Figure 3.1 is an example of the strategy employed in this chapter to study the decoupling benefits of the SRG. On the top row, the pictures from left to right are the uncut Argonne  $v_{18}$  potential in the  $^1S_0$  partial wave, the same potential cut at  $\Lambda = 2.1 \text{ fm}^{-2}$  and the phase-shift calculated from both potentials. The bottom row shows the same three plots except now the Argonne potential is evolved with the SRG to  $\lambda = 2.0 \text{ fm}^{-1}$ . In the top phase shift picture, the calculation from the cut potential fails everywhere; the low-energy observable is lost despite the low-energy matrix elements of the potential being preserved. In the bottom phase shift picture the low-energy phase shift is preserved because the SRG has renormalized the potential and preserved all the information relevant to the calculation.

The phase shift,  $\delta_\ell(E_{k_0})$ , (where  $\ell$  denotes a particular partial wave) is a nuclear scattering observable calculated non-perturbatively from the potential, via the relation  $R_\ell(k, k'; E_{k_0}) = -\frac{\tan\delta_\ell(E_{k_0})}{m_N k_0}$  [51], where  $R_\ell$  is the reaction matrix,

$$\begin{aligned}
R_\ell(k, k', k_0) &= V_\ell(k, k') + \frac{2}{\pi} P \int_0^\infty dp \frac{p^2 V_\ell(k, p) R_\ell(p, k', k_0)}{E_{k_0} - E_p} \\
&= V_\ell(k, k') + \frac{2}{\pi} P \int_0^\infty dp \frac{p^2 V_\ell(k, p) V_\ell(p, k')}{E_{k_0} - E_p} \\
&\quad + \frac{4}{\pi^2} P \int_0^\infty dp dq \frac{p^2 q^2 V_\ell(k, p) V_\ell(p, q) V_\ell(q, k')}{(E_{k_0} - E_p)(E_{k_0} - E_q)} + \dots \\
&= \langle k | V_\ell | k' \rangle + \sum_p \frac{\langle k | V_\ell | p \rangle \langle p | V_\ell | k' \rangle}{(k_0^2 - p^2)/m} + \dots
\end{aligned} \tag{3.1}$$

Where  $V_\ell$  represents the potential in a particular partial wave, and  $k_0$  is the momentum corresponding to the desired on-shell energy of the calculation. The  $P$  here indicates that we are using the Cauchy principal value prescription which keeps matrix elements real, a convenient property for numerical calculations. Cutting the potential as shown in Fig. 3.1 does not lose information for the first order term (linear in  $V$ ) since it represents only one matrix element on the diagonal of the potential. However,

the second (and subsequent) terms involve sums over intermediate states so that matrix elements along the whole row or column involving the state  $k_0$  are necessary to the calculation. When these are arbitrarily cut off as in the top row, the phase shift will fail at any energy.

However, in the bottom row of Fig. 3.1 the SRG has transformed, or renormalized, the potential so that all the relevant information has been placed inside a low-energy region of the potential. Now we can cut the high-energy matrix elements, which are decoupled from the low-energy ones, leaving the phase-shift intact for low energies. Thus we need less of the total basis to represent the low-energy physics we are concerned with reproducing.

The tool we will use to study decoupling is a smooth exponential regulator applied to the potential to cut off momenta above  $\Lambda$ :

$$V_{\lambda,\Lambda}(k, k') = e^{-(k^2/\Lambda^2)^{n_{\text{exp}}}} V_{\lambda}(k, k') e^{-(k'^2/\Lambda^2)^{n_{\text{exp}}}}, \quad (3.2)$$

where  $n_{\text{exp}}$  takes on integer values. From the cut potentials we calculate observables such as phase shifts and ground-state energies and compare to values calculated with the corresponding uncut potential. If there is decoupling between matrix elements in a given potential (evolved or otherwise), we should be able to set those elements to zero in this systematic way and use the relative error in the observable as a metric of the degree of decoupling. By varying  $n_{\text{exp}}$  we can identify quantitatively the residual coupling strength.

Here we are working with NN interactions only and therefore the SRG transformations are truncated at the two-body level, which means that they are only approximately unitary for  $A \geq 3$  such that those observables will vary with  $s$ . In these cases decoupling is tested by comparing cut to uncut potentials at a fixed  $s$ . All two-body

observables calculated with the uncut  $H_s$  are independent of  $s$  to within numerical precision. The actual numerical error depends on the details of the discretization (e.g., the number and distribution of mesh points, usually gaussian) and on the accuracy and tolerances of the differential equation solver. While in practice we can make such errors very small, to avoid mixing up small errors we will also compare cut to uncut potentials rather than to the unevolved ( $s = 0$ ) potential for two-body observables.

### 3.2 Mechanics of Decoupling

The source of decoupling is the partial diagonalization of the Hamiltonian by the SRG evolution [52]. For the NN interaction, the flow Eq. (2.8) can be simply evaluated in the space of discretized relative momentum NN states [28]. For a given partial wave, with units where  $\hbar^2/M = 1$ , we define diagonal matrix elements of momentum  $k$  as<sup>11</sup>

$$\langle k|H_s|k\rangle = \langle k|H_D|k\rangle \equiv e_k , \quad (3.3)$$

and

$$\langle k|T_{\text{rel}}|k\rangle \equiv \epsilon_k = k^2 . \quad (3.4)$$

If we take  $G_s = T_{\text{rel}}$ , the flow equation for each matrix element is

$$\begin{aligned} \frac{d}{ds}\langle k|H_s|k'\rangle &= \sum_q (\epsilon_k + \epsilon_{k'} - 2\epsilon_q) \langle k|H_s|q\rangle \langle q|H_s|k'\rangle \\ &= -(\epsilon_k - \epsilon_{k'})^2 \langle k|V_s|k'\rangle + \sum_q (\epsilon_k + \epsilon_{k'} - 2\epsilon_q) \langle k|V_s|q\rangle \langle q|V_s|k'\rangle . \end{aligned} \quad (3.5)$$

A useful image of the mechanism by which the SRG diagonalizes the potential is shown in Fig. 3.2. The pictures represent a snap shot of the different parts of the flow

<sup>11</sup>Note that the derivation here is only valid for a discretized momentum basis such as the gaussian mesh used here.

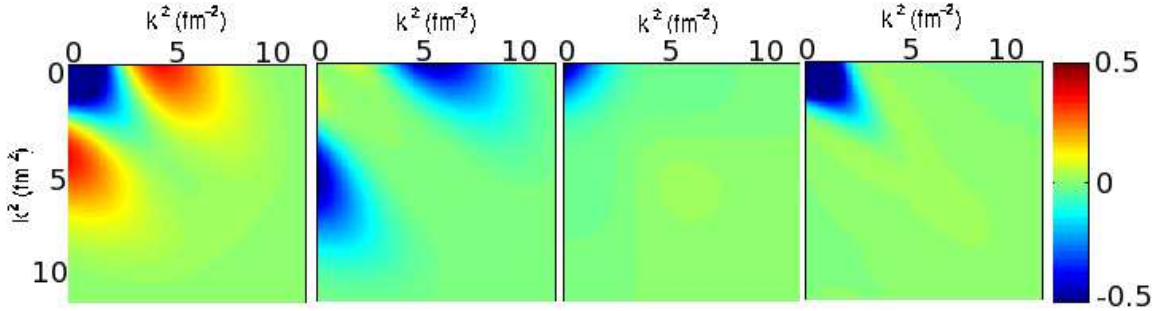


Figure 3.2: A snapshot of the contributions to the flow of the potential when using the  $G_s = T_{\text{rel}}$  choice of SRG. From left to right, the pictures are  $V_{\lambda=2.5}$ , 1st and 2nd rhs terms from Eq. (3.5), and  $V_{\lambda=1.5}$ . The color scale for the middle pictures is scaled up for visibility.

equations contributing to the evolution between two specific values of  $\lambda$ . The plot on the left is the potential evolved down to  $\lambda = 2.5 \text{ fm}^{-1}$  and the plot on the far right is the potential further evolved to  $\lambda = 1.5 \text{ fm}^{-1}$ . The two panels in the middle are the first and second terms of the right-hand side from the flow equations in Eq. (3.5). It is clear that the first term is the dominant contributor to the suppression of off-diagonal matrix elements outside the band of width  $\lambda^2$ . At the same time the second term is providing for the flow of physics information to low-energy states by increasing the magnitude of matrix elements associated with those states. While the first term achieves decoupling by suppressing off-diagonal matrix elements, the second term is preserving unitarity by transforming the information of high-energy matrix elements to low-momentum states.

We can find a semi-quantitative approximation for the flow of off-diagonal matrix elements by keeping only the first term on the right side of Eq. (3.5). Then the flow equation applied to individual off-diagonal matrix elements simplifies to

$$\frac{d}{ds} \langle k | H_s | k' \rangle = \frac{d}{ds} \langle k | V_s | k' \rangle \approx -(\epsilon_k - \epsilon_{k'})^2 \langle k | V_s | k' \rangle, \quad (3.6)$$

which has the simple exponential solution

$$\langle k|V_s|k'\rangle \approx \langle k|V_{s=0}|k'\rangle e^{-s(\epsilon_k - \epsilon_{k'})^2}. \quad (3.7)$$

In Fig. 3.3, we plot  $\langle k|V_s|k'\rangle$  and the approximation from Eq. (3.7) versus  $s$  for some representative off-diagonal points in two partial waves. In almost all cases the approximation gives a reasonable estimate of the monotonic decrease to zero; in the one exception there is a significantly more rapid decrease than predicted.

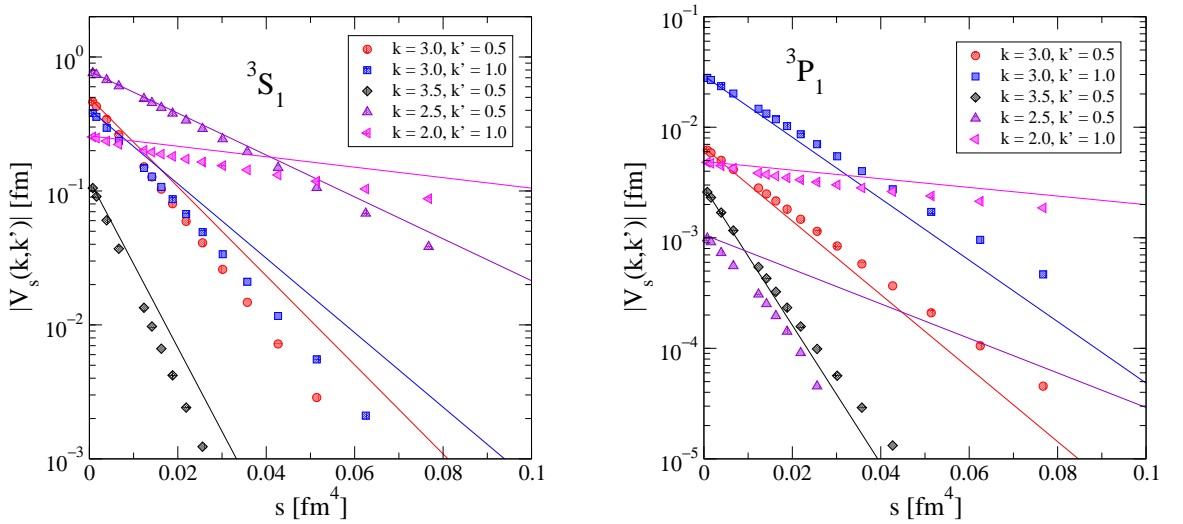


Figure 3.3: Absolute value of the matrix element  $\langle k|V_s|k'\rangle$  for a representative sampling of off-diagonal  $(k, k')$  pairs as a function of  $s$ , compared with the simple solutions from Eq. (3.7), which are straight lines (they agree at  $s = 0$ ). The partial waves  ${}^3S_1$  and  ${}^3P_1$  are shown.

Equation (3.7) shows that it is convenient to switch to the flow variable  $\lambda = 1/s^{1/4}$ , which has units of  $\text{fm}^{-1}$ , because it is a measure of the resulting diagonal width of  $V_s$  in momentum space. More precisely, the matrix  $\langle k|V_s|k'\rangle$  plotted as a function of kinetic energies  $k^2$  and  $k'^2$  will rapidly go to zero outside of a diagonal band roughly of width  $\lambda^2$ , which is verified by numerical calculations [52, 53]. For momenta within  $\lambda$



of the diagonal, the omitted quadratic part of the flow equation is, of course, essential, and drives the flow of physics information necessary to preserve unitarity.

We can examine the flow of off-diagonal matrix elements as a whole by considering the trace of  $H_s^2$ ,  $\text{Tr}[H_s^2] = \text{Tr}[U_s H U_s^\dagger U_s H U_s^\dagger] = \text{Tr}[H^2]$  using  $U U^\dagger = 1$  and the cyclic property of traces [33]:

$$\begin{aligned} \frac{d}{ds} \text{Tr}[H^2] = 0 &= \frac{d}{ds} \sum_{i,j} H_{s,ij} H_{s,ji} \\ &= \frac{d}{ds} \sum_i |\langle i|H_s|i\rangle|^2 + \frac{d}{ds} \sum_{i \neq j} |\langle i|H_s|j\rangle|^2, \end{aligned} \quad (3.8)$$

and therefore we get,

$$\frac{d}{ds} \sum_{i \neq j} |\langle i|H_s|j\rangle|^2 = -\frac{d}{ds} \sum_i |\langle i|H_s|i\rangle|^2 = -2 \sum_i \langle i|H_s|i\rangle \frac{d}{ds} \langle i|H_s|i\rangle. \quad (3.9)$$

In the case of Wegner's choice,  $G_s = H_D$ , the flow equation for each matrix element is

$$\frac{d}{ds} \langle k|H_s|k'\rangle = \sum_q (e_k + e_{k'} - 2e_q) \langle k|H_s|q\rangle \langle q|H_s|k'\rangle. \quad (3.10)$$

then (3.9) simplifies to

$$\begin{aligned} \frac{d}{ds} \sum_{i \neq j} |\langle i|H_s|j\rangle|^2 &= -4 \sum_{k \neq q} e_k (e_k - e_q) |\langle k|H_s|q\rangle|^2 \\ &= -2 \sum_{k \neq q} e_k (e_k - e_q) |\langle k|H_s|q\rangle|^2 - 2 \sum_{k \neq q} e_q (e_q - e_k) |\langle q|H_s|k\rangle|^2 \\ &= -2 \sum_{k \neq q} (e_k - e_q)^2 |\langle k|H_s|q\rangle|^2, \end{aligned} \quad (3.11)$$

which shows a sum of positive definite terms whose derivative is negative, so that the off-diagonal matrix elements decrease with  $s$ . On the other hand using the choice  $G_s = T_{\text{rel}}$  and Eq. (3.5) to simplify Eq. (3.9) we get

$$\begin{aligned} \frac{d}{ds} \sum_{i \neq j} |\langle i|H_s|j\rangle|^2 &= -4 \sum_{k \neq q} \epsilon_k (e_k - e_q) |\langle k|H_s|q\rangle|^2 \\ &= -2 \sum_{k \neq q} (e_k - e_q) (\epsilon_k - \epsilon_q) |\langle k|H_s|q\rangle|^2, \end{aligned} \quad (3.12)$$

so that off-diagonal elements are not guaranteed to decrease monotonically if  $e_k - e_q$  and  $\epsilon_k - \epsilon_q$  have opposite signs (see Ref. [54] for details). However, this does not happen in the range of  $s$  that has been considered in the nuclear case because of the dominance of the kinetic energy.  $T$  is much larger than  $V$  on the diagonal and therefore  $T$  is effectively  $H_D$  in the nuclear case. We should see the difference when we evolve down to a scale at which  $T$  is no longer dominant. At such a scale new bound states appear and the choice  $G_s = T_{\text{rel}}$  cannot order them properly [54]. We don't see any such pathologies in the nuclear case because we have never needed to evolve so far in  $\lambda$  as the scale at which the deuteron appears,  $\sim 0.5 \text{ fm}^{-1}$ <sup>12</sup>.

### 3.3 Phase Shift Errors

In the upper-left panel of Fig. 3.4, we show results for the  $^1\text{S}_0$  phase shifts vs. energy calculated using the unevolved 500 MeV  $\text{N}^3\text{LO}$  potential of Ref. [49] and the corresponding SRG potential evolved to  $\lambda = 2.0 \text{ fm}^{-1}$  and then cut using the regulator of Eq. (3.2) with  $n = 8$ . We do not explicitly show results from uncut SRG potentials, because they are indistinguishable from the unevolved results.

The qualitative pattern is that when the regulator parameter  $\Lambda$  is greater than  $\lambda$ , there is good agreement of phase shifts from uncut and cut potentials at small energies and reasonable agreement up to the energy corresponding to the momentum of the cut,  $E_{\text{lab}} \approx 2\Lambda^2/m$  (with  $\hbar = 1$ ). When  $V_{\text{srg}}$  is cut below  $\lambda$ , there is poor agreement everywhere and the phase shift is zero above this energy (e.g., above  $E_{\text{lab}} = 100 \text{ MeV}$  for  $\Lambda = 1.1 \text{ fm}^{-1}$ ). Thus the decoupling of high and low momentum means that we can explicitly cut out the high-momentum part of the evolved potential

<sup>12</sup>In fact, we will not evolve this low also because we expect the hierarchy of many-body forces to break down at such small  $\lambda$ 's, as is discussed in detail in chapter's 4 and 5.

without significantly distorting low-energy phase shifts as long as we don't cut below  $\lambda$ . Cutting out the high-momentum part of conventional nuclear potentials *does* cause distortions, which has led to the misconception that reproducing high-energy phase shifts is important for low-energy nuclear structure observables [31].

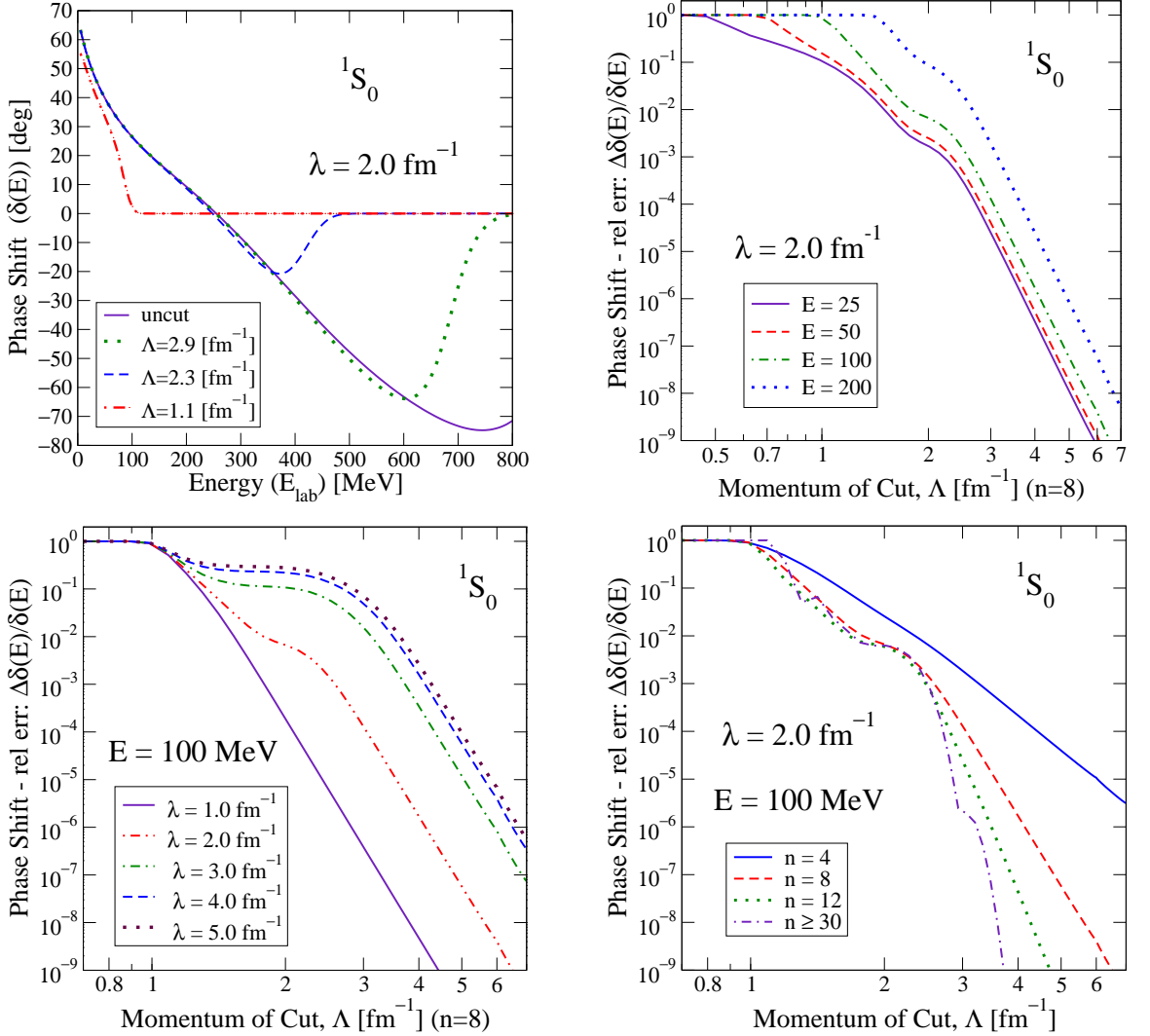


Figure 3.4: Phase shifts and relative errors in the  $^1S_0$  channel for SRG potentials evolved from the  $N^3\text{LO}$  (500 MeV) potential of Ref. [49]. The upper-left graph shows the phase shifts vs. energy for the uncut  $\lambda = 2 \text{ fm}^{-1}$  potential and several cut versions with  $n = 8$ . The other panels show the relative error as a function of the momentum cut parameter  $\Lambda$  at various energies  $E$ ,  $\lambda$ 's, and  $n$ 's, respectively.

The quantitative systematics of SRG decoupling are documented in the other panels of Fig. 3.4, where we look at the relative error as a function of the cutting momentum using log-log plots. In these error plots, three main regions are evident. In the region below the  $\Lambda$  corresponding to the fixed energy, the predicted phase shift goes to zero since the potential has vanishing matrix elements, so that the relative error goes to one. Starting at  $\Lambda$  slightly above the value of  $\lambda$ , there is a clear power-law decrease in the error. In between is a transition region without a definite pattern.

We focus here on the power-law region. In the lower-left pane, we find that this decoupling starts with a shoulder at momenta slightly above  $\lambda$ . This effect saturates when  $\lambda$  becomes comparable to the underlying cutoff of the original potential (see Fig. 3.6). In the upper-right pane we see that the shoulder signaling the start of the power-law decrease is not affected by the energy,  $E$ . This holds for other values of  $\lambda$  and  $n$ . In the lower-right pane we vary the exponent of the regulator,  $n$ , which changes the smoothness of the regulator. The smoothness affects the slope of the power law and the fine details in the intermediate region, but does not change the position of the shoulder near  $\lambda$ . As discussed below, the power-law behavior in the relative error signifies perturbative decoupling with a strength given by the sharpness of the regulator used to cut off the potential.

Indeed, the behavior of the errors in the decoupling region, where  $\Lambda > \lambda$ , can be directly understood as a consequence of the partial diagonalization of the evolved potential. The calculation of the phase shift at a low-energy  $k^2 \ll \lambda^2$  will involve an integral over  $p$  of  $V_{\lambda,\Lambda}(k,p)$ . But the potential cuts off the integral at roughly  $p^2 \approx k^2 + \lambda^2 < \Lambda^2$ , which means that we can expand the difference in the uncut and

cut potentials:

$$\delta V_{\lambda,\Lambda}(k,p) \equiv V_{\lambda}(k,p) - V_{\lambda,\Lambda}(k,p) \approx \left( \frac{k^{2n}}{\Lambda^{2n}} + \frac{p^{2n}}{\Lambda^{2n}} \right) V(k,p). \quad (3.13)$$

Simple perturbation theory in  $\delta V$  then predicts the dependence of the phase shift error to be  $1/\Lambda^{2n}$ , which is the power-law dependence seen in Figs. 3.4 and 3.5. The accuracy of first-order perturbation theory is evidenced by the constant slope of the error curves, which translates into perturbatively small residual coupling.

The detailed dependence on the energy and  $\lambda$  is not so trivially extracted. However, the weak dependence on  $E_{\text{lab}} \leq 100$  MeV and strong dependence on  $\lambda < 3 \text{ fm}^{-1}$  at fixed  $\Lambda$  seen in Fig. 3.4 implies that the integration picks up the scale  $\lambda$ , so that the dominant error scales as  $(\lambda/\Lambda)^{2n}$ . This is, in fact, observed numerically for intermediate values of  $\lambda$  (e.g., for  $1.8 \text{ fm}^{-1} < \lambda < 2.8 \text{ fm}^{-1}$  when  $\Lambda = 3 \text{ fm}^{-1}$ ).

We checked this decoupling behavior in different partial waves and for other N<sup>3</sup>LO potentials and found the same perturbative region in all cases. The plots of Fig. 3.4 are reproduced in Fig. 3.5 for representative partial waves. The potential in the S waves typically passes through zero for momenta in the region of  $\lambda = 2 \text{ fm}^{-1}$  (as in Fig. 2.1), which might lead one to associate decoupling with this structure. The error plots for other partial waves that lack this structure show that it is a more general consequence of the SRG evolution.

Note that in higher partial waves, such as  ${}^3F_3$ , the phase shift is already well decoupled and therefore doesn't benefit as much from the SRG evolution. Errors shown for this partial wave in the bottom strip of Fig. 3.5 are below  $10^{-4}$  at the start of the decoupling region (note the shoulders at  $\lambda$  in the center panel). Such partial waves are the large angular momentum components of the partial wave decomposition. Due to the centrifugal barrier term they probe long-distance forces and have strength

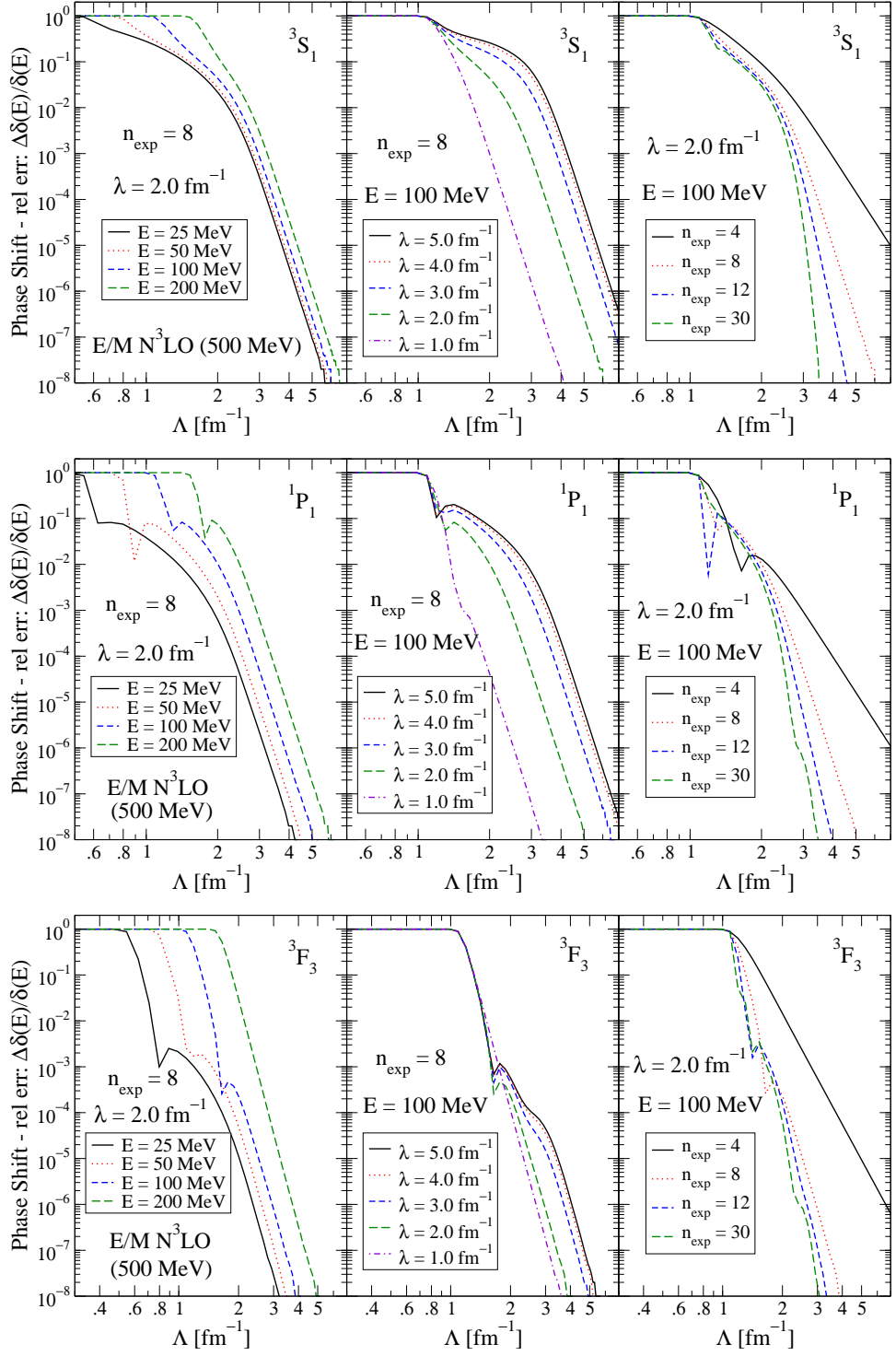


Figure 3.5: The phase shift errors computed in select partial waves. Other channels exhibit the same power-law dependence of the error for  $\Lambda > \lambda$ .

only at low momenta. Therefore, low-momentum and high-momentum states are automatically decoupled in these channels and little change is provided by the SRG here.

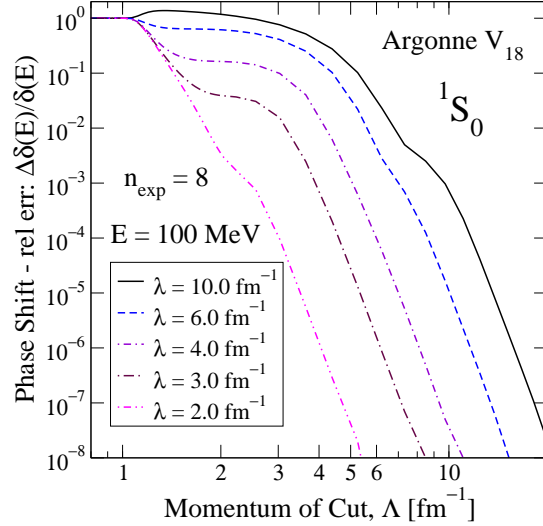


Figure 3.6: The phase shift errors computed in the  $^1S_0$  channel of the Argonne  $V_{18}$  potential. Here the onset of the power-law slope is much less saturated at higher  $\lambda$ 's, because this potential has higher-momentum components to be renormalized.

As noted above, the shoulder in the relative error log-log plots corresponding to the onset of the decoupling region saturates at large  $\lambda$  due to the high-momentum cutoff introduced into the initial potential during its initial formulation. In the plots of Fig. 3.4 the shoulders for the  $\lambda = 4$  and  $5$  curves occurred at about  $\lambda = 3$  since the  $\chi$ EFT potentials did not have off-diagonal matrix elements at momenta larger than about  $k^2 \approx 10 - 11 \text{ fm}^{-2}$ . As counterpoint to this effect, Figure 3.6 shows the relative error plot, with a range of  $\lambda$ 's at  $E = 100 \text{ MeV}$  and  $n_{\text{exp}} = 8$ , using the Argonne  $v_{18}$  potential, which has matrix elements extending out to momenta of  $30 \text{ fm}^{-1}$ . Here one can see less saturation out to  $\lambda = 10$  as there are plenty of off-diagonal matrix

elements for the SRG to suppress between  $k^2 \geq 100 \text{ fm}^{-2}$  and  $k^2 = 36 \text{ fm}^{-2}$ , which corresponds to  $\lambda = 6 \text{ fm}^{-1}$ .

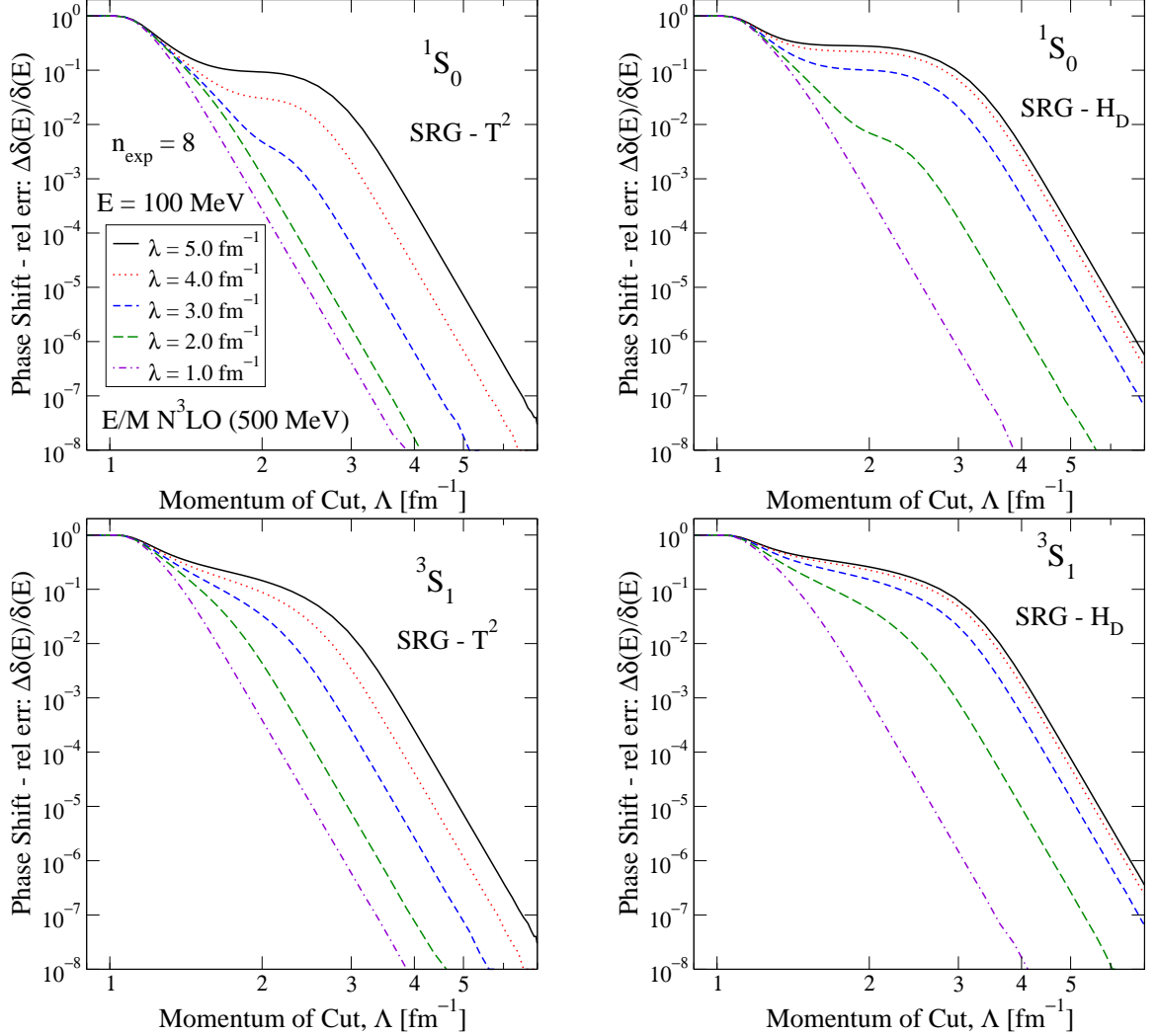


Figure 3.7: Sample phase shift error plots using other choices of  $G_s$ . On the left is  $G_s = T_{\text{rel}}^2$  and on the right is  $G_s = H_D$  for partial waves  $^1S_0$  (top) and  $^3S_1$  (bottom).

We repeated the phase shift calculations with other choices of the SRG generator,  $G_s$ , that are diagonal in momentum space, including  $T_{\text{rel}}^2$  and  $H_D = T_{\text{rel}} + V_D$ , where  $V_D$  is the (running) diagonal part of the bare potential. Samples of these results are



shown in Fig. 3.7. on the left (right) are plots using  $G_s = T^2$  ( $H_D$ ) and on the top (bottom) are  $^1S_0$  ( $^3S_1$ ). We found that these other choices for  $G_s$  do not alter the qualitative features of the power-law behavior region of the previous error plots. This provides further evidence that the high- and low-energy decoupling results primarily from the partially diagonalized nature of the evolved potential.

### 3.4 Decoupling and Deuteron Observables

To test the generality of the observations made for phase shifts, the same decoupling test techniques were applied to other low-energy observables such as the deuteron binding energy, radius, and quadrupole moment. The binding energy and momentum-space wavefunction were computed using standard eigenvalue methods. The computation of  $Q_d$  and  $r_d$  from the wavefunction uses [55],

$$Q_d = -\frac{1}{20} \int_0^\infty dk \left[ \sqrt{8} \left( k^2 \frac{d\tilde{u}(k)}{dk} \frac{d\tilde{w}(k)}{dk} + 3k \tilde{w}(k) \frac{d\tilde{u}(k)}{dk} \right) + k^2 \left( \frac{d\tilde{w}(k)}{dk} \right)^2 + 6 \tilde{w}(k)^2 \right], \quad (3.14)$$

and

$$r_d = \frac{1}{2} \left[ \int_0^\infty dk \left\{ \left( k \frac{d\tilde{u}(k)}{dk} \right)^2 + \left( k \frac{d\tilde{w}(k)}{dk} \right)^2 + 6 \tilde{w}(k)^2 \right\} \right]^{1/2}, \quad (3.15)$$

where  $\tilde{u}(k)$  and  $\tilde{w}(k)$  correspond to the S and D components of the deuteron wavefunction respectively. We again computed relative errors in these observables and, as shown in Fig. 3.8, the errors show the same behavior as observed for the phase shifts. That is, a power-law drop-off in the error begins at  $\Lambda$  just above  $\lambda$ , with a slope determined by the sharpness of the regulator as given by  $n$ .

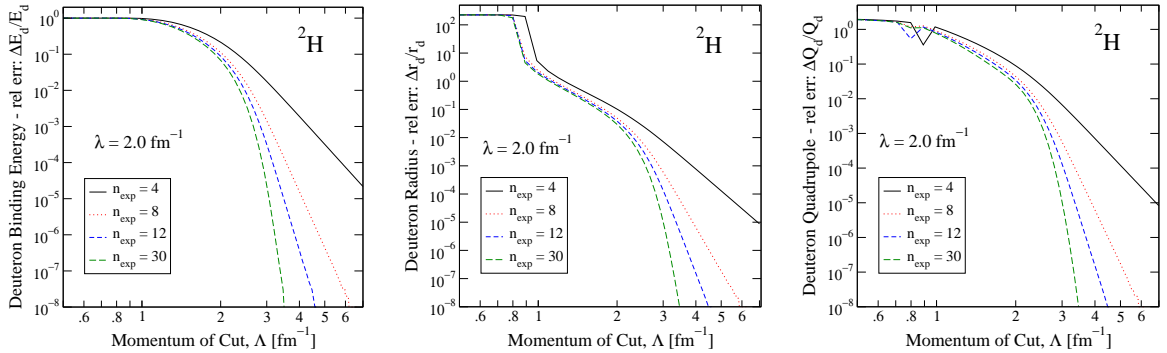


Figure 3.8: The relative error vs. cut parameter  $\Lambda$  of the deuteron energy (left), rms radius (center), and quadrupole moment (left) of the deuteron with several values of the regulator parameter  $n$  indicated in the legends. In each case, the relative error is confirmed by the first-order perturbation theory shown in Eq. (3.13).

As with the phase shift, the analytic dependence of the error from cutting the potential can be estimated directly in perturbation theory. In this case, partial diagonalization of the potential means that the deuteron wave function has negligible momentum components starting slightly above  $\lambda$ . This in turn validates the expansion in Eq. (3.13) and the dependence of the errors on  $1/\Lambda^{2n}$ . The numerical calculation of the error in perturbation theory is plotted in Fig. 3.8 and shows close agreement in the decoupling region  $\Lambda > \lambda$ .

### 3.5 Decoupling and Few-Body Energies with the NCSM

The calculations described above have been only for two-particle systems. We can test whether the high-energy decoupling behavior extends to few-body systems by using No-Core Shell Model (NCSM) calculations of ground-state energies with the Many-Fermion Dynamics (MFD) code [56].

As noted before, the NCSM is a harmonic oscillator basis calculation of many-body systems where states can be explicitly enumerated. The size of the basis is

tracked by the parameter  $N_{\max}$ , the number of oscillator functions used in the basis. Calculations are variational in  $N_{\max}$ , improving accuracy with larger bases, and in  $\hbar\omega$  with a minimum occurring at the optimal value of  $\hbar\omega$  for a given space and  $N_{\max}$ . Here calculations are made for selected  $N_{\max}$  and  $\hbar\omega$  values. Also, note here that the NCSM is a black box calculational tool, which takes as input the harmonic oscillator matrix elements of potentials evolved and cut in momentum-space and provides NN-only calculations of few-body observables like the binding energies of the light nuclei. This is opposed to subsequent chapters where the NCSM machinery will be developed in order to access three-body interaction matrix elements.

Conversion to the oscillator basis introduces a unique truncation of the interaction based on the values of  $N_{\max}$  and  $\hbar\omega$  (as detailed in Appendix B). However, here the two-body Hamiltonian is being evolved in the momentum basis so that the evolved, and therefore decoupled, potential is unitarily equivalent to the initial  $A = 2$  potential. We will take advantage of that decoupling to avoid the oscillator basis truncations at a given basis size,  $N_{\max}$ , and we will use the same systematic cutting as in the previous sections to study the behavior of decoupling in few-body systems.

In this section, only NN interactions have been considered, with the testing of decoupling for many-body forces deferred to later chapters. Because induced three-body (and higher) forces are not included, the converged values will differ significantly with  $\lambda$ . In spite of this, we will still be able to see the evidence for NN decoupling in these systems. Also, note that the general features of the SRG exhibited in Section 3.2 implies that off-diagonal matrix elements of the three-body force will be suppressed as well, with decoupling as an expected consequence. The issue of three-body force evolution will be covered explicitly in chapters 4 and 5.

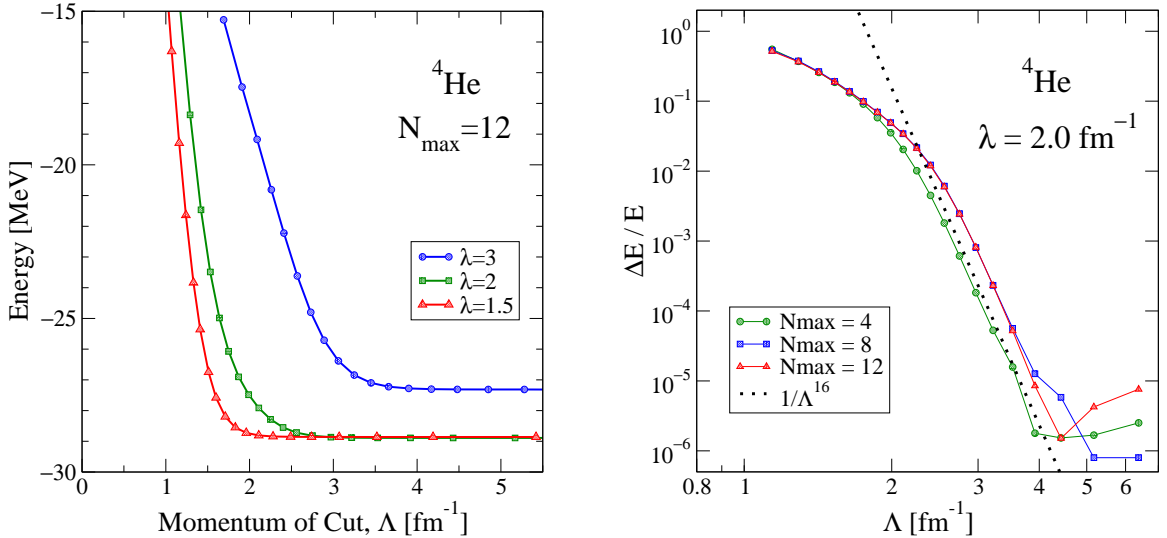


Figure 3.9: Calculations of the  ${}^4\text{He}$  ground-state energy using the NCSM. On the left is the energy obtained from the NCSM for potentials evolved to several different  $\lambda$  values as a function of the cut (regulator) momentum  $\Lambda$  with  $n = 8$ . On the right is the relative error of the energy for the  $\lambda = 2 \text{ fm}^{-1}$  case as a function of the cut momentum (with  $n = 8$ ) for several different harmonic oscillator basis sizes. Also shown is the slope of the error in the decoupling region predicted from perturbation theory (dotted line).

We first verified that the decoupling behavior already observed using a direct calculation of the deuteron wavefunction is reproduced using the MFD. We then calculated a series of larger nuclei, including  ${}^3\text{H}$ ,  ${}^4\text{He}$ , and  ${}^6\text{Li}$ , comparing results from uncut and a range of cut potentials evolved to different values of  $\lambda$ . On the left panel of Fig. 3.9, the  ${}^4\text{He}$  ground-state energy is plotted versus the regulator parameter  $\Lambda$  for several different values of the SRG flow parameter  $\lambda$ . Each of the plotted points is at a basis size  $N_{\text{max}} = 12$  which is within several hundred keV of the energy from extrapolating to  $N_{\text{max}} = \infty$ . A similar plot for  ${}^6\text{Li}$  is given in the left panel of Fig. 3.10 using a basis size  $N_{\text{max}} = 8$ , also within several hundred keV of the extrapolated energy for  $\lambda = 1.5 \text{ fm}^{-1}$  but still several MeV off for  $\lambda = 3.0 \text{ fm}^{-1}$ .

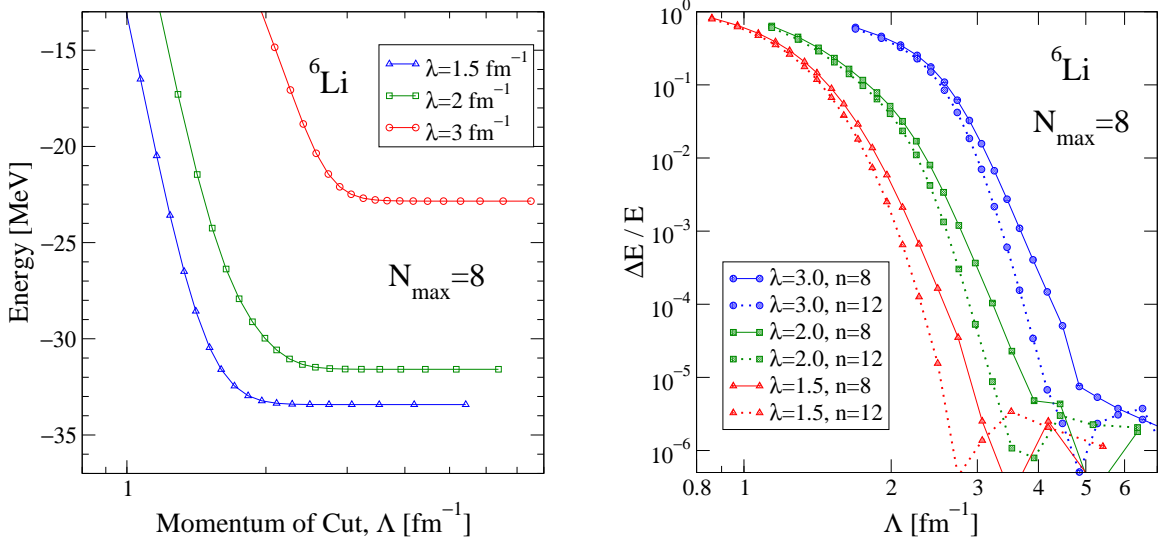


Figure 3.10: Calculations of the  ${}^6\text{Li}$  ground-state energy using the NCSM. On the left is the energy obtained from the NCSM for potentials evolved to several different  $\lambda$  values as a function of the cut (regulator) momentum  $\Lambda$  with  $n = 8$ . On the right is the relative error of the energy for the same  $\lambda$ 's as a function of the cut momentum for the same  $\lambda$  values but with two values of  $n$ .

Both examples show that when the potential is cut with  $\Lambda$  comparable to  $\lambda$  or lower, the converged energy is significantly different from the asymptotic uncut value, while it approaches that value rapidly as  $\Lambda$  moves above  $\lambda$ . This means that, for smaller  $\lambda$ , more high momentum matrix elements can be discarded without a loss of accuracy. This decoupling explains the greatly improved convergence with basis size seen in the NCSM for corresponding  $\lambda$  values [35]. As noted above, the uncut ( $\Lambda \rightarrow \infty$ ) energies vary for each  $\lambda$  because the SRG evolution includes the NN interaction only; the closeness of the results for  $\lambda = 2 \text{ fm}^{-1}$  and  $3 \text{ fm}^{-1}$  for  ${}^4\text{He}$  is coincidental (see Ref. [35] for further discussion about the running of the energies).

The quantitative behavior of the relative error parallels that observed for two-body observables, as seen on the right panels of Figs. 3.9 and 3.10. In all cases, for

a fixed value of  $\lambda$  the power decrease in the error starting with  $\Lambda$  slightly above  $\lambda$  is clearly seen, even though there are fewer digits of precision in the NCSM results (so the relative error is in the range  $10^{-6}$ – $10^{-5}$  at best). The same perturbative residual coupling is seen for different basis sizes, with the slope given by the dependence  $1/\Lambda^{2n}$ , although the onset of the decoupling region shifts to higher  $\Lambda$  until the calculation is near convergence (see Fig. 3.9). Similar results are found for other nuclei and for other values of  $\lambda$ .

### 3.6 Block Diagonalization

As demonstrated in sections 3.3 – 3.5, decoupling between low-energy and high-energy matrix elements is naturally achieved in a momentum basis by choosing a momentum-diagonal flow operator such as the kinetic energy  $T_{\text{rel}}$  or the diagonal of  $H_s$ ; either drives the Hamiltonian toward *band-diagonal* form. Renormalization Group (RG) methods that evolve NN interactions with a sharp or smooth cutoff in relative momentum, known generically as  $V_{\text{low } k}$ , usually rely on equations based on the half-on-shell invariance of the two-nucleon T matrix [57, 55]. These approaches achieve a *block-diagonal* form characterized by a cutoff  $\Lambda_{\text{BD}}$  (see left plots in Figs. 3.11 and 3.12) using a Lee-Suzuki type transformation which unitarily transforms matrix elements into a low-momentum  $P$  space and a high-momentum  $Q$  space. As usually implemented they set the high-momentum matrix elements to zero but this is not required.

The SRG can also produce block-diagonal decoupling similar to the sharp  $V_{\text{low } k}$  form by choosing a block-diagonal flow operator [58, 59],

$$G_s = \begin{pmatrix} PH_sP & 0 \\ 0 & QH_sQ \end{pmatrix} \equiv H_s^{\text{bd}}, \quad (3.16)$$

with projection operators  $P$  and  $Q = 1 - P$ . In a partial-wave momentum representation,  $P$  and  $Q$  are step functions defined by a sharp cutoff  $\Lambda_{\text{BD}}$  on relative momenta. This choice for  $G_s$ , which means that  $\eta_s$  is non-zero only where  $G_s$  is zero, suppresses off-diagonal matrix elements such that the Hamiltonian approaches a block-diagonal form as  $s$  increases (or  $\lambda$  decreases).

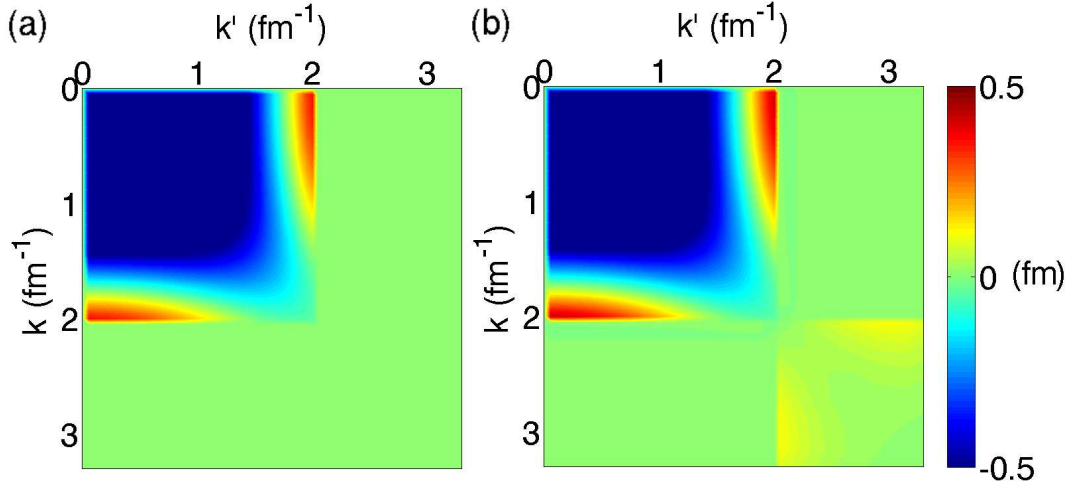


Figure 3.11: Comparison of momentum-space  $V_{\text{low } k}$  (a) and SRG (b) block-diagonal potentials with  $\Lambda_{\text{BD}} = 2 \text{ fm}^{-1}$  evolved from an  $\text{N}^3\text{LO } ^3\text{S}_1$  potential [49].

The plots in Figs. 3.11 and 3.12 show a comparison between the potentials renormalized via the  $V_{\text{low } k}$  procedure (left) and those evolved with the block-diagonal SRG of Eq. (3.16) (right). The initial potential used here is again the  $\text{N}^3\text{LO}$  potential from Ref. [49]. Figure 3.11 uses two-dimensional contour plots as usually presented and Fig. 3.12 uses a three-dimensional surface plot for comparison and reference. Both plots use a value  $\Lambda_{\text{BD}} = 2 \text{ fm}^{-1}$  with the SRG potential being evolved to  $\lambda = 0.5 \text{ fm}^{-1}$ . The agreement between  $V_{\text{low } k}$  and SRG potentials for momenta below  $\Lambda_{\text{BD}}$  is striking. While the color scale is a bit saturated in the former (because we tried to keep the

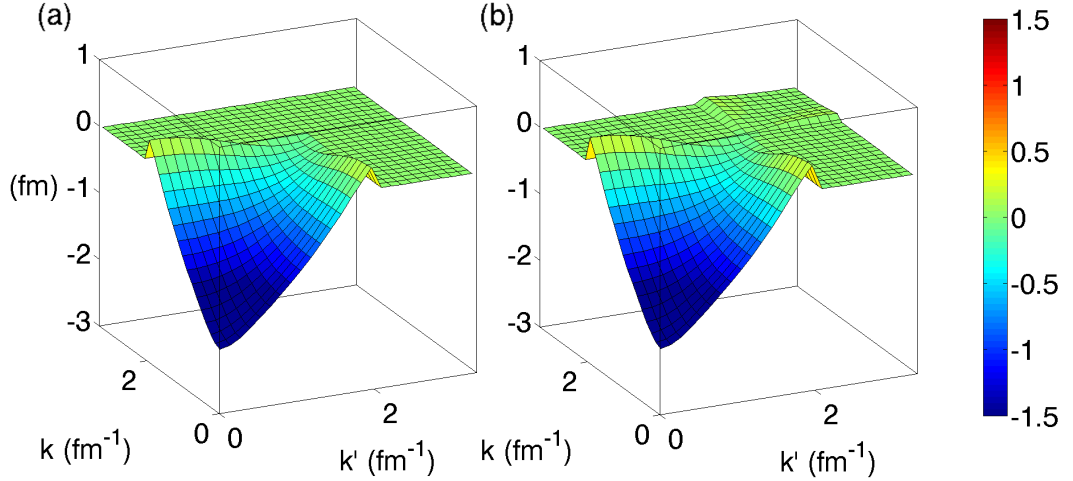


Figure 3.12: Comparison of momentum-space  $V_{\text{low } k}$  (a) and SRG (b) block-diagonal potentials with  $\Lambda_{\text{BD}} = 2 \text{ fm}^{-1}$  evolved from an  $\text{N}^3\text{LO } ^3\text{S}_1$  potential [49].

$Q$ -space visible), the latter helps give perspective. A similar degree of universality is found in the other partial waves. Deriving an explicit connection between these approaches is the topic of an ongoing investigation.

One difference between these procedures is that  $V_{\text{low } k}$  can be formulated as an integral transformation<sup>13</sup> while the SRG is currently only differential; here  $V_{\text{low } k}$  is implemented as a single transformation on the initial matrix, while the SRG flows to the desired amount of transformation. An integrated form of the SRG would be useful in understanding the exact correspondence between the two procedures, and to what extent  $V_{\text{low } k}$  is a subset of these block-diagonal SRG forms.

If one considers a measure of the off-diagonal coupling of the Hamiltonian,

$$\text{Tr}[(QH_sP)^\dagger(QH_sP)] = \text{Tr}[PH_sQH_sP] \geq 0, \quad (3.17)$$

<sup>13</sup> $V_{\text{low } k}$  has been expressed in both integral and differential forms [57].



then its derivative is easily evaluated by applying the SRG equation, Eq. (2.8):

$$\begin{aligned}
& \frac{d}{ds} \text{Tr}[PH_sQH_sP] \\
&= \text{Tr}[P\eta_s Q(QH_sQH_sP - QH_sPH_sP)] \\
&\quad + \text{Tr}[(PH_sPH_sQ - PH_sQH_sQ)Q\eta_sP] \\
&= -2\text{Tr}[(Q\eta_sP)^\dagger(Q\eta_sP)] \leq 0 .
\end{aligned} \tag{3.18}$$

Thus, the off-diagonal  $QH_sP$  block will decrease in general as  $s$  increases [58, 59].

The evolution of the ‘‘off-diagonal’’ matrix elements (meaning those outside the  $PH_sP$  and  $QH_sQ$  blocks) can be roughly understood from the dominance of the kinetic energy on the diagonal. Let the indices  $p$  and  $q$  run over indices of the momentum states in the  $P$  and  $Q$  spaces, respectively. Analogous to the approximation in sec. 3.2, we can replace  $PH_sP$  and  $QH_sQ$  by their eigenvalues  $E_p$  and  $E_q$  in the SRG equations, yielding [58, 59]

$$\frac{d}{ds} h_{pq} \approx \eta_{pq} E_q - E_p \eta_{pq} = -(E_p - E_q) \eta_{pq} \tag{3.19}$$

and

$$\eta_{pq} \approx E_p h_{pq} - h_{pq} E_q = (E_p - E_q) h_{pq} . \tag{3.20}$$

Combining these two results, we have the evolution of any off-diagonal matrix element:

$$\frac{d}{ds} h_{pq} \approx -(E_p - E_q)^2 h_{pq} . \tag{3.21}$$

In the NN case we can approximate the difference of eigenvalues by that for the relative kinetic energies, giving an explicit solution

$$h_{pq}(s) \approx h_{pq}(0) e^{-s(\epsilon_p - \epsilon_q)^2} \tag{3.22}$$

with  $\epsilon_p \equiv p^2/M$ . Thus the off-diagonal elements go to zero with the energy differences just like with the SRG with  $T_{\text{rel}}$ ; one can see the width of order  $1/\sqrt{s} = \lambda^2$  in the  $k^2$  plots of the evolving potential in Figs. 3.13 and 3.14. While in principle the evolution to a sharp block-diagonal form means going to  $s = \infty$  ( $\lambda = 0$ ), in practice we need only take  $s$  as large as needed to quantitatively achieve the decoupling implied by Eq. (3.22).

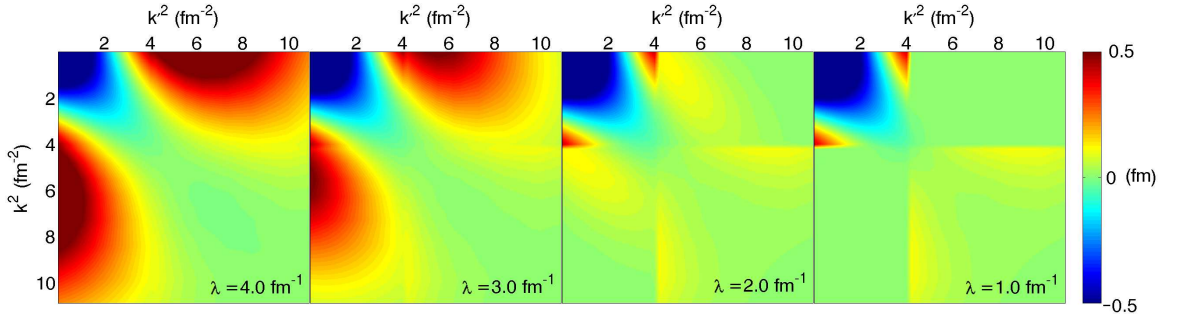


Figure 3.13: Evolution of the  ${}^3\text{S}_1$  partial wave with a sharp block-diagonal flow equation with  $\Lambda_{\text{BD}} = 2 \text{ fm}^{-1}$  at  $\lambda = 4, 3, 2,$  and  $1 \text{ fm}^{-1}$ . The initial  $\text{N}^3\text{LO}$  potential is from Ref. [49]. The axes are in units of  $k^2$  from 0–11  $\text{fm}^{-2}$ . The color scale ranges from  $-0.5$  to  $+0.5 \text{ fm}$  as in Fig. 3.11.

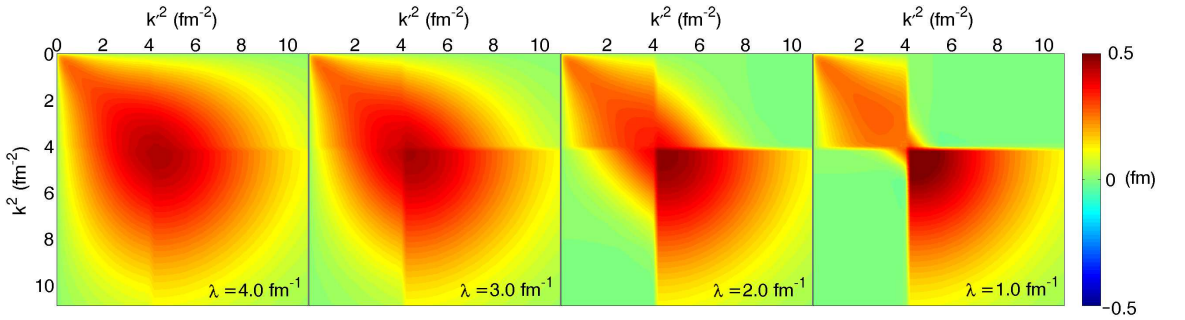


Figure 3.14: Same as Fig. 3.13 but for the  ${}^1\text{P}_1$  partial wave.

This is illustrated in Figs. 3.13 and 3.14 which show the evolution with  $\lambda$  of two representative partial waves ( $^3S_1$  and  $^1P_1$ ) starting with the  $N^3LO$  potential from Ref. [49]. One can clearly see the transformation to a block-diagonal form. Notice the “neck” between the  $P$  and  $Q$  spaces. Its width, especially visible in the  $^1P_1$  channel, is proportional to  $\lambda^2$ . Presumably, though needing further investigation, this finite and smooth interface between the two spaces helps control errors, due to the mixing of  $P$  and  $Q$  space wavefunctions, that have plagued traditional Lee-Suzuki transformations [60].

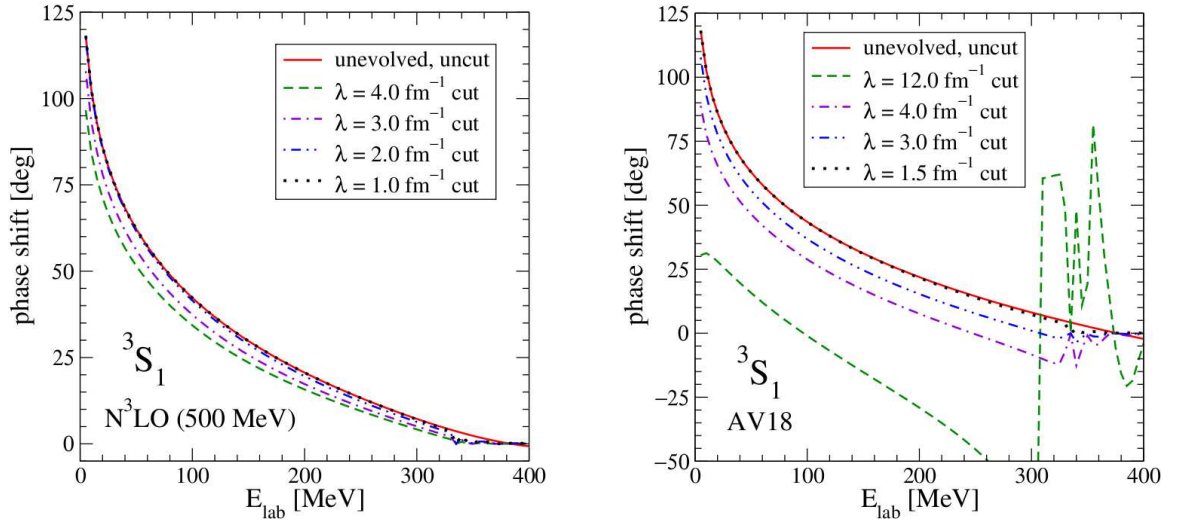


Figure 3.15: Phase shifts for the  $^3S_1$  partial wave from initial potentials  $N^3LO$  and AV18 and the evolved sharp SRG block-diagonal potential with  $\Lambda_{BD} = 2 \text{ fm}^{-1}$  at various  $\lambda$ , in each case with the potential set identically to zero above  $\Lambda_{BD}$ .

Definitive tests of decoupling for NN observables are now possible for  $V_{low k}$  potentials since the unitary transformation of the SRG guarantees that no physics is lost. For example, in Fig. 3.15 we show  $^3S_1$  phase shifts from an SRG sharp block diagonalization with  $\Lambda_{BD} = 2 \text{ fm}^{-1}$  for two different potentials. The phase shifts are

calculated with the potentials cut sharply at  $\Lambda_{\text{BD}}$ . That is, the matrix elements of the potential are set to zero above that point. The improved decoupling as  $\lambda$  decreases is evident in each case. By  $\lambda = 1 \text{ fm}^{-1}$  in Fig. 3.15, the unevolved and evolved curves are indistinguishable to the width of the line up to about 300 MeV.

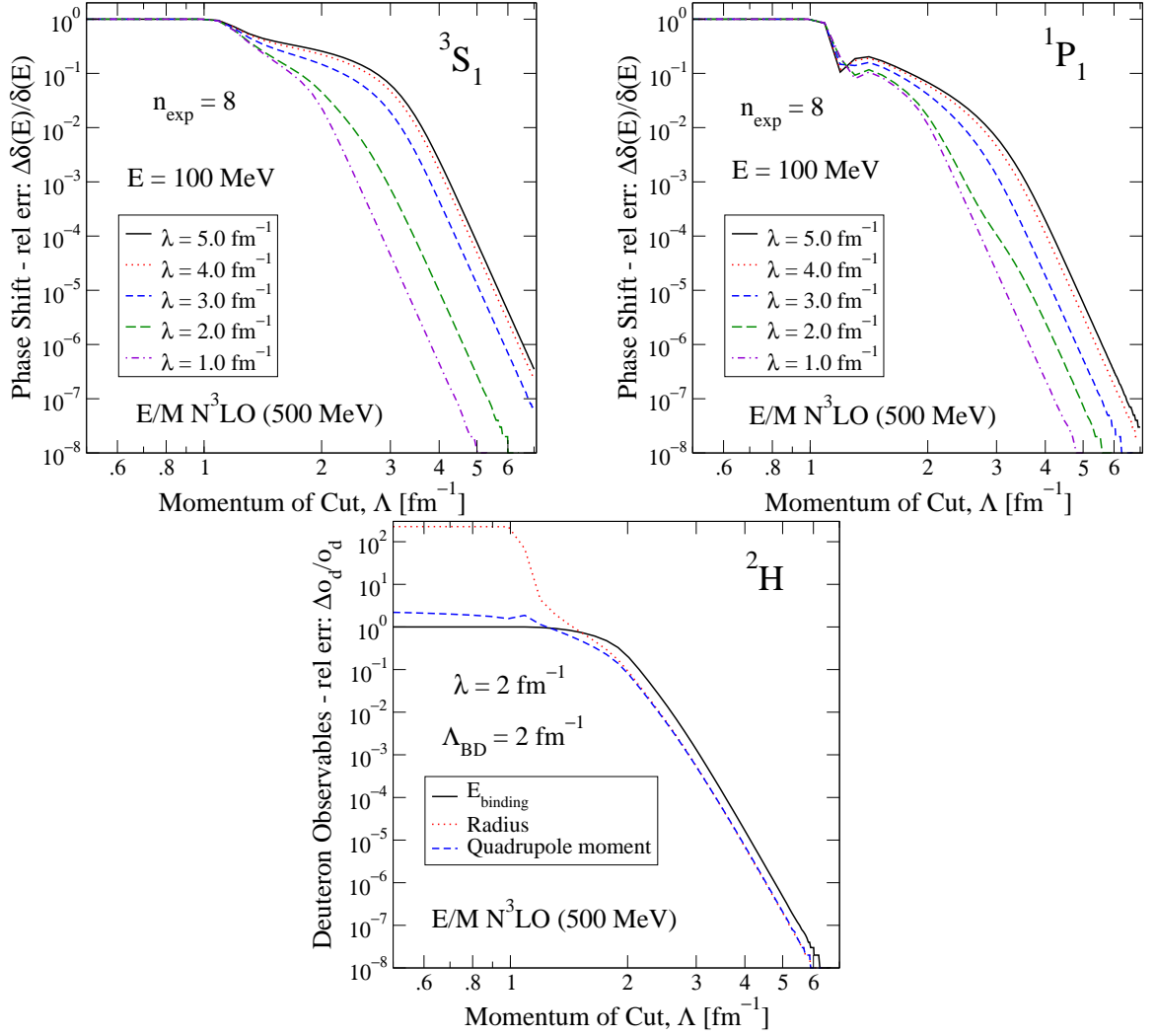


Figure 3.16: Errors in the phase shift (two partial waves) at  $E_{\text{lab}} = 100 \text{ MeV}$  and three deuteron observables for the evolved sharp SRG block-diagonal potential with  $\Lambda_{\text{BD}} = 2 \text{ fm}^{-1}$  for a range of  $\lambda$ 's and a regulator with  $n = 8$ . Two partial waves are shown.

In Fig. 3.16 we show a quantitative analysis of the decoupling as in section 3.3. The figure shows the relative error of the phase shift at 100 MeV calculated with a potential that is cut off as before at a series of values  $\Lambda_{\text{cut}}$ . We observe the same universal decoupling behavior: a shoulder indicating the start of a perturbative decoupling region, where the slope matches the power  $2n$  fixed by the smooth regulator.

Figure 3.17 shows a limiting factor with respect to the decoupling generated by the block-diagonal SRG. The onset of the shoulder in  $\Lambda_{\text{cut}}$  decreases with  $\lambda$  until it saturates for  $\lambda$  near  $\Lambda_{\text{BD}}$ , leaving the shoulder at  $\Lambda_{\text{cut}} \approx \Lambda_{\text{BD}}$ . Thus, as  $\lambda \rightarrow 0$  the decoupling scale is set by the cutoff  $\Lambda_{\text{BD}}$ . Of course, the  $P$  space inside  $\Lambda_{\text{BD}}$  is not transformed (diagonally or otherwise) by the SRG and the potential cannot be decoupled below this scale.

Taking the block diagonal idea further we can apply more general definitions of  $P$  and  $Q$ . To smooth out the cutoff, we can introduce a smooth regulator  $f_\Lambda$ , which we take here to be an exponential form:

$$f_\Lambda(k) = e^{-(k^2/\Lambda_{\text{BD}}^2)^n}, \quad (3.23)$$

with  $n$  an integer. For  $V_{\text{low } k}$  potentials, typical values used are  $n = 4$  and  $n = 8$  (the latter is considerably sharper but still numerically robust). By replacing  $H_s^{\text{bd}}$  with

$$G_s = f_\Lambda H_s f_\Lambda + (1 - f_\Lambda) H_s (1 - f_\Lambda), \quad (3.24)$$

we get a smooth block-diagonal potential.

Fig. 3.18 shows an example of the smooth block-diagonal SRG with  $\Lambda_{\text{BD}} = 2 \text{ fm}^{-1}$  and  $n = 4$ . As we evolve the potential down toward  $\lambda = 1$ , the overlap of the  $P$  and  $Q$  spaces becomes significant and the potential develops new structure instead of becoming simpler. This sort of behavior indicates that there is no further benefit to

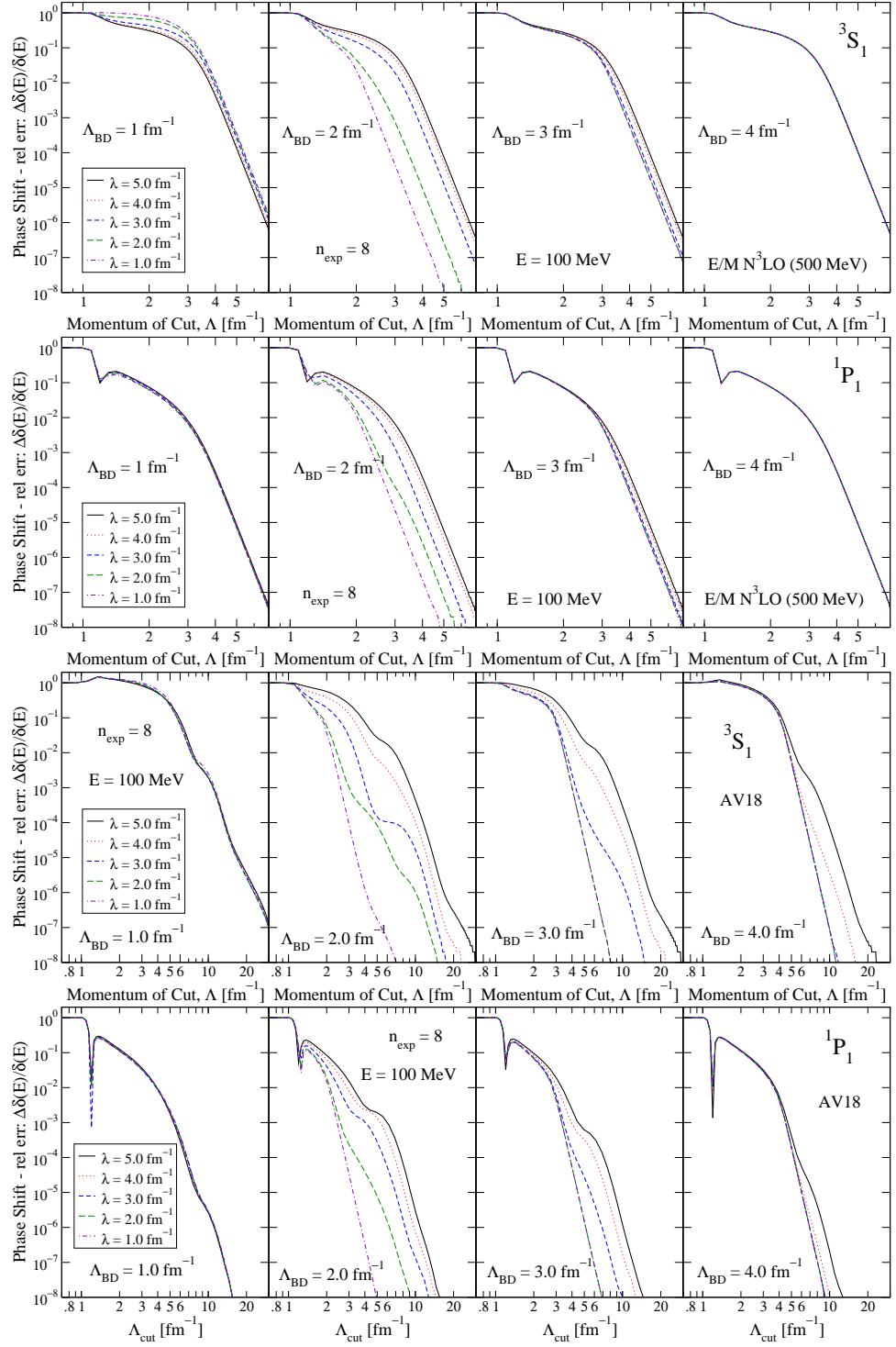


Figure 3.17: Decoupling error plots using the sharp block-diagonal generator on two partial waves ( ${}^3S_1$  and  ${}^1P_1$ ) in two different initial potentials (AV18 and  $N^3\text{LO}$  (500 MeV)).

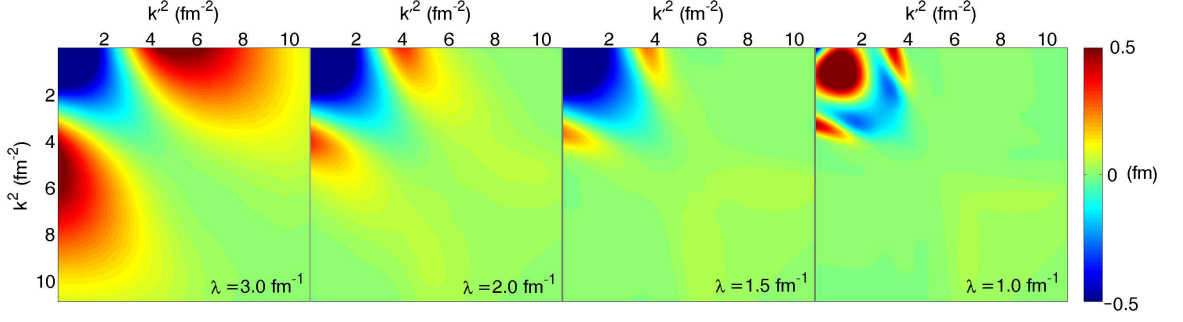


Figure 3.18: Evolution of the  ${}^3S_1$  partial wave with a smooth ( $n = 4$ ) block-diagonal flow equation with  $\Lambda_{\text{BD}} = 2.0 \text{ fm}^{-1}$ , starting with the  $\text{N}^3\text{LO}$  potential from Ref. [49]. The flow parameter  $\lambda$  is 3, 2, 1.5, and 1  $\text{fm}^{-1}$ . The axes are in units of  $k^2$  from 0–11  $\text{fm}^{-2}$ . The color scale ranges from  $-0.5$  to  $+0.5 \text{ fm}$  as in Fig. 3.11.

evolving in  $\lambda$  very far below  $\Lambda_{\text{BD}}$ ; in fact the decoupling worsens for  $\lambda < \Lambda_{\text{BD}}$  with a smooth regulator.

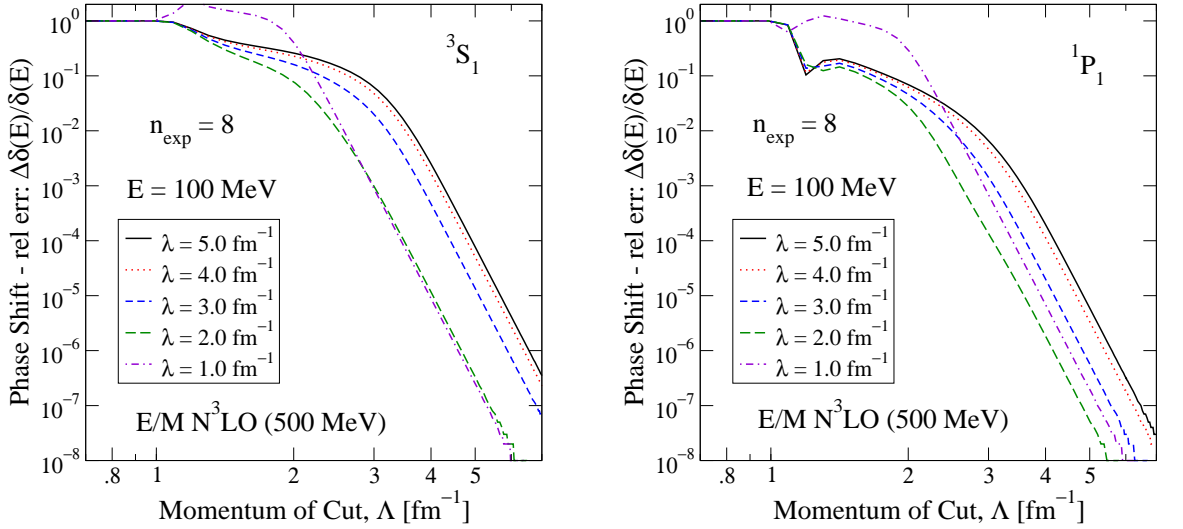


Figure 3.19: Phase shift errors from potentials evolved with the smooth block-diagonal SRG. The block parameter is  $\Lambda_{\text{BD}} = 2$ . Here the regulator of Eq. (3.23) uses  $n = 4$ .

Figure 3.19 shows the phase shift relative error plots for the smooth block-diagonal SRG applied in two partial waves of the N<sup>3</sup>LO potential. Note that as  $\lambda$  is run down below the block parameter  $\Lambda_{\text{BD}}$  the error worsens, signaling a collision of high- and low-energy degrees of freedom due to the overlap of  $P$  and  $Q$  space wavefunctions as defined by the smooth block transformation.

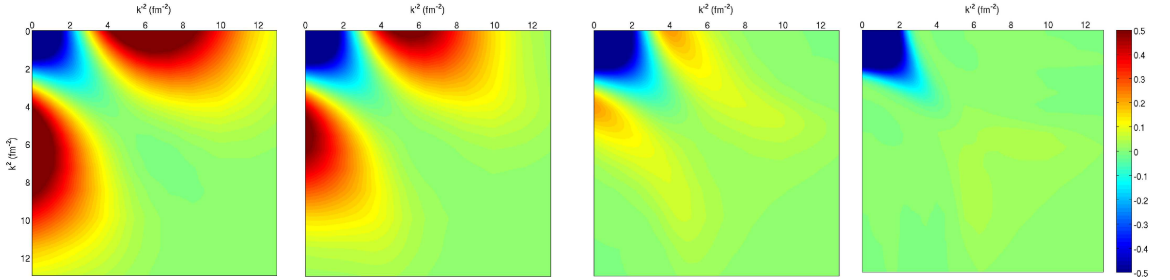


Figure 3.20: Evolution of the  ${}^3\text{S}_1$  partial wave with a second-order exact block-diagonal flow of equation 3.25 with  $\Lambda_{\text{BD}} = 2 \text{ fm}^{-1}$  at  $\lambda = 4, 3, 2,$  and  $1 \text{ fm}^{-1}$ . The initial N<sup>3</sup>LO potential is from Ref. [49]. The axes are in units of  $k^2$  from 0–11  $\text{fm}^{-2}$ . The color scale ranges from  $-0.5$  to  $+0.5 \text{ fm}$  as in Fig. 3.11.

Another type of SRG that is second-order exact and yields similar block diagonalization is defined by

$$\eta_s = [T, PV_s Q + QV_s P], \quad (3.25)$$

which can be implemented with  $P \rightarrow f_\Lambda$  and  $Q \rightarrow (1 - f_\Lambda)$ , with  $f_\Lambda$  either sharp or smooth. Figure 3.20 shows an example of evolution of the N<sup>3</sup>LO potential from Ref. [49] using this choice.

We can also consider bizarre choices for  $f_\Lambda$  in Eq. (3.24), such as defining it to be zero out to  $\Lambda_{\text{lower}}$ , then unity out to  $\Lambda_{\text{BD}}$ , and then zero above that. This means that  $1 - f_\Lambda$  defines both low and high-momentum blocks and the region that is driven to zero consists of several rectangles. Results for two partial waves starting from



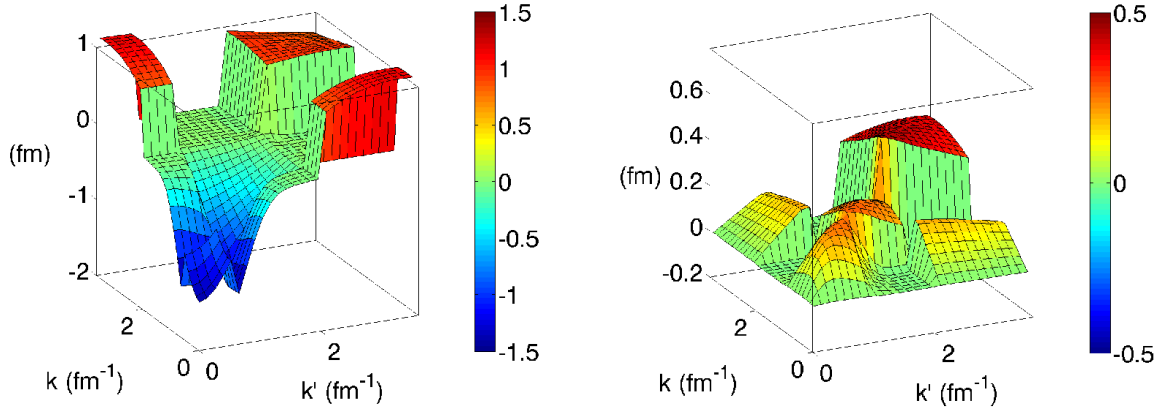


Figure 3.21: Evolved SRG potentials starting from Argonne  $v_{18}$  in the  $^1S_0$  (left) and  $^1P_1$  (right) partial waves to  $\lambda = 1 \text{ fm}^{-1}$  using a bizarre choice for  $G_s$  (see text).

the Argonne  $v_{18}$  potential are shown in Fig. 3.21. Despite the strange appearance, these remain unitary transformations of the original potential, with phase shifts and other NN observables the same as with the original potential. These choices provide a proof-of-principle that the decoupled regions can be tailored to the physics problem at hand.

In the more conventional SRG, where we use  $G_s = T_{\text{rel}}$ , it is easy to see that the evolution of the two-body potential in the two-particle system can be carried over directly to the three-particle system. In particular, it follows that the three-body potential does not depend on disconnected two-body parts [28, 47]. If we could implement  $\eta_s$  as proposed here with analogous properties, we would have a tractable method for generating  $V_{\text{low } k}$  three-body forces. While it seems possible to define Fock-space operators with projectors  $P$  and  $Q$  that will not have problems with disconnected parts, it is not yet clear whether full decoupling in the few-body space can be realized. In fact, if  $P$  and  $Q$  are  $A$ -dependent than the two-body potential

will not be completely fixed by evolution in the two-body space. This is an essential ingredient in the many-body calculations done in this thesis.

## CHAPTER 4

### ONE-DIMENSIONAL MODEL IN THE HARMONIC OSCILLATOR BASIS

As shown formally in Section 2.2, the SRG induces many-body forces as it evolves the Hamiltonian in an  $A$ -body space. For the SRG to be a useful tool, we must develop methods for calculating these induced many-body interactions and establish the conditions under which an initial hierarchy of many-body forces is maintained. In this chapter, we study a one-dimensional system of bosons as a proof-of-principle of a practical method to evolve and evaluate such forces, and establish a road map for full three-dimensional calculations carried out in chapter 5. Beyond this, a one-dimensional system provides a straightforward laboratory that is indispensable in gaining deeper understanding of the SRG's effect on many-body potentials.

Most previous applications of the SRG to nuclear structure have been in a momentum basis, where decoupling between low-energy and high-energy matrix elements is naturally achieved by choosing a momentum-diagonal flow operator such as the kinetic energy  $T_{\text{rel}}$ . However, evolution in a three-body space requires proper handling of the “dangerous delta functions” associated with the spectator particle to the two-body interaction. In a momentum representation, these delta functions are difficult

to resolve in a practical mesh and require solving separate flow equations for each combination of three-body matrix elements.

Since we can evaluate the SRG flow equations Eq. (2.8) with  $G_s = T_{\text{rel}}$  in any convenient basis, an alternative is a discrete basis that allows direct application of the SRG flow equations in each  $A$ -body sector. We adopt this approach in the present chapter, using harmonic oscillator wave functions as our basis and mimicking the formalism used in the no-core shell model (NCSM) [11, 12, 13] to create properly symmetrized (for bosons) matrix elements in relative (Jacobi) coordinates. The restriction to one dimension makes the construction particularly straightforward and requires only moderate matrix sizes. We use bosons in this model for easy comparison with existing model analysis. However, the boson ground states also coincide with fermion ground states when the flavor degeneracy is greater than the number of particles, because the overall anti-symmetrization is realized by the flavor wavefunction.

The choice of the harmonic oscillator basis is important because it is the only orthogonal basis in which the center-of-mass can be factorized. With a translationally-invariant basis we have many fewer basis states and can achieve better convergence in a given  $A$ -body system. Other bases can be translationally invariant, like a system of correlated gaussians, but are non-orthogonal. Others, like Coupled-Cluster calculations are orthogonal but do not have a straightforward truncation in  $N_{\text{max}}$ .

We use simple flavor-independent potentials that imitate the short-range repulsion and mid-range attraction characteristic of realistic local nuclear potentials. Previous studies of the SRG imply that properties of the transformations are primarily due to the matrix structure ( $G_s$ ,  $H_s$ , choice of basis, etc), so we will be able to directly carry over some of our observations to three dimensions. Because the NCSM formalism is

already developed in three dimensions, we will see in chapter 5 that the generalization to three-dimensional fermionic calculations with spin-isospin degrees of freedom and using realistic nuclear interactions is algebraically straightforward, though far more computationally intensive.

Another form of the NCSM uses oscillator wavefunctions associated with lab-frame coordinates and momenta instead of the relative Jacobi coordinates. This basis uses Slater determinants, making it much easier to antisymmetrize. This method is often known as “ $m$ -scheme” [10] as it is organized according to the  $m$  quantum number of the oscillator states. Similarly, a lab-frame NCSM scheme referred to as  $jj$ -coupled [61], takes advantage of the rotational symmetry of specific nuclei to reduce the size of the basis used in CC calculations. The major benefit of lab-frame coordinate based oscillator bases is the ability to generalize to arbitrary  $A$  due to its reliance on a Slater determinant to obtain an antisymmetrized basis as opposed to the recursive procedure used in Jacobi systems that builds on previous antisymmetric subsystems. On the downside, this results in poorer scaling of basis sizes for the  $A$ -body Hamiltonian matrices. As a check of the one-dimensional Jacobi coordinate oscillator basis we built a one-dimensional analog of the  $m$ -scheme NCSM, though it was unwieldy for our current purposes and not developed further. The details of this model are discussed in appendix F.

## 4.1 Symmetrized Jacobi Harmonic Oscillator Basis

The No-Core Shell Model is a wavefunction-based method used to make *ab initio* calculations of nuclear bound-state properties. The basis it uses is built from the eigenfunctions of the harmonic oscillator Hamiltonian (described in Appendix B) up

to a maximum oscillator number,  $N_{\max}$ . The functions are products of a gaussian and polynomials of order less than the value  $N_{\max}$ . The other free parameter in defining this basis is  $\omega$ , which sets the scale of the oscillator wavefunctions. This is usually multiplied by  $\hbar$ , which is set to one in this unitless model.

Each boson (fermion) wavefunction in an  $A$ -body system must be fully symmetric (antisymmetric). Therefore, we must identify and include all the symmetric states which the system may occupy. A general and systematic way to build this basis is to list all the possible states and build a symmetrization operator in this full basis. The eigenstates of this operator with eigenvalue one will be the exclusive set of symmetric states relevant for the system up to the stated  $N_{\max}$ ; those with eigenvalue zero are irrelevant and can be thrown out. Also note that bases of smaller  $N_{\max}$  are a subset of larger bases. The details involving the organization of states for this method is discussed in Appendix C.

The initial two-body potential, usually given in the relative momentum basis, can be converted to the relative oscillator basis simply by inserting a (semi-<sup>14</sup>) complete set of states to expand the momentum states in terms of oscillator wavefunctions. For three-body calculations, this interaction must be embedded in the three-body symmetric basis obtained from the symmetrizer diagonalization. Calculations in higher-body bases require a general iterative procedure. The  $A$ -body basis, being symmetric already, is taken as an explicit set of states to which is added the additional Jacobi oscillator coordinate. A new symmetrizer is built and the  $A + 1$ -body basis is obtained. The potential in the  $A$ -body basis is embedded in the new space. Diagonalization

<sup>14</sup>see Appendix B for a discussion on the incompleteness of the oscillator basis.

or evolution can proceed as usual. The details of this iterative process, including potential embedding and symmetrizer construction, are given in Appendix C.

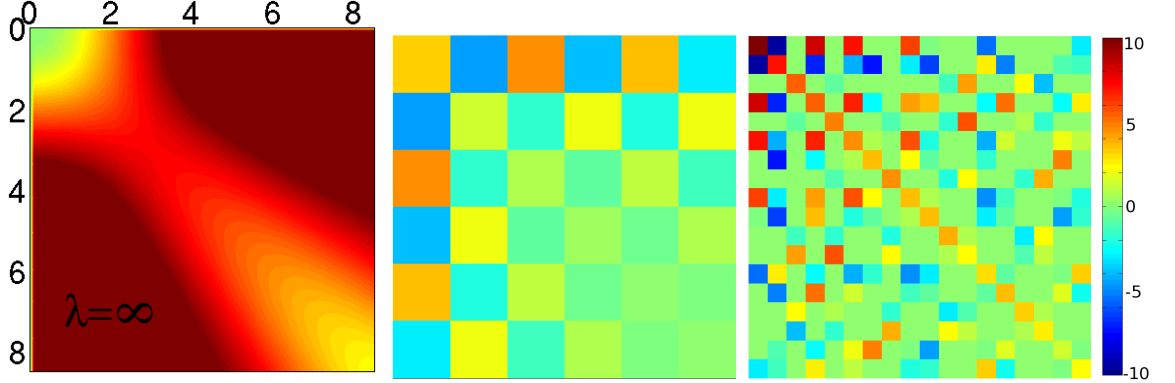


Figure 4.1: A snapshot of the embedding process involving the initial (unevolved) two-body potential. The far left is a two-body, one-dimensional, potential in momentum space [62] with axes labelled by  $k^2$ , the middle shows that potential converted to the two-body symmetric oscillator space, and the far right shows it embedded in the symmetric three-body basis. Each box is a matrix element in the oscillator basis, and the matrix elements are organized in order of increasing energy. The oscillator basis axes are unmarked due to the complicated organization of those bases (see text). For visibility, a small basis with  $N_{\max} = 12$  is shown.

Figure 4.1 shows an example of the process to embed a two-body momentum basis potential into the oscillator bases for  $A = 2$ , and 3. The left shows an initial two-body potential in the momentum basis. The center shows the same potential in the two-body oscillator basis and is physically identical to the momentum basis version except for truncation errors induced by oscillator basis conversion (see appendix B). The far right shows the potential embedded in the three-body basis. The axes here are unmarked because the order of the states is partially arbitrary. Here, as is usual, they are organized in order of increasing energy, labeled by  $N_A$  (for an  $A$ -body state), up to the maximum  $N_{\max}$ . Any degeneracies in  $N_A$  are labeled by an arbitrary index

$i_A$ . Note the many matrix elements on the far right plot which are zero (green in this color scheme) indicating transitions which cannot be described by only two-body forces and a spectator particle. These matrix elements represent unique three-body transitions and, while some of these may remain zero due to symmetry properties, they are now available to the SRG during evolution. Any change in the value of these matrix elements represents three-body forces being induced during evolution in this basis.

Once we have constructed a complete symmetrized basis for  $A$  particles (specified by the value of  $N_{\max}$ ) and evaluated the Hamiltonian matrix elements in this basis, applying the SRG transformations is immediate. That is, we have coupled, first-order differential equations for each matrix element of the Hamiltonian, with the right side of each equation given by a series of matrix multiplications. This is efficiently implemented in any computer language with matrix operations and differential equation solvers. Just as in the momentum basis, individual matrix elements<sup>15</sup> of the Hamiltonian obey the SRG's differential equations:

$$\begin{aligned}
\frac{d}{ds}\langle N'_A i'_A | (V_A)_s | N_A i_A \rangle &= \langle N'_A i'_A | [[T, H_s], H_s] | N_A i_A \rangle \\
&= \langle N'_A i'_A | T H_s H_s | N_A i_A \rangle + \langle N'_A i'_A | H_s H_s T | N_A i_A \rangle \\
&\quad - 2\langle N'_A i'_A | H_s T H_s | N_A i_A \rangle .
\end{aligned} \tag{4.1}$$

We have defined  $dT/ds = 0$  so that all of the flow occurs in the matrix representation of the potential,  $(V_A)_s$ . Using the matrix representations of  $T$  and  $H_s$  in the  $|N_A i_A\rangle$  basis, the right side of Eq. (4.1) is simply a series of matrix multiplications. The initial condition at  $s = 0$  is the initial Hamiltonian,  $\langle N'_A i'_A | T + V_A | N_A i_A \rangle$ , which can have

<sup>15</sup>The  $A$ -body states are labeled by the total energy,  $N_A$  and a quantum number,  $i_A$ , introduced to keep track of states degenerate in  $N$ . In three dimensions this list will include angular momenta and isospin. See appendix C for the complete notation.



few-body components in  $V_A$ . We consider here both two-body-only and two-body plus a three-body component (for  $A \geq 3$ ).

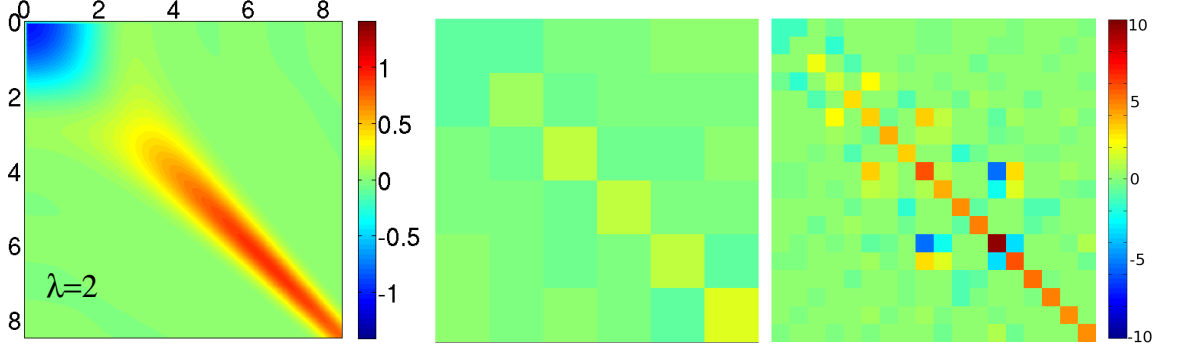


Figure 4.2: Same as in 4.1 but each matrix is now evolved to  $\lambda = 2$  in each basis shown. Again,  $N_{\max} = 12$ .

Figure 4.2 shows an example of evolution in the oscillator bases for  $A = 2$ , and 3. The left shows the evolution, to  $\lambda = 2$ , of a two-body potential in the momentum basis. The center shows the evolution of the potential in the two-body oscillator basis and is physically identical to the momentum basis version again except for errors induced by oscillator basis conversion. The far right shows the evolution in the three-body basis and includes the evolution of two body forces but now also includes induced three-body forces not available in either of the two-body spaces.

The SRG induces few-body forces as it evolves an initial interaction in a few-particle space. To study the contributions of different few-body forces we must isolate these components of the full interaction. The two-body force evolution keeps the  $A = 2$  binding energy invariant under evolution and *defines* the evolved two-body forces. We can isolate the three-body force from the two-body matrix elements by embedding the evolved two-body-only force in the three-particle space and subtracting it from

the full two-plus-three-body evolved interaction. Because we are in a symmetrized basis, this operation is relatively straightforward. However, we must be careful to keep track of the correct combinatoric factors associated with embedding A-body forces in higher spaces. In our MATLAB implementation these procedures take only a few lines of code in addition to the fully unitary calculation.

The NCSM, both one- and three-dimensional, is a variational calculation in the two parameters,  $N_{\max}$  and  $\hbar\omega$ . Largely this can be understood in terms of the truncation effects discussed in Appendix B. Essentially, conversion to an oscillator basis imposes both ultraviolet and infrared cutoffs  $\Lambda_{UV}$  and  $\Lambda_{IR}$  determined by the parameters of the basis  $N_{\max}$  and  $\hbar\omega$ . As derived in the appendix, increasing  $N_{\max}$  improves both cutoffs by raising  $\Lambda_{UV}$  and lowering  $\Lambda_{IR}$ , but changing  $\hbar\omega$  shifts both cutoffs in the same direction. So we will be looking for a sufficiently large value of  $N_{\max}$  and the optimal value of  $\hbar\omega$  for a given  $N_{\max}$ .

## 4.2 One Dimension Potential

The bulk of the calculations in this chapter adopt a model from Ref. [62] that uses a sum of two gaussians to simulate repulsive short-range and attractive mid-range nucleon-nucleon two-body potentials:

$$V^{(2)}(x) = \frac{V_1}{\sigma_1\sqrt{\pi}}e^{-x^2/\sigma_1^2} + \frac{V_2}{\sigma_2\sqrt{\pi}}e^{-x^2/\sigma_2^2} \quad (4.2)$$

or

$$V^{(2)}(p, p') = \frac{V_1}{2\pi\sqrt{2}}e^{-(p-p')^2\sigma_1^2/8} + \frac{V_2}{2\pi\sqrt{2}}e^{-(p-p')^2\sigma_2^2/8}. \quad (4.3)$$

The parameters used in Ref. [62] were chosen so that the one-dimensional saturation properties correspond to empirical three-dimensional properties, but we also want

Table 4.1: Parameter sets for the two-body potential of Eq. (4.3).

name	$V_1$	$\sigma_1$	$V_2$	$\sigma_2$
$V_\alpha$	12.	0.2	-12.	0.8
$V_\beta$	0.	0.0	-2.0	0.8

to explore a range of parameters to test what behavior is general and what relies on specific features. Otherwise, the units for these model interactions are straightforward with the mass (same for all particles) and  $\hbar$  taken to one, though they are displayed explicitly in some equations. We start with the parameters listed in Table 4.1. The potential  $V_\alpha$  is from Ref. [62] and is plotted in Fig. 4.3. We will fix the range of the attractive part and vary the relative strength and range of the repulsive parts and vice versa. We also vary the purely attractive potential  $V_\beta$ , which was used in Ref. [63] and is also plotted in Fig. 4.3. The eigenvalue problem for the relatively small matrices considered here can be solved by any conventional matrix diagonalization program (MATLAB was used here).

To test that the symmetrized harmonic oscillator basis was correctly constructed for  $A = 2, 3$ , and 4 (see below), we first diagonalized the Hamiltonian using the purely attractive gaussian two-body potential  $V_\beta$ . The normalization is such that  $V_\beta(x)$  becomes a delta function with strength  $V_2$  as  $\sigma_2 \rightarrow 0$  [63] (note the numerical factors from the Fourier transform because of our normalization of the Jacobi momenta). This limiting case has a known analytic solution for the (only) bound state of  $A$  bosons. For finite  $\sigma_2$ , we were able to confirm the accuracy of the diagonalizations as a function of the basis size  $N_{\max}$  by comparison to coordinate-space stochastic

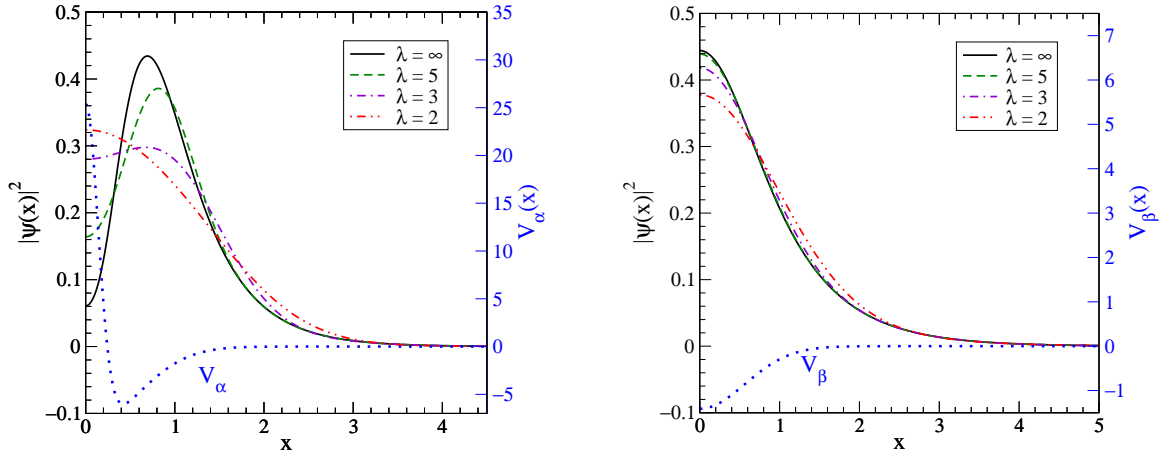


Figure 4.3: Potentials (dotted line, with axis on right) and probability distributions (other lines, with axis on left) for the lowest two-body bound state as a function of  $x = |x_1 - x_2|$  at different stages in the SRG evolution ( $\lambda = 1/s^{1/4}$ ). The left plot is  $V_\alpha$  and the right plot is  $V_\beta$  (see Table 4.1).

variational method (SVM) calculations using a published code [64] adapted to one dimension [65, 66].

We also explore the evolution of Hamiltonians with an initial three-body force. We choose a regulated contact interaction in the three-particle momentum space,

$$V^{(3)}(p, q, p', q') = c_E f_\Lambda(p, q) f_\Lambda(p', q') , \quad (4.4)$$

where  $c_E$  is the strength of the interaction and the form factor  $f_\Lambda$  depends on the Jacobi momenta as

$$f_\Lambda(p, q) \equiv e^{-((p^2+q^2)/\Lambda^2)^n} . \quad (4.5)$$

The regulator cutoff  $\Lambda$  sets the scale of the fall-off in momentum and  $n$  determines the sharpness of this fall-off. This form is analogous to the regulated three-body contact interactions used in chiral effective field theory [67] discussed in Appendix A. We

Table 4.2: Ground-state energies for two-body potentials from Table 4.1 with various strengths of the initial three-body potential Eqs. (4.4)–(4.5) with  $\Lambda = 2$  and  $n = 4$  for  $A = 2, 3$ , and 4.

$V^{(2)}$	$c_E$	$E_2$	$E_3$	$E_4$
$V_\alpha$	-0.10	-0.920	-3.223	-7.125
$V_\alpha$	-0.05	-0.920	-2.884	-5.832
$V_\alpha$	-0.01	-0.920	-2.628	-4.906
$V_\alpha$	0.00	-0.920	-2.567	-4.695
$V_\alpha$	0.01	-0.920	-2.507	-4.494
$V_\alpha$	0.05	-0.920	-2.278	-3.798
$V_\alpha$	0.10	-0.920	-2.027	-3.179
$V_\beta$	-0.10	-0.474	-3.379	-8.412
$V_\beta$	-0.05	-0.474	-2.283	-5.727
$V_\beta$	-0.01	-0.474	-1.792	-4.183
$V_\beta$	0.00	-0.474	-1.708	-3.846
$V_\beta$	0.01	-0.474	-1.626	-3.517
$V_\beta$	0.05	-0.474	-1.370	-2.451
$V_\beta$	0.10	-0.474	-1.240	-1.874

have not explored in detail the impact of adjusting  $\Lambda$  and  $n$  but have focused on how the SRG handles a varying strength  $c_E$ . All results here are for  $\Lambda = 2$  and  $n = 4$ .

A sampling of ground-state energies are given in Table 4.2. A few simple features to note are the fact that the varied three-body force has no effect on the two-body binding energy and that a negative  $c_E$  is added attraction and thus the 3- and 4-body bound states are deeper. For completeness we also include in Table 4.3 the optimal  $\hbar\omega$  for each of these interaction choices.

Most of the figures in this chapter show calculations with  $N_{\max} = 28$ . With this basis size, the ground-state energies are generally converged to one part in  $10^4$ , which is more than sufficient for our purposes. As usual, increasing  $N_{\max}$  leads to rapidly increasing matrix sizes and computation times; times for  $A = 3$  with  $N_{\max} = 32$  are

Table 4.3: Optimal  $\hbar\omega$ s for the potentials in Table 4.2 with  $A = 2, 3,$  and  $4.$

$V^{(2)}$	$c_E$	$\hbar\omega(E_2)$	$\hbar\omega(E_3)$	$\hbar\omega(E_4)$
$V_\alpha$	-0.10	4.4	5.8	5.5
$V_\alpha$	-0.05	4.4	6.1	5.8
$V_\alpha$	-0.01	4.4	5.1	5.6
$V_\alpha$	0.00	4.4	5.0	5.3
$V_\alpha$	0.01	4.4	4.9	5.0
$V_\alpha$	0.05	4.4	4.7	4.4
$V_\alpha$	0.10	4.4	4.5	3.8
$V_\beta$	-0.10	1.1	0.1	0.1
$V_\beta$	-0.05	1.1	0.1	0.1
$V_\beta$	-0.01	1.1	0.5	0.5
$V_\beta$	0.00	1.1	1.6	2.1
$V_\beta$	0.01	1.1	0.5	0.5
$V_\beta$	0.05	1.1	0.2	0.3
$V_\beta$	0.10	1.1	0.1	0.1

a factor of 3 longer than with  $N_{\max} = 28$  and with  $N_{\max} = 40$  the time increases by another factor of 10. These timing and scaling properties of the one dimensional NCSM are explored in depth in Appendix D.

## 4.3 Evolution of Many-Body Forces in Bound States

### 4.3.1 Two-body Results

We first consider the bound state of two identical bosons using the potential  $V_\alpha$ . Because the SRG is a series of unitary transformations, we expect that the binding energy will not be changed by evolving the two-body interaction in the two-particle space. Indeed, we find it to be constant to high accuracy. The ground-state wave function, however, changes dramatically, as seen from the probability densities plotted in Fig. 4.3. The initial probability density exhibits a sizable “wound” near the origin

that is filled in as  $\lambda$  decreases. By  $\lambda = 2$  there is no signature of a repulsive core (and the wave function is modified out to larger  $x$ ). This is the same pattern seen for the S-wave component of deuteron wave functions starting from three-dimensional nucleon-nucleon S-wave potentials with strong repulsive cores such as Argonne  $v_{18}$ , with the “uncorrelated” final wave function at  $\lambda = 2$  roughly comparable to  $\lambda = 1.5 \text{ fm}^{-1}$  for the deuteron [31].

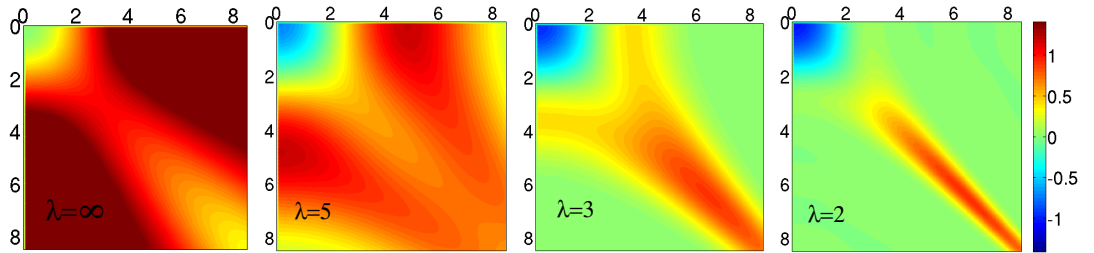


Figure 4.4: Even part of the SRG potential  $[V_s^{(2)}(p, p') + V_s^{(2)}(p, -p')]$  in dimensionless units as a function of  $p$  and  $p'$  for  $\lambda = \infty, 5, 3,$  and  $2$  (where  $\lambda = 1/s^{1/4}$ ). The initial potential is  $V_\alpha$  from Table 4.1.

The evolution of the potential in the momentum basis, shown as a color contour plot in Fig. 4.4, also demonstrates this behavior. (The even part of the potential is shown, which is the analog of the S-wave part.) The initial potential is dominated by strongly repulsive matrix elements coupling low and high momenta. The evolution in  $\lambda$  band diagonalizes the potential to a width in  $p^2$  of roughly  $\lambda^2$  while a soft attractive part emerges in the low-momentum region. The pattern in Fig. 4.4 reflects increasing non-locality as  $\lambda$  is lowered, which in turn reduces the wound in the wave function. From the probability density and the momentum space plots we estimate that evolving to halfway between  $\lambda = 2$  and  $3$  for  $V_\alpha$  corresponds roughly to the  $\lambda$  scale typically used in nuclear structure calculations (around  $2 \text{ fm}^{-1}$ ).

### 4.3.2 Three-body Results

To calculate properties of the three-particle system we construct the Hamiltonian in the basis of symmetric three-particle eigenstates as described in Sec. C.4. The SRG evolution of the potential in the three-particle space leaves the ground state energy invariant if the full Hamiltonian is kept, because the transformations are unitary. However, the Hamiltonian matrix elements in this space do not follow simply from the pairwise sum of the two-body potential matrix elements; as the SRG evolves a three-body force is induced even if its initial strength is zero.

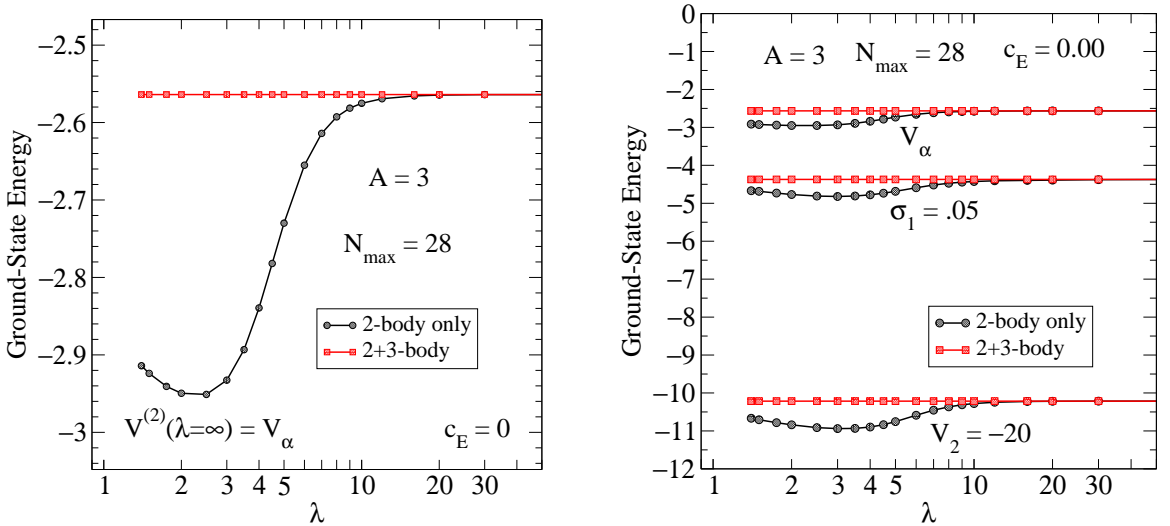


Figure 4.5: The lowest bound-state energy  $E_3$  for a three-particle system as a function of  $\lambda$  with the initial two-body-only potential  $V_\alpha$ . The (red) curves with squares include the full evolution of the Hamiltonian while the (black) curves with circles use the two-body potential evolved in the two-particle system. The right frame shows two additional results from varying  $\sigma_1$  and  $V_2$  from the values in Table 4.1.

The effect of this full three-particle space SRG evolution is shown in Fig. 4.5 for initial two-body potential  $V_\alpha$  and with initial  $V^{(3)} = 0$  (non-zero values of  $c_E$



are considered in the next section). We plot the ground-state energy for the three-particle system both with the initial two-body interaction embedded in the three-particle symmetric space and then evolved (the red curve with squares) and also with the two-body interaction evolved in the two-particle space before embedding in the three-particle space at each  $\lambda$  (the black curve with circles). We can see that the energy evaluated with the two-body interaction alone deviates noticeably as  $\lambda$  drops below 10. This variation is the signature that the two-body transformation is only approximately unitary in the three-particle sector. The error reaches a peak in  $\lambda$  between 2 and 3 and then decreases. The same pattern has been observed for NN potentials in three dimensions [35] and remains qualitatively the same when parameters in the potential are varied (e.g., see the right plot in Fig. 4.5). We made the same calculation using the purely attractive initial two-body potential  $V_\beta$ , which is shown in Fig. 4.6. Here the induced three-body force has the opposite sign and there is no maximum, which implies that the qualitative pattern of evolution is dictated by the interplay between attractive long-range and repulsive short-range parts of the potential. These features are explored further in Sect. 4.4.

### 4.3.3 Results for $A = 4$ and $A = 5$

Next we turn to  $A = 4$  and  $A = 5$ , where we expect to see the effects of induced three-, four- and five-body forces. The key issue is the relative sizes of these contributions; we are looking to test whether an initial hierarchy of few-body interactions is preserved and therefore can be truncated with a controlled error. In Chapter 5 we will address the same question in the realistic NCSM.

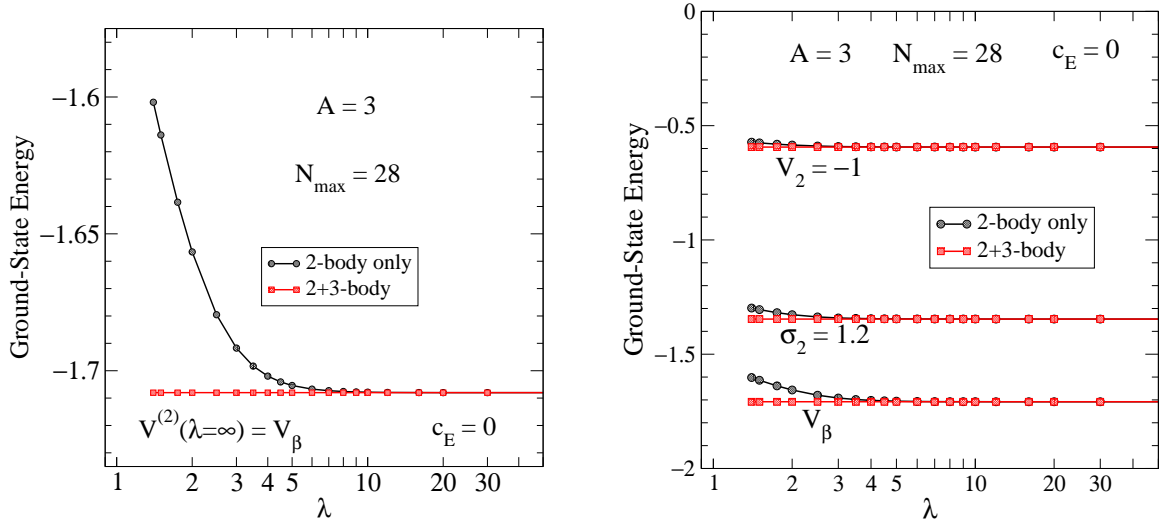


Figure 4.6: Same as Fig. 4.5 but with initial potential  $V_\beta$ . The right frame shows two additional results from varying  $\sigma_2$  and  $V_2$  from the values in Table 4.1.

In applying the SRG in the four-particle space we have three different calculations of the ground-state energy to compare. The first is the two-body potential embedded successively in the three- and four-particle spaces and then evolved in the four-particle space. The resulting unitary transformations will induce three- and four-body interactions that leave the eigenvalues invariant. We can also evolve in the two-particle space before embedding in the three- and four-particle spaces and diagonalizing. As we saw before in Fig. 4.5 and see now in Fig. 4.7, the two-body-only evolution deviates because the Hamiltonian is not evolved by an exactly unitary transformation. Finally, to find the relative size of the three and four-body interactions we can evolve in the three-particle space, thereby inducing only three-body forces. Note that the two and three-body forces must be embedded differently in the four particle space because they have different combinatoric factors associated with them, i.e., there are

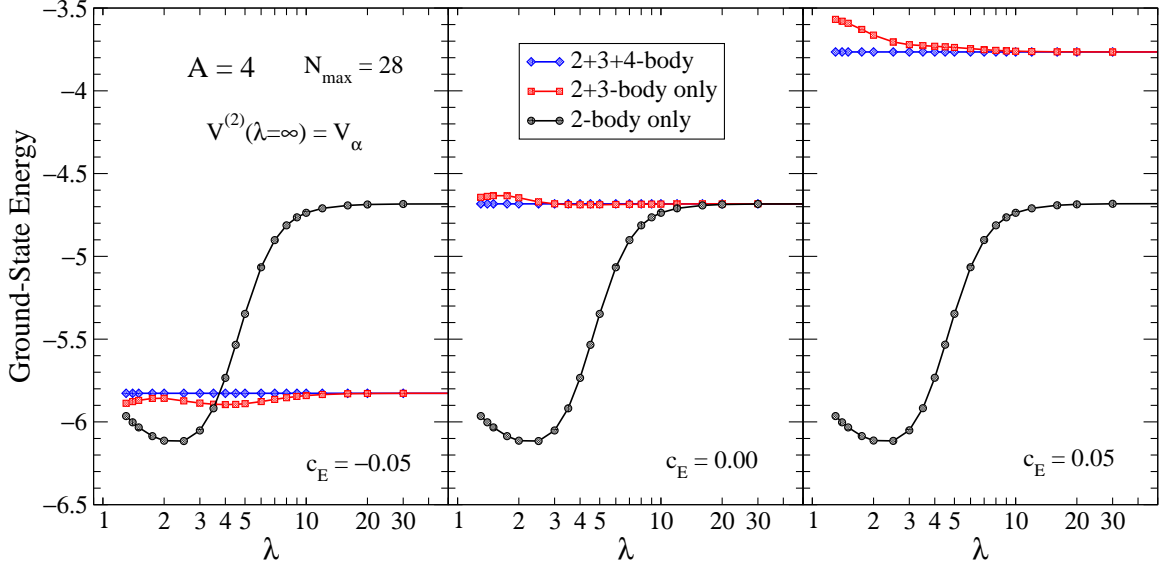


Figure 4.7: The lowest bound-state energy  $E_4$  for a four-particle system as a function of  $\lambda$  with the initial two-body potential  $V_\alpha$  and different initial three-body force strengths ( $c_E = \pm 0.05$ ).

$\binom{4}{2} = 6$  pairs and  $\binom{4}{3} = 4$  triplets. So, the proper mixture of two- and three-body force contributions to the four-particle system interaction is  $V = 6V^{(2)} + 4V^{(3)}$ .

All three of these calculations for  $A = 4$  are shown in Fig. 4.7 for the two-body potential  $V_\alpha$  and several choices of the initial three-body force. The magnitude of  $c_E$  was chosen so that the fractions of the  $A = 3$  and  $A = 4$  ground-state energies from the three-body interaction are roughly comparable to the corresponding fractions for nuclei using typical realistic NN potentials. The qualitative behavior is similar for other choices of  $c_E$  and  $V^{(2)}$ . In all plots the curves for the two-body-only (black line with circles), the two-plus-three (red line with squares), and the full two-plus-three-plus-four interaction (blue line with diamonds) show the hierarchy of different few-body interaction components. The difference between the square and diamond lines represents the contribution of the four-body force, and the difference between

the circle and square lines is the contribution of the three-body force alone. In the left and right panels, where the initial three-body force has been switched on, we can see that it is perturbatively small from the balanced attractive/repulsive contributions.

The four-body contribution is at most ten percent that of the three-body, which is itself small compared to the two-body contribution except when the latter gets small for small  $\lambda$  (note the expanded scales on the figures). Considering calculations with different  $c_E$  values, we see that the  $\lambda$  dependence of the induced four-body part depends on the interplay of initial and induced forces. In some cases noticeable (but small) evolution starts at  $\lambda = 10$  while in other cases it is deferred until much smaller  $\lambda$ . Regardless of the details, we stress that there is no sign that induced many-body forces have rapid growth with  $A$  or exhibit unusual scaling.

We repeated for  $A = 4$  our test of decoupling that was shown in Fig. 4.21 for  $A = 3$ . A similar pattern of decoupling is found, namely an increased degree of decoupling until a  $\lambda$  corresponding to the minimum of the two-body-only ground-state energy of the  $A = 4$  system, after which it deteriorates.

In Fig. 4.8 we show results for the SRG evolution, with initial potential  $V_\alpha$  and no initial three-body interactions, in a five-particle system for several values of  $N_{\max}$ . The right panel, with  $N_{\max} = 28$ , shows the converged result. We see a decreasing hierarchy of induced many-body contributions for all  $\lambda$ ; the five-body contribution is essentially negligible (or not distinguishable from numerical noise). Differences at the lower  $N_{\max}$  sized spaces arise both because the space needs to be large enough for convergence to the exact energy eigenvalues but also because the initial evolution of the potential needs a sufficiently large space. Decoupling may improve this feature but is dependent on the type of SRG used and the basis in which it is implemented.

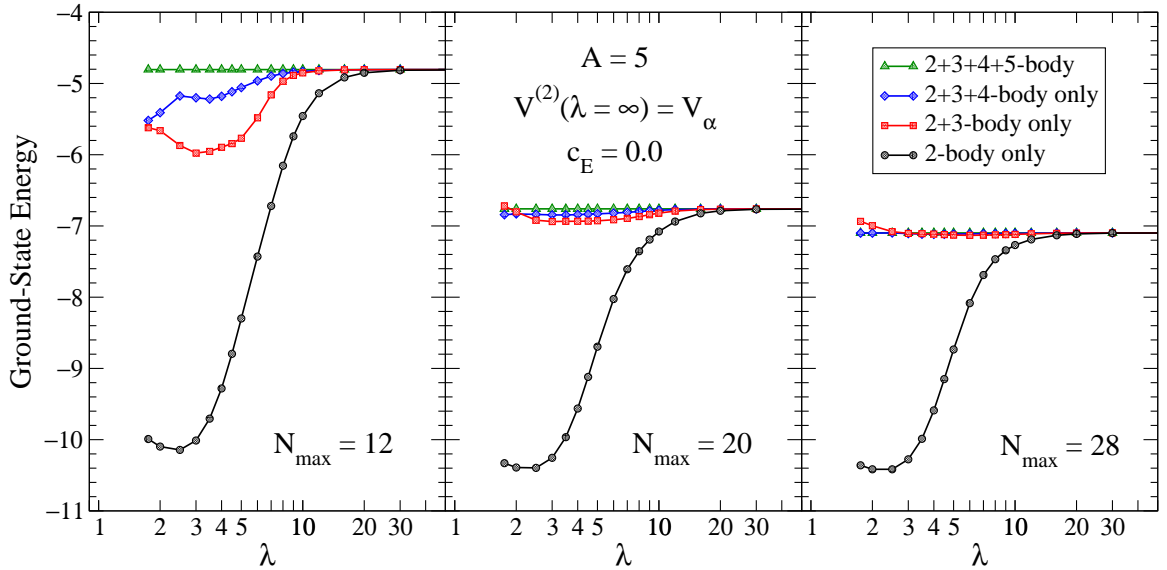


Figure 4.8: The lowest bound-state energy  $E_5$  for a 5-particle system as a function of  $\lambda$  with an initial two-body-only  $V_\alpha$  potential for several values of  $N_{\max}$ .

#### 4.4 Diagrammatic Analysis of Many-Body Force Evolution

In Ref. [47], a diagrammatic approach to the SRG equation was introduced, which organized the independent evolution of two- and three-body (and higher-body) potentials. This formalism is necessary in a momentum basis to avoid “dangerous” delta functions from spectator particles. In this section we examine how induced three-body interactions evolve in our one-dimensional laboratory and make connections to the diagrammatic expansion.

As raw material for this analysis, we plot in Fig. 4.9 the error of the evolving two-body-only binding energy while varying several parameters of the initial two-body interaction  $V_\alpha$  for  $A = 3$  ground-state energies. In the left plots we vary the range (top) and the strength (bottom) of the attractive part of  $V_\alpha$ . In the right plots we vary the range (top) and the strength (bottom) of the repulsive part. In Fig. 4.10 we

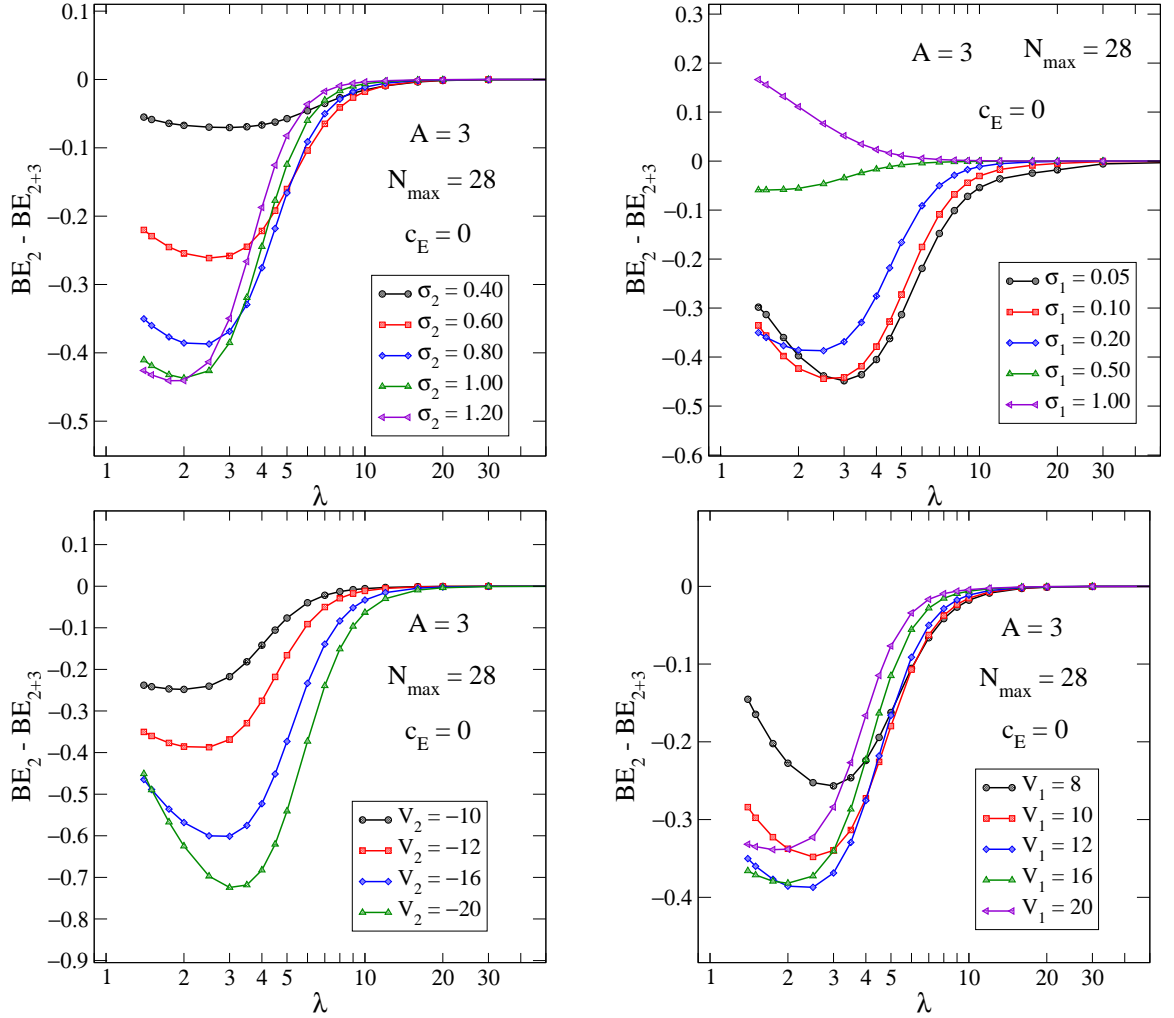


Figure 4.9: Differences of two-body-only and two-plus-three-body  $A = 3$  ground-state energies as a function of  $\lambda$ . Each of the parameters of the potential  $V_\alpha$  are varied in each plot as the other parameters are held constant. The upper panels vary the ranges while the lower vary the strengths; the left vary the attractive part and the right vary the repulsive part.

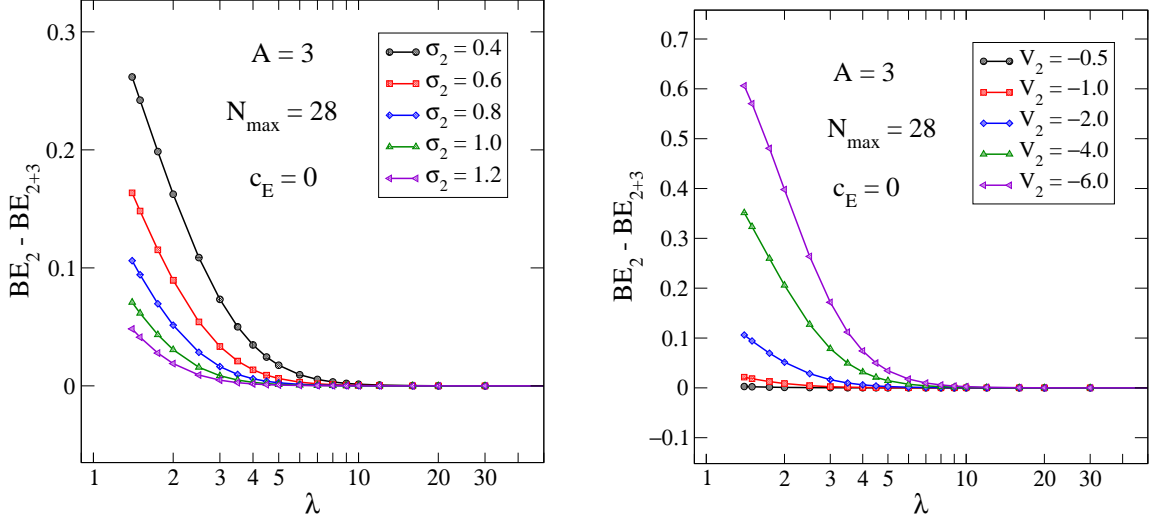


Figure 4.10: Same as Fig. 4.9 but for  $V_\beta$ .

present similar plots for a simpler system that starts with the initial attraction-only two-body potential  $V_\beta$ . Note again that the plots here show the induced error between the two-body-only and two-plus-three-body binding energies.

Certain qualitative features are found as expected in these figures. Shorter ranges imply enhanced coupling from low to high momentum and therefore we anticipate that the evolution will start sooner (i.e., at higher  $\lambda$ ). This is seen clearly on the left in Fig. 4.10 and for the variation of the (shorter-ranged) repulsive potential in Fig. 4.9 (top right plot). There is also an unsurprising increase in the magnitude of the induced three-body interaction at each  $\lambda$  with increased magnitude of the potential, as seen on the right in Fig. 4.10 and on the bottom left in Fig. 4.9. For a more definitive analysis we need to recall the discussion from Ref. [47].

The SRG evolution equation for the three-particle sector in the notation of Ref. [47] is

$$\frac{dV_s^{(2)}}{ds} + \frac{dV_s^{(3)}}{ds} = \overline{\overline{V}}_s^{(2)} + \overline{\overline{V}}_s^{(3)} + [\overline{V}_s^{(2)}, V_s^{(2)}] + [\overline{V}_s^{(2)}, V_s^{(3)}] + [\overline{V}_s^{(3)}, V_s^{(2)}] + [\overline{V}_s^{(3)}, V_s^{(3)}] \quad (4.6)$$

$$\begin{aligned}
\frac{dV_2}{ds} &= \text{Diagram 1} + \text{Diagram 2} - \text{Diagram 3} \\
\frac{dV_3}{ds} &= \text{Diagram 4} + \text{Diagram 5} + \text{Diagram 6} + \text{Diagram 7} + \dots
\end{aligned}$$

Figure 4.11: A diagrammatic decomposition of the SRG Eq. (4.6). A circle at a vertex denotes a commutator with  $T_{\text{rel}}$ .

where each bar denotes a commutator with  $T_{\text{rel}}$ . We remind the reader that  $dT_{\text{rel}}/ds = 0$  by construction. A diagrammatic decomposition of this equation is shown in Fig. 4.11. In the two-body sector, the equation reduces to the first term on the left and the first and third terms on the right (the first row in Fig. 4.11). These terms keep two-particle energy eigenvalues invariant under evolution. In the three-particle sector, Eq. (4.6) results in not only these two-body graphs with a disconnected spectator but additional graphs involving connected combinations of two and three-body interactions. The diagrams with two-body interactions and a disconnected spectator line satisfy the two-body evolution equations, and so will cancel out of the full three-particle-sector evolution equation. Thus the evolution of the three-body interaction is dictated by the connected diagrams (the second row in Fig. 4.11). In summary, the evolution of the  $A$ -body potential in the  $A$ -particle system is given by

$$\frac{dV_s^{(A)}}{ds} = [\eta_s, H_s]_A, \quad (4.7)$$

where the “ $A$ ” subscript on the right side means the fully connected  $A$ -particle terms.



To make a connection between the individual terms in the three-body interaction evolution and the running of the ground-state energy, we need to derive the evolution equations for the *expectation value* of  $V_s^{(3)}$  in the ground state. Denoting the ground-state wave function for the  $A$ -particle system by  $|\psi_s^A\rangle$ , it evolves according to

$$|\psi_s^A\rangle = U_s |\psi_{s=0}^A\rangle, \quad \frac{d}{ds} |\psi_s^A\rangle = \eta_s |\psi_s^A\rangle, \quad (4.8)$$

where  $U_s$  is the SRG unitary transformation at  $s$  and

$$\eta_s = \frac{dU_s}{ds} U_s^\dagger = -\eta_s^\dagger. \quad (4.9)$$

Then the matrix element of an operator  $O_s$  evolves according to

$$\frac{d}{ds} \langle \psi_s^A | O_s | \psi_s^A \rangle = \langle \psi_s^A | \frac{dO_s}{ds} - [\eta_s, O_s] | \psi_s^A \rangle. \quad (4.10)$$

If the operator  $O_s$  evolves according to  $O_s = U_s O_{s=0} U_s^\dagger$ , then the matrix element vanishes, as when  $O_s = H_s$ .

However, if we wish to see how one part of  $H_s$  evolves, such as the expectation value of  $V^{(3)}$ , we obtain

$$\frac{d}{ds} \langle \psi_s^A | V_s^{(3)} | \psi_s^A \rangle = \langle \psi_s^A | \frac{dV_s^{(3)}}{ds} - [\eta_s, V_s^{(3)}] | \psi_s^A \rangle, \quad (4.11)$$

which does not give zero in general because  $V_s^{(3)} \neq U_s V_{s=0}^{(3)} U_s^\dagger$ . In the two-particle case, the analog of Eq. (4.11) gives  $d\langle V^{(2)} \rangle / ds = \langle [\eta_s, T_{\text{rel}}] \rangle$ . In the three-particle case, we can expand Eq. (4.11) as

$$\begin{aligned} \frac{d}{ds} \langle \psi_s | V_s^{(3)} | \psi_s \rangle &= \langle \psi_s | [\eta_s, H_s]_3 - [\eta_s, V_s^{(3)}] | \psi_s \rangle \\ &= \langle \psi_s | [\bar{V}_s^{(3)}, T_{\text{rel}}] + [\bar{V}_s^{(2)}, V_s^{(2)}]_c + [\bar{V}_s^{(2)}, V_s^{(3)}] + [\bar{V}_s^{(3)}, V_s^{(2)}] + [\bar{V}_s^{(3)}, V_s^{(3)}] \\ &\quad - [\bar{V}_s^{(2)}, V_s^{(3)}] - [\bar{V}_s^{(3)}, V_s^{(3)}] | \psi_s \rangle \\ &= \langle \psi_s | [\bar{V}_s^{(3)}, H_s] + [\bar{V}_s^{(2)}, V_s^{(2)}]_c - [\bar{V}_s^{(3)}, V_s^{(3)}] | \psi_s \rangle \\ &= \langle \psi_s | [\bar{V}_s^{(2)}, V_s^{(2)}]_c - [\bar{V}_s^{(3)}, V_s^{(3)}] | \psi_s \rangle, \end{aligned} \quad (4.12)$$

where  $\overline{V}_s^{(2)}$  and  $\overline{V}_s^{(3)}$  are the commutators  $\overline{V}_s^{(2)} = [T_{\text{rel}}, V_s^{(2)}]$  and  $\overline{V}_s^{(3)} = [T_{\text{rel}}, V_s^{(3)}]$ . In the third line, the expectation value of the commutator,  $[\overline{V}_s^{(3)}, H_s]$ , vanishes identically.

The term with the subscript “*c*” has had the two-body disconnected diagrams removed. In our MATLAB implementation, this subtraction is achieved by first embedding the two-particle-space evolved version of this commutator in the three-particle space. Computing  $[\overline{V}_s^{(2)}, V^{(2)}]$  in the two-particle space alone involves only the one-loop two-body interactions, so embedding in the three-particle sector results in only the disconnected parts. This disconnected part can then be subtracted from the total three-particle sector version of the same commutator, leaving only the three-particle fully connected part.

It is most useful for our analysis to convert from derivatives with respect to  $s$  to derivatives with respect to  $\lambda$  using  $\frac{d}{ds} = -\frac{\lambda^5}{4} \frac{d}{d\lambda}$ . In Fig. 4.12 we show the ground-state expectation values of the right side of Eq. (4.11), which are broken down into the two terms from the right side of Eq. (4.12) for  $A = 3$  and various potentials. It is apparent that the drivers of three-body matrix element evolution depend on the interplay between long- and short-range, attractive and repulsive parts. The lower right panel of Fig. 4.12 shows an increasing attractive strength of the three-body force when starting from an attractive-only two-body potential. In this regime the dominant contribution to the evolution of the three-body potential matrix element is the tree-level two-body connected part  $[\overline{V}_s^{(2)}, V_s^{(2)}]_c$ . This observation accounts for the behavior in the right graph of Fig. 4.10, where the size of the error scales (roughly) like  $(V^{(2)})^2$ . Varying the long-range attraction strength in Fig. 4.9 shows a similar effect.

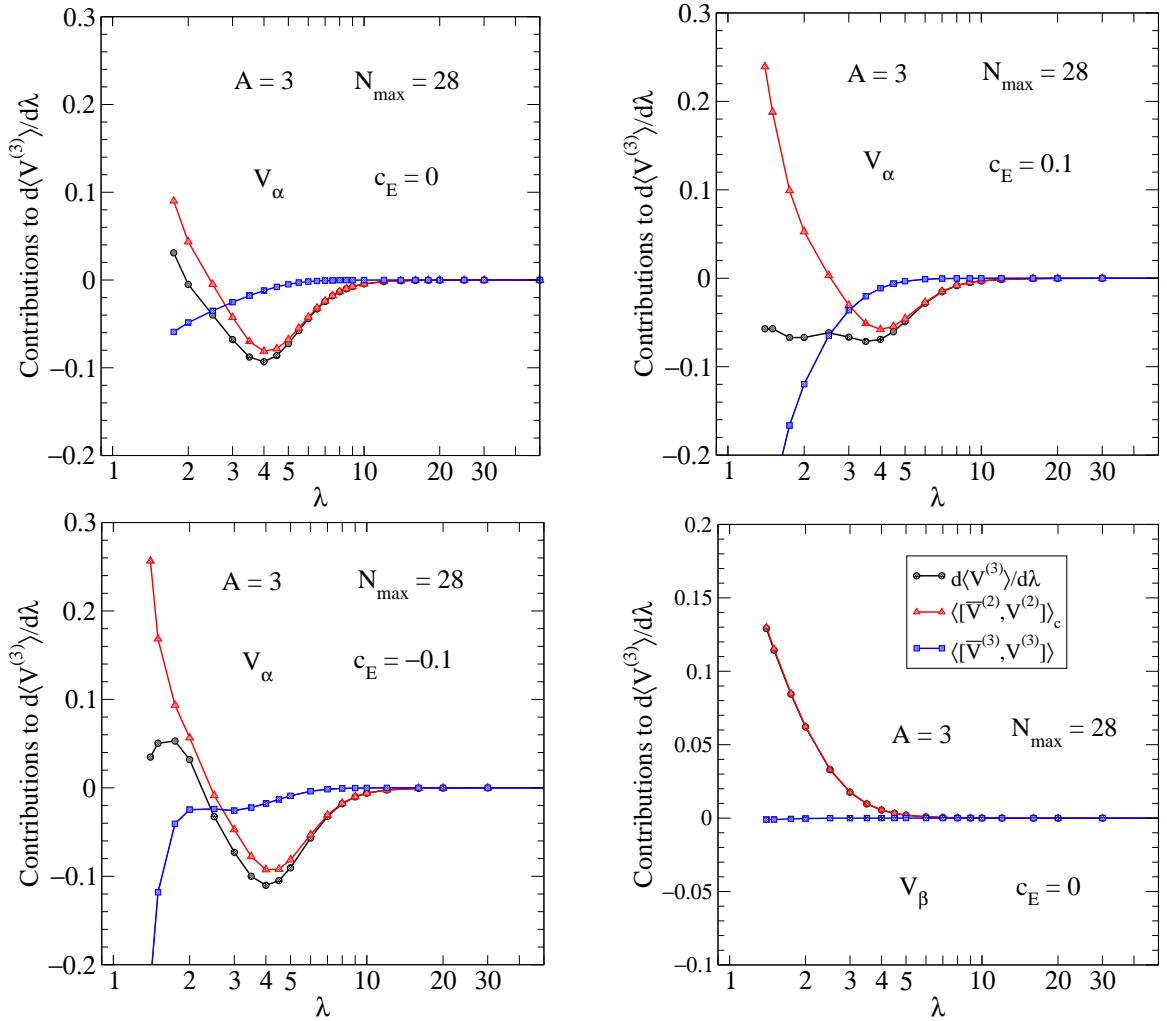


Figure 4.12: Contributions from individual terms to the  $A = 3$  ground-state expectation value  $d\langle V_\lambda^{(3)} \rangle / d\lambda$  for several different two- and three-body potentials, as indicated in the plots. We emphasize that  $\lambda \leq 2$  is very small, comparable to  $\lambda \leq 1.5 \text{ fm}^{-1}$  for NN forces in analogous calculations with the NCSM [35].

More generally, the impact on ground-state energies of the induced three-body interaction depends on the details of the correlations in the wave function. The other plots in Fig. 4.12 for the more realistic initial two-body potential,  $V_\alpha$ , show the interplay between two- and three-body contributions to the three-body matrix element evolution. The three-body contribution to the three-body evolution stays small until

the longer-range attractive part of the potential begins to affect the evolution. Most of the change is from  $\lambda = 8$  to  $\lambda = 3$ , which is dominated by  $\langle \overline{V}^{(2)}, V^{(2)} \rangle$ . Thus, the feedback of the three-body potential depends on the initial conditions, but in general insures that the binding energy contribution stays small.

We can repeat the above analysis for  $A = 4$

$$\begin{aligned} \frac{d}{ds} \langle \psi_s^{(4)} | V_s^{(4)} | \psi_s^{(4)} \rangle &= \langle \psi_s^{(4)} | [\overline{V}_s^{(2)}, V_s^{(3)}]_c + [\overline{V}_s^{(3)}, V_s^{(2)}]_c \\ &\quad + [\overline{V}_s^{(3)}, V_s^{(3)}]_c - [\overline{V}_s^{(4)}, V_s^{(4)}] | \psi_s^{(4)} \rangle \end{aligned} \quad (4.13)$$

where we find no fully connected terms with only two-body forces. Again, disconnected terms involving two and three body potentials cancel out in the lower sectors. The leading terms are commutators with one  $V_s^{(2)}$  and one  $V_s^{(3)}$ , followed by connected terms quadratic in  $V_s^{(3)}$  and one term quadratic in  $V_s^{(4)}$ . All terms are small and additional cancellations among them further suppress the four-body contribution. Thus, the initial hierarchy of many-body forces implies that induced four-body (and higher-body) forces will be small.

In Fig. 4.13 we plot these contributions to the evolution of the four-body expectation value. Again it is more useful to convert the derivatives in  $s$  to derivatives in  $\lambda$ . The interplay of contributions is much more complicated here. We can see the cancellations between the two terms involving  $V_s^{(2)}$  and  $V_s^{(3)}$ , and the term quadratic in  $V_s^{(3)}$ . The total derivative of  $V_s^{(4)}$  is kept small, along with the in term quadratic in  $V_s^{(4)}$ , until below  $\lambda = 2$ . No terms quadratic in  $V_s^{(2)}$  appear as no connected diagrams can be constructed for the four-particle evolution. This keeps the evolution of  $V_s^{(4)}$  low because they are one more order removed from the initial interaction.

Also, note the differences in combinatoric factors when comparing this analysis in different sectors. Between the  $A = 3$  and 4 sectors we can only consider the  $[\overline{V}_s^{(3)}, V_s^{(3)}]$

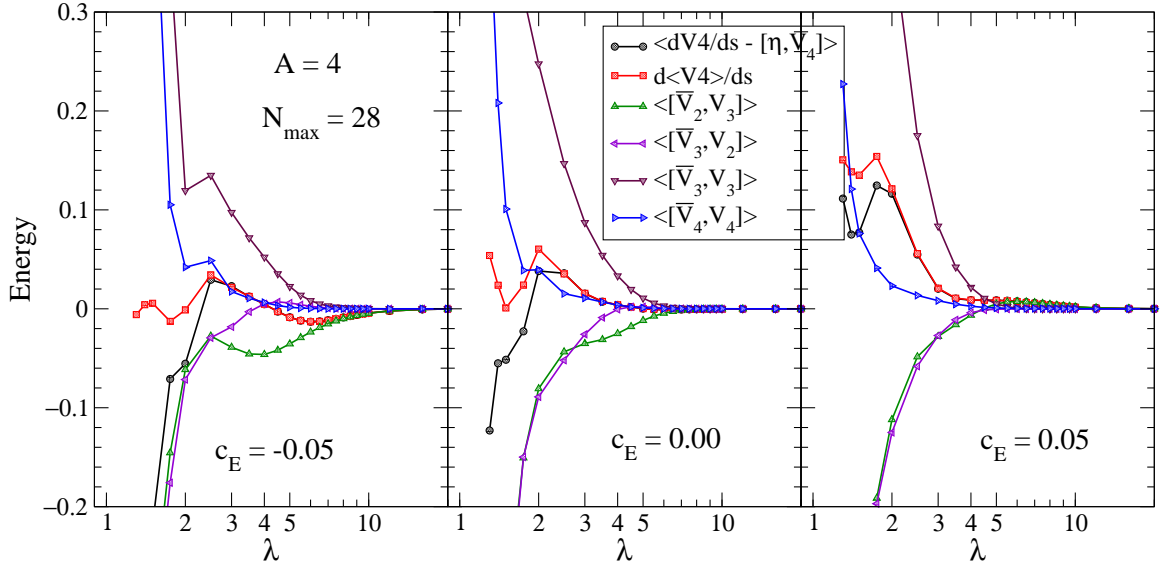


Figure 4.13: Contributions from individual terms to the  $A = 4$  ground-state expectation value  $d\langle V_\lambda^{(4)} \rangle/d\lambda$  for several different initial three-body potentials, as indicated in the plots. We emphasize that  $\lambda \leq 2$  is very small, comparable to  $\lambda \leq 1.5 \text{ fm}^{-1}$  for NN forces in analogous calculations with the NCSM [35].

contribution. Diagrammatically speaking, in the  $A = 3$  sector, this can only include  $\bar{V}_s^{(3)}$  and  $V_s^{(3)}$  fully contracted with each other. However, in the  $A = 4$  sector the connected diagrams are only those contractions with one loop. There are  $3! = 6$  ways to choose the pair legs composing the loop.<sup>16</sup> So the  $[\bar{V}_s^{(3)}, V_s^{(3)}]$  contribution is 6 times larger in four-body sector. This does not negate the effects of the absence of two-body contributions since they would also have large associated combinatoric factors.

<sup>16</sup>There are 6 ways to choose the legs on the receiving term of the diagram but this is true in both sectors and this 6 cancels out of the comparison.

## 4.5 Fitting Three-Body Forces

Figures 4.14 and 4.15 show a simple fitting procedure for the three-body force. In this calculation the initial interaction was evolved only in the  $A = 2$  basis and then embedded up to the  $A = 4$  basis for calculations of the three- and four-particle binding energies. This corresponds to the black curves (circles) in the figures, which are all identical. Before, the interaction was also evolved in the  $A = 3$  basis to obtain a renormalization that is unitary for  $A = 3$  and used to compute the induced four-body forces. Here an independent operator, inspired by a three-nucleon contact term from  $\chi$ EFT, <sup>17</sup> is used to fit the missing three-body interaction to the three-body binding energy:

$$V_{D_0}^{(3)} = D_0 e^{-[(p_1^2 + p_2^2)/\Lambda^2]^{n_{\text{exp}}}} e^{-[(p_1'^2 + p_2'^2)/\Lambda^2]^{n_{\text{exp}}}} \quad (4.14)$$

where  $p_1$  and  $p_2$  are the usual Jacobi momenta, the two regulator parameters,  $\Lambda$  and  $n_{\text{exp}}$ , set the cutoff and sharpness of the regulator and are kept constant over the range of  $\lambda$  in each panel shown, and the strength,  $D_0$ , was fit at each value of  $\lambda$ . Then this fitted term plus the evolved two-body only interaction is embedded to  $A = 4$  to obtain the four-body binding energy. This corresponds to the red lines (squares).

As can be seen in the figures, this fitting procedure reduced the error due to missing three-body forces by 80 to 90 percent. In Fig. 4.14 the regulators sharpness exponent,  $n_{\text{exp}}$ , is held constant and the range,  $\Lambda$ , is varied. A significant dependence on  $\Lambda$  is observed indicating significant momentum dependent structure in the evolved two-body force. In Fig. 4.15, now the range is held fixed but sharpness is varied. Here very little dependence is found indicating less sensitivity to the exact shape of the regulator.

<sup>17</sup>In the  $\chi$ EFT paradigm, any regularized delta function will work for the fitting performed here.

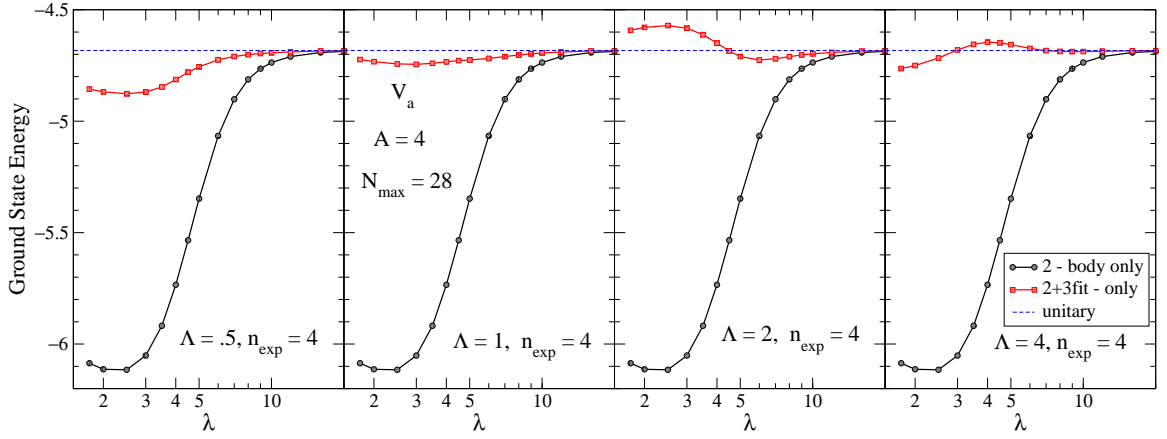


Figure 4.14: Ground-state energy of the  $A = 4$  system with  $NN$  interaction evolved and then a three-body interaction term (with an exponential regulator) fit to the  $A = 3$  ground-state energy. The calculation is repeated with a variation of the range parameter,  $\Lambda$

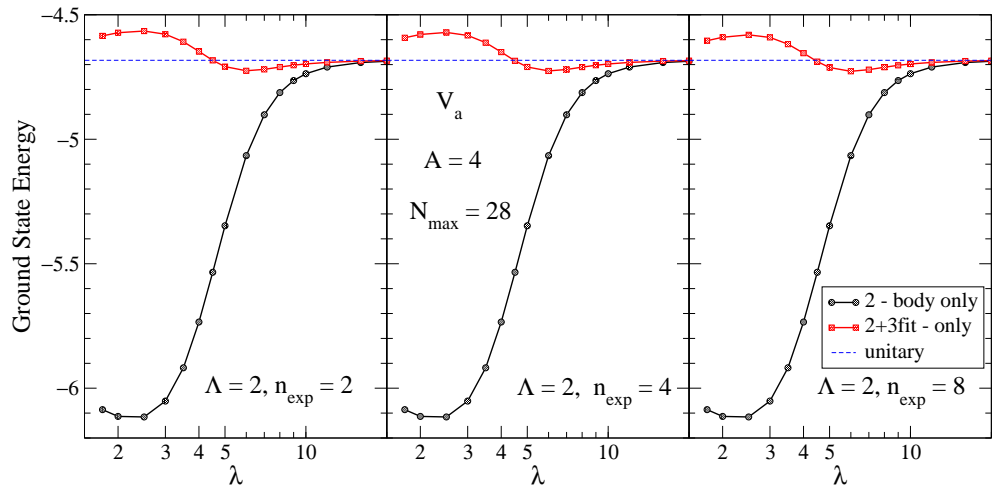


Figure 4.15: Same as Fig. 4.14 but at one value of  $\Lambda$  and a range over the regulator's sharpness parameter,  $n_{\text{exp}}$

The fits shown in Figs. 4.14 and 4.15 show that this one term can accommodate much of the missing three-body force. A natural progression would suggest adding a

second term with gradients as in a Taylor expansion:

$$V_{D_2}^{(3)} = D_2 e^{-(p_1^2 + p_2^2)/\Lambda^2} [p_1^2 + p_2^2 + p_1'^2 + p_2'^2] e^{-[(p_1'^2 + p_2'^2)/\Lambda^2]} \quad (4.15)$$

where  $D_2$  is the new low-energy constant that also must be fit to data. In this one-dimensional model, what we choose as data is arbitrary. A particular fitting strategy used for  $\chi$ EFT's uses the average of  ${}^3\text{H}$  and  ${}^3\text{He}$  binding energies and the triton  $\beta$  decay. In an attempt to be consistent with that work, we have chosen to fit our two parameters to the three-body binding energy (as we did with the one term fitting above) and the first excited state in the three-body spectrum as another piece of three-body data.

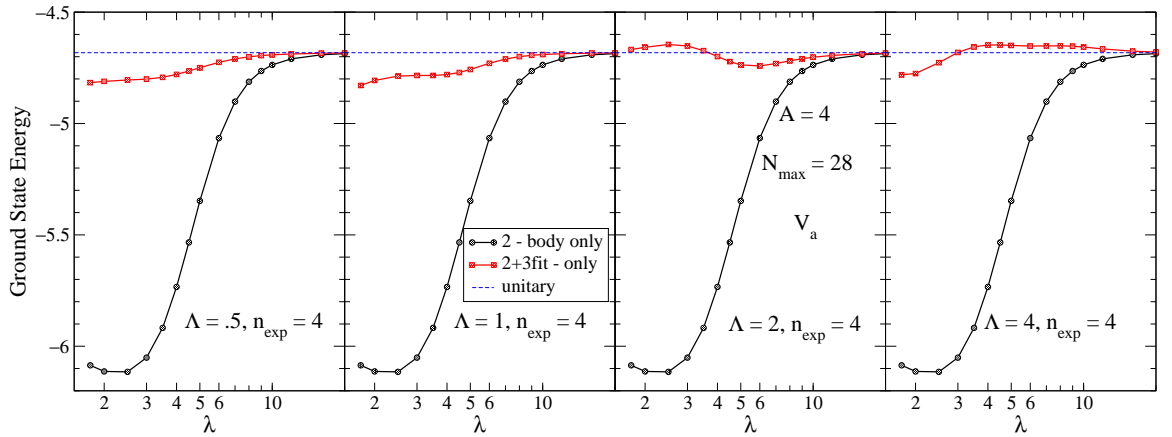


Figure 4.16: Same as Fig. 4.14 but now the  $A = 3$  ground-state energy and a second piece of data, the first excited state for  $A = 3$ , are fit to two three-body interaction terms. The first term is the same as in Fig. 4.14 and the second includes a gradient correction.

Figure 4.16 shows the predictions for the  $A = 4$  binding energy after fitting the two terms to two different three-body quantities. As in Fig. 4.14,  $n_{\text{exp}}$ , is held constant and the range,  $\Lambda$ , is varied. Now we have an expansion in the strength,  $D$ , which



we fit to three-body quantities. The resulting fit three-body interaction can then be used to make predictions of four- and higher-body observables. Here we display the prediction of the  $A = 4$  binding energy after fitting both  $D_0$  and  $D_2$ . The improvement is inconclusive. This is an ongoing investigation and we must next check several features of the system and procedure to determine how much correction we should expect. We may need to choose a different second value for fitting if the one chosen now is already well fit by the first term. A logical next step is to reproduce the fitting approach previously employed in realistic calculations by varying  $\Lambda$  as a function of  $\lambda$ .

Fitting three-body interactions in this manner is another tool to study the form of induced many-body forces. It is complimentary to the vacuum expectation value analysis done in section 4.4, providing another quantitative tool to understand the SRG's behavior. In addition, well controlled fitting procedures will be indispensable in estimating the effects of some induced  $A$ -body forces that cannot be induced explicitly due to the size of a given  $A$ -body basis.

## 4.6 Evolving Individual Operators: A Study of Cutoff Behavior

An aspect of the SRG which contributes to its versatility and power is the ability to evolve individual operators as well as the Hamiltonian. The majority of work in this area is contained in Ref. [43, 42], but some preliminary work was done for few-body systems using a simple operator for the momentum distribution in the wavefunction

of few-body systems [68]:

$$\begin{aligned}
n(k) &= \sum_{i=1}^A \int \psi_A^2(k_1 k_2 \dots k_A) \delta(k - k_i) \delta\left(\sum_{j=1}^A k_j\right) dk_1 dk_2 \dots dk_A \\
&= A \int \psi_A^2(k_1 k_2 \dots k_A) \delta(k - k_A) \delta\left(\sum_{j=1}^A k_j\right) dk_1 dk_2 \dots dk_A \\
&= A \int \psi_A^2(p_1 p_2 \dots p_{A-1}) \delta\left(\sqrt{\frac{A-1}{A}}(p - p_{A-1})\right) dp_1 dp_2 \dots dp_{A-1}
\end{aligned} \tag{4.16}$$

where  $A$  is the number of particles,  $k$ 's are lab-frame momenta and  $p$ 's are Jacobi momenta. The second line is a simplification due to the symmetry properties of the present basis. The wavefunctions are symmetric with respect to all the particles so the total is simply  $A$  times the momentum distribution of one particle. We choose the  $A$ 'th particle (the last one) due to a special property of the last Jacobi coordinate that it can be related directly to the last single-particle coordinate when the center of mass momentum is zero. Using that property, the third line is converted from single particle coordinates to the Jacobi coordinates of the basis.

Figure 4.17 shows the evolution of the momentum distribution within the three-body wavefunction for a series of  $N_{\max}$ 's. In these plots the operator itself is not actually evolved. The expectation value of the evolved operator on the evolved wavefunctions is simply a verification of the unitarity of  $U_s$ , with the curves for all  $\lambda$ 's on top of the  $\lambda = \infty$  curve. Here the interesting part is using the bare operator with the evolved wavefunctions (or vice versa) to compute the momentum distribution. The horizontal axis is in single particle momenta while the cutoffs are in terms of Jacobi momenta. A conversion factor of  $\approx \sqrt{A}$  is needed when analyzing the figures.

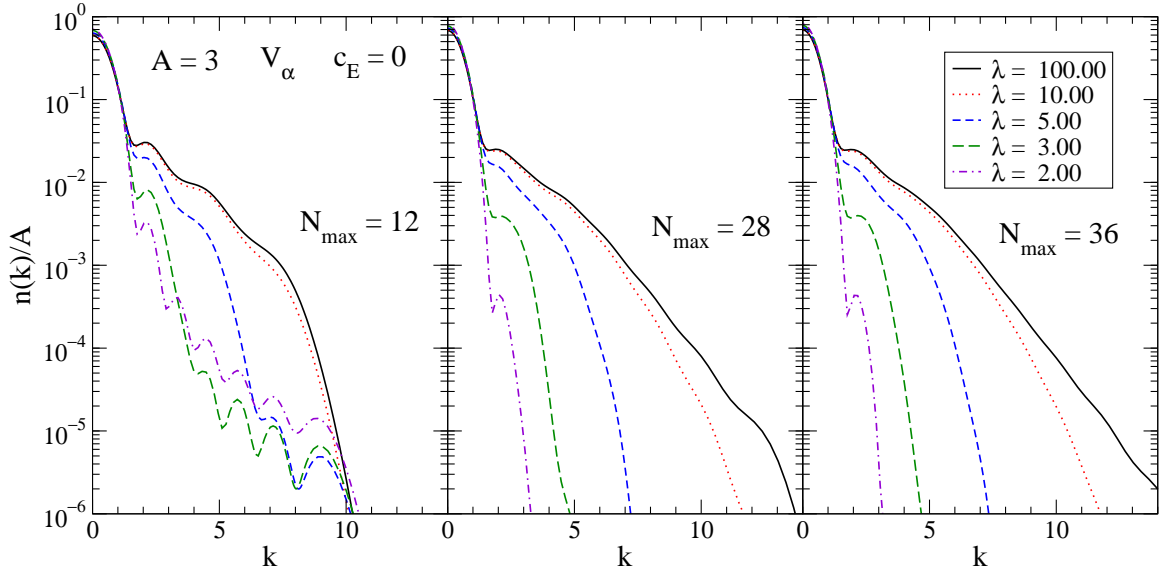


Figure 4.17: A sequence of plots showing the evolving components of the 3-body wavefunction for increasing  $N_{\max}$ . Each of these plots uses  $\hbar\omega = 5$ .

The three panels in Fig. 4.17 show convergence as  $N_{\max}$  is increased. The series of curves in each plot shows that the evolving wavefunction has a considerable decrease in high-momentum components as  $\lambda$  is lowered. At large  $N_{\max}$ , the oscillator basis ultraviolet cutoff ( $\Lambda_{\text{UV}}$ ) is large and sufficient high-momentum information is included. Hence the convergence in the unevolved wavefunctions. At larger  $N_{\max}$ , the evolved wavefunctions are more converged than the unevolved because the high-momentum components have been suppressed and therefore the wavefunction is unaltered by  $\Lambda_{\text{UV}}$ . One can see  $\Lambda_{\text{UV}}$  explicitly in the unevolved wavefunctions using  $\Lambda_{\text{UV}} \approx \sqrt{\hbar\omega N_{\max}}$  with  $\hbar\omega = 5$ . At  $N_{\max} = 12$  we get  $\Lambda_{\text{UV}} \approx 8 \text{ fm}^{-1}$  which is about the location of the right-most shoulder of the unevolved wavefunction. Again at  $N_{\max} = 28$  the cutoff is  $\Lambda_{\text{UV}} \approx 12 \text{ fm}^{-1}$  corresponding to that shoulder. The shoulder in the momentum distribution is the clearest high-momentum structure to compare between the panels,

hence in this instance and at constant  $A$ , we have ignored the Jacobi conversion factor.

As  $N_{\max}$  is lowered we can see the infrared cutoff ( $\Lambda_{\text{IR}} \approx \sqrt{\frac{\hbar\omega}{N_{\max}}}$ ) become significant. The oscillatory behavior in the  $N_{\max} = 12$  panel is the ringing from the  $\Lambda_{\text{IR}}$  cutoff inherent in the small oscillator basis. Given a wavefunction in position space (recall coordinate space plots of the wavefunction in Fig. 4.3) which is cutoff at some point  $x = 2\pi/\Lambda_{\text{IR}}$  will show ringing artifacts from the Fourier transform of the sharp cut. For a square function the minima should be  $\Lambda_{\text{IR}}$  apart. Due to the single-to-Jacobi conversion factor, the minima of the ringing should be  $\sqrt{A}\Lambda_{\text{IR}} \approx \sqrt{(A)\hbar\omega/N_{\max}}$  apart from each other.

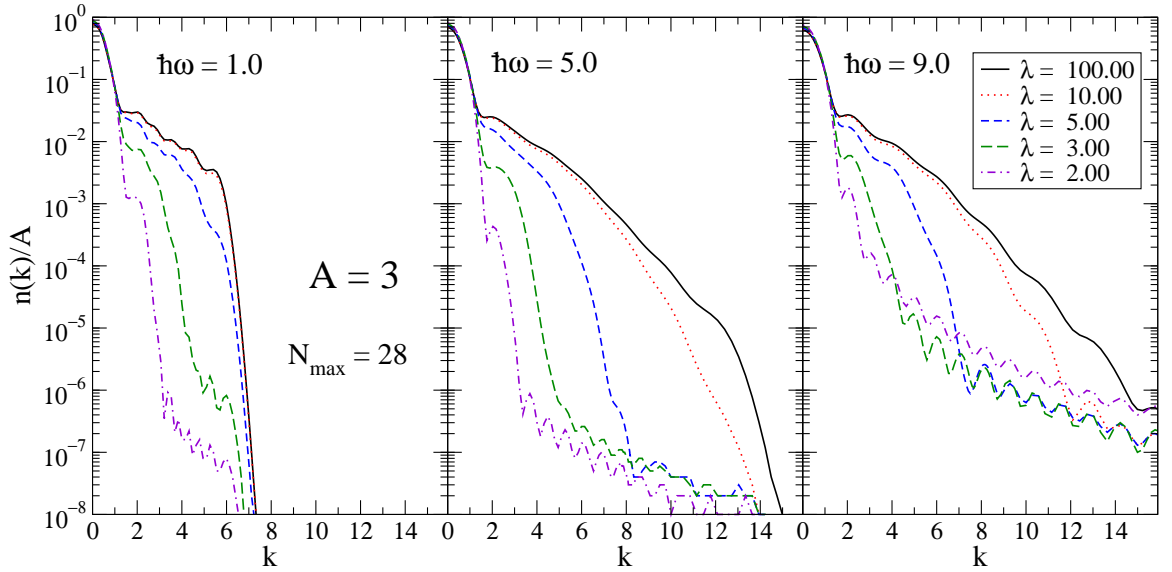


Figure 4.18: A sequence of plots showing the evolving components of the 3-body wavefunction for fixed  $N_{\max}$  and varied  $\hbar\omega$ .

Figures 4.18 and 4.19 further explore the behavior of the cutoffs,  $\Lambda_{\text{IR}}$  and  $\Lambda_{\text{UV}}$ . In the former, all the panels are at the same relatively high  $N_{\max} = 28$  with  $\hbar\omega$  varied.

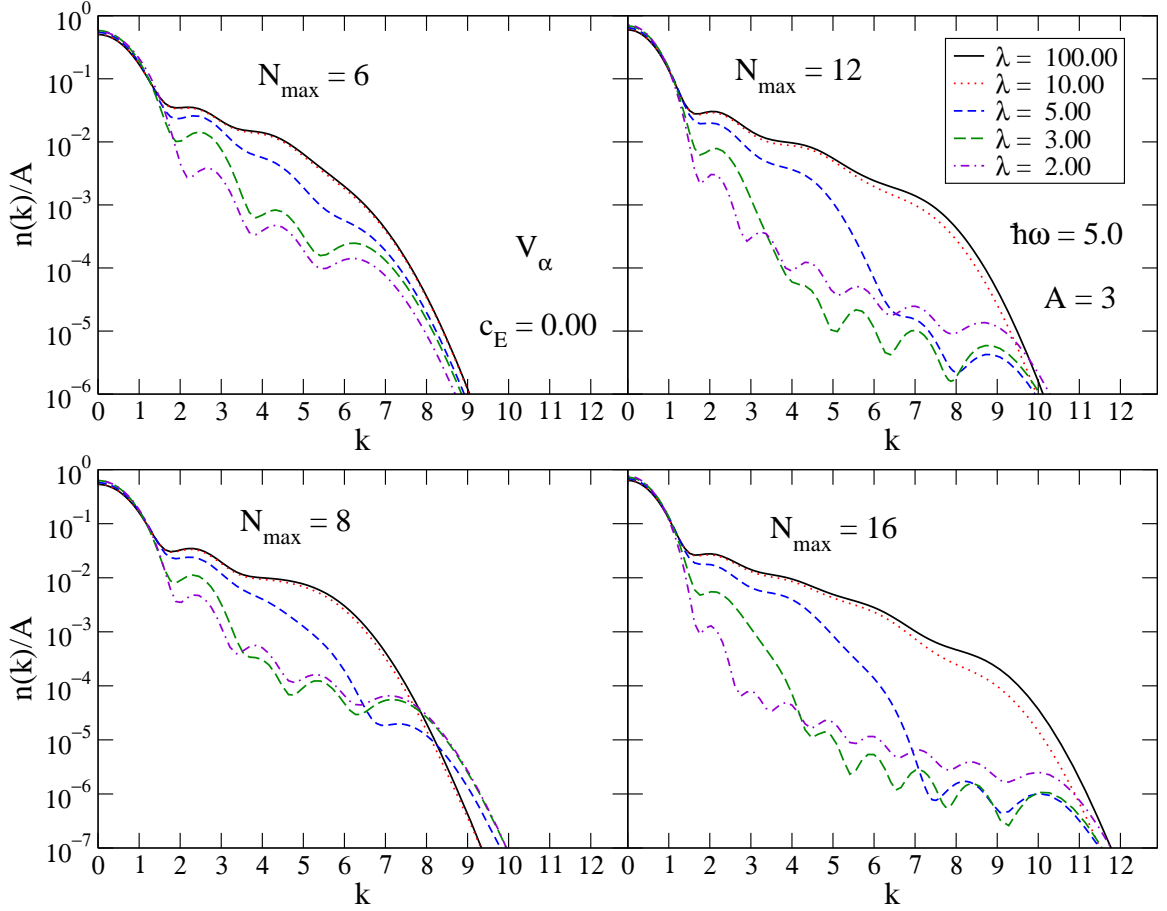


Figure 4.19: A sequence of plots showing the evolving components of the 3-body wavefunction for fixed  $\hbar\omega$  and varied  $N_{\max}$ .

The behavior of the ultraviolet cutoff is evident with the right-most shoulder given by  $\sqrt{\hbar\omega N_{\max}}$ . The infrared is clearer here, with the spacing between oscillations given by  $\approx \sqrt{A\hbar\omega/N_{\max}}$ . This is also evident in Fig. 4.19 where  $N_{\max}$  is varied with a fixed  $\hbar\omega$ . The spacing decreases by a factor  $\sqrt{2}$  from  $N_{\max} = 6 \rightarrow 12$  or  $N_{\max} = 8 \rightarrow 16$ . This is surprisingly accurate in the regions with relatively uniform oscillation spacings at midrange momenta. This is indicative of how much high-momentum details have been transformed by the SRG. We are left with a smooth gaussian-like wavefunction

which is chopped at large distance by the infrared cutoff, leaving straightforward ringing effects.

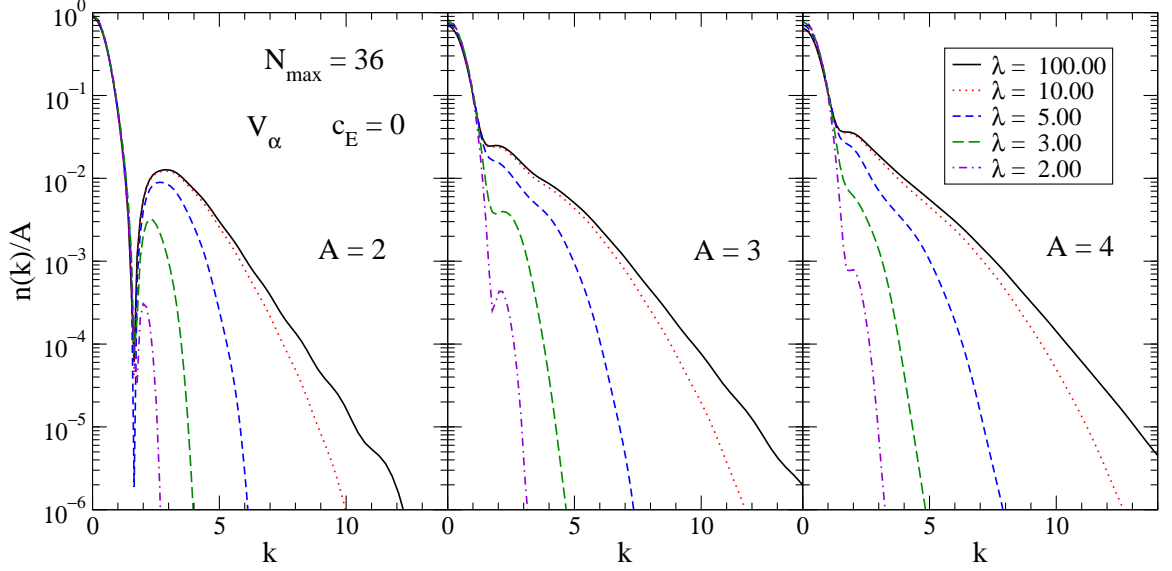


Figure 4.20: A sequence of plots at high  $N_{\max}$  showing the evolving components of the many-body wavefunction for  $A = 2, 3,$  and  $4$ .

The momentum distribution plots of Figure 4.20 shows the same quantity as the previous plots but at a single large  $N_{\max}$  and for different numbers of particles,  $A = 2, 3, 4$ . The same renormalization pattern for high-momentum components is evident regardless of the considered one-dimensional system.

## 4.7 Convergence in the Oscillator Basis

In Fig. 4.21 we test SRG decoupling [52] within the harmonic oscillator basis. The left panel shows the results when only the two-body evolved potential is used to calculate  $A = 3$  binding energies. For the right plot, the potential was evolved in the full three-body space, allowing three-body forces to be induced. The Hamiltonians for

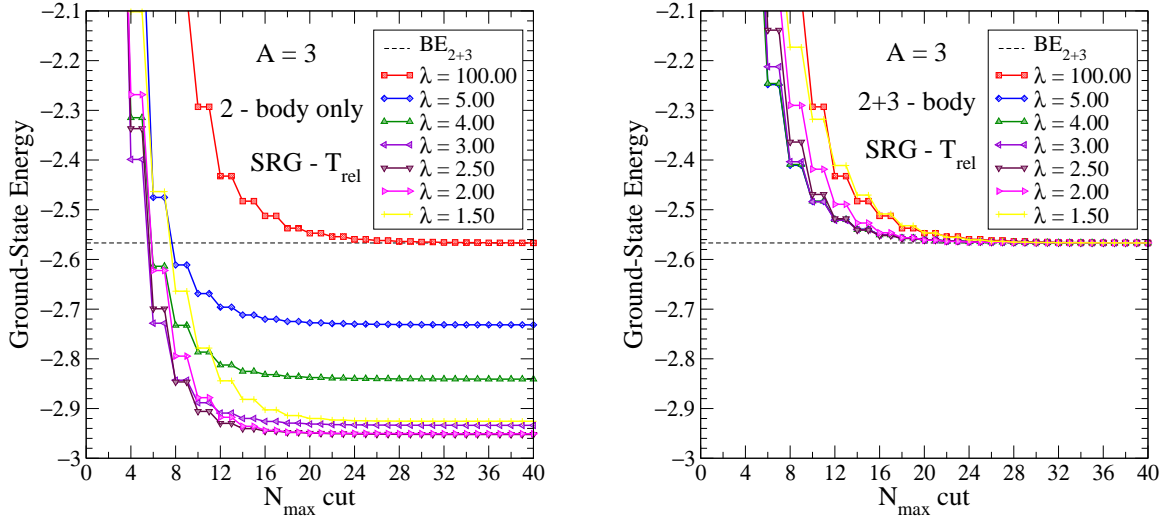


Figure 4.21: Decoupling in the three-particle system using the choice  $G_s = T_{\text{rel}}$ . The initial  $V_\alpha$  potential is evolved to each  $\lambda$  shown in a basis with  $N_{\text{max}} = 40$ . On the left only the two-body potential is evolved and embedded while the right involves the full unitarily transformed potential. Matrix elements of the potential are set to zero if one or both states have  $N > N_{\text{cut}}$  and the resulting Hamiltonian is diagonalized to obtain the ground-state energies plotted.

selected  $\lambda$  values are diagonalized in bases of decreasing size, as measured by “ $N_{\text{cut}}$ ”, which is the cut-off applied to the potential to study its decoupling properties. The potential is set to zero for matrix elements for which one or both states has  $N > N_{\text{cut}}$ . The degree of decoupling is measured by the point of departure, as  $N_{\text{cut}}$  is lowered, from the asymptotic energy for  $N_{\text{max}} = 40$ . As the potential is evolved from the initial potential ( $\lambda = \infty$ ) down to  $\lambda = 2.5$ , decoupling is achieved for smaller spaces, which means convergence is reached for smaller basis sizes. This is the same pattern as found for realistic NN potentials [52]. In the left panel of Fig. 4.21, the ground-state energies asymptote to different values because the evolution is not completely unitary. One might imagine that this would affect the decoupling, but we show this is not the case here. In the right panel, the induced three-body interaction is kept,

so the curves asymptote to the same energy at large  $N_{\max}$ , while the same pattern of decoupling is observed.

We repeated for  $A = 4$  our test of decoupling that was shown in Fig. 4.21 for  $A = 3$ . A similar pattern of decoupling is found, namely an increased degree of decoupling until a  $\lambda$  corresponding to the minimum of the two-body-only ground-state energy of the  $A = 4$  system, after which it deteriorates.

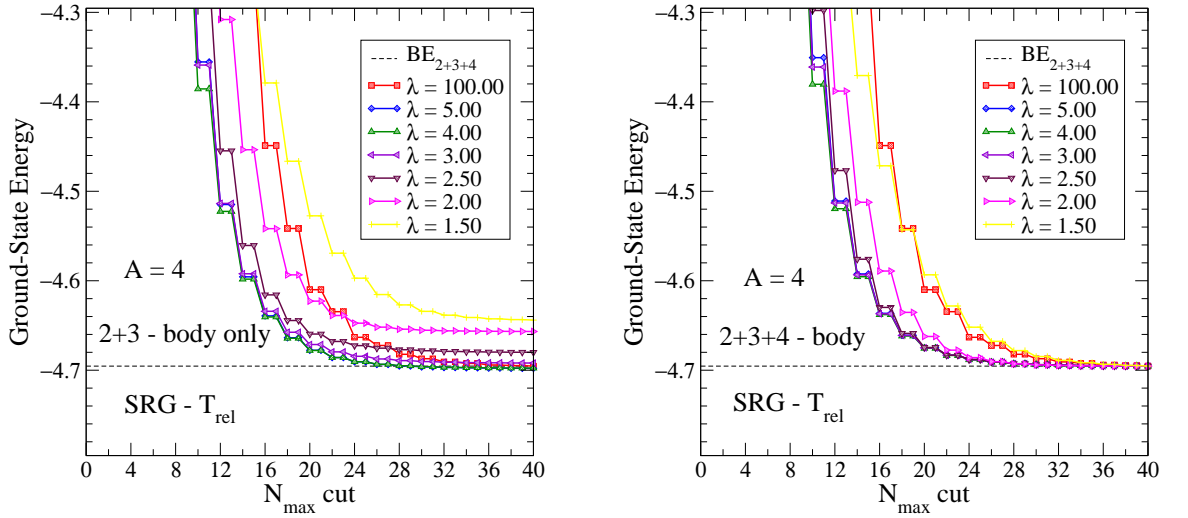


Figure 4.22: Decoupling in the four-particle system using  $G_s = T_{\text{rel}}$ . The initial  $V_\alpha$  potential is evolved to each  $\lambda$  shown in a basis with  $N_{\max} = 40$ . On the left only the two-body potential is evolved and embedded while the right involves the full unitarily transformed potential. Matrix elements of the potential are set to zero if one or both states have  $N > N_{\text{cut}}$  and the resulting Hamiltonian is diagonalized to obtain the ground-state energies plotted.

We note that the decoupling benefits afforded by evolution in the oscillator basis are less straightforward than in the two-body momentum basis studied for NN in [52]. In particular the cut-off errors *increase* for  $\lambda$  smaller than the point at which the two-body-only binding energy is at a minimum (i.e., for  $\lambda = 1.5$  in Fig. 4.21).



In the oscillator basis the Hamiltonian is not being driven towards a diagonal form by the choice  $G = T_{\text{rel}}$ , since it is not diagonal in this basis. In addition, the cuts made in the oscillator basis do not correspond to analogous cutting done to study decoupling in the momentum representation. However, control over cutting in the oscillator basis is the ultimate goal of the improved convergence in calculations with SRG evolution. Therefore, when working in the oscillator basis, one should look for a choice of  $G$  which optimizes the decoupling in that basis.

One possibility is the harmonic oscillator Hamiltonian,  $H_{\text{ho}}$ ,

$$H_{\text{ho}} = T_{\text{rel}} + \frac{1}{2}m\omega^2r^2 \quad (4.17)$$

which in the oscillator basis is simply a diagonal matrix with each state's value equal to  $N\hbar\omega$  for that state. Such a matrix is easy to build from the lists of state quantum numbers readily available from the oscillator basis code. This choice of  $G$  should drive the Hamiltonian to a diagonal form in the oscillator basis.

Figures 4.23 and 4.24 shows the decoupling analogous to Figs. 4.21 and 4.22, but now using  $G_s = H_{\text{ho}}$ . Here the SRG drives the Hamiltonian towards a form diagonal in  $N_{\text{max}}$  (and hence, energy), which is block diagonal in the oscillator basis. Again the calculation on the right has the full three-body (or four) Hamiltonian evolved before being cut to measure the convergence. Here, with  $G = H_{\text{ho}}$  evolution, there is no saturation effect in the increased convergence. Instead the convergence continues to steadily improve with decreasing  $\lambda$ . However, the plot on the left side of the figure has the two-body (two+three-body) Hamiltonian evolved before being embedded to the  $A = 3$  ( $A = 4$ ) space and cut for study. Here, as in the analogous  $T_{\text{rel}}$  evolution plot, we expect to see the asymptotic values of the different  $\lambda$  curves vary according to the missing induced three-body (four-body) forces. But in the  $H_{\text{ho}}$  evolution, the

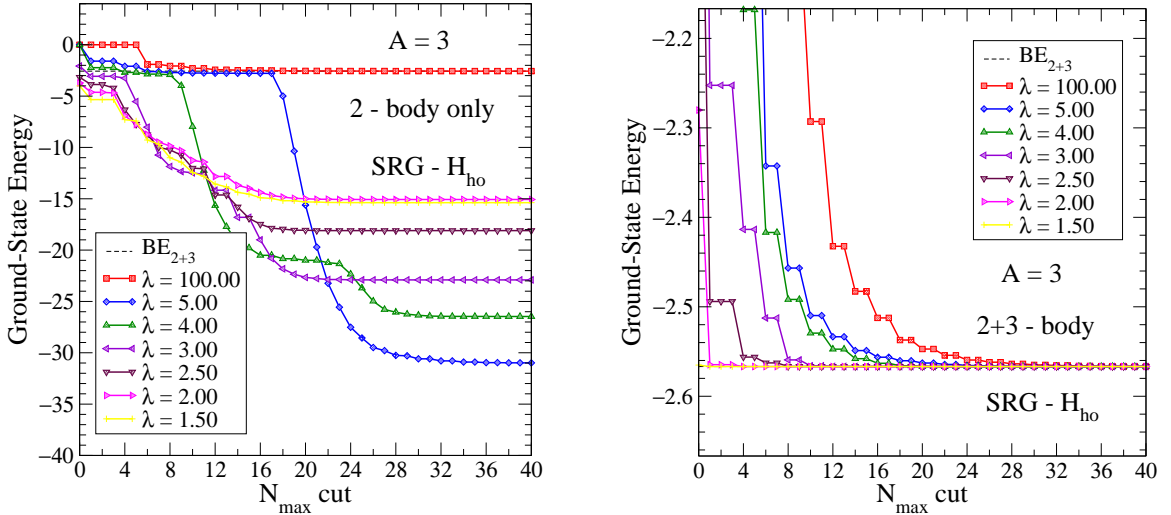


Figure 4.23: Decoupling in the three-particle system with  $G_s = H_{\text{ho}}$ . The initial  $V_\alpha$  potential is evolved to each  $\lambda$  shown in a basis with  $N_{\max} = 40$ . On the left only the two-body potential is evolved and embedded while the right involves the full unitarily transformed potential. Matrix elements of the potential are set to zero if one or both states have  $N > N_{\text{cut}}$  and the resulting Hamiltonian is diagonalized to obtain the ground-state energies plotted.

variance is dramatically larger, due to spurious bound states produced during the evolution of two-body (two+three-body) only matrix elements. These spurious states are a problem for the use of  $H_{\text{ho}}$  as the SRG generator and they are further explored in Appendix E.

In addition to the effects of the generator itself on the Hamiltonian, the method of cutting used here was applied directly from that used to study decoupling in the momentum basis. While cutting in  $N_{\max}$  is a variational technique it is not an exclusive test of high-low energy decoupling because a cut made in the oscillator basis imposes both IR and UV cutoffs while a cut in momentum space is simply a UV cutoff. Therefore the decoupling studies performed here in the oscillator basis cannot be directly connected to the decoupling studies of chapter 3. However, cutting in

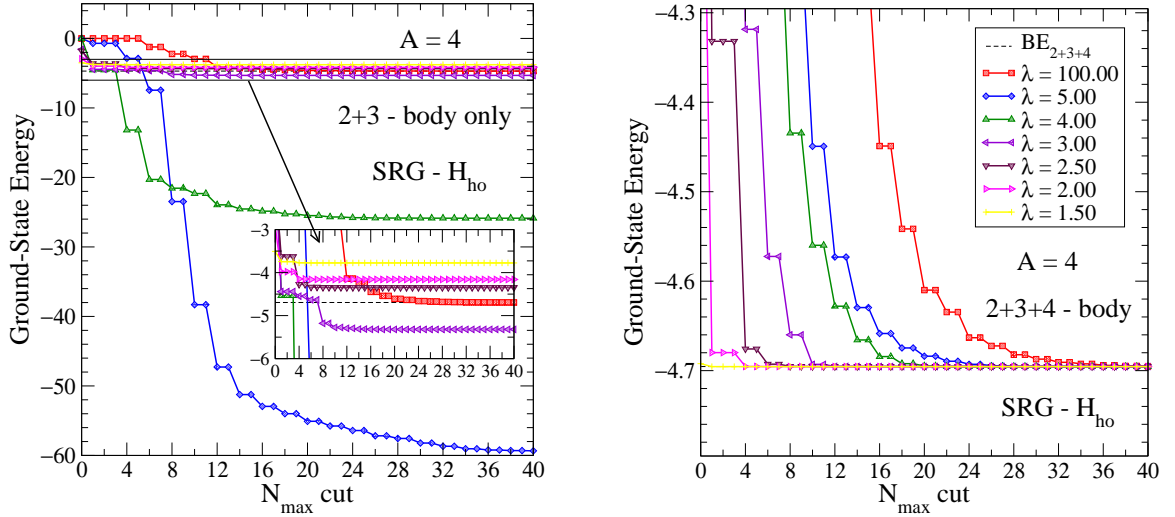


Figure 4.24: Same as for Fig. 4.23 but for the  $A = 4$  binding energy. On the left only the two+three-body potential is evolved and embedded while the right involves the full unitarily transformed potential.

$N_{\max}$  does establish the convergence with basis size and is a direct measure of success in the broader program of controlling resource requirements. The issue of oscillator space decoupling is further informed by the discussion on general oscillator basis features in appendix B.

## CHAPTER 5

### EVOLUTION OF MANY-BODY FORCES IN THE NO-CORE SHELL MODEL (NCSM)

Our calculations are performed in the Jacobi coordinate harmonic oscillator (HO) basis of the No-Core Shell Model (NCSM) [10], which is a direct extension of the one-dimensional oscillator basis built in chapter 4. This is a translationally invariant, anti-symmetric basis for each  $A$ , with a complete set of states up to a maximum excitation of  $N_{\max} \hbar\omega$  above the minimum energy configuration, where  $\omega$  is the harmonic oscillator parameter. Further details of the basis construction are explained in section C.5. Note that the realistic NCSM was built by Navrátil [10] and collaborators long before this thesis work. The work done here consisted of the code modifications necessary to implement the SRG. The procedures used here build directly on those of chapter 4 where we studied the convergence benefits of SRG evolution along with a general analysis of the evolving many-body hierarchy.

Just as in chapter 4 with the one-dimensional model, we start by evolving  $H_s$  in the  $A = 2$  space, which completely fixes the two-body matrix elements. Next, by evolving  $H_s$  in the  $A = 3$  space we determine the combined two-plus-three-body matrix elements. We can isolate the three-body matrix elements by subtracting the evolved two-body elements embedded in the  $A = 3$  basis. Having obtained the

Table 5.1: Definitions of the various calculations used to study SRG evolution.

NN-only	No initial NNN interaction and do not keep NNN-induced interaction.
NN + NNN-induced	No initial NNN interaction but keep the SRG-induced NNN interaction.
NN + NNN	Include an initial NNN interaction <i>and</i> keep the SRG-induced NNN interaction.

separate NN and NNN matrix elements, we can apply them to any nucleus with their appropriate combinatoric factors exactly as described in the one-dimensional case. We are also free to include any initial three-nucleon force in the initial Hamiltonian without changing the procedure. We summarize in Table 5 the different calculations to be made for  ${}^3\text{H}$  and  ${}^4\text{He}$  to confront these questions. If applied to  $A \geq 4$ , four-body (and higher) forces will not be included and so the transformations will be only approximately unitary for those nuclei. The question to be addressed is whether the decreasing hierarchy of many-body forces is maintained as observed in chapter 4 or the induced four-body contribution is unnaturally large.

If needed in the future, we could evolve 4-body matrix elements in  $A = 4$  and will do so when nuclear structure codes can accommodate them. The prospects for such work are straightforward. For  $A = 4$  the Jacobi NCSM used here can be modified to produce the necessary matrix elements for evolution by the SRG. These matrices are very large (see appendix D on basis scaling issues) and may require more sophisticated techniques for computing the many simultaneous differential equations involved in the evolution. Implementing these algorithms should be straightforward, though

computationally intensive. For  $A > 4$  we would have to implement the SRG in a different type of NCSM which uses single particle coordinates and Slater determinants to antisymmetrize the states. This scheme is also well developed and, due to its basis organization, easy to scale in  $A$  but accordingly computationally intensive.

The initial ( $\lambda = \infty$ ) NN potential used here is the 500 MeV N<sup>3</sup>LO interaction from Ref. [49]. The initial NNN potential is the N<sup>2</sup>LO interaction [67] in the local form of Ref. [69] with the additional LEC constants,  $c_D$  and  $c_E$ , fit to the average of triton and <sup>3</sup>He binding energies and to triton beta decay according to Ref. [70]. The values used here are  $c_D = -.205$  and  $c_E = .029$ . We expect similar results from other initial interactions because the SRG drives them toward near universal form [28]; a survey will be given in Ref. [71]. NCSM calculations with these initial interactions yield energies of  $-8.473(4)$  MeV for <sup>3</sup>H and  $-28.50(2)$  MeV for <sup>4</sup>He compared with  $-8.482$  MeV and  $-28.296$  MeV from experiment, respectively. So there is a 20 keV uncertainty in the calculation of <sup>4</sup>He from incomplete convergence (shown in the third decimal place - in parentheses) and a 200 keV discrepancy with experiment. The latter is consistent with the omission of three- and four-body chiral interactions at N<sup>3</sup>LO [72]. These provide a scale for assessing whether induced four-body contributions are important compared to other uncertainties.

It is remarkable how well the one-dimensional model predicts behavior in these three-dimensional calculations. Often serious qualitative differences appear between one- and three-dimensional systems. In this case several factors conspire to damp those differences. First, the three-dimensional potential is usually stated in a partial wave basis, which breaks up the three-vector information based on angular momentum states. So, when we work in a given partial wave, we are working with an effective

one-dimensional potential, one which we were able to successfully mimic in chapter 4. Secondly, and more central to this thesis, the SRG is a simple unitary transformation and its behavior is governed only by the qualitative structure of the matrices it is working to evolve, like the Hamiltonian and the generator. Qualitatively mimicking those, the outcome of SRG evolution will be predictive. This leaves us with a powerful analytic tool in the one-dimensional model of the NCSM to quickly explore other methods to improve many-body calculations beyond just SRG implementation.

## 5.1 Induced Many-Body Forces

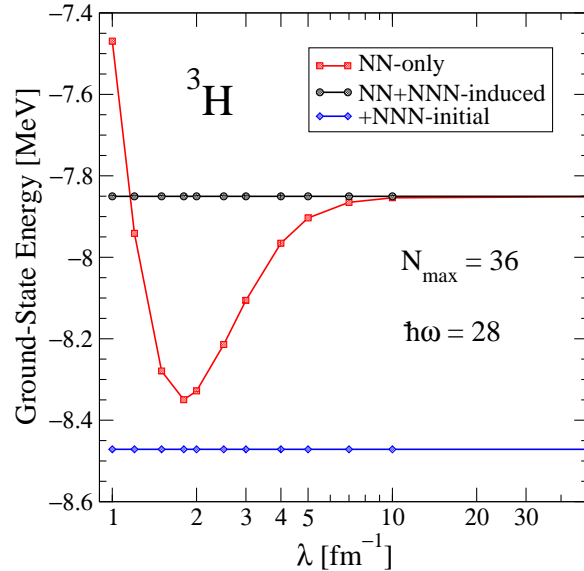


Figure 5.1: Ground-state energy of  ${}^3\text{H}$  as a function of the SRG evolution parameter,  $\lambda$ . See Table 5 for the nomenclature of the curves.

In Fig. 5.1, the ground-state energy of the triton is plotted as a function of the flow parameter  $\lambda$ . Evolution is from  $\lambda = \infty$ , which is the initial (or “bare”) interaction,

toward  $\lambda = 0$ . We use  $N_{\max} = 36$  and  $\hbar\omega = 28$  MeV, for which all energies are converged to better than 10 keV. We first consider an NN interaction with no initial NNN (“NN-only”). If the Hamiltonian is evolved only in an  $A = 2$  system, higher-body induced pieces are lost. The resulting energy calculations will only be approximately unitary for  $A > 2$  and the ground-state energy will vary with  $\lambda$  (squares). Keeping the induced NNN yields a flat line (circles), which implies an exactly unitary transformation; the line is equally flat if an initial NNN is included (diamonds). Note that the net induced three-body is comparable to the initial NNN contribution and thus is of natural size.

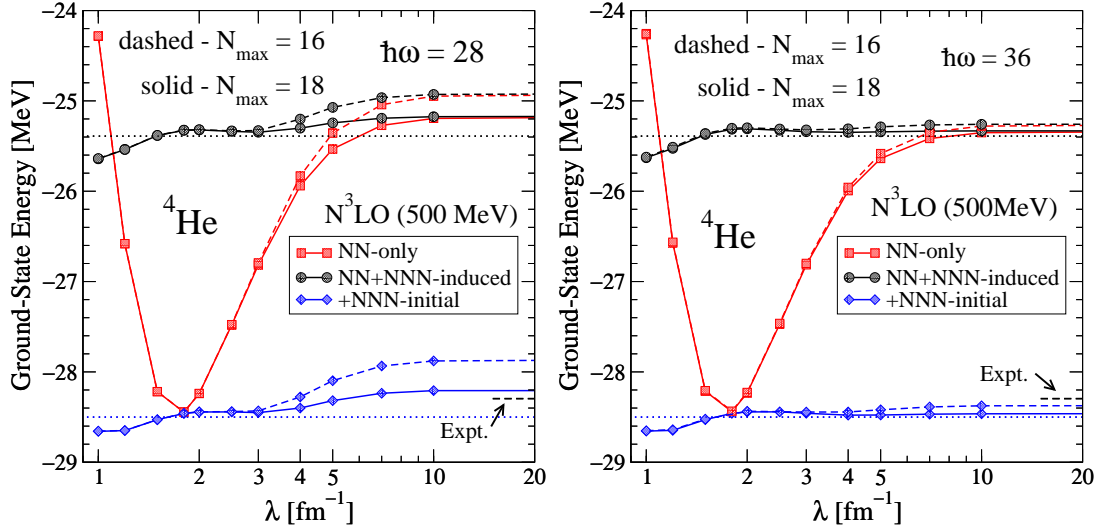


Figure 5.2: Ground-state energy of  ${}^4\text{He}$  as a function of  $\lambda$ . Two  $\hbar\omega$ s (left and right) and two  $N_{\max}$ ’s (overlaid) are shown for comparison.

In Fig. 5.2, we examine the SRG evolution in  $\lambda$  for  ${}^4\text{He}$  with  $\hbar\Omega = 36$  MeV. The two- and three-body matrix elements were evolved in  $A = 2$  and  $A = 3$  with  $N_{\max} = 28$  and then truncated to  $N_{\max} = 18$  (solid) and  $N_{\max} = 16$  (dashed) at each



$\lambda$  to diagonalize  ${}^4\text{He}$ . The NN-only curve has a similar shape as for the triton and when the induced NNN is included, the evolution is close to unitary, the deviation being an indication of the induced four-body force. The pattern only depends slightly on strength and type of an initial NNN interaction.

In both cases with and without an initial three-nucleon force, the dotted lines represent the converged values for their respective initial Hamiltonians. At large  $\lambda$ , the discrepancy is due to a lack of convergence at  $N_{\text{max}} = 18$ , (the level of truncation at this calculation) but by  $\lambda < 3 \text{ fm}^{-1}$  SRG decoupling takes over and the discrepancy is due to induced four-body forces. This is illustrated nicely by the overlay which shows that, for  $\lambda < 3 \text{ fm}^{-1}$ , cutting from  $N_{\text{max}} = 18$  to  $N_{\text{max}} = 16$  introduces no more basis truncation errors, where above  $\lambda = 3 \text{ fm}^{-1}$  there is a significant truncation effect just from 18 to 16. This indicates that the SRG has achieved convergence well inside an  $N_{\text{max}} = 16$  basis for this calculation.

Also, in Fig. 5.2 are shown the same overlay comparison for two  $\hbar\omega$  values, that which is optimal for the initial Hamiltonian to compute  ${}^4\text{He}$  ( $\hbar\omega = 36$ ) and one that is nearer the optimal for that potential evolved to  $\lambda = 2 \text{ fm}^{-1}$  as expected from previous SRG studies. We can see the same converged results at low  $\lambda$  in both  $\hbar\omega$ 's despite the different bare answer. This is consistent with being well converged and thus flat in  $\hbar\omega$ .

The induced four-body forces then make up the difference to the converged value and contribute about 50 keV net at  $\lambda = 2 \text{ fm}^{-1}$ . This is small compared to the rough estimate in Ref. [72] that the contribution from the long-ranged part of the N<sup>3</sup>LO four-nucleon force to  ${}^4\text{He}$  binding is of order a few hundred keV. If needed, we could

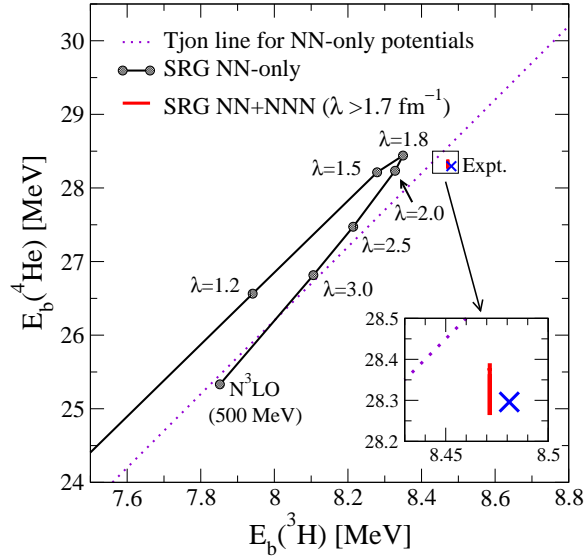


Figure 5.3: Binding energy of the alpha particle vs. the binding energy of the triton. The Tjon line from phenomenological NN potentials (dotted) is compared with the trajectory of SRG energies when only the NN interaction is kept (circles). When the initial and induced NNN interactions are included, the trajectory lies close to experiment for  $\lambda > 1.7 \text{ fm}^{-1}$  (see inset).

evolve 4-body matrix elements in  $A = 4$  and will do so when nuclear structure codes can accommodate them.

The impact of evolving the full three-body force is neatly illustrated as a Tjon plot in Fig. 5.3, where the binding energy of  $^4\text{He}$  is plotted against the binding energy of  $^3\text{H}$ . The experimental values of these quantities are known to a small fraction of a keV and define only a point in this plane (at the center of the X, see inset). The well-known Tjon line (dotted) is the approximate locus of points for phenomenological potentials fit to NN data but not including NNN [73]. The SRG NN-only results trace out a trajectory in the plane that is analogous as it transforms NN forces unitarily but cannot account for the evolving 3NFs in the  $A = 2$  space. In contrast, the short trajectory of the SRG when including the induced NNN interaction (shown

for  $\lambda \geq 1.8 \text{ fm}^{-1}$ ) highlights the small variations from the omitted four-nucleon force. Note that a trajectory plotted for NN+NNN-induced calculations would be a similarly small line at the N<sup>3</sup>LO NN-only point where the initial NNN is zero.

## 5.2 Convergence in $N_{\text{max}}$ : $G = T_{\text{rel}}$

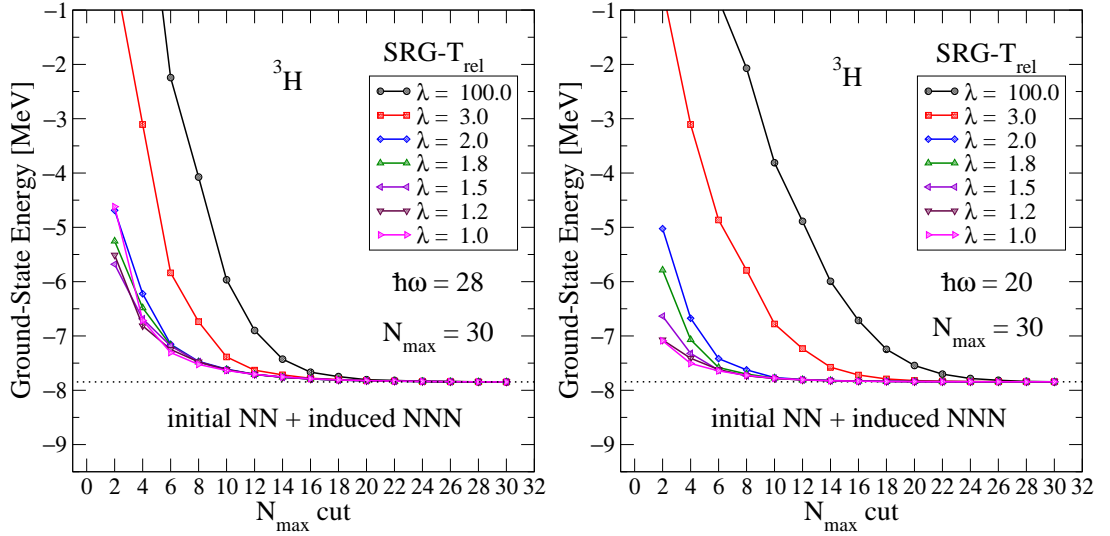


Figure 5.4: Ground-state energy of  ${}^3\text{H}$  as a function of the basis size  $N_{\text{max}}$  for an N<sup>3</sup>LO NN interaction [49] evolved with the SRG using  $G_s = T_{\text{rel}}$  to selected  $\lambda$ 's. The same calculation is shown at two values of  $\hbar\omega$ .

Figure 5.4 shows the convergence properties of the three-body Hamiltonian as it evolves. The initial interaction used here is an N<sup>3</sup>LO NN potential [49] with no initial NNN. The figure shows the same plot for two different  $\hbar\omega$ 's. On the left is  $\hbar\omega = 28 \text{ MeV}$  which is the optimal value for the initial interaction, and on the right is the same plot for  $\hbar\omega = 20 \text{ MeV}$  which is more optimal for significantly evolved potentials (i.e., those evolved to  $\lambda = 2.0 \text{ fm}^{-1}$ ). The calculations are performed by first evolving the initial Hamiltonian in the three-body space to the  $\lambda$  indicated then

truncating the potential at each  $N_{\max}$ -cut by setting matrix elements to zero above the extent of that  $N_{\max}$ -cut. The curve for  $\lambda = 100 \text{ fm}^{-1}$  is essentially unevolved and is approximately equivalent to the initial interaction.

Notice two major features as the initial Hamiltonian is evolved down from  $\lambda = 100 \text{ fm}^{-1}$ . First, the converged value at each  $\lambda$  is the same - the evolution is unitary. As the SRG evolves the Hamiltonian in the three-body basis, it evolves the two-body matrix elements just as in the  $A=2$  basis, but to keep the transformation unitary it must induce three-body forces to account for the high-momentum information it has transformed. These induced three body forces have been kept in the calculation of Fig. 5.4 and hence the ground-state energy is preserved by the transformation. Secondly, the convergence in  $N_{\max}$  improves as  $\lambda$  decreases down to some saturation point. The SRG is suppressing the coupling between states of large and small  $N_{\max}$ . Here we have made the choice of generator  $G_s = T_{\text{rel}}$ , which was diagonal in the momentum representation, and should afford the same decoupling benefits it did there. However, in the oscillator basis,  $T_{\text{rel}}$  has both a diagonal piece and a slightly off-diagonal piece that couples states at  $N_{\max}$  and  $N_{\max} + 2$ <sup>18</sup>. So in this basis the convergence saturates as the Hamiltonian evolves toward the shape of  $T_{\text{rel}}$  and retains a certain amount of coupling. However, the evolution is itself basis independent and this apparent coupling is really due to the structure of the oscillator basis and the way we are required to cut it. Converting these Hamiltonians back to the momentum representation (or working there in the first place) should return to the situation where the potential asymptotically approaches the diagonal. Work along these lines is in progress [37].

<sup>18</sup>see Eq. (C.18) for an example of this in the one-dimensional basis and a sample picture of  $T_{\text{rel}}$  can be found in Fig. E.1.

The situation is already improved from the left panel to the right due to a more optimal value of  $\hbar\omega$  for the evolved Hamiltonians. The point of saturation is as far down as  $\lambda = 1.0 \text{ fm}^{-1}$ . One would like to optimize each point on this plot in  $\hbar\omega$ . Since each combination of  $N_{\text{max}}$  and  $\hbar\omega$  represents a considerable amount of computation, a useful tool would be a simple orthogonal transformation of the Hamiltonian from one value of  $\hbar\omega$  to another without building up a separate basis for each parameter set. Until such a tool is coded and tested, the alternative is to work at sufficiently large  $N_{\text{max}}$  that the energy is converged and relatively flat in (insensitive to)  $\hbar\omega$ . This would result in a curve that may be less smooth and harder to extrapolate but still variational, converging at the large- $N_{\text{max}}$  and optimal  $\hbar\omega$  for the bare potential.

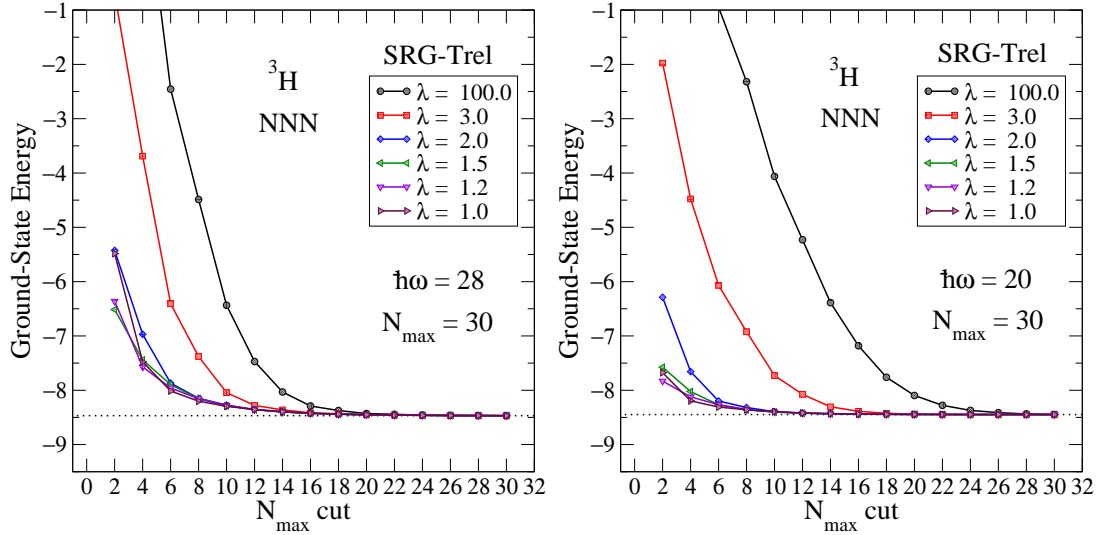


Figure 5.5: Ground-state energy of  ${}^3\text{H}$  as a function of the basis size  $N_{\text{max}}$  for an N<sup>3</sup>LO NN interaction [49] plus an initial NNN interaction [70, 74] evolved with the SRG using  $G_s = T_{\text{rel}}$  to selected  $\lambda$ s.

The initial Hamiltonians used in Fig. 5.4 are NN-only, so to increase the accuracy in calculating observables we must include initial three-body forces in our inputs. One

may be concerned that the exact form of any initial three-body forces will affect the form of the three-body forces induced to maintain unitarity. This question is tested in Fig. 5.5 which repeats the calculation of Fig. 5.4 but now including an initial NNN force at N<sup>2</sup>LO from Ref [67] as stated at the beginning of the chapter. We note that the shapes of the convergence curves in both figures are identical, indicating that the induced three-body forces are of natural size and are insensitive to the details of any initial three-body forces. Therefore the SRG is insensitive to the particulars of a given interaction, which is consistent with the observation that different Hamiltonians evolve to a near universal form.

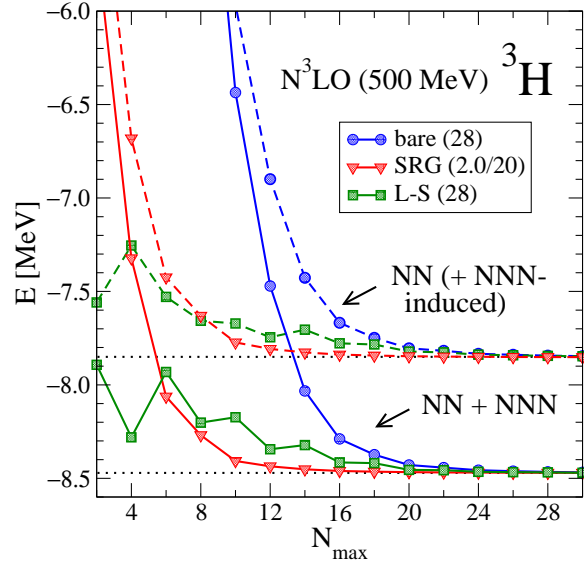


Figure 5.6: Ground-state energy of  ${}^3\text{H}$  as a function of the basis size  $N_{\text{max}}$  for an N<sup>3</sup>LO NN interaction [49] with and without an initial NNN interaction [70, 74]. Unevolved (“bare”) and Lee-Suzuki (L-S) results with  $\hbar\Omega = 28$  MeV are compared with SRG at  $\hbar\omega = 20$  MeV evolved to  $\lambda = 2.0$  fm<sup>-1</sup>.

In Fig. 5.6, we again show the triton ground-state energy as a function of the oscillator basis size,  $N_{\text{max}}$ , to make a comparison between various calculations. The

lower, solid (upper, dashed) curves are with (without) an initial three-body force (see Table 5). The convergence of the bare interaction is shown along with the SRG evolved to  $\lambda = 2.0 \text{ fm}^{-1}$ . The oscillator parameter  $\hbar\omega$  in each case was chosen roughly to optimize the convergence of each Hamiltonian. Here, we compare to a Lee-Suzuki (L-S) effective interaction, which has been used in the NCSM to greatly improve convergence [75, 76]. These effective interactions consist of a block-diagonal type unitary transformation to achieve an effective interaction in the oscillator basis at low  $N_{\text{max}}$ . The resultant matrix is dependent on the model space of a given nucleus in contrast to the free-space nature of the SRG. Notice that the L-S effective interactions are not variational in  $N_{\text{max}}$  due to their model dependence and therefore it is difficult to extrapolate their behavior.

The SRG calculations are variational and converge smoothly and rapidly from above with or without an initial three-body force. The dramatic improvement in convergence rate is seen even though the  $\chi\text{EFT}$  interaction is relatively soft. Thus, once evolved, a much smaller  $N_{\text{max}}$  basis is adequate for a desired accuracy and extrapolating in  $N_{\text{max}}$  is also feasible.

Figure 5.7 illustrates for  ${}^4\text{He}$  the same rapid convergence with  $N_{\text{max}}$  of an SRG-evolved interaction. Here we show results in two different  $\hbar\omega$ 's (in parenthesis) for a Lee-Suzuki calculation, and Hamiltonians evolved to  $\lambda = 2.0 \text{ fm}^{-1}$  and  $\lambda = 1.5 \text{ fm}^{-1}$ . We can see the rapid convergence both in the main plot and more clearly in the inset. It is again smooth and variational despite being an approximately unitary calculation for this sector. In this case the asymptotic value of the energy differs slightly because of the omitted induced four-body contribution. The SRG-evolved asymptotic values for different  $\hbar\omega$  differ by less than 10 keV, so the gap between the

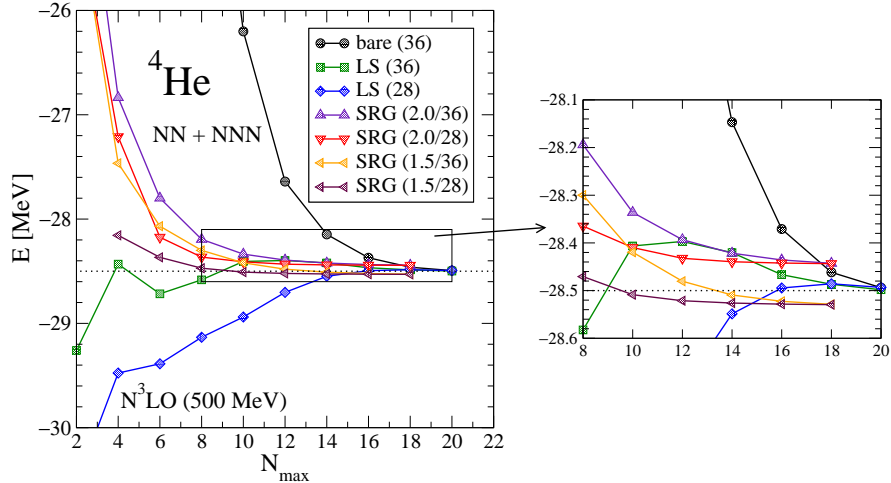


Figure 5.7: Ground-state energy of  ${}^4\text{He}$  as a function of the basis size  $N_{\text{max}}$  for an  $N^3\text{LO}$  NN interaction [49] with an initial NNN interaction [70, 74]. Unevolved (bare) results are compared with Lee-Suzuki (L-S) and SRG evolved to  $\lambda = 2.0 \text{ fm}^{-1}$  at  $\hbar\omega = 28$  and  $36 \text{ MeV}$ .

converged bare/L-S results and the SRG results is dominated by the induced four-nucleon forces rather than incomplete convergence. Convergence is even faster for lower  $\lambda$  values [71], ensuring a useful range for the analysis of few-body systems. The induced four body forces here are about 30-60 keV, which is less than the 200 keV discrepancy with experiment considered to be due to the omission of initial 4NFs from  $\chi\text{EFT}$ . However, because of the strong density dependence of four-nucleon forces<sup>19</sup>, it will be important to monitor the size of the induced four-body contributions for heavier nuclei and nuclear matter. It may be necessary to evolve unitarily in the four-body space to include induced four-body forces, and even initial  $\chi\text{EFT}$  terms in this sector. However, it is doubtful that higher body forces ( $A > 4$ ) will be significant given the strong four particle clustering nature of larger nuclei.

<sup>19</sup>This follows from the power-counting of the  $\chi\text{EFT}$  lagrangian. The coupling constant must have one more power of  $\Lambda^{-3}$ , or density, due to the extra factor of  $N^\dagger N$ .



### 5.3 Convergence in $N_{\max}$ : $G = H_{\text{ho}}$

As shown in Figs. 5.4 and 5.5 the choice of SRG generator,  $G_s = T_{\text{rel}}$ , is not the most efficient choice in the harmonic oscillator basis. Due to the organization of the states and their complicated momentum dependence,  $T_{\text{rel}}$  is not diagonal in this basis and therefore cannot be expected to completely diagonalize the Hamiltonian. We can make a different choice of generator, as already mentioned in chapter 4,  $G_s = H_{\text{ho}}$ , the harmonic oscillator Hamiltonian. This choice is diagonal in the oscillator basis, having the eigenvalues  $E_n = (N_{\max} + 3/2)\hbar\omega$  of each state along the diagonal. In this section we check, in the three-dimensional case, the behavior of this choice of  $G_s$ .

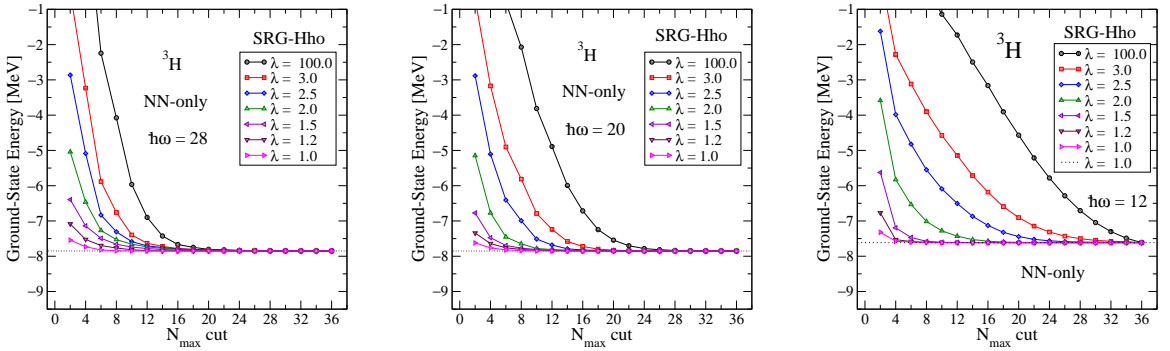


Figure 5.8: Ground-state energy of  ${}^3\text{H}$  as a function of the basis size  $N_{\max}$  for an evolving  $\text{N}^3\text{LO}$  NN interaction [49] without an initial NNN interaction. Three values of oscillator parameter,  $\hbar\omega = 28, 20,$  and  $12$  MeV are shown for comparison.

Figure 5.8 shows the analog of Fig. 5.4 but using  $H_{\text{ho}}$  as the generator. We see, just as in the one-dimensional case, that the convergence improvement does not saturate at a specific point in the evolution but keeps improving as the SRG evolves it further towards the diagonal in the oscillator basis. On the left and center are  $\hbar\omega = 28$  MeV, optimal for the unevolved Hamiltonian, and  $\hbar\omega = 20$  MeV for comparison to

the  $T_{\text{rel}}$  case. The optimal  $\hbar\omega$  for  $H_{\text{ho}}$ -evolved potentials has not been fully explored for specific  $\lambda$ 's, though given the amount of increased convergence it is likely to shift further. We can see in the center panel with  $\hbar\omega = 20$  the convergence is not improved by the same proportions as it was between the  $T_{\text{rel}}$  plots, but on the right we show an even smaller value,  $\hbar\omega = 12$ , than was used for  $T_{\text{rel}}$ . Here we see more improvement in the convergence with a more optimal  $\hbar\omega$  for evolved potentials. However, at  $\hbar\omega = 12$  we start with a less optimal oscillator representation of the Hamiltonian and therefore converge to an under-bound value. Again, this is where a  $\hbar\omega$  switching tool would come in useful as discussed in the last section. The  $\hbar\omega$  dependence would of course have to be tested for each value of  $\lambda$  as discussed in Appendix C. In Fig. 5.9 we show again that the specifics of the initial three-body force do not alter the qualitative pattern of evolution.

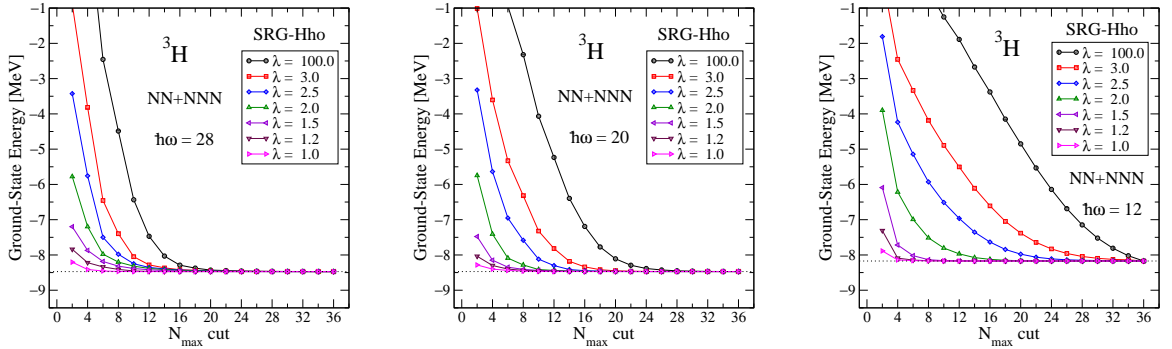


Figure 5.9: Same as in Figure 5.8 but now including the initial NNN force [70, 74]. Note the qualitative form of convergence is not affected.

Unfortunately, the same spurious states appear here in the approximately unitary calculations as did in the one-dimensional version of  $G_s = H_{\text{ho}}$ , leaving concern about the renormalization by unnatural operators. Specifically,  $H_{\text{ho}}$  contains the long-range

operator  $r^2$  which is not present in the Hamiltonian and therefore one might expect it to induce unnaturally large components in various parts of the Hamiltonian as it tries to cancel spurious  $r^2$  physics. On the other hand the choice  $G_s = T_{\text{rel}}$  does not improve convergence very well for long ranged operators like, in fact,  $r^2$  while the  $H_{\text{ho}}$  SRG does. The focus of present investigations [42] has been to consider a hybrid  $G_s$  of the form

$$G_s = T_{\text{rel}} + \alpha r^2 \quad (5.1)$$

that is essentially  $T_{\text{rel}}$  but incorporates a small admixture of the  $r^2$  operator to renormalize long distance operators without contaminating the Hamiltonian's flow. This work has progressed well in the one-dimensional model, and the prospects are promising for such a hybrid  $G_s$  to renormalize both long and short distance operators without inducing large spurious many-body forces. Calculations to verify this behavior in three-dimensions have been slowed by coding complications that will be resolved soon.

## 5.4 Radius Calculations

In addition to binding energies, we would like to understand how the SRG affects other observables, especially long-ranged ones like the root mean square radius,

$$r_{\text{rms}} = \sqrt{\langle \phi_0 | \frac{1}{A} \sum_{i=1}^A (x_i - x_{\text{cm}})^2 | \phi_0 \rangle}, \quad (5.2)$$

where  $|\phi_0\rangle$  is the ground-state wavefunction of the  $A$ -body system,  $x_i$  are the single particle coordinates, and  $x_{\text{cm}}$  is the center of mass coordinate. To obtain  $r_{\text{rms}}$  in terms of Jacobi coordinates we can use the identity [66]

$$A \sum_{i=1}^A (x_i - x_{\text{cm}})^2 \equiv \sum_{j>i=1}^A (x_i - x_j)^2 = \binom{A}{2} (2r_1^2), \quad (5.3)$$

where the  $x_i$  are single particle coordinates and  $r_1$  is the first Jacobi coordinate. The second equality results from our definitions of the Jacobi coordinates and the fact that we are working in a symmetrized basis. This replaces the sum by a multiplicative factor, the total number of pairs in the  $A$ -body system.

This calculation is performed directly within the three-dimensional NCSM code. We can evolve a two-body Hamiltonian and then use the code to compute  $r$  for  ${}^3\text{H}$  or  ${}^4\text{He}$ , and we can also evolve the three-body and embed it to compute  $r$  for  ${}^4\text{He}$ . As of this writing however, complications with the NCSM code have prevented us from producing the unitarily evolved version. We cannot yet evolve  $A$ -body forces and compute  $r$  for the  $A$ -body nucleus. So, the pictures in the figures for  ${}^3\text{H}$  and  ${}^4\text{He}$  are missing the induced three- and four-body forces respectively. This is of high priority in the near future.

In Fig. 5.10 we show the proton rms radius of the triton as a function of  $N_{\max}$  for two values of  $\hbar\omega$ , 20 and 28 MeV (top and bottom). We plot several values of  $\lambda$  along with the bare and Lee-Suzuki effective interaction for comparison. Note the poor convergence in basis size. Unfortunately, evolution with the SRG does not significantly improve convergence for this long ranged quantity, though when comparing the two values of  $\hbar\omega$  the convergence is improved from 28 to 20 MeV.

In Fig. 5.11 we show the same radius calculation for  ${}^4\text{He}$  but for three  $\hbar\omega$ 's from left to right 20, 28, and 36 MeV, which are optimal values for the evolved and bare Hamiltonians respectively. Here both NN-only and NN+NNN-induced calculations are shown, but again the full unitary evolution calculation (including induced four-body forces) is not yet available. Again there is some improvement in convergence for lower values of  $\hbar\omega$ . Those bases have a lower infrared cutoff,  $\Lambda_{\text{IR}}$ , and thus keep more

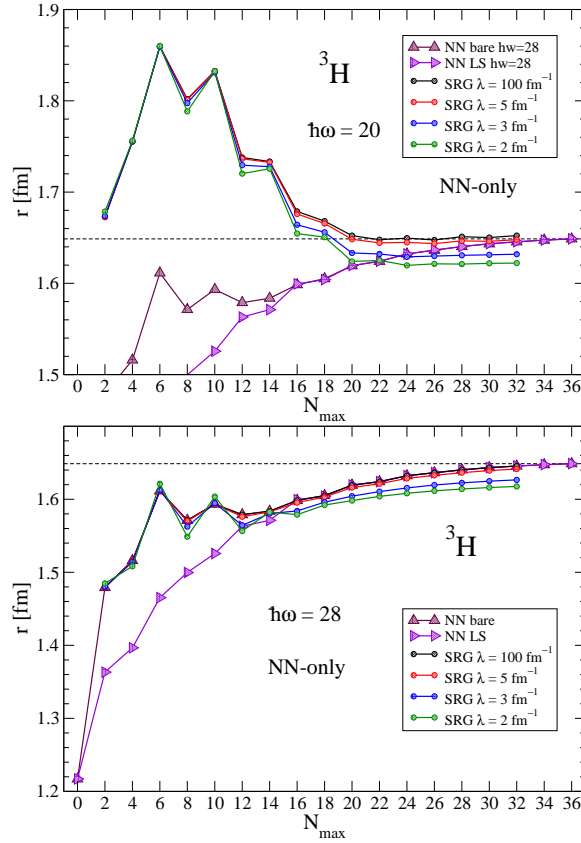


Figure 5.10: The  ${}^3\text{H}$  radius as a function of basis size  $N_{\max}$  for two choices of  $\hbar\omega$ , 20, and 28 MeV, corresponding to the optimal values for the bare and some evolved Hamiltonians. The straight dashed line indicates the best converged value at the optimal  $\hbar\omega$  (28 MeV) for the LS effective potential at  $N_{\max} = 36$ .

long-distance information. Decoupling due to the SRG is then more beneficial to the convergence of the radius calculation. Unfortunately, the ultraviolet cutoff,  $\Lambda_{\text{UV}}$ , is also lower and limits the accuracy of the converged binding energy, in turn limiting the accuracy of the radius. The black and red solid curves at  $\hbar\omega = 20$  approach the converged value much slower than at 28 or 36. At the same time, the green and blue curves are better converged (to the wrong value) at  $\hbar\omega = 20$ . Of course, a higher  $N_{\max}$  would help the situation by pushing  $\Lambda_{\text{IR}}$  down and  $\Lambda_{\text{UV}}$  up.

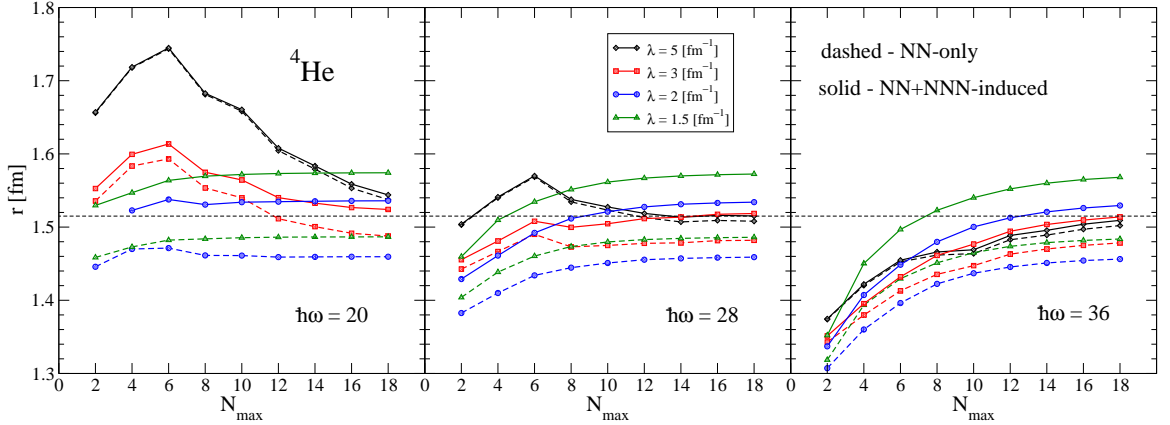


Figure 5.11: The  ${}^4\text{He}$  radius as a function of basis size  $N_{\text{max}}$  for three choices of  $\hbar\omega$ , 20, 28, and 36 MeV (corresponding to the optimal values for the bare and some evolved Hamiltonians). The solid lines are calculations that include induced NNN forces. The dashed lines are NN-only calculations. The straight dashed line indicates the best converged value at the optimal  $\hbar\omega$  (36 MeV) for the LS effective potential at  $N_{\text{max}} = 20$ .

Also, notice in Fig. 5.11 the spread in converged value (at  $N_{\text{max}} = 18$ ) as a function of  $\lambda$ . Here we present the bare operator acting on the evolved four-body wavefunctions. Not only are the effects of induced three- and four-body forces on the wavefunction contributing to the spread, but the evolution of the operator, necessary to preserve unitarity in this calculation, is not included. At  $\hbar\omega = 20$ , this seems to be a much bigger effect than that of the three- and four-body parts the evolved wavefunction, considering a lack of any clear hierarchy between the intervals from the NN-only to the NN+NNN-induced and the NN+NNN-induced to the converged value. At the higher  $\hbar\omega$ 's, the  $r^2$  operator is evolved much less though the converged value is more accurate. Here the three- and four-body hierarchy in the wavefunction is more evident.

As discussed in the previous section, a possible strategy around this has focused on using a hybrid generator,  $G_s = T_{\text{rel}} + \alpha r^2$ , where  $\alpha$  is a constant determining the mixture of the two terms. With this choice, one hopes to balance the renormalization of short- and long-range parts of the potential and increase convergence for all operators [42]. Results of this work in one-dimension are promising with regard to the ability to tune the SRG to given operators and basis structure. As noted in several places, progress in the three-dimensional code has been slowed by coding issues. Most of these relate to the same technical issue of explicitly building the  $r^2$  operator in the NCSM basis. Upon resolution of this problem, many more calculations will become available quickly.

It must be stressed that difficulties in finding an optimal SRG generator stem not from the SRG itself, but from the particular basis we have been working in. The harmonic oscillator basis is convenient to work in, both because it is variational in two parameters with straightforward cutoff implications, and because the center of mass separates trivially from the calculations. However, it is not the best choice for describing certain physical properties, especially long-ranged operators. The oscillator functions simply do not have the same fall-off as an operator like  $r^2$ . Other bases that may prove useful to this work include hyper spherical harmonics, and a basis of correlated gaussians as used in the Stochastic Variational Method (SVM) [64]. These bases should be more efficient at resolving long-distance observables, such as nuclear radii, and the choice of SRG generator may not be as constrained. However, work using these bases has not been as developed as that of the NCSM, especially work to implement the SRG, but progress is on the horizon.

## CHAPTER 6

### CONCLUDING REMARKS

#### 6.1 Recapitulation

For many decades progress in nuclear structure theory has been hampered by the complexity of the nuclear interaction. A strong repulsive core, significant tensor force, and poorly understood many-body forces have all contributed to difficulty in accurately calculating nuclear observables consistently. These features are associated with high-momentum/short distance structure of the nuclear interaction, the details of which are irrelevant to the low-energy structures of bound nuclear systems. More precisely, infinitely many different choices of high-energy details can produce the same low-energy results. The difficulty in many-body calculations stems from the fact that high- and low-energy states are coupled. These coupling matrix elements of the potential require an increased basis size to represent the relevant low-energy physics. Such extra size increases dramatically with the number of particles in the system under consideration. This situation is ripe for a method, such as the SRG, that damps high-energy details without adverse effects to the physics relevant to low-momentum interactions.



In recent years many inroads have been made into the problem of expensive computation being spent on irrelevant interaction components. Foremost is the development of  $\chi$ EFT's, a model independent formulation of pion exchange interaction theory in the mold of Yukawa, but now informed by the underlying principles of QCD. Among its successes, these potentials are able to parametrize many-body forces consistently and robustly with controlled errors at each order. However, while they are much softer than their phenomenological predecessors, they are still computationally expensive for computing all but the lightest nuclei. Also of note is the  $V_{\text{low } k}$  renormalization technique, which has provided a proof of principle that one can unitarily transform a given potential to decouple the irrelevant high-momentum degrees of freedom and retain the relevant physics inside a smaller space. However, this technique has not left a clear path to the consistent treatment of many-body forces inherent in the  $\chi$ EFT (or any other) potential on which it is used.

The Similarity Renormalization Group has proved to be a powerful tool for addressing the above general problems. Its flowing unitary transformations leave the input physics unaffected while transforming the potential to a softened form. Implementation of the SRG is simple in any basis and on any given free-space Hamiltonian while allowing freedom of choice as to the general form of the flow operators. Furthermore, the SRG provides a self-consistent treatment of many-body forces easily understood in either first or second quantized forms. It has been demonstrated to be robust in its scaling of both evolution times and residual errors. With these features, the SRG is well suited to address the needs of the nuclear structure community.

The predominant improvement provided by SRG evolution of a given potential is the decoupling between low- and high-energy states in the two-nucleon (NN) interaction as explored in chapter 3. The degree of decoupling achieved by evolution is studied by measuring errors induced by an arbitrary cutoff on evolved potentials. In this way we can see the clean perturbative scaling of the residual coupling above a given amount of evolution denoted by the momentum scale  $\lambda$  or  $s = 1/\lambda^4$ . Decoupling in the two-body sector was found to propagate universally to many-body calculations and was checked explicitly for few-nucleon systems. In addition, an investigation into the behavior of other SRG forms, set by the choice of the generator  $G_s$ , showed no significant impact on the general decoupling properties expected at a given  $\lambda$ .

The formal discussion in section 3.2 shows that, in principle, the same mechanism of decoupling also improves the convergence properties of the three-body (and higher) forces in an appropriate three-body ( $A$ -body) basis. In addition the SRG induces three-body forces to account for the changes in the two-body potential and keep the evolution fully unitary in the three-body system. In fact, it induces  $A$ -body forces in an  $A$ -particle space and we must verify that these induced forces can be controlled in order for the two-, three-, and four-body evolved potentials to be useful to many-body calculations.

These issues were explored in chapter 4 through the use of a one-dimensional model in a symmetrized harmonic oscillator basis inspired by the highly successful No-Core Shell Model. We demonstrated that the induced three-body forces were as large as expected from previous calculations, and that induced four- and higher-body forces exhibited a hierarchy of decreasing importance. We covered several other topics relevant to realistic calculations such as the convergence properties of the three-body

evolution, the possibility of fitting omitted induced forces (thereby avoiding an explicit evolution in a higher-body space), and evolution of external operators involved in scattering processes. All of these calculations serve to build experience and intuition for the realistic three-dimensional case where angular momentum and other details complicate the calculations.

In chapter 5 we achieved the first evolution of realistic three-body forces using the antisymmetrized Jacobi harmonic oscillator basis of the No-Core Shell Model. Here we duplicated the calculations tested in one-dimension, showing induced three- and four-body forces as a function of the evolution parameter,  $\lambda$ , and studied the improved convergence in  ${}^3\text{H}$  and  ${}^4\text{He}$  energies due to the decoupling achieved in the three-body basis. The same hierarchy of induced forces was exhibited here. We also took a look at a long-range observable, the rms radius of these nuclei, to extend work being done by others in one dimension.

Our experience from the 1D calculations guided progress rapidly and that model continues to be a testing ground for new calculations. All the features of many-body evolution observed in the one-dimensional case were born out semi-quantitatively with the realistic interactions. For instance, all of the induced three- and four-body forces were in the same proportions to those in one-dimension. Often one is wary of trusting the results of a model calculation in one dimension to provide qualitative predictions of three-dimensional physics. Here, the basis structure is very similar to that of the three-dimensional problem which is already broken up in a partial-wave expansion. The SRG is only affected by the general form of the matrices, Hamiltonians and kinetic energies, involved in its flow.

## 6.2 Plans for Future Investigations

A broad range of topics should be considered, or reconsidered, in light of the advantages presented by the Similarity Renormalization Group. Here we discuss a few of the most pressing issues.

While this thesis has shown the induced many-body forces to follow a decreasing hierarchy in many-body calculations, they will continue to be a source of error in all sectors from light nuclei all the way up to nuclear matter. Interactions evolved in a three- or four-nucleon basis are unitarily equivalent for their respective nuclei. However, the use of those potentials, embedded to higher-body spaces, is complicated by the  $A$ -body forces that were not induced in the evolution at a lower space. For example, in chapter 5 results showing increased convergence in  ${}^4\text{He}$  also show a small variability, with  $\lambda$ , in the converged value. This cutoff dependence is small in this calculation, smaller than the error with respect to the experimental value, but that space is only one nucleon higher than that in which the SRG was applied. More calculations are needed to test how much the cutoff dependence will be reduced by including just the induced three- and four-body forces.

A first priority to achieve calculations of larger nuclei is to make the  $A = 3$  evolved potentials available in a usable form to those groups who can perform calculations of larger nuclei. The coupled cluster community uses the single-particle Slater determinant basis to perform their calculations. They have so far achieved much success pushing the boundaries of their calculations with NN-only evolved potentials, reaching as high as  ${}^{56}\text{Ni}$ . Likewise, NCSM calculations which use the Slater determinant basis can also reach much higher nuclei and would be complementary calculations. Codes already exist to convert the matrix elements in the Jacobi basis used here

to the Slater determinant basis, or “m-scheme”, so progress on this front should be rapid.

While induced many-body forces in all sectors will be a source of error, this thesis has shown them to follow a decreasing hierarchy in many-body calculations. To avoid applying SRG evolution in increasingly large  $A$ -body bases, one might control the cutoff dependence by fitting the omitted induced forces to terms inspired by the  $\chi$ EFT expansion. An implementation of this idea was made in chapter 4 with encouraging results and further progress should come easily. Through such a fitting program the pattern of induced many-body forces may even lend itself to extrapolation and increased control on the errors present in approximately unitary calculations.

Another avenue currently under development to test the viability of SRG evolved interactions in larger nuclear systems is to calculate nuclear matter properties using the Hartree-Fock approximation. Here the SRG is applied in the second quantized form demonstrated in section 2.2. Instead of evolving the free-space interaction, the SRG is applied in the medium where normal ordering has different consequences with respect to the induced many-body forces. The induced many-body forces can then be controlled in a qualitatively different way than the free-space calculations.

As mentioned previously the major goal of the UNEDF collaboration is the development of a density functional for nuclei which incorporates microscopic inputs such as those from  $\chi$ EFT’s. In this ongoing project, the SRG is playing a vital role by softening initial interactions [77].

Fundamental to the idea of convergence within a particular basis size is the question of correspondences between various cutoffs in different bases. While the cutting done in the momentum representation in chapter 3 is a straightforward ultraviolet

cutoff, the same procedure in the oscillator basis requires a different interpretation as briefly discussed in appendix B.3. Furthermore, many basis choices exist, each being more suitable to a different physics task. While the NCSM is a relatively straightforward and familiar basis, other bases like hyperspherical harmonics and correlated gaussians are promising choices for describing other nuclear features. In fact, an implementation of the SRG in three-body momentum representation is currently under development, and should provide a check on the evolution done here in the NCSM [37].

One of the major advantages of  $\chi$ EFT's is their natural framework for the inclusion of external operators, for example electromagnetic interactions. The SRG can also be used for consistent, independent, evolution of these and other operators. Work on this topic is already proceeding [43] and involves, among other things, the one-dimensional tool developed for chapter 4 for preliminary studies of operator evolution in a many-body space.

While reproducing the static properties of nuclear bound states is an important task for testing our quantitative understanding of the nuclear interaction, we must address the dynamics associated with reactions. One current avenue is to couple the NCSM technique with the Resonating Group Method, which allows access to information on scattering amplitudes between states within the NCSM basis. These calculations will contribute greatly to the knowledge of how nuclei interact with one another and are a vital diagnostic tool for many experimental setups, especially the inertial confinement fusion experiments coming online at the National Ignition Facility (NIF) at Lawrence Livermore National Laboratory. This work is an exciting new direction for research using the SRG.

The SRG can be applied term by term, as demonstrated by the vacuum expectation value analysis in section 4.4, to explore the interplay between different parts of the flow equations. This analysis needs to be continued in the realistic NCSM where we have access to the different contributions to the three-body force in  $\chi$ EFT. Further down the road, one can envision an analytical application of the SRG to gain general insight to the SRG's treatment of  $\chi$ EFT potentials (or any other physics one wishes to address). The diagrammatic decomposition of SRG evolution would inform and provide checks on the results of such work, but understanding the effects of SRG evolution on individual coupling constants may have significant advantages to the formulation of  $\chi$ EFT's. Specifically, an analytical understanding of the SRG's behavior may provide a practical means to extrapolate its behavior with regard to induced many-body forces.

The Similarity Renormalization Group has enjoyed a meteoric rise in its provision of benefits to nuclear few- and many-body problems. This thesis has provided a review of some of its basic features and initial applications to address calculations. It appears much more is to come.

## BIBLIOGRAPHY

- [1] H. Yukawa, Proc. Phys. Math. Soc. Jap. **17**, 48 (1935).
- [2] R. Machleidt, Adv. Nucl. Phys. **19**, 189 (1989).
- [3] R. Machleidt, Nucl. Phys. A **790**, 17 (2007) [arXiv:nucl-th/0701077].
- [4] H. A. Bethe, Ann. Rev. Nucl. Part. Sci. **21**, 93 (1971).
- [5] I. R. Afnan and D. R. Phillips, Phys. Rev. C **69**, 034010 (2004) [arXiv:nucl-th/0312021].
- [6] S. Weinberg Phys. Lett. B **251**, 228 (1990); Nucl. Phys. B **363**, 3 (1991).
- [7] R. Machleidt, private communication
- [8] J. E. Drut, R. J. Furnstahl and L. Platter, arXiv:0906.1463 [nucl-th].
- [9] R. B. Wiringa, V. G. J. Stoks and R. Schiavilla, Phys. Rev. C **51**, 38 (1995) [arXiv:nucl-th/9408016].
- [10] P. Navrátil, S. Quaglioni, I. Stetcu and B. R. Barrett, J. Phys. G **36**, 083101 (2009) [arXiv:0904.0463 [nucl-th]].
- [11] P. Navrátil, G. P. Kamuntavicius, and B. R. Barrett, Phys. Rev. C **61**, 044001 (2000).
- [12] P. Navrátil, and B. R. Barrett, Phys. Rev. C **59**, 1906 (1999).
- [13] P. Navrátil, and B. R. Barrett, Phys. Rev. C **57**, 562 (1998).
- [14] S. C. Pieper, K. Varga and R. B. Wiringa, Phys. Rev. C **66**, 044310 (2002) [arXiv:nucl-th/0206061].
- [15] S. C. Pieper and R. B. Wiringa, Ann. Rev. Nucl. Part. Sci. **51**, 53 (2001) [arXiv:nucl-th/0103005].
- [16] K. Kowalski, D. J. Dean, M. Hjorth-Jensen, T. Papenbrock and P. Piecuch, Phys. Rev. Lett. **92**, 132501 (2004) [arXiv:nucl-th/0310082].



- [17] G. Hagen, D. J. Dean, M. Hjorth-Jensen, T. Papenbrock and A. Schwenk, Phys. Rev. C **76**, 044305 (2007) [arXiv:0707.1516 [nucl-th]].
- [18] A. Schwenk, private communication
- [19] See <http://unedf.org/> for more details about the UNEDF collaboration
- [20] M. J. Savage, AIP Conf. Proc. **842**, 177 (2006) [arXiv:nucl-th/0601001].
- [21] W. Gloeckle, E. Epelbaum, U. G. Meissner, A. Nogga, H. Kamada and H. Witala, “Nuclear Forces and Few-Nucleon Studies Based on Chiral Perturbation Theory,” [arXiv:nucl-th/0312063].
- [22] S. R. Beane, P. F. Bedaque, W. C. Haxton, D. R. Phillips and M. J. Savage, ”From hadrons to nuclei: Crossing the border,” [arXiv:nucl-th/0008064]
- [23] M. J. Savage, Nucl. Phys. A **721**, 94 (2003) [arXiv:nucl-th/0301058].
- [24] A. M. Green “Hadronic Physics from Lattice QCD”, [arXiv:nucl-th/0409021].
- [25] N. Kaiser, Phys. Rev. **C64** 057001 (2001).
- [26] S. K. Bogner, T. T. S. Kuo, A. Schwenk, D. R. Entem and R. Machleidt, Phys. Lett. **B576**, 265 (2003);
- [27] S. K. Bogner, T. T. S. Kuo and A. Schwenk, Phys. Rept. **386**, 1 (2003).
- [28] S.K. Bogner, R.J. Furnstahl, and R.J. Perry, Phys. Rev. C **75** 061001 (2007).
- [29] S.Y. Lee and K. Suzuki, Phys. Lett. **B91** 173 (1980); K. Suzuki and S.Y. Lee, Prog. Theor. Phys. **64** 2091 (1980).
- [30] S. C. Pieper, V. R. Pandharipande, R. B. Wiringa and J. Carlson, Phys. Rev. C **64**, 014001 (2001) [arXiv:nucl-th/0102004].
- [31] S. K. Bogner, R. J. Furnstahl, R. J. Perry, and A. Schwenk, Phys. Lett. B **649** 488 (2007) .
- [32] S. D. Glazek and K. G. Wilson, Phys. Rev. D **48** 5863 (1993);  
Phys. Rev. D **49** 4214 (1994).
- [33] F. Wegner, Ann. Phys. (Leipzig) **3** 77 (1994);  
Phys. Rep. **348** 77 (2001).
- [34] J. Kehrein, *The Flow Equation Approach to Many-Particle Systems* (Springer, Berlin, 2006).

- [35] S. K. Bogner, R. J. Furnstahl, P. Maris, R. J. Perry, A. Schwenk and J. P. Vary, Nucl. Phys. A **801**, 21 (2008) [arXiv:0708.3754 nucl-th].
- [36] E. Anderson, S. K. Bogner, R. J. Furnstahl, E. D. Jurgenson, R. J. Perry and A. Schwenk, Phys. Rev. C **77**, 037001 (2008) [arXiv:0801.1098 [nucl-th]].
- [37] L. Platter, private communication
- [38] M. A. Preston and R. K. Bhaduri, *Structure of the Nucleus* (Addison-Wesley, Reading, MA, 1975)
- [39] D. C. Zheng, B. R. Barrett, L. Jaqua, J. P. Vary and R. J. McCarthy, Phys. Rev. C **48**, 1083 (1993) [arXiv:nucl-th/9304025].
- [40] D. C. Zheng, J. P. Vary and B. R. Barrett, Phys. Rev. C **50**, 2841 (1994) [arXiv:nucl-th/9405018].
- [41] D. C. Zheng, B. R. Barrett, J. P. Vary, W. C. Haxton and C. L. Song, Phys. Rev. C **52**, 2488 (1995).
- [42] E. R. Anderson, S. K. Bogner, R. J. Furnstahl, E. D. Jurgenson, R. J. Perry, “Operator Evolution via the Similarity Renormalization Group II” in preparation.
- [43] E. R. Anderson, S. K. Bogner, R. J. Furnstahl, E. D. Jurgenson, R. J. Perry, “Operator Evolution via the Similarity Renormalization Group I” in preparation.
- [44] See [http://www.mathworks.com/support/functions/alpha\\_list.html?sec=6](http://www.mathworks.com/support/functions/alpha_list.html?sec=6) and search for “ode23”
- [45] P. Bogacki, and L. F. Shampine, “A 3(2) pair of Runge-Kutta formulas” Appl. Math. Letters **2**, pp 1-9 (1989).
- [46] A. L. Fetter and J. D. Walecka, *Quantum Theory of Many-Particle Systems* (Dover Publications, New York, 2002).
- [47] S. K. Bogner, R. J. Furnstahl and R. J. Perry, Annals Phys. **323**, 1478 (2008) [arXiv:0708.1602 [nucl-th]].
- [48] M. E. Peskin, and D. V. Schroeder, *An Introduction to Quantum Field Theory*, (Westview Press, 1995).
- [49] D. R. Entem and R. Machleidt, Phys. Rev. C **68**, 041001(R) (2003) [arXiv:nucl-th/0304018].
- [50] E. Epelbaum, W. Glöckle and U. G. Meißner, Nucl. Phys. A **747**, 362 (2005) [arXiv:nucl-th/0405048].

- [51] R. H. Landau, *Quantum Mechanics II: A Second Course in Quantum Theory* (Wiley and Sons, New York, 1996).
- [52] E. D. Jurgenson, S. K. Bogner, R. J. Furnstahl, and R. J. Perry, Phys. Rev. C **78**, 014003 (2008).
- [53] See <http://www.physics.ohio-state.edu/~ntg/srg/>
- [54] S. D. Glazek and R. J. Perry, Phys. Rev. D **78**, 045011 (2008) [arXiv:0803.2911 [nucl-th]].
- [55] S.K. Bogner, R.J. Furnstahl, S. Ramanan and A. Schwenk, Nucl. Phys. A **784**, 79 (2007) [arXiv:nucl-th/0609003].
- [56] J.P. Vary, The Many-Fermion Dynamics Shell-Model Code, Iowa State University (1992) (unpublished); J.P. Vary and D.C. Zheng, *ibid.*, (1994) (unpublished).
- [57] S. K. Bogner, T. T. S. Kuo and A. Schwenk, Phys. Rept. **386**, 1 (2003) [arXiv:nucl-th/0305035].
- [58] E.L. Gubankova, H.-C. Pauli, F.J. Wegner, and G. Papp, “Light-cone Hamiltonian flow for positronium,” [arXiv:hep-th/9809143].
- [59] E. Gubankova, C. R. Ji and S. R. Cotanch, Phys. Rev. D **62**, 074001 (2000) [arXiv:hep-ph/0003289].
- [60] W. C. Haxton, “The Form of the Effective Interaction in Harmonic-Oscillator-Based Effective Theory,” arXiv:0710.0289 [nucl-th].
- [61] G. Hagen, T. Papenbrock, D. J. Dean and M. Hjorth-Jensen, Phys. Rev. Lett. **101**, 092502 (2008) [arXiv:0806.3478 [nucl-th]].
- [62] C. Alexandrou, J. Myczkowski, J. W. Negele, Phys. Rev. C **39**, 1076 (1989).
- [63] D. Van Neck, A. E. L. Dieperink, and M. Waroquier, Phys. Rev. C **53**, 2231 (1996).
- [64] K. Varga and Y. Suzuki, Comp. Phys. Comm. **106**, 157 (1997).
- [65] E. Anderson, private communication.
- [66] Y. Suzuki and K. Varga, *Stochastic variational approach to quantum-mechanical few body problems* (Springer, Berlin, 1998).
- [67] E. Epelbaum, A. Nogga, W. Gloeckle, H. Kamada, U. G. Meissner and H. Witala, Phys. Rev. C **66**, 064001 (2002) [arXiv:nucl-th/0208023].

- [68] L. Frankfurt, M. Sargsian and M. Strikman, *Int. J. Mod. Phys. A* **23**, 2991 (2008) [arXiv:0806.4412 [nucl-th]].
- [69] P. Navratil, *Few Body Syst.* **41**, 117 (2007) [arXiv:0707.4680 [nucl-th]].
- [70] D. Gazit, S. Quaglioni and P. Navratil, “Three-Nucleon Low-Energy Constants from the Consistency of Interactions and Currents in Chiral Effective Field Theory,” [arXiv:0812.4444 [nucl-th]].
- [71] E.D. Jurgenson, P. Navratil, and R.J. Furnstahl, (Submitted to PRL) [arXiv:0905.1873 [nucl-th]].
- [72] D. Rozpedzik *et al.*, *Acta Phys. Polon. B* **37**, 2889 (2006) [arXiv:nucl-th/0606017].
- [73] A. Nogga, S.K. Bogner and A. Schwenk, *Phys. Rev. C* **70**, 061002(R) (2004).
- [74] E. Epelbaum, H.W. Hammer and U.G. Meissner, arXiv:0811.1338 [nucl-th] and references therein.
- [75] A. Nogga, P. Navrátil, B.R. Barrett and J.P. Vary, *Phys. Rev. C* **73**, 064002 (2006).
- [76] P. Navratil, V.G. Gueorguiev, J.P. Vary, W.E. Ormand and A. Nogga, *Phys. Rev. Lett.* **99**, 042501 (2007) [arXiv:nucl-th/0701038].
- [77] J. E. Drut, R. J. Furnstahl and L. Platter, “Toward ab initio density functional theory for nuclei,” [arXiv:0906.1463 [nucl-th]].
- [78] D. B. Kaplan, M. J. Savage and M. B. Wise, *Phys.Lett.B* **424**, 390 (1998) [arXiv:nucl-th/9801034].
- [79] S. R. Beane, D. B. Kaplan and A. Vuorinen, “Perturbative nuclear physics,” arXiv:0812.3938 [nucl-th].
- [80] E. Epelbaum, ”Few-Nucleon Forces and Systems in Chiral Effective Field Theory”, [arXiv:nucl-th/0509032].
- [81] E. Epelbaum, W. Gloeckle, and U. G. Meissner, *Nucl.Phys.A* **637**, 107 (1998) [arXiv:nucl-th/9801064].
- [82] E. Epelbaum, W. Gloeckle and U. G. Meissner, *Nucl.Phys.A* **747**, 362 (2005) [arXiv:nucl-th/0405048].
- [83] P. F. Bedaque, U. van Kolck, ”Effective Field Theory for Few-Nucleon Systems”, [arXiv:nucl-th/0203055].

- [84] J. A. Eden and M. F. Gari, Phys. Rev. C **53**, 1510 (1996) [arXiv:nucl-th/9601025].
- [85] I. Tamm, J. Phys (USSR) **9** 449 (1945);  
S. M. Dancoff, Phys.Rev. **78** 382 (1950)
- [86] S. Okubo, Prog. Theor. Phys. (Japan) **12**, 603 (1954).
- [87] E. Epelbaum, "Four-Nucleon Force in Chiral Effective Field Theory", [arXiv:nucl-th/0511025].
- [88] D. J. Griffiths, *Introduction to Quantum Mechanics*, Prentice Hall, Upper Saddle River, New Jersey (1995).
- [89] R. Liboff, *Introductory Quantum Mechanics*, Addison-Wesley (2002).
- [90] M. Moshinsky, Y.F. Smirnov, *The Harmonic Oscillator in Modern Physics*, Harwood Academic Publishers, Amsterdam, (1996).
- [91] S. Shlomo, J. Phys. A **16**, 3463-3469 (1983).
- [92] L. Trlifaj, Phys. Rev. C **5**, 1534 (1972).
- [93] A. Deveikis and G. Kamuntavicius, Lith. Phys. J. **35**, 14 (1995) [arXiv:nucl-th/9808053].
- [94] N. Barnea and A. Novoselsky, Ann. Phys. **256**, 192 (1997).
- [95] P. Navratil and B. R. Barrett, Phys. Rev. C **54**, 2986 (1996) [arXiv:nucl-th/9609046].

## APPENDIX A

### CHIRAL EFFECTIVE FIELD THEORIES

The original efforts to build Chiral Effective Field Theories ( $\chi$ EFT's) with more than one nucleon were based on a suggestion by Weinberg [6] to use a non-perturbative treatment of the power counting rules from the perturbative Chiral Perturbation Theory ( $\chi$ PT). A non-perturbative development is necessary in order to describe nuclear bound states. Weinberg used a  $\chi$ PT power counting scheme to build the nuclear potential and used the Lippmann-Schwinger equation to iterate it non-perturbatively.

The motivation for this non-perturbative scheme is the reproduction of the deuteron binding energy, scattering lengths, and other low energy observables. The above discussion of renormalization scales and momentum contributions is important to this, but it does not solve the bound state problem completely. Naive dimensional analysis (NDA) can only give an estimate of the effective coupling constants, referred to as Low Energy Constants (LECs). Only a careful calculation and renormalization procedure can fix their values and even signs. The power counting rule used here is based on an assumption of naturalness. That after renormalization, the LEC's will be of order one. Also, the LECs are assumed to serve as counter terms to loops in the irreducible diagrams. In practice, in  $\chi$ EFT these absorptions are achieved by a fit to data.

Shortly after Weinberg's proposal there was an attempt to develop a perturbative treatment of pions in an EFT. This was formally worked out by Kaplan, Savage, and Wise [78], and is known as KSW power counting. While still non-perturbative in the contact interactions, the authors conjectured that the pion dynamics might be weak enough to treat perturbatively. Unfortunately, it turned out that the breakdown scale in this approach is too low to be of practical use in nuclear structure, though new variations have been proposed [79]. This approach will not be discussed here further.

## A.1 Basics of power counting

To explain the method of power counting due to Weinberg and used in Ref. [80], we will start by writing out part of a chirally symmetric Lagrangian for  $\chi$ EFT

$$\begin{aligned}
\mathcal{L}^{(0)} &= \frac{1}{2} \partial_\mu \boldsymbol{\pi} \cdot \partial^\mu \boldsymbol{\pi} - \frac{1}{2} M^2 \boldsymbol{\pi}^2 + N^\dagger \left[ i \partial_0 + \frac{g_A}{2F_\pi} \boldsymbol{\tau} \vec{\sigma} \cdot \vec{\nabla} \boldsymbol{\pi} - \frac{1}{4F_\pi^2} \boldsymbol{\tau} \cdot (\boldsymbol{\pi} \times \dot{\boldsymbol{\pi}}) \right] N \\
&\quad - \frac{1}{2} C_S (N^\dagger N) (N^\dagger N) - \frac{1}{2} C_T (N^\dagger \vec{\sigma} N) (N^\dagger \vec{\sigma} N) + \dots, \\
\mathcal{L}^{(1)} &= N^\dagger \left[ 4c_1 M^2 - \frac{2c_1}{F_\pi^2} M^2 \boldsymbol{\pi}^2 + \frac{c_2}{F_\pi^2} \dot{\boldsymbol{\pi}}^2 + \frac{c_3}{F_\pi^2} (\partial_\mu \boldsymbol{\pi} \cdot \partial^\mu \boldsymbol{\pi}) \right. \\
&\quad \left. - \frac{c_4}{2F_\pi^2} \epsilon_{ijk} \epsilon_{abc} \sigma_i \tau_a (\nabla_j \pi_b) (\nabla_k \pi_c) \right] N \\
&\quad - \frac{D}{4F_\pi} (N^\dagger N) (N^\dagger \vec{\sigma} \boldsymbol{\tau} N) \cdot \vec{\nabla} \boldsymbol{\pi} - \frac{1}{2} E (N^\dagger N) (N^\dagger \boldsymbol{\tau} N) \cdot (N^\dagger \boldsymbol{\tau} N) + \dots \quad (\text{A.1})
\end{aligned}$$

where the superscripts refer to the chiral dimension,  $\Delta_i$ , of a vertex  $i$ . The operators  $\sigma$  and  $\tau$  are Pauli spin and isospin matrices. The epsilons are Levi-Civita symbols necessary to achieve proper tensor multiplication. The constants  $F_\pi$  and  $g_A$  are associated with basic pion interactions and are determined elsewhere<sup>20</sup>. The LEC's here are  $c_i$ ,  $C_{S,T}$ ,  $D$ , and  $E$ . Notice  $E$  is the LEC corresponding to the first 3NF contact

<sup>20</sup>  $F_\pi$  and  $g_A$  are parametrizations of weak nuclear interactions between pions and nucleons. They can be measured in processes such as pion decay and nuclear  $\beta$  decay.

term. This Lagrangian is complete up to  $N^2LO$  including only isospin symmetric terms.

In this power counting approach we calculate the T-matrix directly via the Lippmann-Schwinger equation (given here schematically),

$$T = V + VG_0T, \quad (\text{A.2})$$

where we will define the potential,  $V$ , to be the sum of all irreducible diagrams up to a certain order in  $\nu$  as defined below. An irreducible graph is defined as one which has no purely nucleonic intermediate states. The need for this definition will become apparent momentarily. The intermediate state Green's function,  $G_0$  will play a crucial role in the power counting and will be defined also.

All irreducible graphs can be categorized by their contribution  $\sim O(Q/\Lambda)^\nu$  governed by the power counting rule

$$\nu = 2(N + L - C - 1) + \sum_i V_i \Delta_i \quad \text{and} \quad \Delta_i = d_i + n_i/2 - 2. \quad (\text{A.3})$$

The variables  $N$ ,  $L$ ,  $C$ ,  $V_i$ ,  $\Delta_i$ ,  $d_i$ , and  $n_i$  are the numbers of nucleons, loops, connected pieces, vertices of type  $i$ , chiral dimension of vertex type  $i$ , derivatives or factors of  $m_\pi$  at vertex  $i$ , and nucleon lines at vertex  $i$  respectively. At any given order only a finite number of time-ordered irreducible graphs are needed to compute the exact potential at that order. Chiral Symmetry sets a lower bound at  $\Delta_i \geq 0$ . The simplest graph we can have is one with no nucleons and two pions (pion propagator  $\sim m_\pi^2$ ) or two nucleons and one derivative provided by a pion interaction or four nucleons and no pions (contact interaction). Those are the lowest-order options in the Lagrangian in Eq. (A.1). Given the bounds on  $\Delta_i$ , the lower bound on  $\nu$  is 0, thus we have a lowest order in the expansion and a valid power counting scheme.



Let us apply Eq. (A.3) to a few example graphs from Fig. 1.5 in section 1.4. Take the simple 1PE graph at LO. The graph has two vertices, each with two nucleon lines and one derivative (from pion interaction) giving  $\Delta_i = 0$ . There are 2 nucleons in this graph, no loops, and 1 connected piece. The grand total is  $\nu = 0$  (LO) which matches with the table. For a different example, consider the 1PE-contact graph for a 3NF at  $\nu = 3$  ( $N^2LO$ ). There are two vertices, one with two nucleon lines and one pion based derivative gives  $\Delta_i = 0$ , and the other with four nucleon lines and the pion interaction derivative (the term with the LEC “D”) gives  $\Delta_i = 1$ . So, with the sum over vertices giving one, three nucleons, no loops, and one connected piece we have a total of  $\nu = 3$ . So, all graphs are organized according to their contribution  $Q^\nu$  given by Eq. (A.3) and Eq. (A.1). Note that no contributions survive of order  $\nu = 1$ .

The derivation of Eq. (A.3) appears in many forms throughout the literature [81, 82, 83]. Start by considering a general graph and sum up momentum contributions via naive dimensional analysis. The momentum contribution,  $Q$ , for that graph is 4 for each loop integration ( $L$ ),  $-2$  for each internal pion ( $P$ ),  $-1$  for each internal nucleon ( $I$ ),  $+1$  for each vertex derivative( $D$ ). We obtain the expression

$$\nu = 4L - I - 2P + \sum_i V_i d_i . \quad (\text{A.4})$$

We can change the form of this using the well-established topological identities

$$L = P + I - \sum_i V_i + 1 , \quad (\text{A.5})$$

and

$$2I + E = \sum_i V_i n_i , \quad (\text{A.6})$$

where  $n_i$  is the number of nucleon lines at vertex of type  $i$  and  $E$  is the number of external nucleon legs ( $E = 2N$ ). The particular form of Eq. (A.3) presented here also

requires some non-trivial transformations associated with the formulation of graphs in an energy independent way [81] such as the method of unitary transformations that separates the purely nucleonic part of the Fock space from the rest [84]. Finally one arrives at the convenient expression of Eq. (A.3) for  $\nu$ . The variables N, L, and C are easy to count and  $\Delta_i$  provides us with a way of organizing vertex types as discussed above.

## A.2 Many-body forces

One of the beautiful aspects of using field theoretic techniques to describe the nuclear interactions is the consistent and straightforward generalization to few and many body forces. In chapter 1, we briefly mentioned why few-body forces are guaranteed to exist in the  $\chi$ EFT expansion. We argued that the renormalization intrinsic to an EFT is responsible for integrating out the high-energy effects, so that in a few-body problem, certain components of the interaction will be hidden from the experiment (i.e. they will occur at distance scales much smaller than we can resolve). These effects can be divided roughly into three types. First, the  $\Delta$  resonance can play a role in the interactions and is discussed in the next section. Second, simple high-momentum nucleonic intermediate states like a box diagram with a large momentum running around the loop. Third, relativistic corrections which modify the kinetic energy of the intermediate nucleon states (i.e. through pair production) allow for irreducible diagrams with high-energy intermediate states that are (at low lab energy) highly virtual and will occur over very small distances. As stated above, these are the major contributions that cannot be resolved at the relevant lab energies and

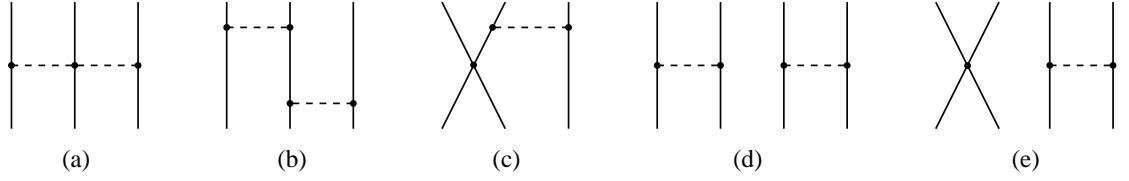


Figure A.1: 3 and 4 nucleon amplitudes that occur at  $\nu = 2$ . These terms will cancel each other out in an energy-independent formulation. Figure courtesy of Ref. [80].

therefore must be renormalized into a 3N contact force. Thus a 3NF appearing in the EFT Lagrangian is inevitable due to any of the above three effects.

A simple NDA consideration leads us to expect that the basic 3NF terms should become relevant at  $\nu = 3$ . To see this, consider the 3NF contact term compared to the NN contact term at LO ( $\nu = 0$ ). All other things being equal, the only difference should be that the 3NF has an extra pair of nucleon legs ( $NN^\dagger$ ) each of order  $3/2$  for a total of 3 extra orders of the momentum scale  $Q$ . Thus we should expect 3NFs to become relevant at  $\nu = 3$ .

If we use the power counting of Eq. (A.3) to build the simplest three- and four-body diagrams we find the first contributions appearing at  $\nu = 2$  which seems to contradict the above NDA argument. However, these first 3NF and 4NF terms (shown in Fig. A.1) will not actually contribute. If we draw out all possible graphs from the possible topologies at this order we will find that they cancel each other out. This vanishing is evident when we formulate the nuclear force in an energy-independent way [85, 86].

Finally, at  $\nu = 3$  we will find the leading 3NF terms. With  $E = 3$ ,  $L = 0$ ,  $C = 1$ , and one  $\Delta = 1$  vertex we can draw all such diagrams as shown in Fig. A.2. The

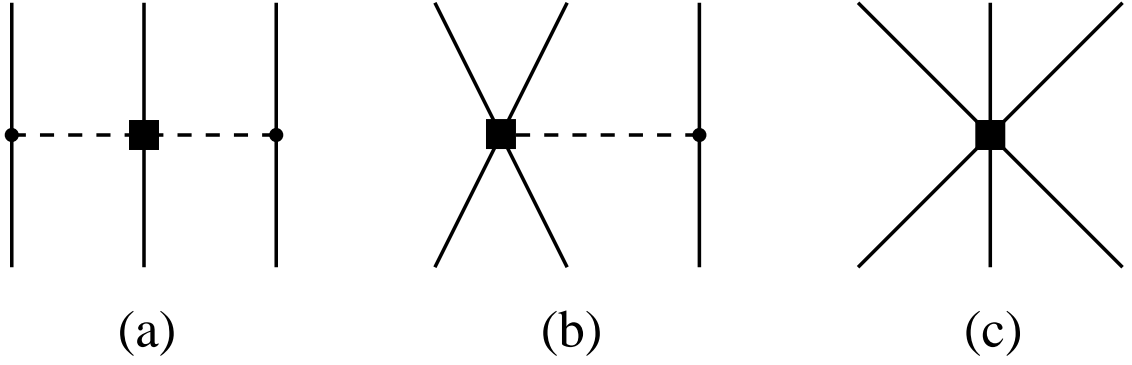


Figure A.2: The leading order 3NFs at  $\nu = 3$ . Figure courtesy of Ref. [80]

contributions to the potential from these three graphs are given by [80]

$$V_{2\pi}^{(3)} = \sum_{i \neq j \neq k} \frac{1}{2} \left( \frac{g_A}{2F_\pi} \right)^2 \frac{(\vec{\sigma}_i \cdot \vec{q}_i)(\vec{\sigma}_j \cdot \vec{q}_j)}{(\vec{q}_i^2 + M_\pi^2)(\vec{q}_j^2 + M_\pi^2)} F_{ijk}^{\alpha\beta} \tau_i^\alpha \tau_j^\beta, \quad (\text{A.7})$$

with

$$F_{ijk}^{\alpha\beta} = \delta^{\alpha\beta} \left[ -\frac{4c_1 M_\pi^2}{F_\pi^2} + \frac{2c_3}{F_\pi^2} \vec{q}_i \cdot \vec{q}_j \right] + \sum_\gamma \frac{c_4}{F_\pi^2} \epsilon^{\alpha\beta\gamma} \tau_k^\gamma \vec{\sigma}_k \cdot [\vec{q}_i \times \vec{q}_j], \quad (\text{A.8})$$

and

$$V_{1\pi, \text{cont}}^{(3)} = - \sum_{i \neq j \neq k} \frac{g_A}{8F_\pi^2} D \frac{\vec{\sigma}_j \cdot \vec{q}_j}{\vec{q}_j^2 + M_\pi^2} (\boldsymbol{\tau}_i \cdot \boldsymbol{\tau}_j) (\vec{\sigma}_i \cdot \vec{q}_j), \quad (\text{A.9})$$

and

$$V_{\text{cont}}^{(3)} = \frac{1}{2} \sum_{j \neq k} E (\boldsymbol{\tau}_j \cdot \boldsymbol{\tau}_k), \quad (\text{A.10})$$

where  $i, j, k$  refer to nucleons, and  $\vec{q}_i \equiv \vec{p}_i' - \vec{p}_i$ ;  $\vec{p}_i$  ( $\vec{p}_i'$ ) is the initial (final) momentum of the nucleon  $i$ . These will involve vertices with  $\Delta_i = 1$ . These expressions for the potential look complicated, but they must reproduce the structure of the pion interactions that they are parametrizing. Thus the intricate structures of spin and isospin matrices.

At  $\nu = 4$  we find the first corrections to the 3NF terms and the leading order 4NF's. Some of these diagrams are shown in Fig. A.3 while a more complete list

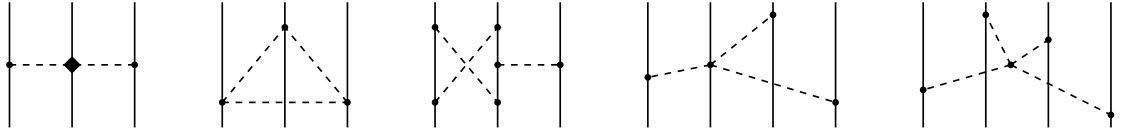


Figure A.3: Sample 3NF corrections and leading 4NFs at  $\nu = 4$ . A more complete list of 4NFs is in Fig. A.4. Figure courtesy of Ref. [80]

of 4NF diagrams can be found in Fig. A.4 from ref. [87], which also presents the analytic expressions for the potential contribution from these graphs. It has also been shown that all disconnected diagrams at this order vanish completely in an energy independent formulation [84].

In many-body systems we must also consider disconnected graphs that involve fewer-body interactions and spectators. This is accounted for in Eq. (A.3) by the value of  $C$ . For instance a contribution to a three-body system might include a diagram with a 2N interaction and one spectator nucleon. Another might be a four nucleon system with a 3NF interaction and one spectator or two disconnected NN interactions (such as the  $\nu = 2$  interactions in Fig. A.1). Such disconnected diagrams are expected to be two orders of momentum more important than their corresponding tree graphs, though many formally vanish and must be carefully worked out [80].

It should be clear that the complexity and sheer number of graphs increases quickly with the order in momenta ( $\nu$ ) under consideration. However, numerical calculations indicate [87] that graphs with  $\nu \geq 4$  have a negligible contribution, though these results are very preliminary and not conclusive.

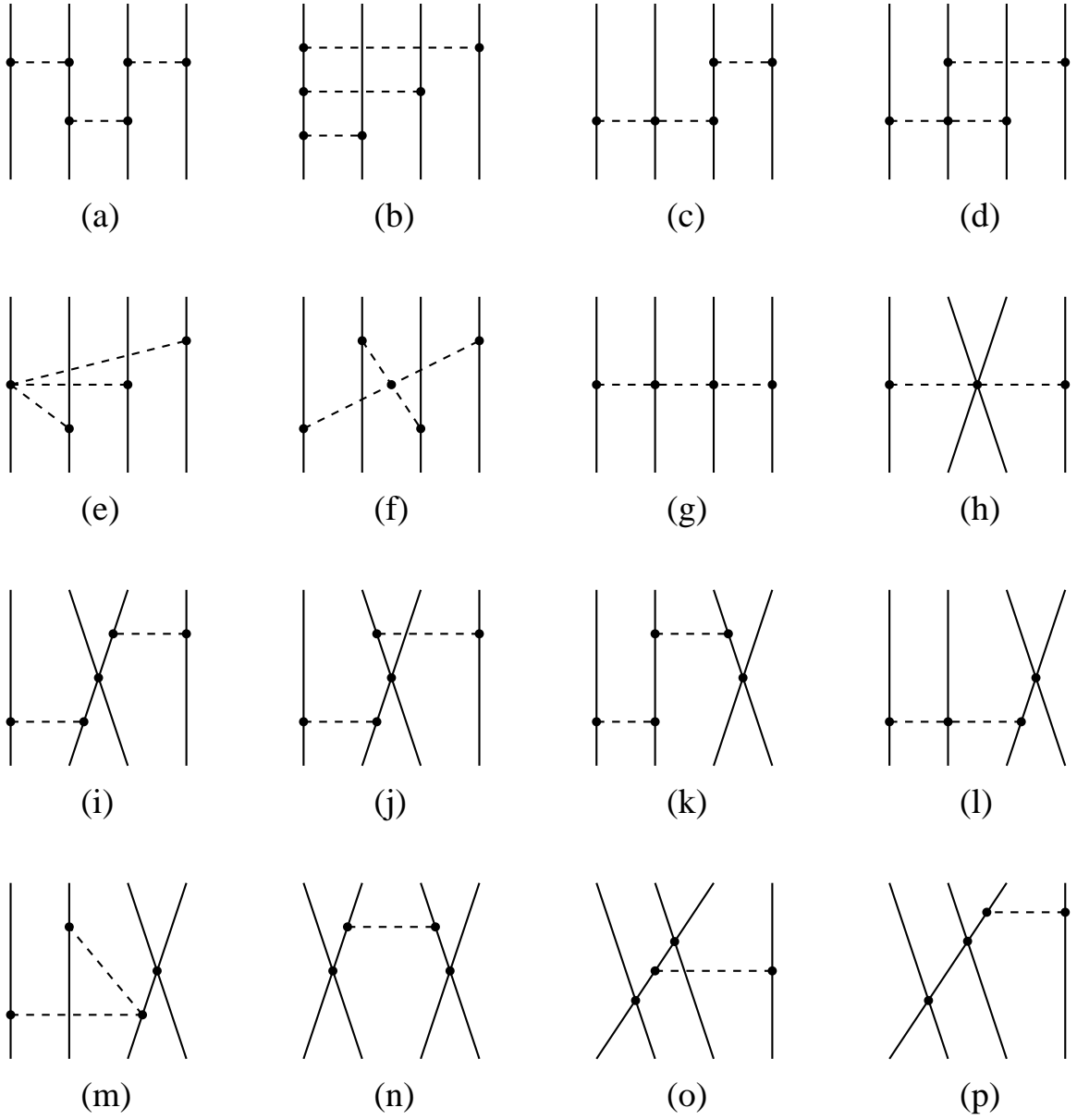


Figure A.4: Leading 4NFs at  $\nu = 4$ . Permutations of vertex ordering and nucleon lines are implicit. Figure courtesy of Ref. [87]

### A.3 The role of the $\Delta$ resonance

The  $\Delta$ -isobar is a baryon with mass  $m_\Delta = 1232$  which is only 300 MeV above the mass of the nucleon. The  $\Delta$  is composed of 3 non-strange quarks and being in the quartet of isospin  $3/2$  and spin  $3/2$  can have an integral charge from  $-1$  to  $+2$ . For historical reasons, one might also hear the  $\Delta$  referred to as an excited state of the nucleon especially given the strong resonance in  $\pi N$  scattering. This view comes out of the simple quark model where the  $\Delta$  is a very short lived (decays via strong interactions) particle whose main decay channel is to a pion and nucleon.

So far we have ignored the question of the effects of an explicit  $\Delta$  degree of freedom in the Lagrangian. Whatever effects there might be would be treated as short ranged and encoded in the LEC's of our existing theory. If they are not sufficiently short the LEC's will become unnaturally large. But some work has been done on a Weinberg-like power counting scheme with the assumption  $m_\Delta - m_N \sim 2m_\pi$ . This is a simplification however since  $m_\Delta - m_N$  is yet another small momentum parameter in which to make a possible expansion.

An example Lagrangian for a  $\chi$ EFT involving an explicit  $\Delta$  is [80]

$$\mathcal{L} = \Delta^\dagger (i\partial_0 - \Delta m) \Delta + \frac{h_A}{2F_\pi} \left( N^\dagger \vec{S} \mathbf{T} \Delta + \text{h. c.} \right) \cdot \vec{\nabla} \boldsymbol{\pi} - D_T N^\dagger \vec{\sigma} \boldsymbol{\tau} N \cdot \left( N^\dagger \vec{S} \mathbf{T} \Delta + \text{h. c.} \right), \quad (\text{A.11})$$

where  $h_A$  and  $D_T$  are LECs and  $S_i$  and  $T_a$  are spin and isospin matrices. These matrices are  $2 \times 4$  because they must describe the interactions between nucleons and deltas, the doublet and quartet channels respectively, in spin and isospin space.

The first contributions involving explicit  $\Delta$ 's are NN graphs involving two pion exchange and shown in Fig. A.5. One can see the  $\Delta$ 's dominance in the LECs at

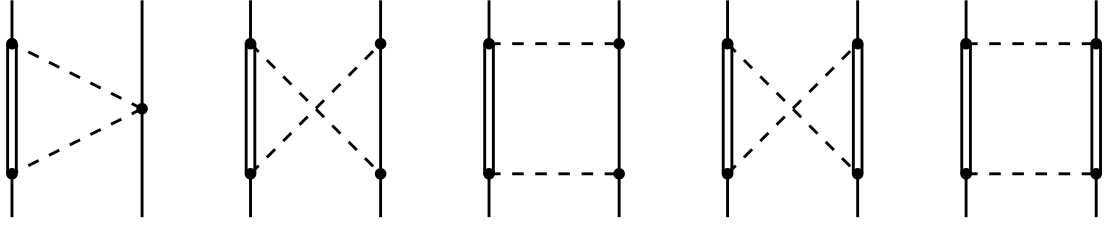


Figure A.5: Leading NN two pion exchange graphs with explicit  $\Delta$  (double solid line) arising at  $\nu = 2$ . Figure courtesy of Ref. [80]

this order. The potentials corresponding to the one- $\Delta$  2PE box graphs are identical in form to their analogous graphs without  $\Delta$ s. Matching up the LECs, we can see  $c_3 = 2c_4 = g_A^2/2(m_\Delta - m_N)$  and as above the mass scale appearing is  $(m_\Delta - m_N)$  rather than  $m_\pi$ .

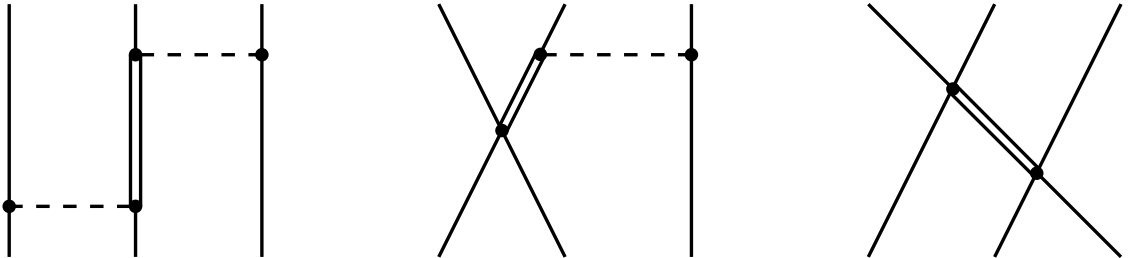


Figure A.6: Leading order 3NFs with explicit  $\Delta$  arising at  $\nu = 3$ , an enhancement over the deltaless theory. Figure courtesy of Ref. [80]

The 3NF terms with explicit  $\Delta$  resonances show up at  $\nu = 2$ , instead of non- $\Delta$  3NF terms starting at  $\nu = 3$ . There is basically one major contribution at this order; the first graph in Fig. A.6 is analogous to the leading 3NF graphs that had reducibility



cancellations. Now because of the existence of a  $\Delta$  in the intermediate state, these cancellations don't occur. The other two 3NF graphs at this order formally cancel out due to Pauli exclusion [67].

In summary, the  $\Delta$  can be included explicitly to achieve higher accuracy or it can be excluded for simplicity leaving those higher energy details to be encoded in the LECs of some  $\Delta$ -less  $\chi$ EFT.

## APPENDIX B

### GENERAL FEATURES OF THE HARMONIC OSCILLATOR BASIS

#### B.1 One-Dimensional Harmonic Oscillator Wavefunctions

The one-dimensional harmonic oscillator functions in momentum space are given by [88]

$$\psi_n(p) = \left( \frac{1}{\pi m \hbar \omega 2^{2n} n!^2} \right)^{1/4} \exp \left[ -\frac{p^2}{2m\hbar\omega} \right] H_n \left[ \frac{p}{\sqrt{m\hbar\omega}} \right] \quad (\text{B.1})$$

where  $H_n$  are the Hermite polynomials

$$\begin{aligned} H_0(y) &= 1 \\ H_1(y) &= 2y \\ H_2(y) &= 4y^2 - 2 \\ H_3(y) &= 8y^3 - 12y \\ H_4(y) &= 16y^4 - 48y^2 + 12 \\ H_5(y) &= 32y^5 - 160y^3 + 120y \end{aligned} \quad (\text{B.2})$$

or more formally

$$H_n(y) = (-1)^n \exp^{y^2} \frac{d^n}{dy^n} \exp^{-y^2}. \quad (\text{B.3})$$

We will often make the approximation

$$H_n(y) \approx (2y)^n, \quad (\text{B.4})$$

since this is the dominant term in the polynomial for large  $y$ .

These oscillator functions are displayed in Fig. B.1 on the left, in a standard MATLAB color scheme, with reds positive, blues negative, and green zero. The vertical axis is increasing oscillator number,  $n$ , downward. The horizontal axis is momentum,  $p$ , from negative to positive  $k_{\text{max}}$ . On the right, the truncated momentum delta function,

$$\sum_{n=1}^{N_{\text{max}}} \psi_n(p)\psi_n(p') \approx \delta(p - p')\Theta(p_{\text{max}} - p) \quad (\text{B.5})$$

is a demonstration of the incompleteness of the finite oscillator basis. In the limit  $N_{\text{max}} \rightarrow \infty$  the sum should go to a delta function,  $\delta(p - p')$ . Here, because of the finite nature of the oscillator basis, the delta function is truncated at a point we will refer to as  $p_{\text{max}}$  (referred to in other contexts as the ultraviolet cutoff,  $\Lambda_{\text{UV}}$ ). The  $p_{\text{max}}$  of the truncation and the extent of the last oscillator function in the basis correspond to one another.

The coordinate space version of B.1 is

$$\psi_n(r) = \left( \frac{m\hbar\omega}{\pi\hbar^2 2^{2n} n!^2} \right)^{1/4} \exp \left[ -\frac{m\hbar\omega r^2}{2\hbar^2} \right] H_n \left[ \sqrt{\frac{m\hbar\omega}{\hbar^2}} r \right]. \quad (\text{B.6})$$

Note that the only difference in form is that the factor of  $m\hbar\omega$  is flipped in relation to the variable  $r$  as it was to  $p$  in B.1. This will be important later in an analytical discussion of infrared and ultraviolet cutoffs due to basis conversions.

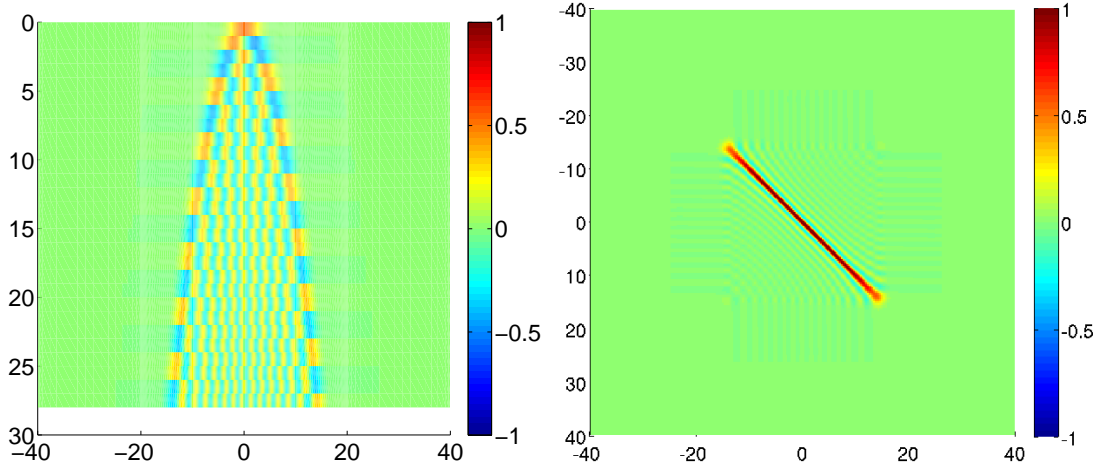


Figure B.1: On the left are shown the harmonic oscillator functions. On the right is the truncated momentum delta function  $\delta(p-p')\Theta(p_{\max}-p)$ . In this MATLAB color scheme the red is positive and blue is negative.

## B.2 Truncation

When converting a momentum space potential into the oscillator basis as in

$$V(n, n') = \int_{-k_{\max}}^{k_{\max}} \psi_n(p) \psi_{n'}(p') V^{(2)}(p, p') dp dp' \quad (\text{B.7})$$

or

$$\langle n|V|n'\rangle = \int_{-k_{\max}}^{k_{\max}} \langle n|p\rangle \langle p|V^{(2)}|p'\rangle \langle p'|n'\rangle dp dp' \quad (\text{B.8})$$

the potential becomes truncated due to the finite nature of the oscillator basis. When we try to convert back to the momentum basis we find that we have effectively multiplied by the truncated delta function of Eq. B.5.

This truncation is shown in Fig. B.2 for different sized oscillator bases, each using the same value for the oscillator parameter,  $\hbar\omega$ . Notice that as  $N_{\max}$  increases we retain more of the original potential, and parts of it smooth out to their original form. There are also residual oscillatory effects left at the edges of the converted potential.

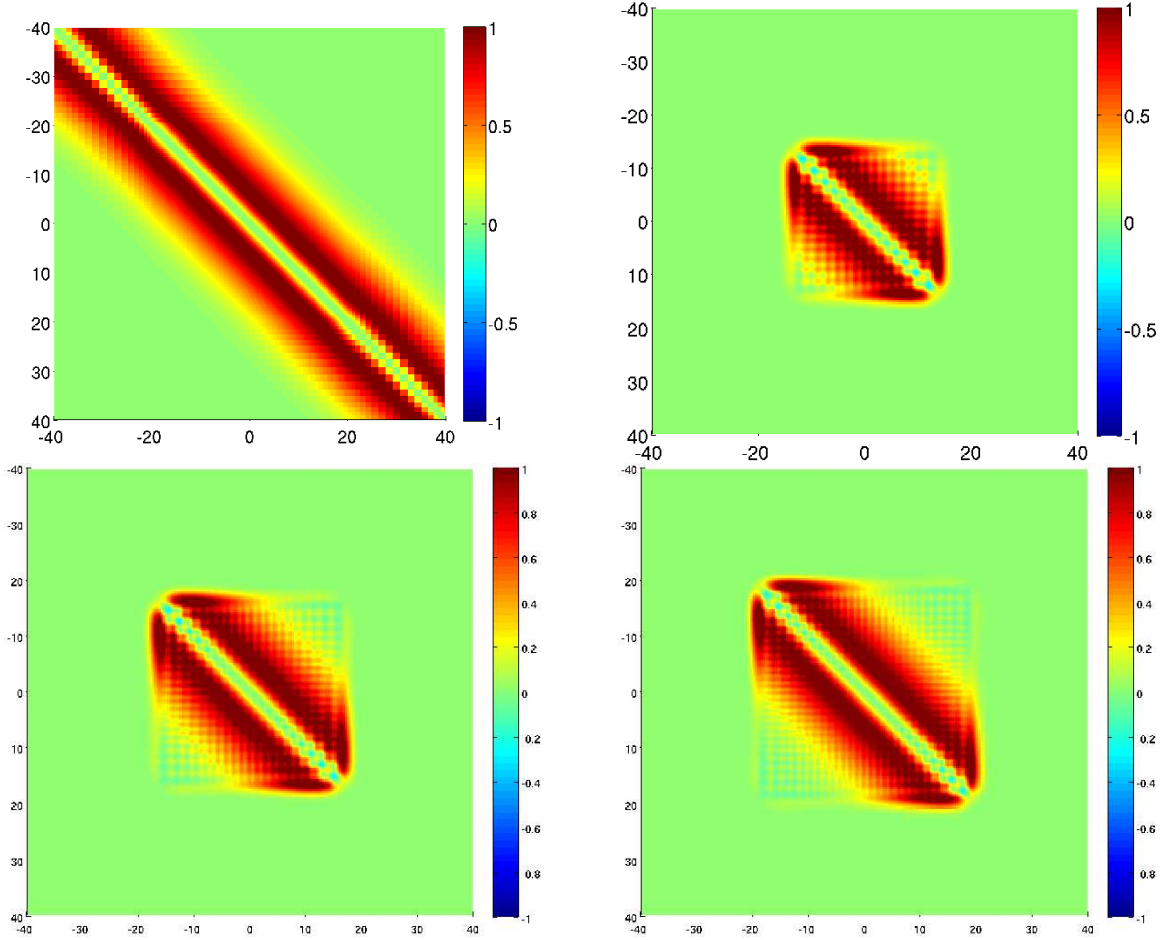


Figure B.2: A two-body potential in the momentum representation. The axes are initial and final momenta,  $k$  and  $k'$ , from  $-k_{\max}$  to  $k_{\max}$ . On the upper-left is the original momentum basis two-body potential. The other three plots are the same potential after being converted to an oscillator basis and back. Notice the truncation of matrix elements above each  $p_{\max}$  of the oscillator basis.

As stated above the truncation at  $p_{\max}$  corresponds to the extent in momentum space to the highest harmonic oscillator wavefunction in the oscillator basis,  $\psi_{N_{\max}}(p)$ . Two variables affect the value of  $p_{\max}$ : the oscillator parameter  $\hbar\omega$  and the basis size  $N_{\max}$ . We will consider the dependence on each of these variables in order.

A quick look at the harmonic oscillator wavefunctions in Eq. B.1 shows a simple proportionality between  $p$  and  $\hbar\omega$ . The change in  $p_{\max}$  should scale like the square root of the change in  $\hbar\omega$ . Numerically this can be verified by looking at the furthest extent of oscillator functions for different  $\hbar\omega$ 's. Shown in Fig. B.3 are the oscillator bases for  $N_{\max}=28$  and  $\hbar\omega=2,4,8$  and 16. An increase in  $\hbar\omega$  by a factor of four doubles  $p_{\max}$ . In Fig. B.3, looking down the vertical axis in the plots of shows a similar dependence on  $N_{\max}$ . The curve formed by the edge of the oscillator wavefunctions looks like a square root function implying  $p_{\max} \approx n^{1/2}$ .

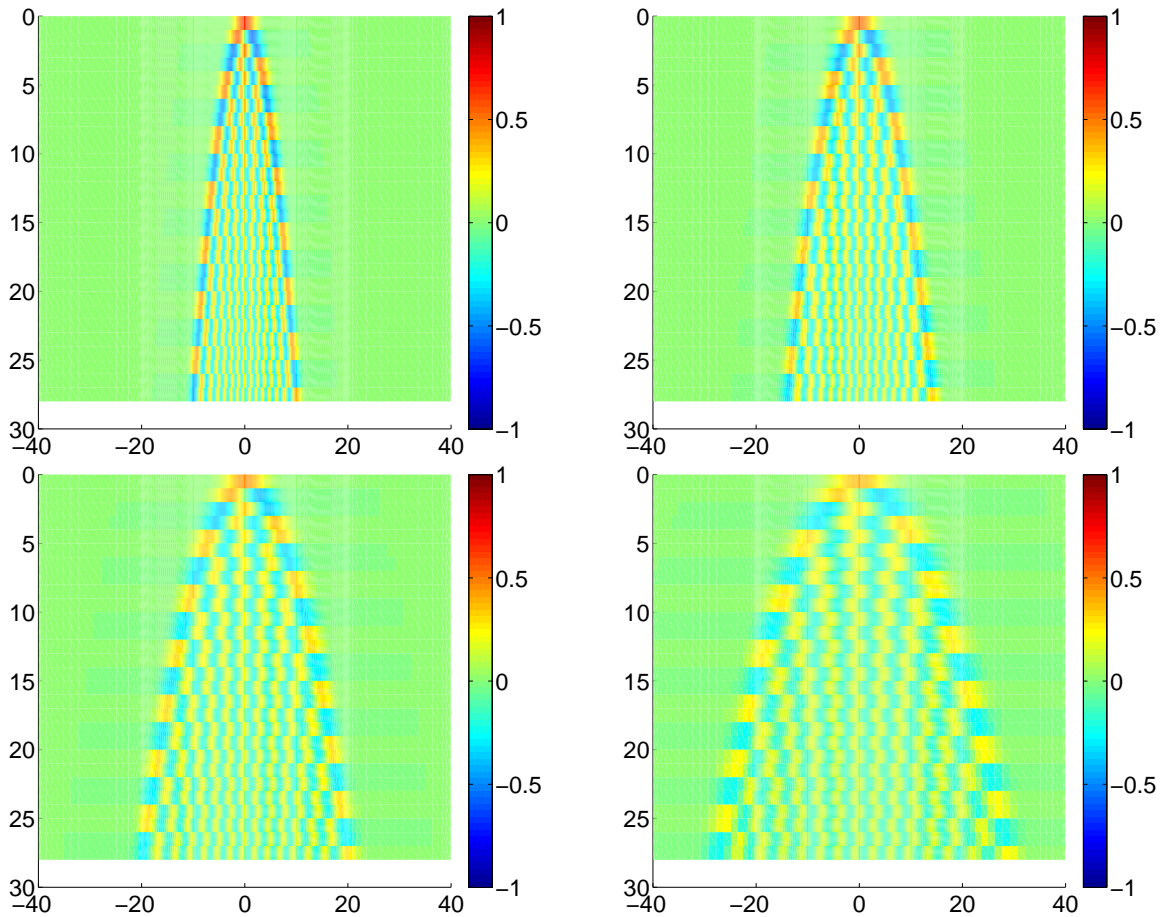


Figure B.3: Harmonic oscillator functions up to  $N_{\max}=28$  for  $\hbar\omega = 2, 4, 8,$  and 16.

We can measure these dependencies more quantitatively by picking out the mesh point at which each oscillator function passes a certain minimum threshold:

$$|\psi_n(p_{\max})| = \psi_{\min} . \quad (\text{B.9})$$

In Fig. B.4 we show an example of such a measurement. The value  $\psi_{\min} = .01$  is used to plot the variation of  $p_{\max}$  with  $\hbar\omega$  on the left and with  $n$  on the right. In this log-log plot the dependence on  $\hbar\omega$  is a clean power law with a slope of .5 as expected from the oscillator wavefunctions dependence on  $p/\sqrt{\hbar\omega}$ .

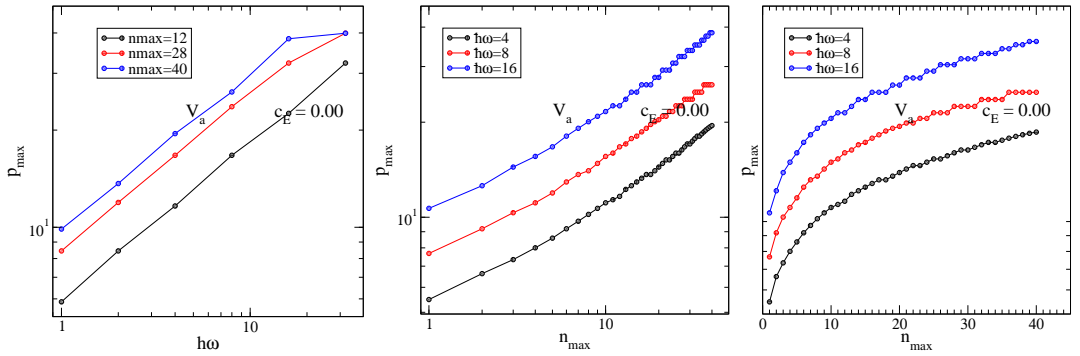


Figure B.4: Variation of  $p_{\max}$  with  $\hbar\omega$  on the left and with  $n$  on the right.

### B.3 Cutoff Derivation

Now, taking a more analytical approach to understanding the cutoffs inherent in the finite oscillator basis, let us first consider the momentum space harmonic oscillator function of Eq. B.1. This function is essentially a gaussian shifted to the right by the largest  $N_{\max}$  polynomial term. The local maximum will be correlated with the high-momentum cutoff,  $\Lambda_{UV}$ , or  $p_{\max}$ . Making the substitution,  $U = p_{\max}/\sqrt{m\hbar\omega}$  we

can write the large- $n$  approximation by

$$\psi(U) = A(2U)^n \exp^{-U^2/2} . \quad (\text{B.10})$$

Differentiating with respect to  $U$ , we get

$$\frac{d\psi}{dU} = (2U)^{n-1}(n - (2U)U) \exp^{-U^2/2} . \quad (\text{B.11})$$

The maximum, at  $\frac{d\psi}{dU} = 0$ , yields

$$U \sim \sqrt{n} \longrightarrow \Lambda_{UV} = p_{\max} \sim \sqrt{mN_{\max} \hbar\omega} . \quad (\text{B.12})$$

which is the large  $N_{\max}$  behavior for the ultraviolet cutoff caused by converting to the harmonic oscillator basis. As expected, when either  $N_{\max}$  or  $\hbar\omega$  is increased, then the scope of the basis also increases and we keep more of the momentum space potential.

For the infrared cutoff,  $\Lambda_{IR}$ , we can make the same analysis, but now using the coordinate space oscillator wavefunctions where  $p^2/m\hbar\omega \longrightarrow m\hbar\omega r^2$ . We again ask about the  $N_{\max}$  dependence of the local maximum of  $\psi(U)$ . Here we get a maximum extent in coordinate space,

$$r_{\max} = \sqrt{\frac{n\hbar^2}{m\hbar\omega}} \quad (\text{B.13})$$

which implies an infrared cutoff

$$\Lambda_{IR} \sim \sqrt{\frac{m\hbar\omega}{N_{\max}}} \quad (\text{B.14})$$

setting a bound on the size of objects that can be accurately described in a given  $N_{\max} \hbar\omega$  basis. When  $\hbar\omega$  grows large, individual oscillations are large and lose resolution on the small details in the momentum basis potential corresponding to large  $r$  structures. However, high  $N_{\max}$  polynomials have many small oscillations at low momenta compensating for the large  $\hbar\omega$  value. Thus, both  $\Lambda_{IR}$  and  $\Lambda_{UV}$  are pushed



back (down and up respectively) by increasing  $N_{\max}$  which one expects as the basis is extended towards completeness.

## B.4 Three-Dimensional Harmonic Oscillators

To build the NCSM in three-dimensions, we must use the isotropic Harmonic oscillator eigenfunctions [89],

$$\psi_{klm}(r, \theta, \phi) = N_{kl} r^l e^{-\nu r^2} L_k^{(l+1/2)}(2\nu r^2) Y_{lm}(\theta, \phi), \quad (\text{B.15})$$

where  $\nu$  is defined as

$$\nu \equiv \frac{\mu\omega}{2\hbar}, \quad (\text{B.16})$$

with  $\mu$  the reduced mass ( $m$  is now reserved for the magnetic moment quantum number) and  $\omega$  is again the oscillator parameter. The normalization constant,  $N_{kl}$ , is

$$N_{kl} = \sqrt{\sqrt{\frac{2\nu^3}{\pi}} \frac{2^{k+2l+3} k! \nu^l}{(2k+2l+1)!!}}. \quad (\text{B.17})$$

The

$$L_k^{(l+\frac{1}{2})}(2\nu r^2) \quad (\text{B.18})$$

are generalized Laguerre polynomials are given by

$$L_n^{(\alpha)}(x) = \frac{x^{-\alpha} e^x}{n!} \frac{d^n}{dx^n} (e^{-x} x^{n+\alpha}). \quad (\text{B.19})$$

The first few generalized Laguerre polynomials are:

$$\begin{aligned} L_0^{(\alpha)}(x) &= 1 \\ L_1^{(\alpha)}(x) &= -x + \alpha + 1 \\ L_2^{(\alpha)}(x) &= \frac{x^2}{2} - (\alpha + 2)x + \frac{(\alpha + 2)(\alpha + 1)}{2} \\ L_3^{(\alpha)}(x) &= \frac{-x^3}{6} + \frac{(\alpha + 3)x^2}{2} - \frac{(\alpha + 2)(\alpha + 3)x}{2} + \frac{(\alpha + 1)(\alpha + 2)(\alpha + 3)}{6} \end{aligned} \quad (\text{B.20})$$

The first several spherical harmonic functions

$$Y_\ell^m(\theta, \phi) = \sqrt{\frac{(2\ell + 1)(\ell - m)!}{4\pi(\ell + m)!}} P_\ell^m(\cos \theta) e^{im\phi}, \quad (\text{B.21})$$

are given by

$$\begin{aligned} Y_0^0(\theta, \phi) &= \frac{1}{2} \sqrt{\frac{1}{\pi}} & Y_2^{-2}(\theta, \phi) &= \frac{1}{4} \sqrt{\frac{15}{2\pi}} \sin^2 \theta e^{-2i\phi} \\ Y_1^{-1}(\theta, \phi) &= \frac{1}{2} \sqrt{\frac{3}{2\pi}} \sin \theta e^{-i\phi} & Y_2^{-1}(\theta, \phi) &= \frac{1}{2} \sqrt{\frac{15}{2\pi}} \sin \theta \cos \theta e^{-i\phi} \\ Y_1^0(\theta, \phi) &= \frac{1}{2} \sqrt{\frac{3}{\pi}} \cos \theta & Y_2^0(\theta, \phi) &= \frac{1}{4} \sqrt{\frac{5}{\pi}} (3 \cos^2 \theta - 1) \\ Y_1^1(\theta, \phi) &= \frac{-1}{2} \sqrt{\frac{3}{2\pi}} \sin \theta e^{i\phi} & Y_2^1(\theta, \phi) &= \frac{-1}{2} \sqrt{\frac{15}{2\pi}} \sin \theta \cos \theta e^{i\phi} \\ & & Y_2^2(\theta, \phi) &= \frac{1}{4} \sqrt{\frac{15}{2\pi}} \sin^2 \theta e^{2i\phi} \end{aligned} \quad (\text{B.22})$$

At large  $r$ , we can simplify the expression for  $\psi_{k\ell m}$  as

$$\begin{aligned} \psi_{k\ell m}(r, \theta, \phi) &\approx \sqrt{\left(\frac{\mu\omega}{2\hbar}\right)^{\ell+3/2}} r^\ell e^{-\nu r^2} (\nu r^2)^k Y_\ell^m(\theta, \phi) \\ &= \left(\frac{\mu\omega}{2\hbar}\right)^{3/4} r^{2k+\ell} \left(\sqrt{\frac{\mu\omega}{2\hbar}}\right)^{2k+\ell} e^{-\frac{\mu\omega}{2\hbar} r^2} Y_\ell^m(\theta, \phi). \end{aligned} \quad (\text{B.23})$$

If we make the substitution  $2k + \ell \rightarrow n$  this has exactly the form of Eq. (B.6) and we can make the same analysis of the cutoff as done in section B.3 for the one-dimensional oscillator functions. Indeed, the quantity  $n = 2k + \ell$  is the quantum number for the energy of a state in the three-dimensional harmonic oscillator trap. The eigenvalues are

$$E_n = (2k + \ell + 3/2)\hbar\omega \quad (\text{B.24})$$

with a degeneracy of  $(n + 1)(n + 2)/2$ .

So, the three-dimensional oscillator basis has the same variational properties as the one-dimensional discussed above. The exact values of  $\hbar\omega$  and convergence in  $N_{\max}$  (maximum allowed  $n = 2k + \ell$ ) will vary due to different potentials and dimensional factors such as the cube in the normalization factor. But the cutoff behavior is the same between the one- and three-dimensional cases.

## B.5 Variational Properties

Any harmonic oscillator basis such as the NCSM, both one- and three-dimensional, is a variational calculation in the two parameters,  $N_{\max}$  and  $\hbar\omega$ . Larger  $N_{\max}$  allows inclusion of more of the momentum basis potential, increasing  $\Lambda_{\text{UV}}$ . Larger  $\hbar\omega$  extends the reach of a given polynomial of order  $N_{\max}$  but damps the resolution of the polynomials oscillations, raising both  $\Lambda_{\text{UV}}$  and  $\Lambda_{\text{IR}}$ . Smaller  $\hbar\omega$  increases the resolution but hampers the reach of the  $N_{\max}$ th polynomial, resulting in lowering both  $\Lambda_{\text{UV}}$  and  $\Lambda_{\text{IR}}$ . So bigger  $N_{\max}$  is always better (except for increasing computational requirements) by raising  $\Lambda_{\text{UV}}$  and lowering  $\Lambda_{\text{IR}}$ , but the optimal  $\hbar\omega$  must result from a tuning of  $\Lambda_{\text{IR}}$  and  $\Lambda_{\text{UV}}$  at a particular  $N_{\max}$ .

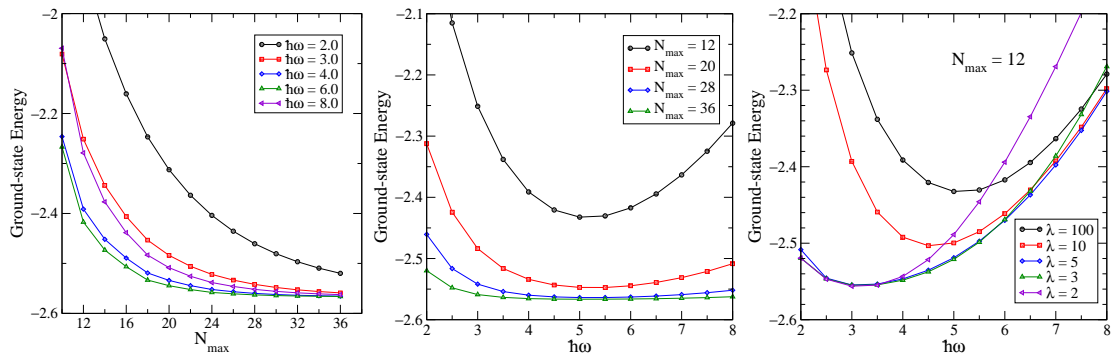


Figure B.5: Plots showing the variational nature of the harmonic oscillator basis and the effect of SRG transformations within it.

These variational properties are shown nicely in Fig. B.5. The left plot shows the increasing convergence with the size of the basis,  $N_{\max}$ . Here several select values of  $\hbar\omega$  show that one curve is optimal for most of the range in  $N_{\max}$  considered. As  $N_{\max}$  grows larger, more polynomials are available for the expansion of momentum basis wavefunctions and the dependence on  $\hbar\omega$  flattens out. The center panel also

shows this by plotting instead versus  $\hbar\omega$  where the minimum is clear and the increase in  $N_{\max}$  is apparent but less quantitative. Again the dependence on  $\hbar\omega$  flattens as  $N_{\max}$  grows. The overall goal in these calculations is to balance convergence in  $N_{\max}$  (bringing a reduced sensitivity to  $\hbar\omega$ ) with the increasing computational requirements the larger basis demands. This is further explored in Appendix D.

The far right plot of Fig. B.5 shows the effects the SRG has on convergence properties of a potential in the oscillator basis. The curves are plotted by taking a potential at a large  $N_{\max}$  ( $\sim 40$ ) and evolving it in that basis, then cutting it to a specified  $N_{\max}$  ( $\sim 28$ ) before computing the binding energy<sup>21</sup>. This procedure was repeated at multiple values of  $\hbar\omega$  for comparisons and we can see several effects. First, the SRG evolves the initial potential to a new and different Hamiltonian and therefore the optimal  $\hbar\omega$  for that Hamiltonian's expansion will be different. In fact, it will be lower due to the way in which the Hamiltonian has been altered; high momentum matrix elements have been reduced and simplified so that the Hamiltonian needs less basis size to achieve the same convergence as before. Therefore the basis can accommodate information with a smaller  $\hbar\omega$  and gets the benefit of increased resolution due to the smaller  $\hbar\omega$ . In other words, a lower  $\Lambda_{UV}$  is sufficient so a lower  $\Lambda_{IR}$  is affordable. Thus the optimal  $\hbar\omega$  shifts downward. Furthermore, each step in the evolution increases the convergence at a given basis size and so the overall dependence on  $\hbar\omega$  decreases and the curves flatten out as  $\lambda$  decreases.

<sup>21</sup>This calculation is analogous to the situation in Ref. [35] where the NN potential was evolved in momentum space ( $N_{\max} \rightarrow \infty$ ) and then converted to some finite oscillator basis.

## APPENDIX C

### SYMMETRIC JACOBI OSCILLATOR BASIS IN ONE AND THREE DIMENSIONS

#### C.1 Jacobi Coordinates

The initial (i.e., unevolved) one-dimensional Hamiltonian for  $A$  bosons of equal mass  $m$  with a local two-body potential has the first-quantized form (in units with  $\hbar = 1$ )

$$H = \frac{1}{2m} \sum_{i=1}^A k_i^2 + \sum_{i<j=1}^A V(x_i - x_j) , \quad (\text{C.1})$$

where the  $x_i$  are single-particle coordinates and the  $k_i$  are single-particle momenta. To connect to the nuclear problem of interest that uses potentials given in a momentum basis (e.g., chiral effective field theory potentials), we calculate matrix elements using harmonic oscillator basis states in Jacobi momentum coordinates. This representation also provides a clean visual interpretation of the SRG evolution of potentials.

With equal-mass particles, a convenient set of relative momentum Jacobi coordinates is defined by (for  $j = 1$  to  $A - 1$ )

$$p_j = \sqrt{\frac{j}{j+1}} \left( \frac{1}{j} \sum_{i=1}^j k_i - k_{j+1} \right) , \quad (\text{C.2})$$

where the  $k_i$  are the single-particle momenta of the  $A$  particles. This is one particular choice of normalization for the Jacobi coordinates. This choice is especially useful here

because it sets the reduced masses for each coordinate equal to each other, simplifying rotation operations performed later. We define the Fourier transform  $V(x_1 - x_2)$  to  $V(p_1, p'_1)$  as

$$V(p_1, p'_1) = \int V(\sqrt{2}\ell_1) e^{-i(p_1 - p'_1)\ell_1} d\ell_1, \quad (\text{C.3})$$

where  $\ell_1 = (x_1 - x_2)/\sqrt{2}$  is the coordinate conjugate to the Jacobi momentum  $p_1$ . We introduce a set of harmonic oscillator states  $|n_j\rangle$  corresponding to each of the coordinates of Eq. (C.2), so a general product basis state has the form

$$\prod_{j=1}^{A-1} \langle p_j | n_j \rangle, \quad (\text{C.4})$$

with  $n_j = 0, 1, 2, \dots, N_{\max}$  for each  $j$ . In the next section we discuss how to build linear combinations of these states that have the appropriate symmetry.

## C.2 Transformation Brackets

Transformation brackets are the expansion coefficients in the oscillator basis of one system of coordinates in terms of another [90, 91]. We apply them to relate two different choices of Jacobi coordinates. Here, we show the relevant transformation using the three-particle harmonic oscillator states defined in Eq. (C.4) and then generalize at the end.

The single particle momenta are  $k_1$ ,  $k_2$ , and  $k_3$ . The unprimed Jacobi momenta [see Eq.( C.2)] are

$$\begin{aligned} p_1 &= \frac{1}{\sqrt{2}}(k_1 - k_2), \\ p_2 &= \sqrt{\frac{2}{3}}((k_1 + k_2)/2 - k_3), \end{aligned} \quad (\text{C.5})$$

and the primed coordinates are obtained from exchanging  $k_2$  and  $k_3$ :

$$\begin{aligned} p'_1 &= \frac{1}{\sqrt{2}}(k_1 - k_3), \\ p'_2 &= \sqrt{\frac{2}{3}}((k_1 + k_3)/2 - k_2). \end{aligned} \tag{C.6}$$

After some algebra, the transformation that exchanges the last two particles (i.e.,  $k_2$  and  $k_3$ ) can be written as

$$\begin{pmatrix} p'_1 \\ p'_2 \end{pmatrix} = \begin{pmatrix} \frac{1}{2} & \frac{\sqrt{3}}{2} \\ \frac{\sqrt{3}}{2} & -\frac{1}{2} \end{pmatrix} \begin{pmatrix} p_1 \\ p_2 \end{pmatrix}. \tag{C.7}$$

which enables us to express the primed oscillator states in terms of the unprimed ones.

We denote the three-particle oscillator basis by  $|n_1 n_2\rangle = \eta_1^\dagger \eta_2^\dagger |0\rangle$  where we have set  $\hbar\omega = 1$  for simplicity in this appendix. Note that the transformation brackets will not depend on the value of  $\hbar\omega$ . The transformation that exchanges the last two single-particle coordinates can again be written as

$$\begin{pmatrix} \eta'_1 \\ \eta'_2 \end{pmatrix} = \begin{pmatrix} \frac{1}{2} & \frac{\sqrt{3}}{2} \\ \frac{\sqrt{3}}{2} & -\frac{1}{2} \end{pmatrix} \begin{pmatrix} \eta_1 \\ \eta_2 \end{pmatrix}, \tag{C.8}$$

The derivation of the harmonic oscillator transformation bracket follows directly as

$$\begin{aligned}
\langle n'_1 n'_2 | n_1 n_2 \rangle_3 &= \langle 0 | \frac{1}{\sqrt{n_1! n_2! n'_1! n'_2!}} \eta_1^{m'_1} \eta_2^{m'_2} \eta_1^{\dagger n_1} \eta_2^{\dagger n_2} | 0 \rangle \\
&= \langle 0 | \frac{1}{\sqrt{n_1! n_2! n'_1! n'_2!}} \left[ \frac{1}{2} \eta_1 + \frac{\sqrt{3}}{2} \eta_2 \right]^{n'_1} \\
&\quad \times \left[ \frac{\sqrt{3}}{2} \eta_1 - \frac{1}{2} \eta_2 \right]^{n'_2} \eta_1^{\dagger n_1} \eta_2^{\dagger n_2} | 0 \rangle \\
&= \langle 0 | \frac{1}{\sqrt{n_1! n_2! n'_1! n'_2!}} \sum_{k=0}^{n'_1} \binom{n'_1}{k} \left[ \frac{1}{2} \eta_1 \right]^{n'_1-k} \left[ \frac{\sqrt{3}}{2} \eta_2 \right]^k \\
&\quad \times \sum_{j=0}^{n'_2} \binom{n'_2}{j} \left[ \frac{\sqrt{3}}{2} \eta_1 \right]^{n'_2-j} \left[ -\frac{1}{2} \eta_2 \right]^j \eta_1^{\dagger n_1} \eta_2^{\dagger n_2} | 0 \rangle \\
&= \frac{1}{\sqrt{n_1! n_2! n'_1! n'_2!}} \sum_{k=0}^{n'_1} \sum_{j=0}^{n'_2} \binom{n'_1}{k} \binom{n'_2}{j} \left[ \frac{1}{2} \right]^{n'_1-k+j} \left[ \frac{\sqrt{3}}{2} \right]^{n'_2-j+k} (-1)^j \\
&\quad \times n_1! n_2! \delta_{n'_1-k+n'_2-j, n_1} \delta_{k+j, n_2} \\
&= \sqrt{\frac{n_1! n_2!}{n'_1! n'_2!}} \sum_{k=0}^{n_1} \binom{n'_1}{k} \binom{n'_2}{n_2-k} \left[ \frac{1}{2} \right]^{n'_1+n_2-2k} \left[ \frac{\sqrt{3}}{2} \right]^{n'_2-n_2+2k} (-1)^{n_2} \quad (\text{C.9})
\end{aligned}$$

The second line is obtained from operating the transformation on the creation operators  $\eta_s^\dagger$ . The third line is the application of the binomial theorem. The fourth balances the oscillator creation and annihilation, and the fifth is just some simplification.

In the general A-particle system the transformation to exchange the last two particles,  $k_{A-1}$  and  $k_A$ , can be written as

$$\begin{pmatrix} \eta'_{A-2} \\ \eta'_{A-1} \end{pmatrix} = \begin{pmatrix} \sqrt{\frac{1}{d+1}} & \sqrt{\frac{d}{d+1}} \\ \sqrt{\frac{d}{d+1}} & -\sqrt{\frac{1}{d+1}} \end{pmatrix} \begin{pmatrix} \eta_{A-2} \\ \eta_{A-1} \end{pmatrix}, \quad (\text{C.10})$$

where  $d = (A-1)^2 - 1$  is the number of generators of the rotation group,  $U(A-1)$ , or the group  $U(A)$  with the center of mass coordinate held fixed. An expression for the bracket  $\langle n_{A-2} n_{A-1} | n'_{A-2} n'_{A-1} \rangle_{A(A-2)}$ , which appears in Eq. (C.14), is obtained from Eq. (C.9) by substituting the general coordinate transformation Eq. (C.10) for the



three-particle transformation Eq. (C.8), or  $\sqrt{1/(d+1)}$  and  $\sqrt{d/(1+d)}$  for  $1/2$  and  $\sqrt{3}/2$ .

### C.3 Symmetrization

We carry out the SRG evolution for each  $A$ -particle subsystem in a complete basis of properly symmetrized states, which will be linear combinations of the basis states of Eq. (C.4). The symmetrization procedure is adapted from the procedure developed for NCSM calculations [11, 12, 13]. This entails symmetrizing first the two-particle system and then using a recursive procedure to go from the  $(A-1)$ -particle basis to an  $A$ -particle basis. At each stage we keep only symmetric states, identified as eigenstates of the symmetrizer with eigenvalue unity.

The two-particle system is specified by the oscillator number  $n_1$ . The symmetrizer is  $(1 + P_{12})/2$ , where  $P_{ij}$  is the exchange operator between particles  $i$  and  $j$ . Because  $P_{12}|n_1\rangle = (-1)^{n_1}|n_1\rangle$ , the symmetrizer in the two-particle case has eigenvalue one acting on states with  $n_1$  even and zero when acting on states with  $n_1$  odd. Thus the symmetric basis states have  $n_1$  even and we simply omit the odd states. Following conventions from Ref. [11], we label these eigenstates as  $|N_2 i_2\rangle$ , where  $N_2$  is the total oscillator number of the symmetric state and  $i_2$  is an arbitrary label that distinguishes states degenerate in  $N_2$ . In the two-particle case the notation is trivial, with  $N_2 = n_1$  even and  $i_2 = 1$ . We write eigenstate projection coefficients as  $\langle N_2 i_2 || n_1 \rangle = \delta_{N_2, n_1} (1 + (-1)^{n_1})/2$ . These are referred to in the literature as the ‘‘coefficients of fractional parentage’’.

A three-particle basis is specified by product states of the two-body symmetric eigenstates,  $|N_2 i_2\rangle$ , and single-particle states with the oscillator number corresponding to the third particle,  $|n_2\rangle$ . The symmetrizer for this system is governed by the permutation group,  $S_3$ , which can be defined by just two of its generators. Here we choose the permutation operators  $P_{12}$  and  $P_{23}$ . The symmetrization operator can be written as

$$S = \frac{1}{6}(1 + P_{12} + P_{23} + P_{12}P_{23} + P_{23}P_{12} + P_{12}P_{23}P_{12}) . \quad (\text{C.11})$$

We build this symmetrizer in the basis  $|N_2 i_2; n_2\rangle \equiv |N_2 i_2\rangle |n_2\rangle$  where the states  $|N_2 i_2\rangle$  are already eigenstates of  $P_{12}$  with eigenvalue one, so Eq. (C.11) reduces to  $S = (1 + 2P_{23})/3$ .

In this basis, the matrix elements of  $P_{23}$  can be expressed as

$$\langle N'_2 i'_2; n'_2 | P_{23} | N_2 i_2; n_2 \rangle = \delta_{N', N} \langle n'_1 n'_2 | n_1 n_2 \rangle_3 , \quad (\text{C.12})$$

where  $N \equiv N_2 + n_2 = N'_2 + n'_2 = N'$  and  $\langle n'_1 n'_2 | n_1 n_2 \rangle_3$  is the one-dimensional harmonic oscillator transformation bracket for particles with mass ratio 3 [92]. We construct these transformation brackets and generalize to mass ratio  $d$  in section C.2. By diagonalizing this symmetrizer we identify the symmetric eigenstates of the system as the ones with eigenvalue unity. We keep only those states and discard the others. This set of eigenvectors gives us the coefficients of fractional parentage,  $\langle N_2 i_2; n_2 || N_3 i_3 \rangle$ , of the three-boson symmetric eigenstates,  $|N_3 i_3\rangle$ , in terms of the original partially symmetrized three-particle space,  $|N_2 i_2; n_2\rangle$ . Note that  $i_3$  is not trivial like  $i_2$ , because in the three-body system there are eigenstates degenerate in the total oscillator

number,  $N_2 + n_2$ . The label  $i_3$  keeps track of those degeneracies. We find in the one-dimensional system of bosons that the fraction of symmetric basis states for  $A = 3$  is about one-fifth. For  $A = 4$  the reduction in number of states is above 90%.

The symmetrizer can now be coded directly in the three-particle oscillator space. A picture of the resulting matrix is shown in Fig. C.1. This matrix has the three-particle oscillator basis states organized in a block diagonal form because the total oscillator number,  $N = n_1 + n_2$ , is a conserved quantum number proportional to the total energy of a state.

Remembering that we need only the physical eigenstates of the symmetrizer, we diagonalize the matrix and obtain the eigenvectors. We keep only those vectors which have nonzero eigenvalue (the physical states), thus resulting in a symmetrizing matrix about one-fifth the size of the original oscillator basis. A picture of the sorted eigenvectors is shown in Fig. C.2. These are all the symmetric states as expressed in the three-particle oscillator basis. The symmetrizer in this basis is, of course, diagonal, and all the eigenvalues are unity.

The color scheme in Figs. C.1 and C.2 is displayed to the right of each graph; green is zero, red is positive, and blue is negative. Notice that the eigenvectors are normalized to one. The easiest non-trivial case is the second vector where each of the two components is  $1/\sqrt{2} \approx .7$ , which is shown in a bright red.

To construct the basis states for higher  $A$ , we generalize this procedure. To go from  $A - 1$  to  $A$  we need only to symmetrize between the last two particles, so we construct the symmetrizer

$$S_A = \frac{1}{A}(1 + (A - 1)P_{(A-1)A}) \quad (\text{C.13})$$

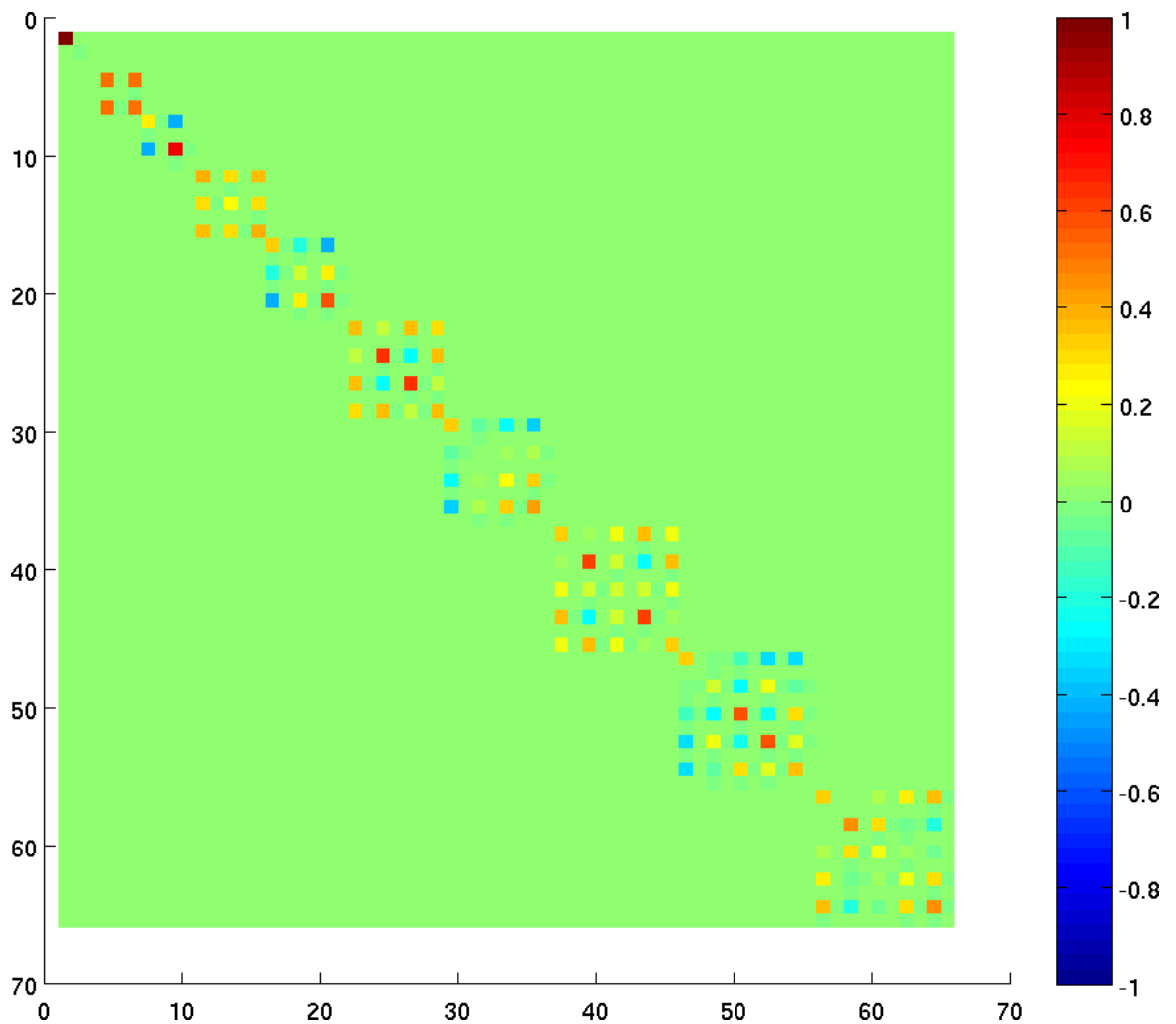


Figure C.1: The full symmetrizer for the  $|N_2 i_2; n_2\rangle$  space, with both physical and spurious states. A small,  $N_{\max} = 10$ , basis is shown for clarity. Note also that Matlab has chopped off the last column when making the figure; this is a symptom of my very simple plotting routine.

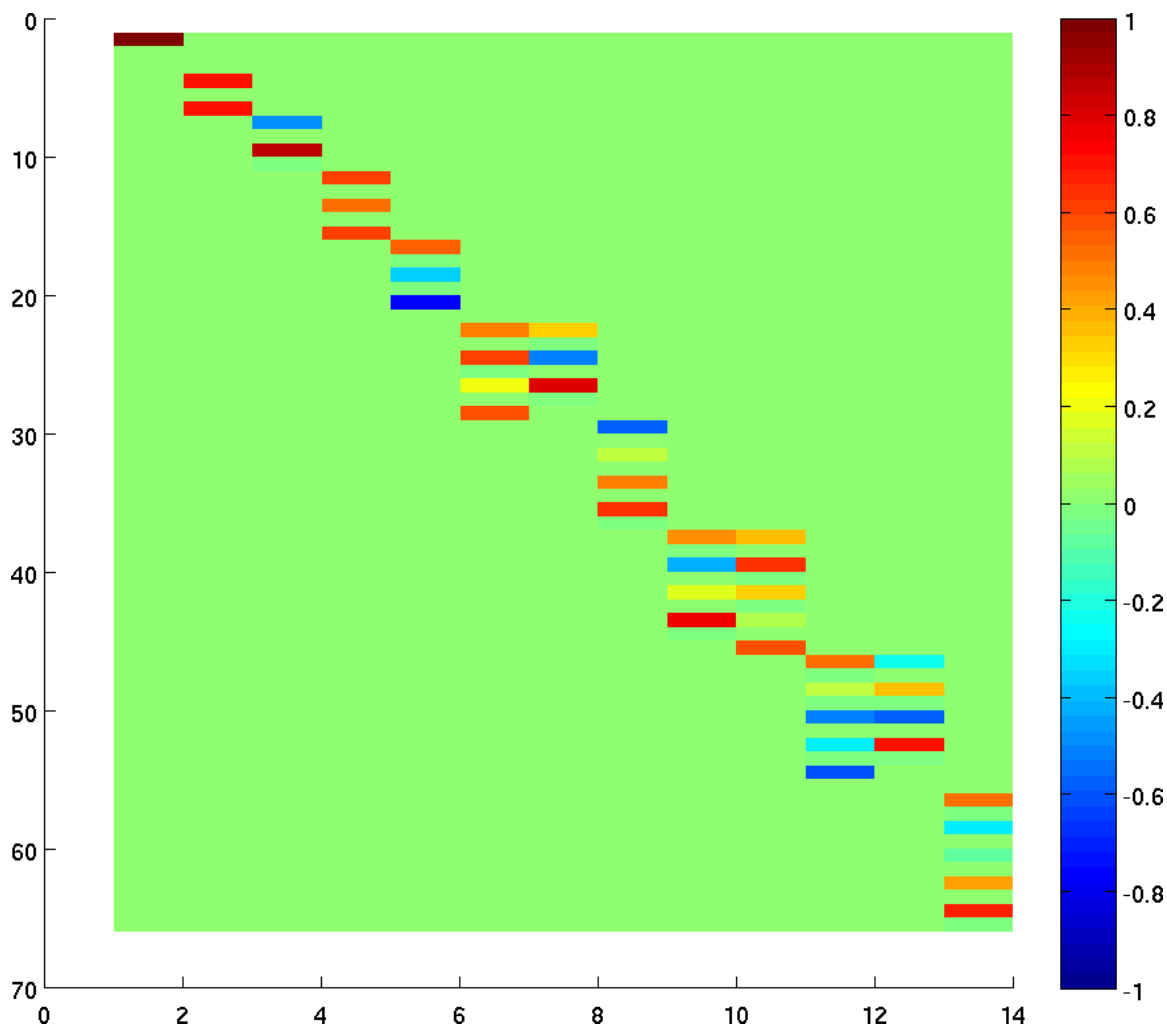


Figure C.2: The physical eigenvectors of the symmetrizer. Note vector components corresponding to  $N_{\max}$  blocks in Fig. C.1. The same size basis as in Fig. C.1,  $N_{\max} = 10$ , is shown. Again, Matlab has chopped off the last column.

in the space of  $(A-1)$ -particle symmetric eigenstates and the additional Jacobi state,  $n_{A-1}$ . We label the basis of this space as  $|N_{A-1}i_{A-1}; n_{A-1}\rangle$ . The matrix element of the exchange operator in this space is

$$\begin{aligned} & \langle N'_{A-1}i'_{A-1}; n'_{A-1} | P_{(A-1)A} | N_{A-1}i_{A-1}; n_{A-1} \rangle \\ &= \delta_{N'_{A-1}+n'_{A-1}, N_{A-1}+n_{A-1}} \sum \langle N'_{A-1}i'_{A-1} || N_{A-2}i_{A-2}; n'_{A-2} \rangle \\ & \quad \times \langle N_{A-2}i_{A-2}; n_{A-2} || N_{A-1}i_{A-1} \rangle \langle n'_{A-2}n'_{A-1} | n_{A-2}n_{A-1} \rangle_{A(A-2)} \end{aligned} \quad (\text{C.14})$$

where the sum is over  $N_{A-2}$ ,  $i_{A-2}$ ,  $n_{A-2}$  and  $n'_{A-2}$ . The only significant difference from the three-particle case is that we must sum over the components of the  $A-1$  subcluster symmetric states to get all the contributions to the exchange of the last two bosons,  $n_{A-2}$  and  $n_{A-1}$ . The parameter  $d = A(A-2)$  can be derived by taking the last two Jacobi coordinates  $p_{A-2}$  and  $p_{A-1}$ , as defined in Eq. (C.2), and finding the transformation that exchanges particles labeled by  $k_{A-1}$  and  $k_A$ . This procedure was explained in section C.2

For fermions, we need a complete basis of fully anti-symmetrized states. If we consider the one-flavor case, the procedure for our one-dimensional model is a trivial modification of Eqs.(C.11) and (C.13), namely all odd permutations come with a minus sign. Thus, for  $A=3$  the anti-symmetrizer can be written

$$A = \frac{1}{3}(1 - 2P_{23}), \quad (\text{C.15})$$

where  $P_{23}$  acts on the flavor space as well. If there are more flavors than particles and the interaction is flavor independent, the spatial wavefunction for the ground state will be symmetric and correspond to our boson ground state wavefunctions. For realistic three-dimensional nuclei, the required construction of an anti-symmetric

Jacobi basis with full angular momentum coupling has been worked out for the NCSM by Navratil et al. [11, 12, 13] and is briefly discussed in section C.5.

## C.4 Hamiltonian Matrix Elements

To obtain the Hamiltonian in the symmetric eigenbasis of the general  $A$ -particle system, we employ a recursive embedding procedure that utilizes the partially symmetric bases developed for the symmetrization operator. First we treat the kinetic energy and then the potential.

The relative kinetic energy in the three-particle system is the total minus the center-of-mass kinetic energies:

$$\begin{aligned}
T_{\text{rel}} &\equiv T_{\text{tot}} - T_{\text{cm}} \\
&= \frac{k_1^2}{2m} + \frac{k_2^2}{2m} + \frac{k_3^2}{2m} - \frac{(k_1 + k_2 + k_3)^2}{2(3m)} \\
&= \frac{p_1^2 + p_2^2}{2m}, \tag{C.16}
\end{aligned}$$

where the  $p_i$ 's are defined in Eq. (C.2). Momentum basis states are organized by increasing kinetic energy. We can project  $T_{\text{rel}}$  directly onto the three-particle oscillator basis by using the ladder operator definitions of the Jacobi momenta. The projection of  $T_{\text{rel}}$  into the  $|n_1 n_2\rangle$  basis is

$$\begin{aligned}
\langle n'_1 n'_2 | T_{\text{rel}} | n_1 n_2 \rangle &= \langle n'_1 n'_2 | \frac{p_1^2 + p_2^2}{2m} | n_1 n_2 \rangle \\
&= \frac{1}{2m} \frac{-m\omega}{2} \langle n'_1 n'_2 | (\eta_1^\dagger - \eta_1)^2 + (\eta_2^\dagger - \eta_2)^2 | n_1 n_2 \rangle, \tag{C.17}
\end{aligned}$$

where the  $\eta_1$  and  $\eta_2$  operators act on the  $n_1$  and  $n_2$  spaces, respectively. Continuing, we get

$$\begin{aligned}
\langle n'_1 n'_2 | T_{\text{rel}} | n_1 n_2 \rangle &= \frac{1}{2m} \frac{-m\omega}{2} [\langle n'_1 | (\eta_1^\dagger - \eta_1)^2 | n_1 \rangle \delta_{n_2, n'_2} + \langle n'_2 | (\eta_2^\dagger - \eta_2)^2 | n_2 \rangle \delta_{n_1, n'_1}] \\
&= \frac{-\omega}{4} \left[ (\sqrt{(n_1+1)(n_1+2)} \delta_{n'_1, n_1+2} + \sqrt{n_1(n_1-1)} \delta_{n'_1, n_1-2} \right. \\
&\quad \left. - (2n_1+1) \delta_{n'_1, n_1} \right) \delta_{n'_2, n_2} \\
&\quad + (\sqrt{(n_2+1)(n_2+2)} \delta_{n'_2, n_2+2} + \sqrt{n_2(n_2-1)} \delta_{n'_2, n_2-2} \\
&\quad \left. - (2n_2+1) \delta_{n'_2, n_2} \right) \delta_{n'_1, n_1} \Big]. \tag{C.18}
\end{aligned}$$

As noted, we keep only the  $n_1$ -even states using the projector  $\langle N_2 i_2 || n_1 \rangle$ , and we can symmetrize the full three-particle system with the symmetric eigenstates,  $|N_3 i_3\rangle$  whose components are given by  $\langle N_3 i_3 || N_2 i_2; n_2 \rangle$ .

To derive the  $A$ -body kinetic energy in the symmetrized basis,  $(T_A)_{\text{sym}}$ , we use a recursive procedure on the  $(A-1)$ -body result to find the  $A$ -particle space operator matrix elements:

$$\begin{aligned}
(T_A)_{\text{sym}} &= \langle N'_A i'_A | T_A | N_A i_A \rangle \equiv \langle N'_A i'_A | \sum_{i=1}^{A-1} p_i^2 / 2m | N_A i_A \rangle \\
&= \langle N'_A || N'_{A-1} n'_{A-1} \rangle \langle N'_{A-1} n'_{A-1} | T_A | N_{A-1} n_{A-1} \rangle \langle N_{A-1} n_{A-1} || N_A \rangle \\
&= \langle N'_A || N'_{A-1} n'_{A-1} \rangle \left[ \langle N'_{A-1} n'_{A-1} | (T_{A-1})_{\text{sym}} \right. \\
&\quad \left. + p_{A-1}^2 / 2m | N_{A-1} n_{A-1} \rangle \right] \langle N_{A-1} n_{A-1} || N_A \rangle \\
&= \langle N'_A || N'_{A-1} n'_{A-1} \rangle \left[ \langle N'_{A-1} | (T_{A-1})_{\text{sym}} | N_{A-1} \rangle \delta_{n'_{A-1}, n_{A-1}} \right. \\
&\quad \left. + \delta_{N'_{A-1}, N_{A-1}} \langle n'_{A-1} | p_{A-1}^2 / 2m | n_{A-1} \rangle \right] \langle N_{A-1} n_{A-1} || N_A \rangle \\
&= \langle N'_A || N'_{A-1} n'_{A-1} \rangle \left[ (T_{A-1})_{\text{sym}} \delta_{n'_{A-1}, n_{A-1}} \right. \\
&\quad \left. - \frac{\omega}{4} \delta_{N'_{A-1}, N_{A-1}} (\delta_{n'_{A-1}, n_{A-1}} (2n_{A-1} + 1) - \delta_{n'_{A-1}+2, n_{A-1}} \sqrt{n_{A-1}^2 - n_{A-1}} \right. \\
&\quad \left. - \delta_{n'_{A-1}-2, n_{A-1}} \sqrt{(n_{A-1}+1)(n_{A-1}+2)}) \right] \langle N_{A-1} n_{A-1} || N_A \rangle, \tag{C.19}
\end{aligned}$$



where we have suppressed the  $i_A$ 's and  $i_{A-1}$ 's for simplicity after the first line. Intermediate summations over  $N_{A-1}$ ,  $n_{A-1}$ ,  $i_{A-1}$ ,  $N'_{A-1}$ ,  $n'_{A-1}$ , and  $i'_{A-1}$  are implicit.

In the same manner as the kinetic energy, we can recursively embed the potential in the  $A$ -particle space, starting with the two-body interaction between the first two particles. Because we are working in fully symmetrized few-body spaces we do not need to consider all pair-wise interactions, but only one such pair and scale by the number of interactions. For instance, in the three-particle system the full two-body interaction is  $V^{(2)} = V_{12} + V_{23} + V_{13} = 3V_{12}$ . In a general  $A$ -particle space, this becomes  $V^{(2)} = \binom{A}{2}V_{12}$ . The matrix element of a two-body potential,  $V_{12}$ , in the relative coordinate harmonic oscillator basis,  $|n_1\rangle$ , is  $\langle n'_1|V_{12}|n_1\rangle = \int \langle n'_1|p'_1\rangle \langle p'|V_{12}|p\rangle \langle p|n_1\rangle dp dp'$  where the matrix elements of  $\langle p'|V_{12}|p\rangle$  are given by Eq. (C.3).

Once in the oscillator basis, embedding in a larger particle space is a straightforward process. Starting with the two-body interaction,  $V_{12}$ , the two-body oscillator symmetric states are isolated using the projector  $\langle N_2 i_2 | n_1 \rangle$  which picks out just the  $n_1$ -even states. Embedding this interaction in the three-particle space involves adding a new Jacobi coordinate,  $|n_2\rangle$ , to the existing system. With respect to the two-body interaction,  $V_{12}$ , this additional coordinate is associated with a delta function,  $\delta_{n_2, n'_2}$ . Finally we obtain the symmetric three-particle states by using the projector,  $\langle N_3 i_3 | |N_2 i_2; n_2\rangle$ . Multiplying by  $\binom{3}{2} = 3$  gives us the full strength of the two-body interaction.

In general we can write this procedure as an expansion of the final  $A$ -particle symmetric space matrix elements of  $V_{12}$ :

$$\begin{aligned}
(V_A^{(2)})_{\text{sym}} &= \langle N'_A i'_A | V_A^{(2)} | N_A i_A \rangle \equiv \binom{A}{2} \langle N'_A i'_A | V_{12} | N_A i_A \rangle \\
&= \langle N'_A || N'_{A-1} n'_{A-1} \rangle \langle N'_{A-1} n'_{A-1} | V_A | N_{A-1} n_{A-1} \rangle \langle N_{A-1} n_{A-1} || N_A \rangle \\
&= \langle N'_A || N'_{A-1} n'_{A-1} \rangle \\
&\quad \times \langle N'_{A-1} n'_{A-1} | (V_{A-1})_{\text{sym}} \delta_{n'_{A-1}, n_{A-1}} | N_{A-1} n_{A-1} \rangle \langle N_{A-1} n_{A-1} || N_A \rangle.
\end{aligned} \tag{C.20}$$

where again we have dropped the  $i_A$ 's after the first line for simplicity and intermediate sums are implicit. We remind the reader that  $n_{A-1}$  can only take values from 0 to  $N - N_{A-1}$ , where  $N$  is the total oscillator quantum number used to organize the states. We start with the two-particle space and work our way up to the  $A$ -body space, embedding the interactions successively in each sector using Eq. (C.20).

When symmetrizing  $V_A$  we must embed the symmetrized  $V_{A-1}$  with the appropriate combinatoric factor included as explained above. This factor derives from the fact that we had embedded a 2-body force in the  $A - 1$  space that is now to be extracted and embedded in the  $A$ -particle space. Thus we must remove the old factor  $\binom{A-1}{2}$  and multiply by the new  $\binom{A}{2}$  factor, which has the net effect of multiplying by  $A/(A-2)$ .

Any initial three-body force (discussed below) is embedded in the same manner as above except that it originates in the three-particle space. The initial three-body force is a function of two Jacobi momenta, which we transform directly into the partially symmetrized three-particle oscillator space and then use all of the same embedding procedures developed above. Note that two- and three-body forces must be embedded in higher spaces with different symmetry factors,  $\binom{A}{2}$  and  $\binom{A}{3}$  respectively.

In previous formulations of this recursive approach [11], subsequent potential embeddings are achieved by making a change of coordinates for the last two Jacobi momenta. For systems with  $A > 5$ , the three-body force requires a similar change of coordinates for the last three Jacobi momenta. Such a scheme is unnecessary here.

## C.5 Three-Dimensional NCSM

In this thesis, only the one-dimensional NCSM was built for SRG studies. However, the three-dimensional codes were modified and used for the realistic calculations in chapter 5. In three dimensions the Jacobi harmonic oscillator basis differs in several significant ways that complicate the expressions involved considerably, though in a straightforward way. However, the basic form of the basis remains the same as in the one-dimensional case.

The three-dimensional NCSM basis is, like the one-dimensional case, organized in  $N_{\max}$  blocks, so scaling up the basis size or making cuts to study decoupling is a simple matter. It is variational in  $N_{\max}$  and  $\hbar\omega$  as noted in App. B. It is built recursively from one  $A$ -body sector to the next, and the Hamiltonian is embedded in subsequent sectors with combinatoric factors, taking advantage of the symmetry properties.

The three-dimensional NCSM was built to calculate systems of nucleons, which are fermions, while the one-dimensional model was built based on a system of bosons with no spin or angular momentum. So in three-dimensions, we have to build an antisymmetrizer to find fully antisymmetric states in which fermions would reside. This still employs the same strategy of building on the  $A - 1$  subcluster. So a new Jacobi coordinate is added to the  $A - 1$  space and the matrix elements of the

antisymmetrizer,

$$\chi = \frac{1}{A}(1 - (A - 1)P_{(A-1)A}) , \quad (\text{C.21})$$

are computed. As before,  $P_{(A-1)A}$  is the permutation operator between the  $A$ th and  $(A - 1)$ st nucleons. Here the only difference is the minus sign. And the fact that  $P$  now also transforms angular momenta.

Now in three dimensions, we use the three-dimensional isotropic harmonic oscillator wavefunctions as displayed in Sec. B.4. The quantum numbers of the nuclear system are now  $n, \ell, s, j$ , and  $t$ , the radial, orbital angular momentum, spin, total angular momentum, and isospin of the state. In the three-dimensional oscillator, the conserved energy is  $N = 2n + \ell$  which will impact embedding procedures from one  $N_{\max}$  sized basis to another. Now the anti-symmetrized states are labeled as

$$\begin{aligned} |N_A i_A J_A T_A\rangle &= \sum \langle N_{A-1} i_{A-1} J_{A-1} T_{A-1}; n_{A-1} \ell_{A-1} j_{A-1} || N_A i_A J_A T_A\rangle \\ &\quad \times |N_{A-1} i_{A-1} J_{A-1} T_{A-1}; n_{A-1} \ell_{A-1} j_{A-1}\rangle , \end{aligned} \quad (\text{C.22})$$

where the  $\langle N_{A-1} i_{A-1} J_{A-1} T_{A-1}; n_{A-1} \ell_{A-1} j_{A-1} || N_A i_A J_A T_A\rangle$  are the three-dimensional coefficients of fractional parentage. These are given by the eigenstates of the antisymmetrizer in the non-antisymmetrized basis just as their one-dimensional counterparts were obtained from the eigenstates of the symmetrizer.

To build the antisymmetrizer,  $\chi$ , the matrix elements of  $P_{(A-1)A}$  in the non-antisymmetrized basis can be written as

$$\begin{aligned}
& \langle N'_{A-1} i'_{A-1} J'_{A-1} T'_{A-1}; n'_{A-1} \ell'_{A-1} j'_{A-1} JT | P_{(A-1)A} | N_{A-1} i_{A-1} J_{A-1} T_{A-1}; n_{A-1} \ell_{A-1} j_{A-1} JT \rangle \\
&= \delta_{N',N} \sum \langle N_{A-2} i_{A-2} J_{A-2} T_{A-2}; n'_{A-2} \ell'_{A-2} j'_{A-2} || N'_{A-1} i'_{A-1} J'_{A-1} T'_{A-1} \rangle \\
&\quad \times \langle N_{A-2} i_{A-2} J_{A-2} T_{A-2}; n_{A-2} \ell_{A-2} j_{A-2} || N_{A-1} i_{A-1} J_{A-1} T_{A-1} \rangle \\
&\quad \times T_{A-1} T'_{A-1} (-1)^{T_{A-1}+T'_{A-1}+j_{A-2}+j'_{A-2}} \begin{Bmatrix} 1/2 & T_{A-2} & T_{A-1} \\ 1/2 & T & T'_{A-1} \end{Bmatrix} \\
&\quad \times j'_{A-2} j_{A-2} j'_{A-1} j_{A-1} J'_{A-1} J_{A-1} K^2 \begin{Bmatrix} J_{A-2} & j'_{A-2} & J'_{A-1} \\ j_{A-2} & K & j'_{A-1} \\ J_{A-1} & j_{A-1} & J \end{Bmatrix} \\
&\quad \times \begin{Bmatrix} \ell'_{A-2} & \ell_{A-1} & K \\ j_{A-1} & j'_{A-2} & 1/2 \end{Bmatrix} \begin{Bmatrix} \ell_{A-2} & \ell'_{A-1} & K \\ j'_{A-1} & j_{A-2} & 1/2 \end{Bmatrix} \begin{Bmatrix} \ell'_{A-1} & \ell_{A-2} & K \\ \ell_{A-1} & \ell'_{A-2} & L \end{Bmatrix} \\
&\quad \times L^2 (-1)^{\ell_{A-2}+\ell'_{A-1}+L} \langle n'_{A-1} \ell'_{A-1} n'_{A-2} \ell'_{A-2} L | n'_{A-2} \ell'_{A-2} n'_{A-1} \ell'_{A-1} L \rangle_{A(A-2)}, \quad (C.23)
\end{aligned}$$

where the quantities in curly brackets are the Wigner  $6j$  and  $9j$  symbols used to compute the couplings between the angular momenta and isospin quantum numbers. The last line is the three-dimensional oscillator transformation bracket as derived in various sources with various methods [90, 91, 92].

Given the scaling properties of this basis discussed in appendix D, several techniques have been developed to improve the efficiency of the three-dimensional technique. In Ref. [93] a method is introduced that allows computation of only some antisymmetrizer matrix elements instead of requiring the full antisymmetrizer. Another technique deals with the cumbersome increase of angular momentum channels with  $A$ . Some authors [94] have developed techniques to better organize these channels and make the coding more manageable. Another approach to this problem is to convert to the single-particle, or Slater determinant, basis where the all the angular momentum embedding procedures are more straightforward. However, those

calculations require large clusters and sophisticated memory handling techniques to calculate even the lightest nuclei at small  $N_{\max}$ . The details of the single-particle basis scaling are discussed in appendix D. A one-dimensional single-particle basis was constructed and is presented in appendix F.

## APPENDIX D

### SCALING PROPERTIES

In this appendix we document the computational scaling features of the various calculations in this thesis. An introduction to the scaling issues involved in schemes such as the NCSM is necessary to appreciate the computational improvements brought about by the SRG.

#### D.1 Momentum Space NN calculations

The first problems addressed in chapter 3 involved applying the SRG to interactions projected onto a momentum representation. The mesh used here is most often gaussian quadrature with the grid dimension at about 100. Figure D.1 shows the time as a function of the evolution parameter,  $s$  to evolve two different potentials, on the left a  $\chi$ EFT and on the right AV18, in several partial waves. We expect the evolution to be linear in  $s$  and indeed find such behavior. On the left plot, as  $s$  increases, we find no hint of stiffening of the differential equations. The dependence is strictly linear all the way to  $s = 1$  ( $\lambda = 1$ ).

The right, log-log, plot of Argonne partial waves shows something a little more interesting. At smaller  $s$  the evolution is also linear, but as  $s$  increases, the dependence in some partial waves stiffens somewhat. Some investigations suggest this may happen

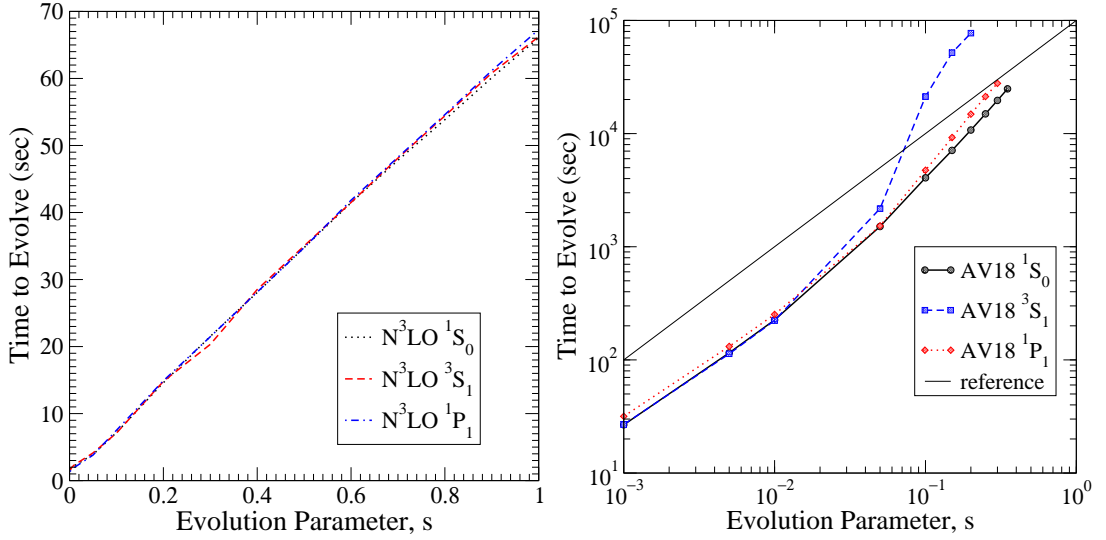


Figure D.1: SRG timings vs the parameter  $s$  show no stiffening for large  $s$  (small  $\lambda$ ). The left shows timing results for N<sup>3</sup>LO (500 MeV) potentials in several partial waves and the right shows the same for Argonne  $v_{18}$  but in a log-log plot.

when the potential has been driven to the desired decoupling and due to the larger number of matrix elements the flow is working hard to maintain a degree of accuracy that is unnecessary. It seems that freezing the high energy parts of the potential, when they have reached a sufficient evolution, works extremely well to improve the time scaling.

## D.2 One Dimensional Jacobi Model

In the one-dimensional version of the no-core shell model, we must build a basis of harmonic oscillator states (see Chap. C). This basis provides for a variational calculation with the accuracy directly connected to the the basis size,  $N_{\max}$ . Therefore, we need to understand how the basis scales and the resources that are consumed to build larger bases. Figure D.2 has on the left the size of matrices for different



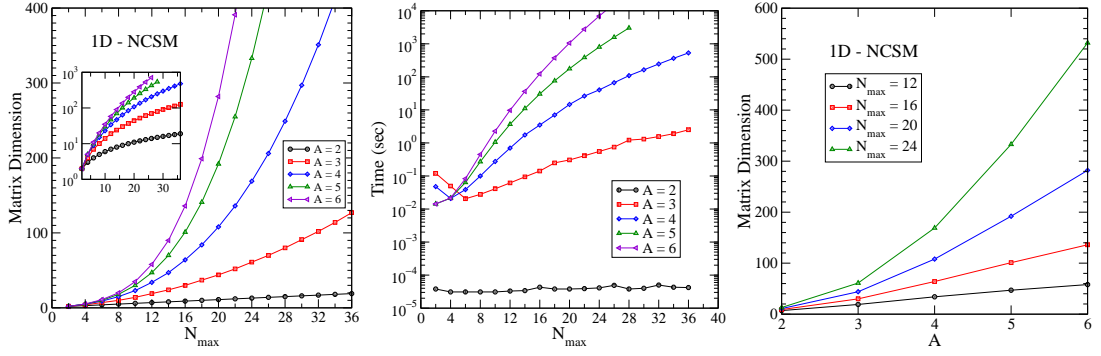


Figure D.2: Plots showing the scaling of One-D NCSM basis size and time to build those bases as a function of  $N_{\max}$  for  $A = 2, 3, 4, 5,$  and  $6$  bosons.

$A$ -body spaces as a function of  $N_{\max}$  and in the center a log-log plot showing the time to build the list of states for those bases. Note the log-log inset on the left plot shows the same dependence in  $N_{\max}$  as the timing plot indicating the build time is linear with the number of matrix elements. Here we can see dramatic increase in size and time as  $A$  increases from 2 to 6. The far right plot recasts this data as basis dimension versus  $A$  for several choices of  $N_{\max}$ . Again we can see the importance of bringing down the  $N_{\max}$  required for convergence in larger  $A$  systems. At small  $N_{\max}$  the size dependence on  $A$  is roughly linear. As  $N_{\max}$  increases we get back into the exponential region.

Again we must check on the scaling behavior of the SRG evolution with increasing basis size. The left panel of Fig. D.3 shows the evolution time in seconds as a function of the linear flow parameter,  $s$ , for several sample  $N_{\max}$  values. All are linear in  $s$ , again indicating no stiffening of the problem. On the right panel we display the same quantities in a log-log plot for better visibility. The slope of a straight line in this type of plot indicates the exponent of a power-law dependence, here the slope is unity and

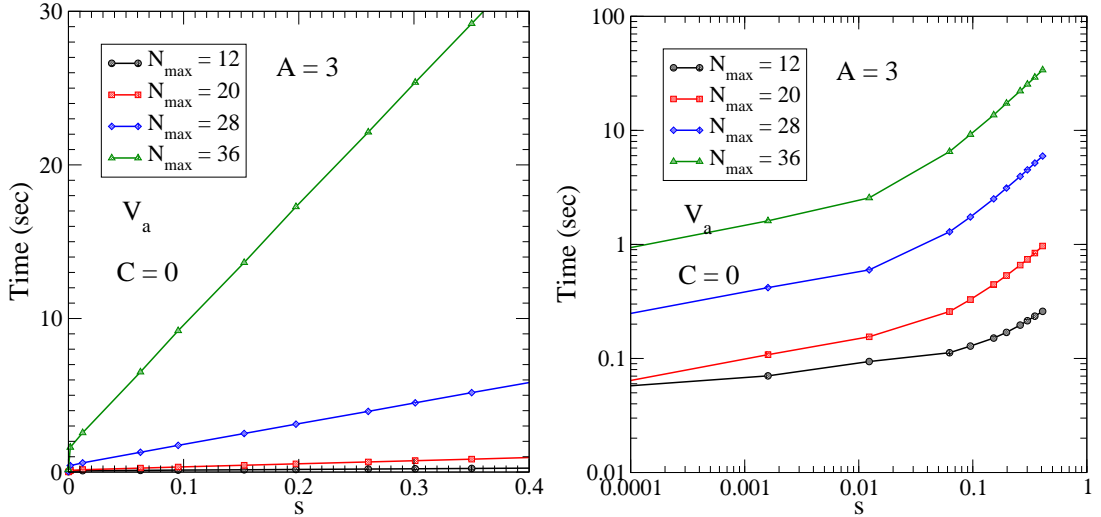


Figure D.3: SRG timings vs the parameter  $s$  show no stiffening for large  $s$  (small  $\lambda$ ). The log-log plot on the right gives a better view of the low  $N_{\max}$  samples.

the limits are set to make this apparent. The vertical shift indicates the difference in the slopes on the linear scale.

### D.3 Three Dimensional Jacobi NCSM

In the left plot in Fig. D.4 we can see a similar scaling of basis size with  $N_{\max}$  as in the one-dimensional version. This is yet another area where the one-dimensional model mirrors the behavior of realistic calculations and lends credence to its predictive power. The right panel of Fig. D.4 shows the SRG evolution is again robustly linear in  $s$  despite the different and complicated basis and embedding procedures of the realistic NCSM. This data had to be obtained from file write times so the curves are shifted vertically by an indeterminate amount of disk writing time.

Practical coding considerations have so far prevented realistic calculations in the relative Jacobi NCSM for nuclei larger than  $A = 4$ . As covered in appendix C the

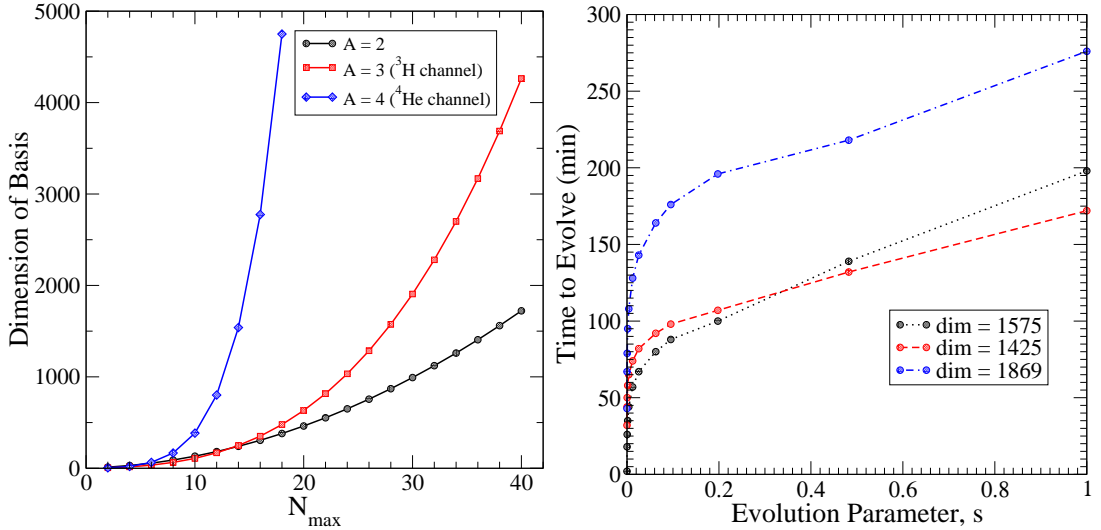


Figure D.4: The left plot shows scaling of NCSM basis size with  $N_{\max}$  for the two-, three-, and four-body systems. The right plot shows evolution timings vs.  $s$  in realistic NCSM calculations for selected  $A = 3$  partial waves. The legend indicates the dimension of the matrices being evolved.

calculation of larger systems is accomplished by converting the Jacobi matrix elements into the single-particle, or  $m$ -scheme, basis. This scaling is discussed in the next section with Fig. D.5. These problems have nothing to do with SRG implementation, but they have an incidental impact on how quickly progress can be made. Implementing the SRG independently in the  $m$ -scheme basis is a different body of work and will be an important check though the return may not be high for evolving extremely large sparse matrices. The initial potential would have to be in a basis close to convergence; previous work using the SRG within  $m$ -scheme calculations [35, 52] did the evolutions in the momentum basis, which is effectively  $N_{\max} = \infty$ .

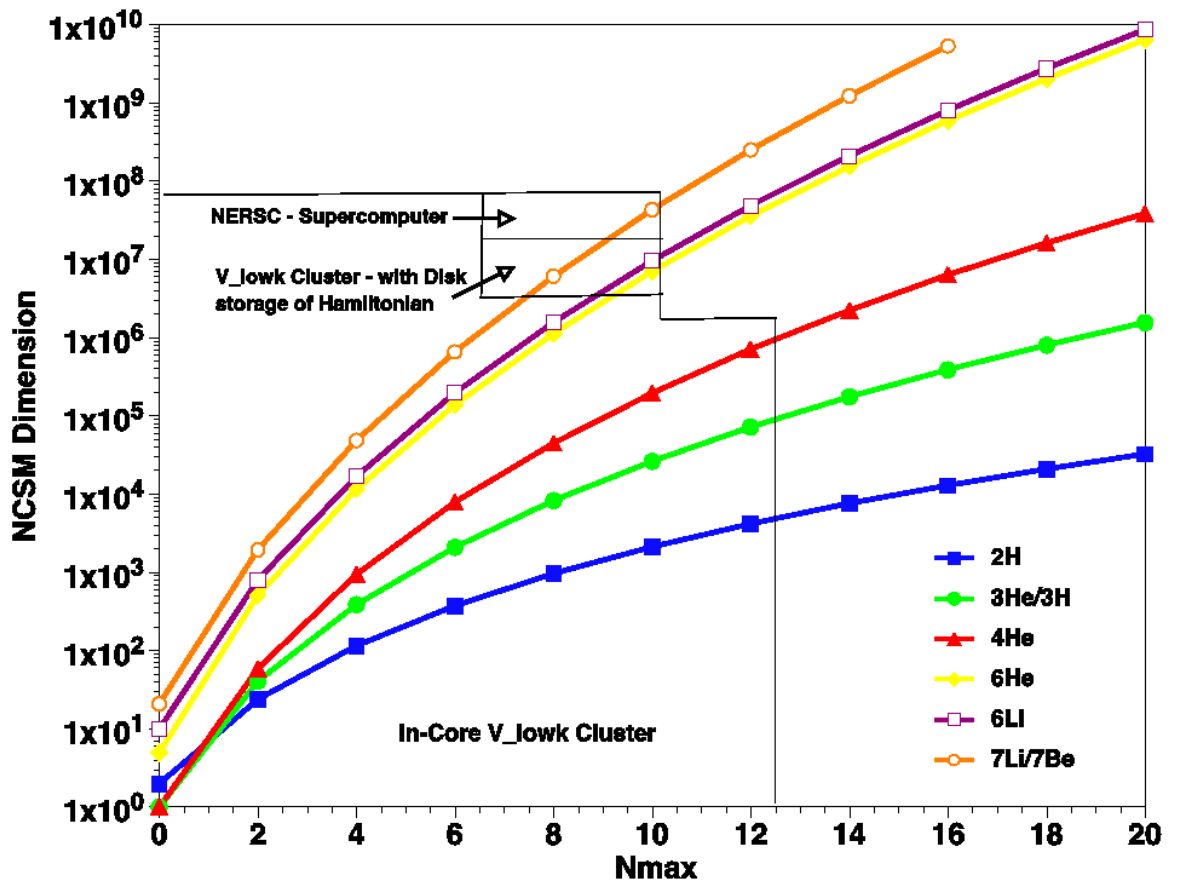


Figure D.5: Size of  $m$ -scheme basis as a function of  $N_{\max}$  for several light nuclei. Note the logarithmic scale in basis size.

## D.4 Lab Frame in One and Three Dimensions

In the decoupling studies of chapter 3 we used evolved NN forces embedded in the single particle NCSM, referred to as  $m$ -scheme, to compute light nuclei. It is important to note how much benefit the SRG provides to these particular calculations. Figure D.5 shows a plot on a log scale of the basis size verses  $N_{\max}$  for several lighter nuclei up to  $A = 7$ . The boxes indicate the extent of computational abilities for various systems. The box marked “V\_lowk Cluster - with Disk storage of Hamiltonian” indicates the limits of our abilities with our local cluster of 32 processors with the limitation of writing the large files to disk, which is a considerable slowdown. Also the basis dimension is not quite as daunting as it seems since these matrices are fairly sparse; the number of actual nonzero elements is in the range of the basis dimension itself. Still this is a very large number of matrix elements to compute and store. Clearly we would like to have converged results for the  $N_{\max}$  values within the larger box marked “In-Core V\_lowk” so that we can perform the calculations without expensive supercomputer resources. As shown in section 3.5 the decoupling afforded by the SRG enables these calculations to achieve just such a convergence.

Figure D.6 shows the scaling of basis sizes in the one-dimensional lab-frame basis. Note the dramatic increase in basis size over the one-dimensional Jacobi basis. This calculation has not been developed further due to its poor scaling properties as compared to the Jacobi version. However, it is an important check on the accuracy of calculations performed in the Jacobi basis, and further developments for this purpose will be straightforward as discussed in section F.4.

In one dimension, the lab-frame basis is not as efficient as the Jacobi basis in achieving convergence with basis size and therefore the Jacobi basis is preferred.

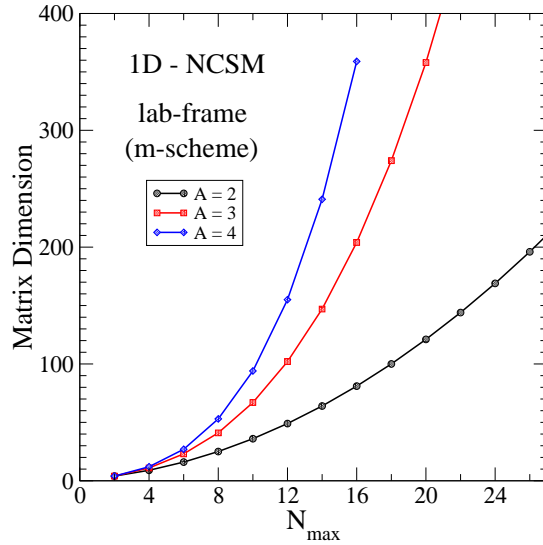


Figure D.6: A plot showing the scaling of One-D NCSM lab-frame basis or “ $m$ -scheme” size as a function of  $N_{\max}$  for  $A = 2, 3, 4$  bosons. Compare to Jacobi plots of Jacobi basis size in Fig. D.2.

However, in three-dimensions, angular momentum considerations change the situation. In the Jacobi basis for a given  $A$ -body calculation, one must include multiple angular momentum channels, or partial waves, to obtain accurate results. The coding involved in correctly accounting for all the necessary channels is apparently very involved due to the iterative procedure that builds on successive symmetrized  $A$ -body clusters. In contrast, the  $m$ -scheme strategy builds an  $A$ -body basis and symmetrizer from scratch and embeds the two- and three-body interactions directly into that space. Therefore the balance is tipped in favor of using large supercomputing to handle the large bases of the  $m$ -scheme, instead of continuing to develop code in the Jacobi basis.

## APPENDIX E

### SPURIOUS STATES FROM $G_S = H_{\text{ho}}$

In this appendix we will consider the spurious bound states which appear during the evolution with certain choices of the SRG generator,  $G_s$ . In the one dimensional model, we explored various features of these spurious states qualitatively through observing the evolution of potential matrix elements in the 1D basis. Watching the flow of individual elements can be very instructive when trying to understand the qualitative behavior of the SRG. Here we plot various potentials in the oscillator basis at  $N_{\text{max}} = 12$ , which is convenient for looking directly at the potentials and seeing the interplay among matrix elements.

Figure E.1 shows a film strip of evolving potentials in the three-body basis of the one-dimensional model. The top shows evolution using the choice  $G_s = T_{\text{rel}}$  and the bottom uses  $G_s = H_{\text{ho}}$ . The advantage of  $H_{\text{ho}}$  over  $T_{\text{rel}}$  with respect to the amount of diagonalization achieved in this basis is obvious as noted in chapter 4. However, problems arise when we try to isolate the evolving two- and three-body forces.

Figure E.2 shows the result of evolving the two-body potential using  $G_s = H_{\text{ho}}$  in that basis before embedding in the  $A = 3$  space and computing the two-body-only contribution to the  $A = 3$  bound state. The resulting evolution curve is analogous to that of Fig. 4.5 where we chose  $G_s = T_{\text{rel}}$  and the result was a nice smooth

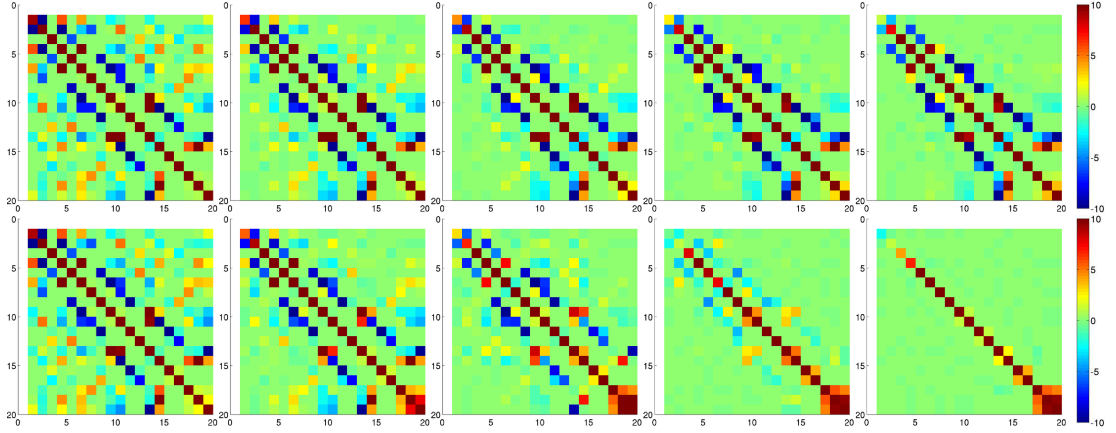


Figure E.1: A series of plots of the oscillator basis Hamiltonian in a reduced  $N_{\max}$  basis as it is evolved using  $G_s = T_{\text{rel}}$  (top) and  $G_s = H_{\text{ho}}$  (bottom) to  $\lambda = 7, 5, 4, 3, 2$ . The size of the basis shown is only  $N_{\max} = 12$  for visibility. Larger bases look qualitatively similar.

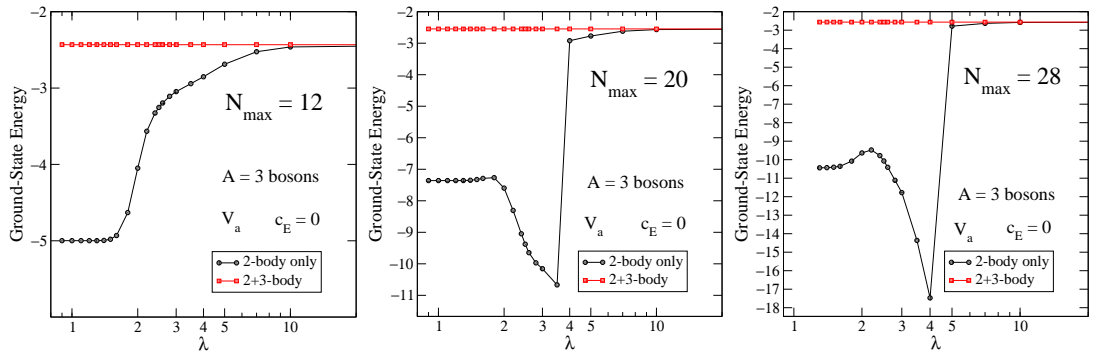


Figure E.2: An example of the discontinuous curves of two-body-only calculations characteristic of the  $G_s = H_{\text{ho}}$  SRG. The two-body-only curves computed by evolving the  $A = 2$  potential using  $G_s = H_{\text{ho}}$  and embedding the result in the  $A = 3$  basis to obtain the three-boson binding energy. The straight line labeled “2+3-body” is a check on the unitary evolution in the  $A = 3$  space.



Table E.1: A sampling of evolving  $A = 3$  spectra under the choice  $G_s = H_{\text{ho}}$ . The table uses values at  $N_{\text{max}} = 20$ , which is large enough to display the effect, but small enough to display the entire spectrum.

state	$\lambda = 100$	$\lambda = 5$	$\lambda = 4$	$\lambda = 3$	$\lambda = 2$
1	-2.547	-2.772	-2.920	-10.156	-7.597
2	0.049	-0.295	-0.456	-10.090	-7.497
3	1.713	1.192	0.370	-3.377	-5.129
4	3.103	2.479	0.760	-2.994	-4.199
5	5.709	4.847	2.126	-0.895	-3.649
6	6.615	5.595	2.701	-0.571	-3.544
7	7.525	6.830	3.771	0.672	-1.171
8	10.828	9.221	5.090	1.113	-0.878
9	12.276	10.627	7.192	1.634	0.114
10	13.401	11.291	7.670	2.614	0.190

curve indicating the effect of induced three-body forces, in the lone bound state, as a function of  $\lambda$ . Now, using  $G_s = H_{\text{ho}}$ , the curves are discontinuous<sup>22</sup> and the magnitude of induced three-body forces is much larger than expected. This plot turns out to be contaminated by the appearance of multiple three-body bound states due to the evolution of the two-body matrices with this  $G_s$ .

Table E.1 shows a sample of the first few states in the spectrum as the initial Hamiltonian is evolved with  $G_s = H_{\text{ho}}$ . The evolution proceeds as expected up to a  $\lambda$  value where new states begin to appear. As  $\lambda$  is increased further all the bound states deepen dramatically, though the precise behavior is dependent on the choice of  $G_s$ .

To further explore the origins of these states, we looked at the NN-only  $A = 3$  matrices as they are evolved and embedded. Figure E.3 compares the choices of  $T_{\text{rel}}$

<sup>22</sup>Note that the lines in Fig. E.2 are drawn to guide the eye from one point to the next. More sample  $\lambda$ 's may reveal this drop to be simply very steep.

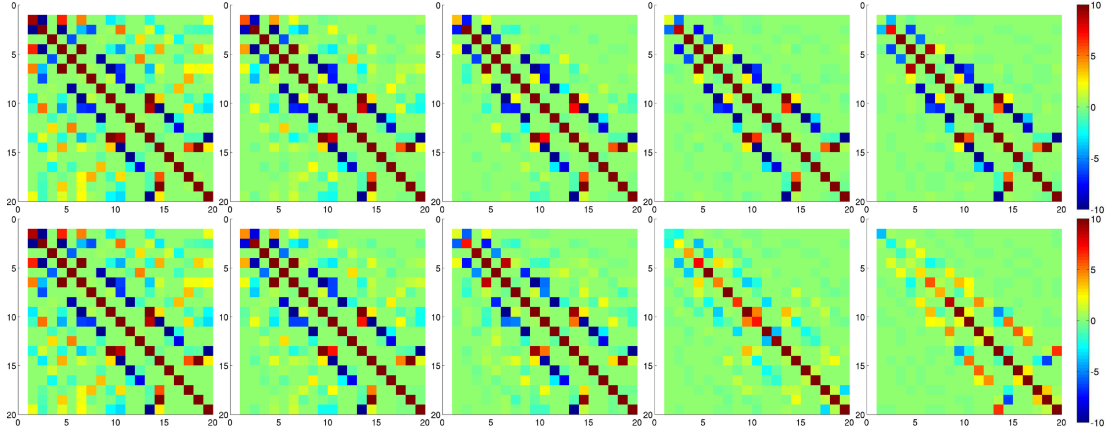


Figure E.3: A series of plots of the  $A = 3$  oscillator basis Hamiltonian in a reduced  $N_{\max}$  basis as it is evolved using  $G_s = H_{\text{ho}}$ .

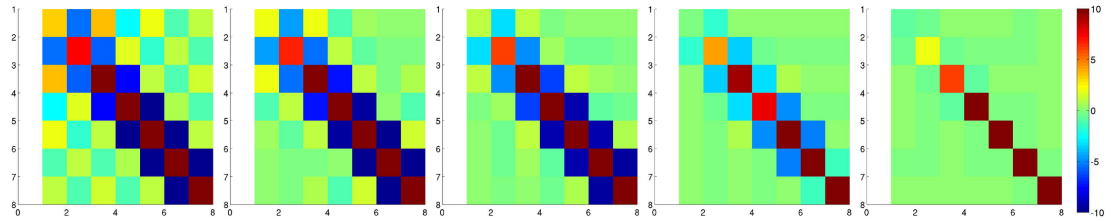


Figure E.4: A series of plots of the  $A = 2$  oscillator basis Hamiltonian in a reduced  $N_{\max}$  basis as it is evolved using  $G_s = H_{\text{ho}}$ .

and  $H_{\text{ho}}$  with film strips of these. Notice that while the  $T_{\text{rel}}$  version converges on a shape similar to  $T_{\text{rel}}$  itself, the  $H_{\text{ho}}$  version moves toward the diagonal and then recedes from it, ending up at a shape similar to the  $T_{\text{rel}}$  component but of opposite sign. This suggests that the fully unitary transformations are kept constant by means of large three-body forces being induced to compensate for some unknown effect in transformation of the two-body forces.

In figure E.4 a film strip is shown of evolving  $A = 2$ , matrices corresponding to the  $A = 3$  evolutions shown above. Notice how some matrix elements along the

diagonal mysteriously decrease so that they are not being driven to a monotonically increasing pattern as set by  $G_s = H_{\text{ho}}$ . As seen in chapter 3, the SRG tries to drive the matrix toward a shape dictated by the choice of  $G_s$ . With the matrix elements out of order according to the SRG form, it appears to induce strength in off-diagonal matrix elements coupling these smaller states. This in turn demands large off-diagonal three-body forces to be induced to compensate for this reordering. The exact cause of the disrupted ordering of states is not well understood presently but is a subject of ongoing investigation.

Moving up to the next many-body sector, we can look at the effect of the  $H_{\text{ho}}$  choice in a four-body system. In Table E.2 we show the evolving spectra for the two-body-only and two-plus-three calculations of the  $A = 4$  system. The former is on the top block of the table and the latter is on the bottom. In the top we can see the effect is magnified in the larger system. In the bottom the onset of the spurious states appears to be earlier, which is consistent with the different shape of two-plus-three body calculations of the four-body system. That is, the induced four-body force may be compensating for additional spurious contributions occurring in the  $A = 3$  sector.

In order to study the scale at which these spurious states appear, we also tried setting the potential to zero, leaving the initial Hamiltonian to be  $H_{s=0} = T_{\text{rel}}$ . We find that the spurious states appear suddenly at a specific value of the evolution parameter,  $\lambda = \sqrt{\hbar\omega}$ . This is expected since with  $V = 0$ , and most physical constants set to one,  $\hbar\omega$  is the only scale left in the problem, having units of energy or  $[\lambda]^2$ . By increasing the sampling of  $\lambda$  around the value,  $\sqrt{\hbar\omega}$ , we find that the onset of spurious states is indeed discontinuous, at least in the case of zero initial potential.

Table E.2: A sampling of evolving spectra for  $A = 4$  under the choice  $G_s = H_{\text{ho}}$ . Again the table uses values at  $N_{\text{max}} = 20$ . The upper block displays the two-body-only calculation while the lower block includes the two- and induced three-body forces.

state	$\lambda = 100$	$\lambda = 5$	$\lambda = 4$	$\lambda = 3.5$	$\lambda = 3$	$\lambda = 2$
1	-4.609	-5.496	-9.697	-42.757	-10.156	-33.059
2	-1.558	-2.752	-8.415	-34.195	-10.090	-27.979
3	0.812	-0.792	-6.021	-34.112	-3.377	-27.549
4	2.254	0.446	-3.215	-22.265	-2.994	-27.152
5	2.733	0.990	-2.301	-21.183	-0.895	-26.934
6	5.483	2.999	-1.974	-20.878	-0.571	-25.851
7	6.742	4.252	-1.912	-17.088	0.672	-25.692
8	7.620	5.152	-0.665	-16.396	1.113	-23.746
9	8.077	5.741	0.147	-15.059	1.634	-22.920
10	9.372	6.465	0.951	-14.269	2.614	-21.483
1	-4.609	-4.674	-29.265	-11.822	-6.029	-4.039
2	-1.558	-2.969	-11.135	-5.366	-4.016	0.745
3	0.812	-0.235	-8.177	-5.155	-3.004	1.856
4	2.254	0.735	-7.319	-4.190	-1.838	1.983
5	2.733	2.475	-4.210	0.154	0.398	5.157
6	5.483	5.361	0.083	2.472	2.378	8.707
7	6.742	5.529	1.500	3.532	4.328	11.501
8	7.621	6.095	2.001	4.142	6.327	11.619
9	8.077	7.414	6.263	5.964	8.342	13.510
10	9.372	7.473	6.382	7.188	9.963	16.678

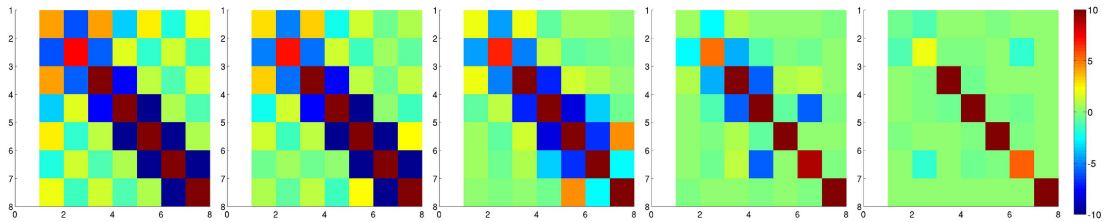


Figure E.5: A series of plots of the  $A = 2$  oscillator basis Hamiltonian in a reduced  $N_{\text{max}}$  basis as it is evolved using  $G_s = H_{\text{d,osc}}$ .

Table E.3: A sampling of evolving  ${}^3\text{H}$  spectra under the choice  $G_s = H_{\text{ho}}$  in the realistic three-dimensional NCSM. The table uses values at  $N_{\text{max}} = 20$  which is large enough to display the effect, but small enough to display the entire spectrum.

state	$\lambda = 100$	$\lambda = 5$	$\lambda = 2$	$\lambda = 1.5$	$\lambda = 1.2$	$\lambda = 1$
1	-7.4758	-7.5540	-8.7177	-10.0938	-145.6345	-118.5970
2	2.1186	2.0412	0.9895	-0.8918	-130.2285	-116.3076
3	6.5599	6.4646	5.1126	3.1332	-123.0114	-109.9408
4	6.8592	6.8040	5.8956	4.5028	-106.4009	-91.1749
5	12.7642	12.7365	11.0206	6.5762	-105.4125	-88.3281
6	13.5303	13.3832	11.7719	10.0159	-97.4654	-87.8343
7	15.7025	15.6187	13.9796	10.6716	-94.8004	-86.9702
8	16.4911	16.4027	14.7041	11.5136	-88.8669	-84.5732

We also tried other choices of  $G_s$  that are diagonal in the oscillator basis. In Fig. E.5 we show the evolution the  $A = 2$  Hamiltonian using  $G_s = H_{\text{d,osc}}$ , where  $H_{\text{d,osc}}$  is the diagonal part of the evolving Hamiltonian in the oscillator basis. Here we can still see the matrix elements evolving out of order and subsequent development of large off-diagonal elements in the evolution to push strength to low momentum. Here the effect is more dramatic than in the  $H_{\text{ho}}$  case, since the moving strength is jumping several states. This again forces large induced three-body forces to compensate for these evolved short range interactions.

We repeated this experiment in the three-dimensional NCSM code for calculations of the triton. The scale of the spurious states, relative to the initial bound states in that calculation, was similarly large. The spurious states appeared in the NN-only calculations in qualitatively similar ways. Table E.3 recreates the results of table E.2 using the three-dimensional NCSM. The first few states in the spectrum are shown at selected  $\lambda$ 's.

As can be seen in Fig. E.5 the SRG evolution on the two-body Hamiltonian seems to be driving information from high to low  $N_{\max}$  in an off-diagonal way. This pattern is indicative of spurious states being developed as the SRG builds large strength matrix elements at high-momenta and compensates for that by inducing large three-body forces.

So, while the lone constraint on  $\eta_s$  of anti-hermiticity grants a freedom of choice in choosing the form,  $G_s$ , of evolution, we must be careful of the effects that choice may have on the physics during renormalization of different parts of the interaction. Work is currently underway to investigate various choices of  $G_s$  which achieve convergence not only for binding energies but for other long-range observables such as the RMS radius. [42]

## APPENDIX F

### SINGLE PARTICLE COORDINATE OSCILLATOR BASIS

An important check on the Jacobi oscillator basis calculations done in this thesis is to repeat them in a different basis. An oscillator basis in single particle, or lab-frame coordinates has already been developed in three-dimensions and is used to compute nuclei above the practical range of the Jacobi basis. Here we develop a one-dimensional analog to the single-particle basis in the spirit of Ref. [95] and compare the results with our Jacobi basis calculations.

The general strategy used here for the lab-frame oscillator basis approach to the many-body problem is very similar to the Jacobi basis version. The allowed basis states are explicitly constructed and the states' quantum numbers listed. The nuclear interaction is embedded in the constructed basis. A symmetrization operator is built to isolate the physical states of the system. The symmetric  $A$ -body Hamiltonian is then diagonalized to obtain the energy spectrum. However there are several important differences in each of these steps; we will treat them in turn.

#### F.1 Embedding

Here we are working exclusively in single particle coordinates,  $k_1$  and  $k_2$ , but we have the potential in terms of Jacobi momenta because we already had a function

for it from the previous one-dimensional work. We must first convert our interaction from the Jacobi basis to the single particle basis. We will use the Talmi-Moshinsky transformation brackets that we are already familiar with from the Jacobi basis in appendix C. Formally, we can express this transformation of the potential as:

$$\begin{aligned}\langle n_1 n_2 | V | n'_1 n'_2 \rangle &= \langle n_1 n_2 | N n \rangle \langle N n | V | N' n' \rangle \langle N' n' | n'_1 n'_2 \rangle \\ &= \langle n_1 n_2 | N n \rangle \delta_{N, N'} \langle n | p \rangle V(p, p') \langle p' | n' \rangle \langle N' n' | n'_1 n'_2 \rangle\end{aligned}\quad (\text{F.1})$$

In our MATLAB implementation, Eq. (F.1) is accomplished by matrix multiplications. The matrix representing the transformation from momenta to oscillators,  $\langle n | p \rangle$ , is the same set of single-coordinate oscillator wavefunctions as used previously. The matrix representation of  $V(p, p')$  is read in directly from the expression of Eq. (4.3) as before. The delta function,  $\delta_{N, N'}$ , is embedded so that we are working in a full two particle basis organized by the total oscillator number,  $N_{tot} = N + n$  (i.e.,  $|Nn\rangle = |00\rangle, |01\rangle, |10\rangle, |02\rangle, |11\rangle, |20\rangle, |03\rangle, \dots$ ). The transformation brackets used here can be obtained from Eq. (C.9) by using  $d = 1$  instead of  $d = 3$  used there. This gives the rotation from the Jacobi center of mass, and first relative coordinate to the two single-particle coordinates.

As in the Jacobi case, the relative kinetic energy can be built from creation and annihilation operators:

$$\begin{aligned}\langle n_1 n_2 | T_{\text{rel}} | n'_1 n'_2 \rangle &= \langle n_1 n_2 | \frac{(k_1 - k_2)^2}{2m} | n'_1 n'_2 \rangle \\ &= \frac{1}{2m} \frac{-m\omega}{2} \langle n_1 n_2 | (a_1^\dagger - a_1 - a_2^\dagger + a_2)^2 | n'_1 n'_2 \rangle.\end{aligned}\quad (\text{F.2})$$

Or, we can take the kinetic energy as built in the Jacobi basis and convert using the transformation brackets as for the potential above. These two approaches are identical and important checks that our construction is consistent. However, for  $A > 2$  the



only practical option is the first option if we do not want to build transformation brackets for each  $A$ -body space conversion.

To calculate properties of an  $A$ -body system, we must be able to embed the two-, three-, and higher-body forces into the  $A$ -body space. First we build a list of the possible states in that space,  $|n_1 n_2 n_3 \dots n_A\rangle$ , and organize them into groups of total  $N \equiv \sum_{i=1}^A n_i$  up to the maximum,  $N_{\max}$ . For example, for  $A = 3$  the list starts out as: 0,0,0; 0,0,1; 0,1,0; 1,0,0; 0,0,2; 0,1,1; 0,2,0; 1,0,1; 1,1,0; 2,0,0; etc up to  $N = N_{\max}$ .

It is a relatively simple matter to look through the lab-frame states and place matrix elements of the two-body lab-frame interaction in the appropriate matrix elements of the  $A$ -body lab-frame basis. For a two-body interaction, we look through every pair of incoming and outgoing particles in every matrix element of the  $A$ -body basis and require a delta function in the initial and final energy of all other particles in the system. If these conditions are met, the appropriate two-body interaction matrix element is added to the  $A$ -body representation of  $V^{(2)}$ . A similar routine must be coded separately for embedding the three-body forces. This routine would likewise consider all triplets of particles and require a delta function in the others. This method of embedding is not the most efficient especially with regard to obtaining matrix elements between symmetric states as discussed below.

## F.2 Symmetrization

In lab-frame coordinates, to get a symmetric state of bosons (or antisymmetric for fermions), we must simply take the permanent (determinant) of matrices in the full oscillator representation. For example, the symmetric state with one particle in

an oscillator state  $n_i = 2$  and the other with oscillator 0 would be:

$$(\langle 02| + \langle 20|)V^{(2)}(|02\rangle + |20\rangle)/2 = (V(02; 02) + V(02; 20) + V(20; 02) + V(20; 20))/2; , \quad (\text{F.3})$$

where the 2 is the product of both normalization factors,  $1/\sqrt{2}$ .

Here we have used existing machinery to accomplish the permanent by building a symmetrizer matrix,  $S$ , and requiring that it be a projector,  $S^2 \equiv S$ . Instead of the Jacobi version, where we needed some complicated combination of transformation brackets to build  $S$ , simple factors of one over the number of permutations of a given state ensure that  $S$  is a projector for the single particle basis. By keeping the eigenstates of this matrix with eigenvalue one (and discarding those with eigenvalue zero), we obtain a non-square matrix analogous to the ‘‘coefficients of fractional parentage’’ used in the Jacobi case. The Hamiltonian and other operators expressed in the full single particle basis can be symmetrized using the physical eigenstate matrix just as done in the Jacobi case to obtain an operator in that basis.

For  $A = 2$ , both of these matrices can be seen in Fig. F.1. The symmetrizer shown on top has a simple structure with factors of  $1/2$  for those states with 2 permutations (i.e.:  $|02\rangle$  and  $|20\rangle$ ) and 1 for those which are already symmetric like (i.e.:  $|11\rangle$ ). Note that the eigenvectors of displayed in the bottom panel, have the correct normalization factors,  $1/\sqrt{2}$  for a symmetrized two-particle state.

For  $A > 2$ , we can build a symmetrizer operator from the list of total possible states discussed above. Now we have to be more careful of the permutations of states involved in symmetrizing. The number of permutations of a given state is computed and recorded as the list is built. By counting the number of particles with a certain oscillator number, the number of permutations of the state is given

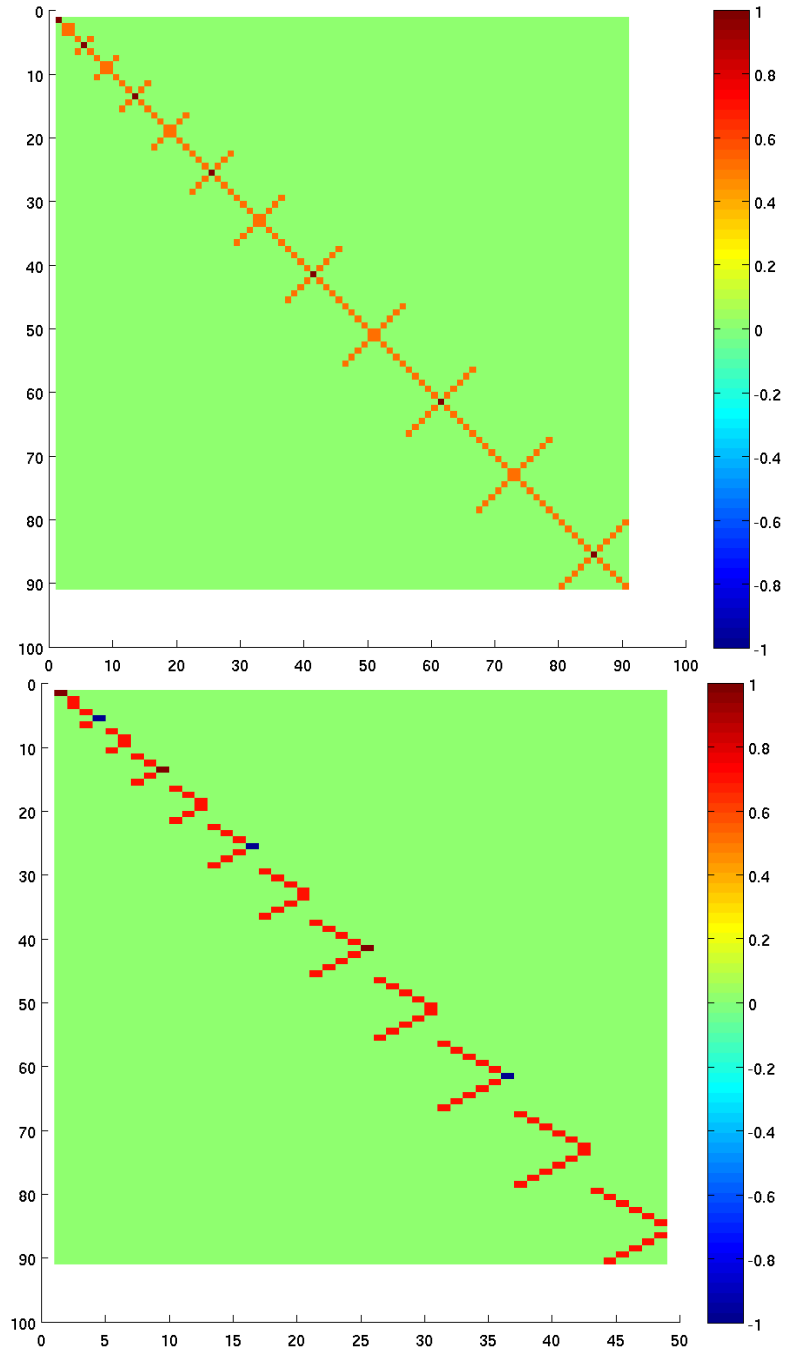


Figure F.1: A sample of the symmetrizer for the 2-body lab-frame problem on the top, and the corresponding non-zero eigenstates of the symmetrizer on the bottom. Here  $N_{\max} = 12$  as a more realistic  $N_{\max}$  would not be visible on the page.

by  $(A! / \prod_i^{N_{\max}} k_i)$  where  $k_i$  is the number of particles in the oscillator state  $i$ . To build the symmetrizer, we simply loop through the matrix elements of the full single-particle basis and compare the initial and final states. If one state is a permutation of the other and their number of permutations are recorded as the same, then one over that number is recorded for that matrix element of the symmetrizer.

Figure F.2 shows an example of the symmetrizer and the corresponding symmetric eigenstates for the  $A = 3$  system up to  $N_{\max} = 6$ . Note the smaller colors compared to the  $A = 2$  case because with more particles, there are more permutations of a given energy content. For instance, the faintest yellow corresponds to a value of  $1/6$  for states with 6 permutations (i.e.:  $|021\rangle$ ). The darker yellow is  $1/3$  for states like  $|112\rangle$ .

The matrices displayed in Figs. F.1 and F.2 for the physical symmetric eigenstates are the lab-frame analog to the coefficients of fractional parentage used in the Jacobi basis. Now, however, the construction of an  $A$ -body basis does not rely on an iterative procedure on the  $A - 1$  symmetrized basis. We can build the  $A$ -body basis from scratch, embed the two- and three- (and higher) body forces in that basis, and symmetrize them with the  $A$ -body symmetrizer built as just described.

This approach to building a symmetrized basis for lab-frame momenta is not the same as employed in three-dimensions. The overhead of building a large set of states and distilling out the symmetric states is very large in three-dimensions. Convergence is only feasible in one-dimensional calculations because of an overall reduction in basis size due to the omission of angular momentum quantum numbers. However, this is a useful check on the general procedure used in the Jacobi case, and can still be a useful tool for scaling up in  $A$  in one dimension. The method used here of building

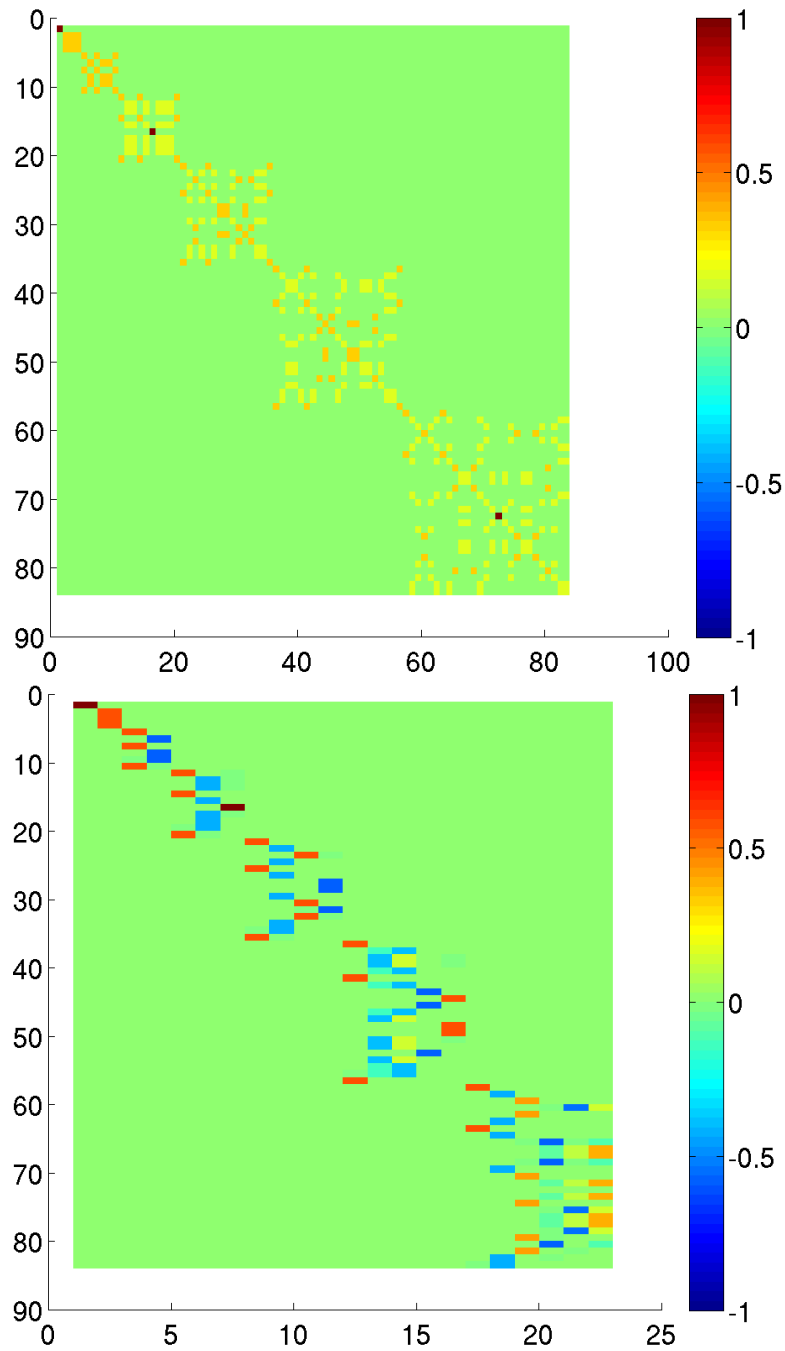


Figure F.2: The same as for Fig. F.1 but for  $A = 3$ . Here  $N_{\max} = 6$  as a more realistic  $N_{\max}$  would not be visible on the page.

a relatively simple symmetrizer operator can also be viewed as a first step to check future algorithms which may be less straightforward to code.

### F.3 Center of Mass Separation

A major difference from the Jacobi basis approach is the presence of the center of mass energy in the single-particle basis. For each value of the total center of mass energy, the  $A$ -body system has the same intrinsic spectrum. However, in our basis these copies of the spectrum are mixed up together, so we must separate them to obtain meaningful results. We can add some quantity which will boost the unwanted copies up in energy and isolate them. The harmonic oscillator Hamiltonian,  $H_{\text{cm}}$ , has the straightforward behavior in the oscillator basis that it doesn't mix up the intrinsic physics. Therefore, we can subtract off its effects to regain the desired spectrum.

So, in order to isolate the different center of mass states we will have to add

$$\beta(H_{\text{cm}} - (n + 1/2)\hbar\omega) \tag{F.4}$$

to the total interaction. The constant  $\beta$  is a large positive number which will provide large separation between the spectra at each of the center-of-mass eigenstates denoted by  $n$  ( $n = 0$  is the center-of-mass ground state). The value of  $n$  determines which center-of-mass solution we will isolate exactly, free of factors of  $\beta\hbar\omega$ . Spectra at center of masses less than  $n$  will be kicked downward and those greater than  $n$  will be kicked upward.

Writing out the center-of-mass Hamiltonian using creation and annihilation operators is a simple matter in the general  $A$ -body space:

$$\begin{aligned}
& \langle n_1 n_2 \dots n_A | H_{\text{cm}} | n'_1 n'_2 \dots n'_A \rangle \\
&= \frac{\hbar\omega}{8mA} \langle n_1 n_2 \dots n_A | \left( \sum_{i=1}^A a_i^\dagger + a_i \right)^2 - \left( \sum_{i=1}^A a_i^\dagger - a_i \right)^2 | n'_1 n'_2 \dots n'_A \rangle \\
&= \frac{\hbar\omega}{8mA} \langle n_1 n_2 \dots n_A | 2 \sum_{i,j=1}^A (a_i^\dagger a_j + a_i a_j^\dagger) | n'_1 n'_2 \dots n'_A \rangle \\
&= \frac{\hbar\omega}{8mA} \langle n_1 n_2 \dots n_A | 2 \sum_{i=1}^A (a_i^\dagger a_i + a_i a_i^\dagger) + 4 \sum_{i=1}^A \sum_{j=i+1}^A (a_i^\dagger a_j) | n'_1 n'_2 \dots n'_A \rangle \\
&= \frac{\hbar\omega}{8mA} \langle n_1 n_2 \dots n_A | 2 \sum_{i=1}^A (2n'_i + 1) \delta_{n_i, n'_i} \\
&\quad + 4 \sum_{i=1}^A \sum_{j=i+1}^A \sqrt{n'_j} \sqrt{n'_i + 1} \delta_{n'_i+1, n_i} \delta_{n'_j-1, n_j} | n'_1 n'_2 \dots n'_A \rangle . \tag{F.5}
\end{aligned}$$

This is written in the same basis as the potential and kinetic energy and can be symmetrized by the same process as described in section F.2.

Table F.1 shows an example of the separation of different center of mass spectra due to  $H_{\text{cm}}$ . Columns showing the labels of the center-of-mass and intrinsic states are meant to aid the reader's eye when viewing these spectra. The left shows the spectra from different center-of-mass energies entangled. For instance, all the ground states are collected together as the lowest energies and next the first excited states. Separating these by hand is not a trivial matter, especially in larger systems. In contrast, the right side shows the same spectrum but now separated by a strong  $\beta$  term. The spectrum from the lowest center of mass appears at the head of the list. The next spectrum is multiplied by  $\beta\hbar\omega$  (here  $\beta = 1000$  and  $\hbar\omega = 5$ ), the third by  $2\beta\hbar\omega$ , etc.

Table F.1: A sample of the spectrum resulting from the lab-frame basis at a small  $N_{\max}$  before and after separation by a  $H_{\text{cm}}$  term. The columns right of each list of energies show the center of mass and intrinsic energy level numbers,  $n$  and  $l$ . The last column shows the effective  $N_{\max}$  for the right-most spectra. The value of  $\beta\hbar\omega$  here is 5000. Note the “separated” values should be scaled by  $10^4$ .

mixed	$(n, l)$	separated ( $\times 10^4$ )	$(n, l)$	eff. $N_{\max}$
-0.812294429336271	(0, 0)	-0.000081229442933	(0, 0)	6
-0.487362126673450	(1, 0)	0.000409822038397	(0, 1)	6
-0.487362126673446	(2, 0)	0.001080597080727	(0, 2)	6
-0.482179966274186	(3, 0)	0.002687021583751	(0, 3)	6
-0.482179966274182	(4, 0)	0.499951263787332	(1, 0)	5
4.098220383969666	(0, 1)	0.500489798221359	(1, 1)	5
4.817772759274547	(5, 0)	0.501990571277867	(1, 2)	5
4.817772759274551	(6, 0)	0.999951263787332	(2, 0)	4
4.897982213589284	(1, 1)	1.000489798221359	(2, 1)	4
4.897982213589287	(2, 1)	1.001990571277867	(2, 2)	4
10.805970807270517	(0, 2)	1.499951782003372	(3, 0)	3
12.846759311682062	(4, 1)	1.501284675931167	(3, 1)	3
12.846759311682076	(3, 1)	1.999951782003373	(4, 0)	2
19.905712778674406	(1, 2)	2.001284675931168	(4, 1)	2
19.905712778674410	(2, 2)	2.500481777275925	(5, 0)	1
26.870215837516941	(0, 3)	3.000481777275927	(6, 0)	0

Each of the spectra obtained in this way are identical in a complete  $N\hbar\omega$  space, but we must work in a truncated space. The most accurate spectrum is that of  $n = 0$  because the other spectra begin at larger and larger center of mass energies and have fewer basis states available to contain their excited states. In this way we can see the effect of truncation in  $N_{\max}$  as we look up in center-of-mass energy. There are fewer and fewer states in the spectrum until the center-of-mass energy is  $N_{\max}$  and there is no more “space” for excitations in the basis. Note that this truncation is identical to that done explicitly in the Jacobi calculations. On the right side of table F.1 we show



the effective  $N_{\max}$  for each center-of-mass spectrum. The ground states for each of these spectra are identical to the ground states from the Jacobi calculations truncated to the  $N_{\max}$  shown in the last column.

## F.4 Evolution Results

Just as in the Jacobi basis, implementation of the SRG's flow equations is a straightforward matter in the lab-frame coordinates. The Hamiltonian and generator are given to a differential equation solver and the resulting evolved Hamiltonian is diagonalized to produce a spectrum of states for that  $A$ -body system. Also as in the Jacobi basis, evolved  $n$ -body forces must be isolated and embedded with the appropriate symmetry factor into the  $A$ -body space. At present, existing algorithms are only sufficient for embedding two-body operators into an  $A$ -body space. This limits us to NN-only and fully unitary calculations of  $A$ -body spaces. Additional codes are needed before the  $m$ -scheme version can be used to check the hierarchy of induced many-body forces in systems with  $A > 3$ . However, for  $A = 3$  we can perform the calculation analogous to that of Fig. 4.5 and find identical results to within expected numerical errors. Further coding to check the hierarchy for larger  $A$  is a straightforward next step for this tool.